Distinct element modeling for fundamental rock fracturing and application to hydraulic fracturing

Hiroyuki Shimizu

ACKNOWLEDGMENTS

CONTENTS

Chapter 3 Distinct element analysis for rock failure considering AE events generated by the slip at crack surfaces

Chapter 4 Distinct element analysis for Class II behavior of rocks under uniaxial compression

Chapter 5 Distinct element analysis for hydraulic fracturing in hard rock considering fluid viscosity and particle size distribution

Chapter 6 Distinct element analysis for hydraulic fracturing in unconsolidated sands

LIST OF FIGURES AND TABLES

Chapter 2

Chapter 3

Chapter 4

Chapter 5

Chapter 6

APPENDIX

NOMENCLATURE

Chapter 1

P_b	break down pressure
P_0	initial pore pressure
σ_1	maximum compressive stress
σ_3	minimum compressive stress
T	tensile strength of the rock

Chapter 2

f_n	increments of normal force
f_s	increments of tangential force
f_θ	increments of moment
k_n	stiffness of normal springs
k_s	stiffness of shear springs
k_θ	stiffness of rotational springs
dn	normal displacements of a particle
ds	shear displacements of a particle
$d\theta$	rotation of a particle
r_i, r_j	radii of the bonded particles
L	bond length
D	bond diameter
C_n	coefficients of viscous damping in normal direction
C_s	coefficients of viscous damping in shear direction
m_{ij}	reduced mass
m_i, m_j	particle mass
A	cross-sectional area of the bond
I	moment of inertia of the bond
E_p	Young's modulus of particle and bond
ν_p	Poisson's ratio of particle
α	shear/normal spring stiffness ratio
σ	normal stress acting on the cross-section of the bond
τ	shear stress acting on the cross-section of the bond
$\lvert \tau/\sigma \rvert$	shear-tensile stress ratio

E_k	strain energy at the contact point
k_{nn}	stiffness of the contact springs in the normal direction
k_{ss}	stiffness of the contact springs in the shear direction
$d_{contact}$	contact diameter
F	contact normal compression force
s	contact spring stiffness ratio
G	shear modulus
C_{nn}	coefficients of viscous contact damping in normal direction
C_{ss}	coefficients of viscous contact damping in shear direction
$f_{s\,max}$	maximum frictional force
$\tan\phi_p$	coefficient of friction
ε_1	axial strain
ε_2	radial strain
F_{platen}	total force acts on the upper loading platen
d	diameter of the model for Brazilian test
l	length of the model for Brazilian test

Chapter 3

E_{slip}	released strain energy due to the slip occurrence
$E_{kbefore}$	strain energy at the time step before slip occurrence
E_{kafter}	strain energy at the time step after slip occurrence
ε_v	bulk strain
M	magnitude of AE event
N	the number of AE events of magnitude M or greater
a	a constant value
b	seismic b-value
M_m	minimum magnitude of AE event

Chapter 5

Q	volumetric laminar flow
w	aperture of a channel
L_p	length of a channel
ΔP	change in pressure across a channel
μ	viscosity of the fluid

w_0	initial aperture of a channel
F_0	normal force at which the channel aperture decreases to half of its initial aperture
dP	change in fluid pressure
$\sum Q$	total flow from the surrounding channels
dt	duration in one time step
K_f	fluid bulk modulus
V_r	apparent volume of the domain
dV_r	the change in the volume of the domain
u	velocity distribution for laminar flow between parallel plates
τ_f	shear stress at a surface element parallel to a plate
τ_{f0}	wall shear stress
f_c	total force acting on a plate caused by fluid flow
P	fluid pressure
f_d	total force that act on the center of a particle
φ	corner half-angle of a domain
S_t	saturation factor in each domain
V_f	volume of fluid that exists in the domain
po	assumed porosity of the model
Q_{steady}	steady flow rate
W	height of the model for permeability test
H	width of the model for permeability test

Chapter 6

f_a	tensile force acting between the particles in unconsolidated sand
k_a	stiffness of the spring in unconsolidated sand
ε	strain of the spring
σ_{max}	maximum tensile stress (tensile strength)
ε_{max}	maximum strain
k	permeability of the unconsolidated sand model
q	injection rate of the fracturing fluid
μ	viscosity of the fracturing fluid

Chapter 1
Introduction

1.1. Introduction

Due to the rapid advance of computer technology, various numerical analysis techniques have been developed and applied to various problems in the rock engineering fields. Numerical simulation makes it possible to consider generation of microcracks that are difficult to measure in the experiment, and give us rational understandings for complicated fracturing process in many materials.

Traditional numerical techniques, such as the finite element method (FEM) and the boundary element method (BEM) are powerful techniques for various problems in many areas of engineering and science, and can be applied to both quantitative and qualitative research. However, since these simulation algorithms relied on a grid or a mesh, adaptive techniques and complex remeshing procedures are required to treat nonlinear material behavior such as microcrack generation, large deformation and propagation of arbitrarily complex crack paths,.

In contrast, the Distinct Element Method (DEM) is a numerical technique that originally developed for discontinuum materials, and directly represents grain-scale microstructural features of rock like materials [1,2], such as pre-existing flaws, pores, microcracks and grain boundaries. These grain-scale discontinuities in the DEM model induce complex macroscopic behaviors without using complicated constitutive laws/equations. This means that the DEM model may be more realistic and appropriate representation of rock fracturing comparing with other numerical simulation techniques such as FEM.

The DEM have been applied for solving many rock mechanics problems at laboratory scales, such as triaxial testing of rocks with complete stress-strain curves [3], failure around a circler opening under biaxial compression [4], direct shear test of a rock fracture [5], acoustic emissions (AE) [6,7] and hydraulic fracturing tests of granite [8] for laboratory scale simulations. Also DEM has been used to simulate large field scale rock engineering problems such as tunnel/cavern excavation and evaluation of EDZ [3], tunnel face stability [9], design of tunnel lining [10], rock cutting and slope stability analysis [11]. However, the fracturing process of rock is complicated, and the damage behavior of brittle materials is still remains a challenging task.

Based on this situation, in order to give the rational explanation to the complex fracturing process of brittle materials, a series of simulations are performed by newly

developed Distinct Element Method (DEM) code that can model the microcracking behavior in brittle materials. Although development of own calculation code from scratch is a long and tedious process, it should give us great advantages in numerical study. By developing own code, I know where everything is, and exactly what the code is doing. This information is useful for modification of source code and interpretation of simulation results.

In this thesis, several new findings for the following three critical issues in rock engineering projects are presented.

The first issue is to better understand the behavior and the properties of the brittle rock in the pre- and post-failure region. In particular, the post-failure behavior of the brittle rock is of significant importance for rock engineering because it directly influences the sudden and violent fracture of rock that well known as a rockburst in the mining industry. The rockburst was first reported in England in 1738, and now becomes one of the most serious geological hazards during deep underground excavation, such as the deep mining, the deep buried long tunnel and the long-term disposal of High-level Radioactive Waste (HLW). Therefore, the rockburst has attracted a high degree of attention in engineering geology and rock mechanics, and understanding of the mechanism of rock failure under compressive stress conditions is of vital interest. However, at present, it is still difficulties to accurately obtain the fracturing behavior of brittle rocks not only in laboratory experiments but also numerical simulations because it suddenly falls into uncontrolled when the compressive stress exceeds the peak strength. Therefore, a new approach which accurately describe the pre-failure as well as the post-failure behavior of brittle materials must be developed.

The second issue is the hydraulic fracturing. Most of rock engineering projects, such as the production of hydrocarbon reservoirs and extraction of geothermal energy are all closely related to fluid flow in fractured rock mass. Since the conditions of fluid flow in many cases depend on the mechanical behavior of rocks, coupling between the liquid phase and the rock matrix should be considered. Hydraulic fracturing is a method used to create fractures. Highly pressurized fluid is pressed into the borehole, and an artificial fracture that extends from a borehole into rock mass is generated. Hydraulic fracturing technique is originally applied for the production of oil and natural gas [12]. Recently, hydraulic fracturing is also applied to disposal of waste by injection into suitable deep rock formations [13], heat production from the hot dry rock (HDR) geothermal reservoir [14,15], and as a method to measure the in situ stresses [16,17,18]. Whatever purpose it is, to use the hydraulic fracturing effectively and control the fracture geometry so as to maximize the benefits, it is necessary to clarify the mechanism of the hydraulic

fracturing. Hydraulic fracturing processes are affected by many factors, such as grain size of the rock [19], permeability of the rock [20,21], viscosity of the fracturing fluids [22,23], confining pressure [24,25], etc. Therefore, even at present, it is still difficult to investigate the hydraulic fracturing mechanisms consistently due to the complicated process of the hydraulic fracturing and the multitude of variables involved.

The third issue is to clarify the hydraulic fracturing behavior in unconsolidated sands. Recently, hydraulic fracturing is applied on various conditions, even if the targeted strata are located below sea bottom. One of the applications is production of the methane hydrate. The methane hydrate is expected as a new energy resource that takes the place of oil and gas [26]. The methane hydrate mainly exists in unconsolidated sediments below a sea bottom, and it takes neither a form of gas nor liquid but ice-like solid. However, the technique of hydraulic fracturing mentioned above has been originally developed assuming to be applied to consolidated rock, such as sandstone and granite, but not unconsolidated sediments, such as sand and mud layer. Therefore, it is unclear whether fracture-like structure is formed or not when high fluid pressure is applied to such unconsolidated sediments in hydraulic fracturing procedure. To clarify the hydraulic fracturing behavior in unconsolidated sands, and to design it effectively, a new approach different from the conventional theoretical model for the consolidated rock is required.

In this chapter, the previous researches on these subjects are reviewed, and the objectives and outline of this thesis are presented.

1.2. Literature review

1.2.1 Fundamental brittle rock fracturing

The brittle fracture of rocks has been the most studied issue in rock mechanics fields, and it is commonly agreed that the microcracking in brittle rock is very important because macroscopic behaviors, such as fracture and local failure, are strongly controlled by the generation and interaction of microcracks [27]. Actual rock specimen contains many pre-existing flaws such as pores, microcracks and grain boundaries. The fracturing process of rock is complicated and sometimes shows probabilistic aspects because such microstructures in a rock specimen cause the heterogeneous transmission, orientation and concentration of microscopic forces and moments, which directly influence the sudden and violent fracture of rock

In addition, the post-peak behavior of rocks is one of the key issues for rock mechanics problems because it is closely related to the sudden and violent fracture that

sometimes causes a serious disaster in some deep mines. It is called as the rockburst. For the better understanding such a mechanical behavior of brittle rocks, many laboratory experiments have been performed. In the 1960's, many uniaxial compression tests using high stiff testing machine were carried out to understand the failure mechanism of brittle rocks, and they enable to obtain the post-peak behavior of rocks such as complete stress-strain curves [28,29]. Wawersik [30,31] obtained successfully the complete stress-strain curves for various rocks using a stiff testing machine, and classified rock mechanical behavior under uniaxial compression into Class I and Class II according to complete stress-strain curves. For Class I behavior, axial strain rate keeps constant even though the axial stress exceeds the peak strength, and the stress-strain curve monotonically increases in axial strain. On the other hand, for the Class II behavior, it suddenly falls into uncontrolled when the axial stress exceeds the peak strength and the curve can not be obtained by usual manner. Therefore, it is necessary to control violent collapse of the specimen to obtain the Class II complete stress-strain curve [32]. Hudson *et al*. conducted the uniaxial compression tests with servo-controlled testing machine in which the radial strain rate was controlled constant, and obtained the Class II complete stress-strain curve successfully [33,34].

Recently, servo-controlled testing machine is commonly used, and various experimental values were selected as the feedback signal. Sano *et al*. controlled inelastic volumetric strain rate [35]. Terada *et al*. accomplished the servo-controlled uniaxial compression test using AE rate [36]. Okubo *et al*. proposed the control method with linear combination of axial stress and strain [37,38]. These recently developed servo-controlled testing machines and various testing methods enable to investigate the failure behavior of rock in detail [39,40]. However, at present, there are still difficulties to obtain complete stress-strain curve of brittle rocks in the laboratory experiments, and the Class II post-peak behavior has not been sufficiently clarified. Therefore, a series of DEM simulation for fundamental rock tests are performed by using own DEM code, and new approaches to reveal the mechanisms of the brittle behavior of rock in the pre- and post-failure region are provided in this thesis.

1.2.2 Hydraulic fracturing in consolidated rock

To better understand the mechanics of hydraulic fracturing, a considerable amount of research both in laboratory and field scale has been carried out in the past few decades.

Hubbert and Willis theoretically showed that hydraulic fracture is created by tensile crack and extend along the direction of maximum compressive principal stress [41]. According to their theory of hydraulic fracturing, the breakdown pressure associated with the formation of a radial fracture is given by

$$P_b = 3\sigma_3 - \sigma_1 + T - P_0 \qquad\qquad (1.1)$$

where σ_1 and σ_3 are the maximum and minimum compressive stress and T is the tensile strength of the rock.

Based on their theory, methods for measuring tectonic stress using the hydraulic fracturing have been developed and applied to problems in mining engineering, civil engineering, petroleum engineering and geophysics [16,42].

However, several problems remain to be investigated in applying the breakdown pressure to the tectonic stress measurements. One major problem for the breakdown equation derived from Hubbert and Willis is that they further assumed the pressurized wellbore fluid did not infiltrate into the rock matrix prior to the fracturing. Neglecting the infiltration of the fluid would lead the overestimation of the maximum principal stress.

To solve these problems, Haimson [43,44] developed a more sophisticated model and theoretically derived an expression similar to equation (1.1) when fluid penetration occurs. Ito *et al*. [17,20] developed a new theory based on the point stress criterion. The point stress criterion assumes that the fracture would initiate when the tensile stress inside the rock (not on the borehole surface) reaches the tensile strength of a rock.

To validate these theoretical models mentioned above, monitoring of acoustic emission (AE) has been used to clarify how the hydraulic fracturing extends. The AE monitoring was widely applied to investigate the hydraulic fracturing behavior at large field scale [45], such as HDR geothermal energy extraction [46,47], reservoir stimulation in the hydrocarbon industry [48,49] and in waste reinjection experiments [50]. Also the AE monitoring has been applied to laboratory scale hydraulic fracturing experiments. Based on the results of laboratory experiments, Lockner and Byerlee [51] proposed a relationship between flow rate and AE. Zoback *et al*. [22] showed that viscous fluids could induce fractures in the maximum compressive stress direction even though the borehole included pre-existing cracks crossing in other directions. Matunaga *et al*. [19] and Sasaki *et al*. [52] examined fracturing mechanisms in granite, marble, andesite and acrylic by obtaining AE source locations and fault plane solutions. Ishida *et al*. [23] carried out laboratory hydraulic fracturing experiments with slick water and high viscous oil, and investigated the influence of the fluid viscosity.

However, although AE monitoring experiment revealed the mechanisms of the hydraulic fracturing from the recorded AE wave form, the results does not generally agree with assumed mechanisms in conventional theoretical models. Most of the fault

plane solutions derived from AE events that are recorded during both in laboratory and field scale have been classified as the shear type mechanism, whereas the theoretical models based on the linear elastic fracture mechanics (LEFM) theory generally assume tensile fracture growth. The disagreement between conventional theory and the AE monitoring results has not yet been solved.

Moreover, efforts to give the rational explanation to such disagreement and to better understand the hydraulic fracturing mechanism have been made using the numerical simulation. The FEM and the BEM have been used to simulate hydraulic fracturing in complex three-dimensional structures [53,54]. Al-Busaidi *et al.* [55] performed the simulation of hydraulic fracturing in granite by using the DEM, and compared the results with the AE data from the experiment. However, the previous simulation results did not solve sufficiently the disagreement mentioned above. Hence, in this thesis, simulations for hydraulic fracturing in consolidated rock are performed by using the flow-coupled DEM code to discuss the influence of the fluid viscosity and the particle size distribution, and to obtain insights that gave the rational explanation to the disagreement between conventional theory and the AE monitoring results.

1.2.3 Hydraulic fracturing in unconsolidated sands

Hydraulic fracturing is now widely used not only in petroleum industry, but also in many other fields. Thousands of operations are successfully conducted in very diverse geological settings.

Due to the increasing importance of hydraulic fracturing, a significant amount of work has been done in the theoretical modeling of hydraulic fractures in rocks in the last half century. Earlier works on theoretical modeling of hydraulic fracturing involved to find approximate solutions for simple fracture geometries. The model developed by Perkins and Kern [56] adapted the classical plane strain crack solution of Sneddon and Elliot [57], so-called the PK model. The work by Perkins and Kern was further improved by Nordgren [58] and this model is called the PKN model. In the PKN model, the effect of fluid loss into the surrounding rock mass was investigated. Another model, known as the KGD model was developed by Khristianovic and Zheltovand [59] and by Geertsma and de Klerk [60]. This model assumes that the fracture deformation and propagation evolve in a situation of plane strain. Moreover, analytical solutions for Penny-shaped or radial crack problems are given by Sneddon [61]. Abé *et al.* [62,63] considered the dynamics of linearly propagating three-dimensional penny-shaped cracks.

These conventional models for hydraulic-fracture are based on the LEFM theory.

LEFM assumes that the material is isotropic, linear elastic and impermeable or low permeable, and that the inelastic deformation is small compared with the size of the crack. Based on the assumptions, the stress field near the crack tip is calculated using the theory of elasticity, and the fractures initiate and propagate when the stress intensity factor at crack tip exceeds the material fracture toughness. However, unconsolidated sands are characterized by extremely high permeability, little or no tensile strength and non-linear mechanical behavior. Hence, fluid leak off and large non-linear tip deformations become very important for fracture initiation and growth.

Therefore, LEFM can not explain sufficiently the hydraulic fracturing in unconsolidated sands. In fact, field data show that conventional models relying on classical brittle-rock fracture mechanics do not adequately represent fracturing in poorly consolidated rocks [64-67]. To obtain the knowledge concerning the fundamental aspects of hydraulic fracturing in unconsolidated sands, and to resolve the various problems of interpretation, control, and promotion of failure, extensive studies have been conducted in last few decades.

For example, Khodaverdian and McElfresh [64] performed a series of hydraulic fracturing injection experiments in unconsolidated sands, and found that fracture propagation in unconsolidated sands is primarily a result of shear failure in a process zone ahead of the fracture tip. They also suggest that the shear failure is governed by pore pressure increase within the fracture tip due to the permeation of the fracturing fluid.

Di Lullo *et al*. [68] provided an alternative mechanism for the initiation and propagation of the shear-failure zones based on their experiments. Chang [69] conducted several experiments to investigate the principal fundamental mechanisms of hydraulic fracturing in particulate materials and determine relevant scaling relationships. Moreover, de Pater and Dong [70] injected bentonite slurry into the borehole without creating a clear fracture, and observed large shear deformation starting from the borehole. Wang and Sharma [66] measured the mechanical properties of poorly consolidated sands.

In addition, some models for the numerical simulation of the hydraulic fracturing process have been presented. Zhai [71], Zhai and Sharma [72] proposed a new approach to modeling the mechanical behavior of unconsolidated sands that models permeability and porosity as a function of effective stress. As a result, they successfully reproduced the creation of an anisotropic zone of increased porosity and permeability along the plane of maximum in-situ stress. Wu [73] introduced a hydraulic fracturing model that explicitly describes the fracture front and the fluid flow. The model is consistent with

experimental observations and is based on the physical mechanism of shear band. A numerical simulation using a two-dimensional finite difference program (FLAC^{2D}) was conducted to gain insight into the shear band hypothesis. Moreover, they also conducted a series of numerical experiments to model fluid injection into a particulate material by using the commercially available DEM code (particle flow code: PFC). These works presented successful results in particular geological conditions. However, they could not be used to predict the fracturing behavior in unconsolidated sands under different and untried geological conditions.

Regarding this situation, Igarashi *et al*. [74,75] performed a series of laboratory hydraulic fracturing experiment under true triaxial compression in unconsolidated sand specimen with varying control parameters such as the properties of materials and injected fracturing fluids, boundary conditions, initial stress states, and injection volumes and rates. As a result, it is found that the hydraulic fracturing behavior is strongly affected by the viscosity of fracturing fluid, the pressurization rate and the permeability of the specimen. However, the detail of the mechanism for hydraulic fracturing behavior has not been sufficiently clarified. Therefore, in this thesis, a new DEM code for the unconsolidated sand is developed, and the mechanism of the hydraulic fracturing in the unconsolidated sands was discussed in detail to give rational explanation to the hydraulic fracturing behavior observed in the laboratory experiments.

1.3. The objectives and the outline of this thesis

As mentioned in the first section, in this thesis, the results of the DEM simulations for the three critical issues in rock engineering projects are presented. The objectives of this thesis are;

1) to describes the two-dimensional (2-D) DEM approach to model the mechanical behavior of consolidated rock;

2) to discuss the mechanism of the brittle failure of rocks in both pre- and post-failure region;

3) to demonstrate that this application replicates real hydraulic fracturing behavior in consolidated rock and obtain insights that gave the rational explanation to the hydraulic fracturing behavior observed in actual experiments;

4) to develop a new DEM code applicable to unconsolidated sand and discuss the mechanism of the hydraulic fracturing behavior in unconsolidated sands in detail.

This thesis contains seven chapters. The outline of each chapter is described as follows.

In chapter 1, the previous researches on these subjects are reviewed, and the objectives and outline of this thesis are presented.

In chapter 2, summary of formulations for the mechanical behavior of bonded particles in the two-dimensional DEM was given. Moreover, a series of rock test simulations, such as uniaxial compression, uniaxial tension and Brazilian tests are performed to verify the applicability of own DEM code, and investigate the effects of particle number and size distribution on macroscopic mechanical properties of rock models.

In chapter 3, as the fundamental research of the rock fracturing, a simulation for uniaxial compression test has been performed. The simulation results are compared with the fracturing process deduced from AE measurements in the laboratory experiments conducted by many researchers to discuss the process in which microcracks are accumulated inside a rock and result in a macroscopic fracture.

In chapter 4, the radial strain control method for uniaxial compression tests was introduced in the DEM codes and the Class II post failure behavior of rocks was simulated. The effect of loading condition is investigated and the mechanism of the Class II behavior was discussed in detail from the microscopic point of view.

In chapter 5, the fluid flow algorithm that can consider the fluid viscosity and permeability is introduced into DEM program to reproduce the hydraulic fracturing. A series of simulations for hydraulic fracturing in hard rock was performed by using the flow-coupled DEM code to discuss the influence of the fluid viscosity and the particle size distribution, and to obtain insights that gave the rational explanation to the disagreement between conventional theory and the AE monitoring results.

In chapter 6, a new DEM code applied to unconsolidated sands was further developed, and a series of simulations for hydraulic fracturing in unconsolidated sand was performed. The mechanism of the hydraulic fracturing in the unconsolidated sands was discussed in detail from the viewpoint of the fracturing fluid viscosity, the pressurization rate and the permeability of the specimen which strongly affect the fracture growth patterns.

In chapter 7, the results and findings obtained from this study and future works are summarized

References

[1] Cundall PA and Strack ODL. A discrete numerical model for granular assemblies. Geotechnique, 1979; 29(1): 47-65.

[2] Potyondy DO and Cundall PA. A bonded- particle model for rock. Int J Rock Mech Min Sci, 2004; 41: 1329-1364.

[3] Aoki K, Mito Y, Mori T, Morioka H and Maejima T. Evaluation of behavior of EDZ around rock cavern by AE measurement and DEM simulation using bonded particle model. Proc. of the third Asian rock mechanics symposium, Mill Press, Rotterdam, 2004; 327-333.

[4] Fakhimi A, Carvalho F, Ishida T and Labuz JF. Simulation of failure around a circular opening in rock. Int J Rock Mech Min Sci, 2002; 39: 507-515.

[5] Cundall PA. Numerical experiments on rough joints in shear using a bonded particle model. Aspects of tectonic faulting, 2001; 1-9.

[6] Hazzard JF and Young RP. Simulating acoustic emissions in bonded-particle models of rock. Int J Rock Mech Min Sci, 2000; 37(5): 867-872.

[7] Hazzard JF and Young RP. Dynamic modeling of induced seismicity. Int J Rock Mech Min Sci, 2004; 41(8): 1365-1376.

[8] Al-Busaidi A, Hazzard JF and Young RP. Distinct element modeling of hydraulically fractured Lac du Bonnet granite. J Geophys Res, 2005; 110: B06302.

[9] Okabe T, Haba T, Mitarashi Y, Tezuka H and Jiang Y. Study on the effect of tunnel face stabilization using the distinct element method. Proc. of the third Asian rock mechanics symposium, Mill Press, Rotterdam, 2004; 1301-1304.

[10] Tannant DD and Wang C. Thin tunnel liners modeled with particle flow code. Eng Comput, 2004; 21(2/3/4): 318-342.

[11] Wang C, Tannant DD and Lilly PA. Numerical analysis of the stability of heavily jointed rock slopes using PFC2D. Int J Rock Mech Min Sci, 2003; 40(3): 415-424.

[12] Howard G.C and Fast CR. Hydraulic Fracturing. Soc Petrol Eng AIME, 1989

[13] Warpinski NR, Branagan PT, Wolhart SL, Moschovidis ZA and Mahrer KD. Microseismic Monitoring of the Mounds Drill Cuttings Injection Tests. Proc. 37th U.S. Rock Mechanics Symposium, Vail Colorado, 1999; 1025-1032.

[14] Baria R and Green ASP. Seismicity induced during a viscous stimulation at the Camborne School of Mines Hot Dry Rock geothermal project in Cornwall, England. Proc Progress in Acoustic Emission III, Japanese Soc NDI; 407-429.

[15] Evans KF, Cornet FH, Hashida T, Hayashi K, Ito T, Matsuki K and Wallroth T. Stress and rock mechanics issues of relevance to HDR/HWR engineered geothermal systems: review of developments during the past 15 years. Geothermics, 1999; 28(4-5): 455-474.

[16] Haimson BC. The Hydrofracturing stress measuring method and recent field results. Int J Rock Mech Min Sci, 1978; 15(4): 167-178.

[17] Ito T and Hayashi K. Physical background to the breakdown pressure in hydraulic fracturing tectonic stress measurements. Int J Rock Mech Min Sci, 1991; 28(4): 285-293.

[18] Zoback MD and Pollard DD. Hydraulic fracture propagation and the interpretation of pressure time records for in-situ stress determination. Proc. 19th US Rock Mech Symp, 1978; 14-22.

[19] Matsunaga I, Kobayashi H, Sasaki S and Ishida T. Studying hydraulic fracturing mechanism by laboratory experiments with acoustic emission monitoring. Int J Rock Mech Min Sci Geomech Abstr, 1993; 30(7): 909-912.

[20] Ito T. Effect of pore pressure gradient on fracture initiation in fluid saturated porous media: Rock. Engineering Fracture Mechanics, 2008; 75(7): 1753-1762.

[21] Schmitt DR and Zoback MD. Infiltration effects in the tensile rupture of thin walled cylinders of glass and granite: implications for the hydraulic fracturing breakdown equation. Int J Rock Mech Min Sci Geomech Abstr, 1993; 30: 289-303.

[22] Zoback MD, Rummel F, Jung R and Raleigh CB. Laboratory hydraulic fracturing experiments in intact and pre-fractured rock. Int J Rock Mech Min Sci Geomech Abstr, 1977; 14(2): 49-58.

[23] Ishida T, Chen Q, Mizuta Y and Roegiers JC. Influence of fluid viscosity on the hydraulic fracturing mechanism. Transactions of the ASME, Journal of Energy Resource Technology, 2004; 126: 190-200.

[24] Solberg P, Lockner D and Byerlee JD. Hydraulic fracturing in granite under geothermal conditions. Int J Rock Mech Min Sci Geomech Abstr, 1980; 17(1): 25-33.

[25] Solberg P, Lockner D and Byerlee JD. Shear and tension hydraulic fractures in low permeability rocks. Pure and Applied Geophysics, 1977; 115(1-2): 191-198.

[26] Milkov AV. Global estimates of hydrate-bound gas in marine sediments: how much is really out there? Earth-Science Reviews, 2004; 66: 183-197.

[27] Ashby MF and Sammis CG. The damage mechanics of brittle solids in compression. Pure and Applied Geophysics, 1990; 133(3): 489-521.

[28] Cook NGW. The failure of rock. Int J Rock Mech Min Sci, 1965; 2(4): 389-404.

[29] Fairhurst CE and Hudson JA. Draft ISRM suggested method for the complete stress-strain curve for intact rock in uniaxial compression. Int J Rock Mech Min Sci, 1999; 36: 279-289.

[30] Wawersik WR. Detailed analysis of rock failure in laboratory compression tests. Ph.D thesis, University of Minnesota, 1968.

[31] Wawersik WR and Brace WF. Post-failure behavior of a granite and diabase. Rock

Mechanics, 1971; 3: 61-85.

[32] Wawersik WR and Fairhurst C. A Study of brittle rock fracture in laboratory compression experiments. Int J Rock Mech Min Sci, 1970; 7(5): 561-575.

[33] Hudson JA, Brow ET and Fairhust C. Optimizing the control of rock failure in servo-controlled laboratory test. Rock Mech, 1971; 3: 217-224.

[34] Hudson JA, Crouch SL and Fairhust C. Soft, stiff and servo-controlled testing machines: A review with reference to rock failure. Eng Geol, 1972; 6: 155-189.

[35] Sano O, Terada M and Ehara S. A Study of the time-dependent microfracturing of oshima granite. Tectonophysics, 1982; 84: 343-362.

[36] Terada M, Yanagidani T and Ehara S. A. E. rate controlled compression test of rocks. In: Proceedings of the 3rd conference on acoustic emission microseismic activity in geologic structures and materials. Trans-Tech, Clausthal, 1984; 159-171.

[37] Okubo S. Uniaxial compression testing using a linear combination of stress and strain as the control variable. Int J Rock Mech Min Sci, 1985; 22(5): 323-330.

[38] Okubo S, Nishimatsu Y and He C. Loading rate dependence of class II rock behaviour in uniaxial and triaxial compression tests—an application of a proposed new control method. Int J Rock Mech Min Sci Geomech Abstr, 1990; 27: 559-562.

[39] Read HE and Hegemier GA. Strain softening of rock, soil and concrete - a review article. Mech of Materials, 1984; 3: 271-294.

[40] Labuz JF and Biolzi L. Class I vs class II stability: A demonstration of size effect. Int J Rock Mech Min Sci, 1991; 28: 199-205.

[41] Hubbert MK and Willis DG. Mechanics of hydraulic fracturing. Trans AIME, 1957; 210: 153-166.

[42] Mizuta Y, Sano O, Ogino S and Katoh H. Three dimensional stress determination by hydraulic fracturing for underground excavation design. Int J Rock mech Min Sci, 1987; 24: 15-29.

[43] Haimson BC. Hydraulic fracturing in porous and nonporous rock and its potential for determining in-situ stresses at great depth. Ph.D thesis, University of Minnesota, 1968.

[44] Haimson BC and Fairhurst C. Initiation and Extension of Hydraulic Fracture in Rocks. Soc Petr Engrs J, 1967; 310-318.

[45] Talebi S and Cornet FH. Analysis of the microseismicity induced by a fluid.injection in a granitic rock mass. Geophys Res Lett, 1987; 14(3): 227-230.

[46] Baria R, Baumgärtner J, Gérard A, Jung R and Garnish J. European HDR research programme at Soultz-sous-Forêts (France) 1987-1996. Geothermics, 1999; 28: 655-669.

[47] Sasaki S. Characteristics of microseismic events induced during hydraulic fracturing experiments at the Hijiori hot dry rock geothermal energy site, Yamagata, Japan. Tectonophysics, 1998; 289:171-188.

[48] Urbancic TI, Shumila V, Rutledge JT and Zinno RJ. Determining hydraulic fracture behavior using microseismicity. Proc 37th US Rock Mech Symp, 1999: 991-997.

[49] Rutledge JT and Zinno RJ. Microseismic mapping of a Cotton Valley hydraulic fracture using decimated downhole arrays. in Society of Exploration Geophysicists, International Exposition and 68th Annual Meeting, New Orleans, Louisiana, 1998; 338-341.

[50] Warpinski NR, Branagan PT, Mahrer KD, Wolhart SL and Moschovidis ZA. Microseismic monitoring of the Mounds drill cuttings injection tests. in Rock Mechanics for Industry, Balkema, Vail, Colorado, 1999; 1025-1032.

[51] Lockner DA and Byerlee JD. Hydrofracturing in Weber sandstone at high confining pressure and differential stress. J Geophys Res, 1977; 82: 2018-2026.

[52] Sasaki S. A Study on Characteristics and Source Mechanism of Acoustic Emission Induced by Hydraulic Fracturing. Ph.D thesis, Tohoku University, 1995. (in Japanese).

[53] Shah KR, Carter BJ and Ingraffea AR. Hydraulic fracturing simulation in a parallel computing environment. Int J Rock mech Min Sci, 1997; 34(3-4): Paper No.282.

[54] Vandamme L and Curran JH. A three-dimensional hydraulic fracturing simulator. Int J Numer Methods Eng, 1989; 28: 909-27.

[55] Al-Busaidi A, Hazzard JF and Young RP. Distinct element modeling of hydraulically fractured Lac du Bonnet granite. J Geophys Res, 2005; 110(B6): B06302.

[56] Perkins TK, Kern LR. Widths of hydraulic fractures. J Pet Tech 1961; 13(9): 937-49.

[57] Sneddon IN, Elliot HA. The opening of a Griffith crack under internal pressure. Q Appl Math 1946; 4: 262-7.

[58] Nordren RP. Propagation of a vertical hydraulic fracture. SPE J, 1972; 12(8): 306-14.

[59] Khristianovic SA, Zheltov YP. Formation of vertical fractures by means of highly viscous liquid. Proc. of the 4th world petroleum congress, Rome, 1955; 579-86.

[60] Geertsma J, de Klerk F. A rapid method of predicting width and extent of hydraulically induced fractures. J Pet Tech 1969; 21: 1571-81.

[61] Sneddon IN. The distribution of stress in the neighbourhood of a crack in an elastic

solid. Proc R Soc London A, 1946; 187: 229-60.

[62] Abé H, Mura FT and Keer LM. Growth rate of a penny-shaped crack in hydraulic fracturing of rocks. J Geophys Res, 1976; 81(B29): 5335-5340.

[63] Abé H, Keer LM and Mura FT. Theoretical study of hydraulically fractured penny-shaped cracks in hot, dry rocks. Int J Numer Anal Meth Geomech, 1979; 3(1): 79-96.

[64] Khodaverdian M, McElfresh PM. Hydraulic fracturing stimulation in poorly consolidated sand: mechanisms and consequences. SPE Annual Technical Conference and Exhibition, 2000; 1-4. (SPE 63233).

[65] Abou-Sayed A, Zaki K, Wang G, Meng F and Sarfare M. Fracture propagation and formation disturbance during injection and frac-pack operations in soft compacting rocks. In SPE Annual Technical Conference and Exhibition, Houston, TX, 2004; 26-29. (SPE 90656).

[66] Wang E and Sharma MM. Unconsolidated sand grain shape, size impact on frac-pack design. Oil and Gas Journal, 1997; 95(20): 67-72.

[67] Bohloli B and de Pater CJ. Experimental study on hydraulic fracturing of soft rocks: influence of fluid rheology and confining stress. J Pet Sci Eng, 2006; 53: 1-12.

[68] Gino Di Lullo, James Curtis, Julio Gomez and BJ Services Company. A Fresh Look At Stimulating Unconsolidated Sands With Proppant-Laden Fluids. SPE Annual Technical Conference and Exhibition, Houston, Texas, 2004; 26-29.

[69] Chang H. Hydraulic Fracturing in Particulate Materials. Ph.D thesis, Georgia Institute of Technology, 2004.

[70] Pater CJ and Dong Y. Experimental study of hydraulic fracturing in sand as a function of stress and fluid rheology. Hydraulic Fracturing Technology Conference, Society of Petroleum Engineers, 2007, SPE 105620.

[71] Zhai Z. Fracturing and fracture reorientation in unconsolidated sands and sandstones. Ph.D thesis, University of Texas, 2006.

[72] Zhai Z and Sharma MM. A New Approach to Modeling Hydraulic Fractures in Unconsolidated Sands, SPE 96246, Dallas, Texas, USA, October, 2005

[73] Wu R. Some fundamental mechanisms of hydraulic fracturing. Ph.D thesis, Georgia Institute of Technology, 2006.

[74] Ito T, Igarashi A and Yamamoto K. Laboratory Test of Hydraulic Fracturing in Unconsolidated Deformable Rocks, Proc. of the 4th Biot Conf. on Poromechanics, 2009;1001-1006.

[75] Igarashi T. PhD thesis, Tohoku University, 2008. (in Japanese).

Chapter 2
Effects of particle number and size distribution
on macroscopic mechanical properties of rock models in DEM

2.1. Introduction

All DEM simulations require proper selection of microscopic parameters such as stiffness and strength of the bonds between particles [1,2]. These microscopic parameters are decided by means of calibration processes in both laboratory scale and field scale depending on the intended application of the DEM model. Although the desirable set of microscopic parameters used in the DEM decided mainly by try and error, there have been many attempts to improve and simplify the calibration procedure [3].

On the other hand, there has been no commonly accepted standard to determine the model geometry, such as model scale, particle size distribution and the number of particles. For most of applications, the sizes of models and particles are determined not according to material behavior but engineering needs or computer memory limitations, often without checking their impacts on final results. A great number of particles are required to reproduce the microscopic features of an actual rock. However, the DEM simulation with too many particles requires significantly long time for calculations. Therefore, the number of particles and particle radius should be selected not only to decrease the variance for calculated values of macroscopic mechanical properties, but also to perform simulations/calculations effectively. This is important issue because the model geometry significantly influences on microstructural features of the DEM model [2,4-7]. Koyama *et al*. [4] showed that the variance of the calculated macroscopic mechanical properties such as Young's modulus and Poisson's ratio increase significantly as the number of particles decreases.

Regarding this situation, a number of rock models have been developed, and the uniaxial compression tests, uniaxial tension test and Brazilian tests are simulated by newly developed DEM code [8-10]. In this study, the simulation results are compared with the results obtained from the laboratory tests to verify the applicability of the DEM code. Moreover, the influence of the model geometry, such as model scale, the number of particles and particle size distribution are discussed in detail.

2.2. Simulation Methodology

2.2.1 Formulation of mechanics of bonded particles

In this study, two-dimensional distinct element method (2D DEM) was employed. The DEM for granular materials was originally developed by Cundall and Strack [1]. The calculations performed in the DEM can be expressed as the translational and rotational motion of particles with the force and moment acting at each contact of the particles. The force-displacement law is employed to calculate the contact forces and moment generated from the relative motion of particles at each contact. The forces and moment calculated from all contacts on a particle are summed yielding a resultant forces and moment, and Newton's second law gives the translational and rotational motion of particles resulting from the contact force and moment acting between particles. The new state of contacts is re-evaluated by the newly computed translational and rotational motion of particles, and a new cycle of computation progresses.

Since thorough details of fundamental DEM algorithm can be seen in Refs.1 and 2, only a summary of formulation for the mechanical behavior of bonded particles which seems to be the primary difference between the DEM code used in this research and the parallel-bond model in the PFC^{2D} [2] will be given in this chapter.

Though the DEM is one of the numerical techniques based on the discontinuum model, it can be applied also to the continuum by introducing bonds between particles. In two dimensional DEM, the intact rock is modeled as a dense packing of small rigid circular particles. Neighboring particles are bonded together at their contact points with a set of three kinds of springs as shown in Fig.2.1 and interact with each other.

(a) Normal spring   (b) Shear spring

(c) Rotational spring
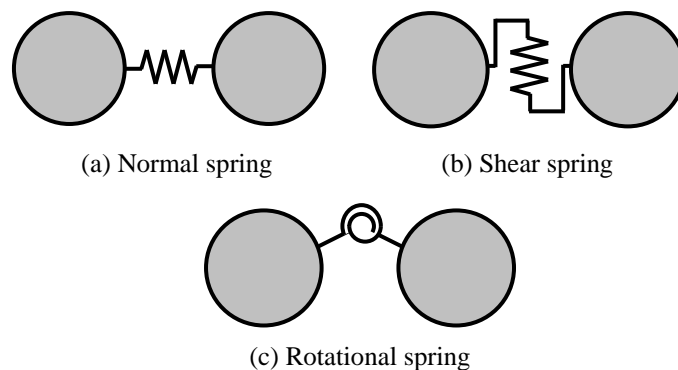
Fig.2.1　Three kinds of springs between two bonded particles.

The increments of normal force f_n, the tangential force f_s, and the moment f_θ can be calculated from the relative motion of the bonded particles, and are given as

$$f_n = k_n \left(dn_j - dn_i \right) \tag{2.1}$$

$$f_s = k_s \left\{ ds_j - ds_i - \frac{L}{2} \left(d\theta_j + d\theta_i \right) \right\} \tag{2.2}$$

$$f_\theta = k_\theta \left(d\theta_j - d\theta_i \right) \tag{2.3}$$

where, k_n, k_s and k_θ are the stiffness of normal, shear, and rotational springs, respectively; dn, ds and $d\theta$ are normal and shear displacements and rotation of particles; r_i and r_j are the radii of the bonded particles. A bond between the particles is presented schematically as a gray rectangle in Fig.2.2, where, L and D are the bond length and the bond diameter, respectively. D is obtained from harmonic mean of the radius of two particles. L and D are given by

$$L = r_i + r_j \tag{2.4}$$

$$D = 2 \cdot \frac{2 r_i r_j}{r_i + r_j} \tag{2.5}$$
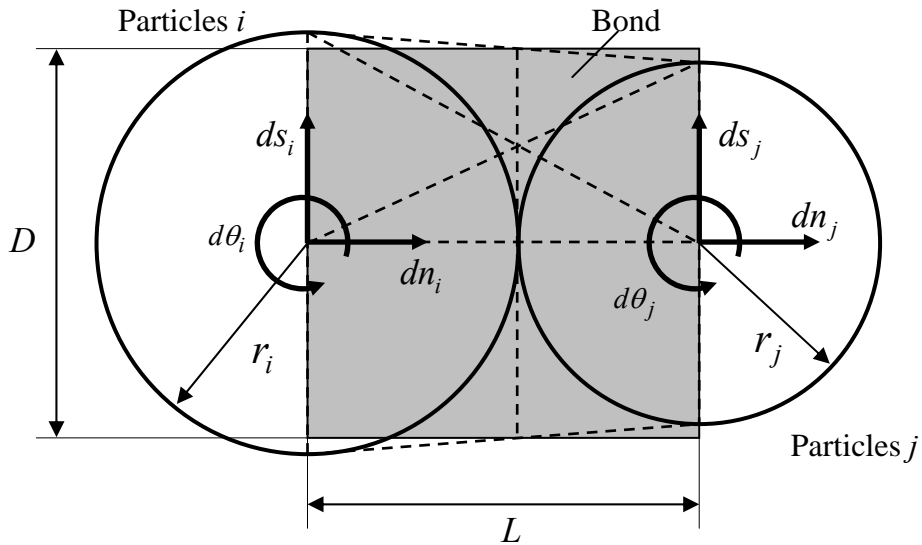
Fig.2.2   Bonded particles model.

Since the DEM is formulated as a fully dynamic system, small amounts of viscous damping are necessary to provide dissipation of high-frequency vibration. If contact damping was not introduced, the assemblies will not be able to reach exact equilibrium condition. Contact damping operates on the relative velocities at the contacts and is represented by dashpots acting in the normal and shear directions at the contact points.

Since the simulation of laboratory rock tests, such as uniaxial compression test, require quasi-static loading, the coefficients of viscous contact damping are determined to provide critical viscous damping that approximates quasi-static loading. The coefficients of viscous contact damping in both normal and shear directions are given by C_n and C_s, respectively with the following equations.

$$C_n = 2\sqrt{m_{ij} k_n} \tag{2.6}$$

$$C_s = C_n \sqrt{k_s / k_n} \tag{2.7}$$

where, m_{ij} is given by the weight of two particles m_i and m_j.

$$m_{ij} = 2\frac{m_i m_j}{m_i + m_j} \tag{2.8}$$

If the stiffness of the springs, k_n, k_s and k_θ are set as tuning parameters treated independently, a large effort will be required to determine appropriate values for them. Therefore, the stiffness of the normal and rotational springs, k_n and k_θ are calculated using beam theory, and the stiffness of shear springs k_s is calculated by multiplying the stiffness of the normal spring k_n and a constant stiffness ratio α. Thus, the stiffness of the springs given by the following equations

$$k_n = \frac{E_p A}{L} \tag{2.9}$$

$$k_s = \alpha \cdot k_n \tag{2.10}$$

$$k_\theta = \frac{E_p I}{L} \tag{2.11}$$

where, A is the cross-sectional area of the bond, and I is the moment of inertia of the bond. E_p is the Young's modulus of particle and bonds. The moment of inertia I depends on the shape of the cross-section, and rectangular cross-section is assumed in this study.

Young's modulus E_p given to the particles and stiffness ratio α are microscopic parameters, and these values are different from Young's modulus and the Poisson's ratio of the rocks obtained from the laboratory experiments and simulation of the uniaxial compression tests.

The normal stress σ and shear stress τ acting on the cross-section of the bond are calculated using the following equations. The stress and the strain are positive in compression.

$$\sigma = \frac{f_n}{D} \tag{2.12}$$

$$\tau = \frac{f_s}{D} \tag{2.13}$$

2.2.2 Microcrack generation and classification of crack modes

When σ exceeds the strength of normal spring σ_c or τ exceeds the strength of shear spring τ_c, then the bond breaks and three springs are removed from the model altogether. Each bond breakage represents the generation of microcracks. As shown in Fig.2.3, a microcrack is generated at the contact point between two particles, and the direction of it is perpendicular to the line joining the two centers.

(Bond break criterion 1) $|\sigma| \geq \sigma_c$ and $\sigma < 0$ (Tensile stress)
(Bond break criterion 2) $|\tau| \geq \tau_c$
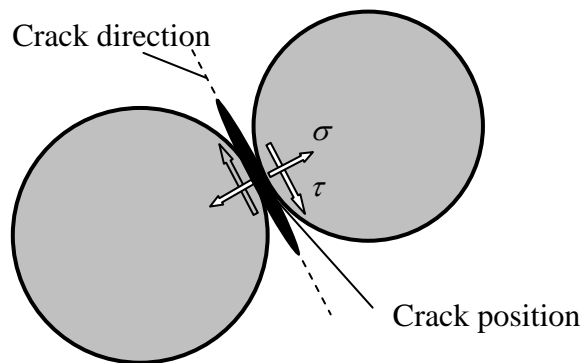
Fig.2.3　Crack position and direction.

In the parallel-bond model developed by Potyondy and Cundall [2], the moment acting on the parallel-bond (which is expressed as elastic beam) contributes the normal stress acting on the particles. This means that the bond breakage is judged by the maximum tensile stress acting on the cross-section of the assumed elastic beam of their model. On the other hand, in this study, since the spring is introduced to restrict the rotation of the particles and used only to calculate the moment acting on the particles, the normal stress calculated by equation (2.12) does not include the moment of the elastic beam. This means that the bond breakage in the model presented here is judged by the average normal stress acting on the cross-section of the assumed elastic beam. This is the difference in the mechanism of particle bondage between the parallel-bond model proposed by Potyondy and Cundall and the model presented in this research.

In the AE measurement during the laboratory experiment, the AE hypocenter can be calculated from the arrival time of the P-wave first motion and the source mechanism of AE events are determined from the spatial distribution of the P-wave first motion polarities [11]. For tensile cracks, all sensors detect the P-wave first motion as compression wave. On the other hand, for shear cracks, both compressional and dilatational P-wave first motions are detected as shown in Fig.2.4. This polarity of the P-wave first motion will depend on the stress state at the crack generation. Therefore, in this study, the crack modes can be classified using shear-tensile stress ratio $|\tau/\sigma|$ regardless of broken spring type (normal or shear springs) as follows.

(Crack classification criterion 1) $|\tau/\sigma| \leq 1$ and $\sigma < 0$ (Tensile stress)$\cdots$Tensile Crack
(Crack classification criterion 2) $|\tau/\sigma| > 1$ and $\sigma < 0$ (Tensile stress)$\cdots$Shear Crack
(Crack classification criterion 3) $\sigma > 0$ (Compressive stress)$\cdots$Shear Crack
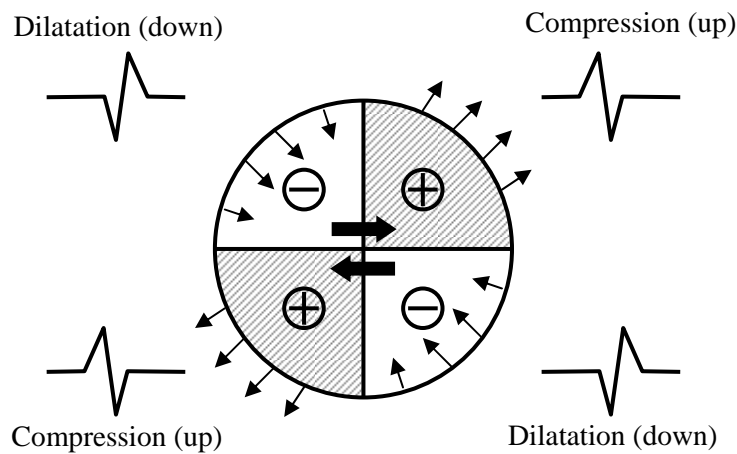
Fig.2.4   Polarity of P-wave first motions.

When a microcrack is generated, the strain energy stored in both normal and shear springs at the contact point is released. This produces a force imbalance, and subsequent stress redistribution induces an AE event. The magnitude of this AE event is related to the kinetic energy generated in the model, which propagates outward from the bond breakage points.

Though the strain energy at the contact point does not equal to the magnitude of AE event, the magnitude of AE event would strongly relate to the released strain energy. For this reason, the strain energy E_k calculated using equation (2.14) is assumed to be the energy corresponding to the magnitude of AE event.

$$E_k = \frac{f_n^{\,2}}{2k_n} + \frac{f_s^{\,2}}{2k_s} \qquad (2.14)$$

2.2.3 Contact behavior between unbonded particles

When the unbonded particles are in contact or particles with bond breakage are again in contact with each other, springs and dashpots are introduced into the contact points in both normal and tangential directions, and compressive normal force f_n and tangential (frictional) force f_s act at the contact points. The no-tension constraint condition should be satisfied for the springs in the normal direction. The increments of normal contact force f_n and the tangential contact force f_s are given as

$$f_n = k_n \left(dn_j - dn_i \right) \qquad (2.15)$$

$$f_s = k_s \left\{ ds_j - ds_i - \left(r_j d\theta_j + r_i d\theta_i \right) \right\} \qquad (2.16)$$

The stiffness of the contact springs in the normal direction is given by the following equation using the normal compression force F based on the Hertz's contact theory [12,13]. Fig.2.5 shows the analytical model for Hertz theory of elastic contact.

$$k_{nn} = \frac{\pi E_p}{2\left(1 - v_p^{\,2}\right)\left(\dfrac{2}{3} + \ln \dfrac{4r_1}{d_{contact}} + \ln \dfrac{4r_2}{d_{contact}} \right)} \qquad (2.17)$$

$$d_{contact}^{\,2} = \frac{32\left(1 - v_p^{\,2}\right)}{\pi E_p} \cdot \frac{r_1 r_2}{r_1 + r_2} \cdot F \qquad (2.18)$$

where, r is the particle radius and $d_{contact}$ is the diameter of the contact surface. E_p and ν_p are Young's modulus and Poisson's ratio of particles, respectively.

When particles and a flat plate (wall boundary) such as the loading platen are in contact, the stiffness of contact springs in the normal direction is given by the following equations [12,13].

$$k_{nn} = \frac{\pi}{\left(\dfrac{1-\nu_p^2}{E_p} + \dfrac{1-\nu_w^2}{E_w} \right)\left(\dfrac{1}{3} + \ln \dfrac{4r_1}{d_{contact}} \right)} \tag{2.19}$$

$$d_{contact}^2 = \frac{16r_1}{\pi}\left(\frac{1-\nu_p^2}{E_p} + \frac{1-\nu_w^2}{E_w} \right)\cdot F \tag{2.20}$$

where, E_w and ν_w are Young's modulus and Poisson's ratio of the wall. Equation (2.17) and (2.18) represent the contact between cylinders, and Equation (2.19) and (2.20) represent the contact between a cylinder and a flat plate. More thorough details of these equations can be seen Refs.12 and 13.

The stiffness of shear contact springs k_{ss} can be calculated by multiplying the stiffness of the normal contact spring k_{nn} and a stiffness ratio, s, as follows:

$$k_{ss} = s \cdot k_{nn} \tag{2.21}$$

where the stiffness ratio, s, can be calculated from shear modulus G and Young's modulus E as

$$s = \frac{G}{E} = \frac{1}{2(1+\nu)} \tag{2.22}$$
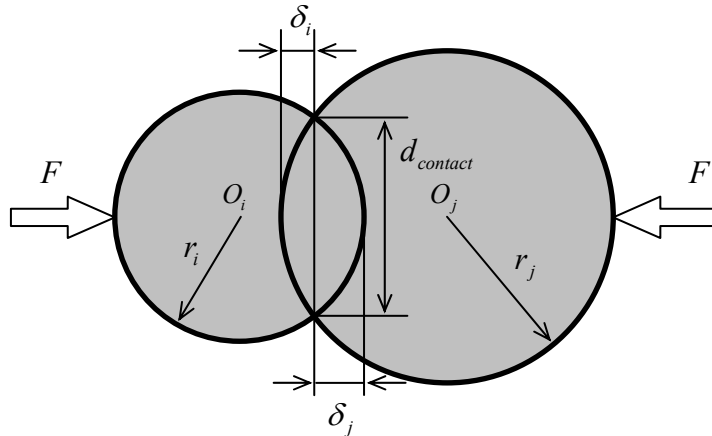
Fig.2.5 Analytical model for Hertz theory of elastic contact.

The coefficients of viscous contact damping in both normal and shear directions, C_{nn} and C_{ss} can be expressed as

$$C_{nn} = 2\sqrt{m_{ij} \cdot k_{nn}} \qquad (2.23)$$

$$C_{ss} = C_{nn}\sqrt{k_{ss}/k_{nn}} \qquad (2.24)$$

If the frictional force f_s exceeds the critical value $f_{s\,max}$, the slip occurs at the contact points between the particles and the frictional force f_s will be replaced to $f_{s\,max}$. According to the Coulomb's frictional law, the critical value $f_{s\,max}$ is calculated by the following equation.

$$f_{s\,max} = \tan\phi_p \cdot f_n \qquad (2.25)$$

where $\tan\phi_p$ is a coefficient of friction.

2.3. Overview of the simulation for each rock test

2.3.1 Uniaxial compression test

Fig.2.6(a) shows the loading condition for the simulation of uniaxial compression tests. The platen under the rock model was fixed and the upper loading platen was moved downward slowly at a certain displacement rate to simulate the uniaxial compression tests. Frictional force was acting between the rock model and the platens.

The axial stress applied to the rock model during the uniaxial compression test was calculated from total force acting on the upper loading platen from particles and model width. The strain is calculated by displacements of the monitored particles. As shown in Fig.2.6(a), four particles located slightly inside from the edge of the rock model are selected, and the displacement of these particles was measured. The distances between measuring points is 90% of the rock model width and height, respectively. Axial strain ε_1 and radial strain ε_2 can be calculated using the following equations.

$$\text{Axial Strain}: \varepsilon_1 = \frac{\left(y_4^0 - y_2^0\right) - \left(y_4^t - y_2^t\right)}{y_4^0 - y_2^0} \qquad (2.26)$$

$$\text{Radial Strain}: \varepsilon_2 = \frac{\left(x_3^0 - x_1^0\right) - \left(x_3^t - x_1^t\right)}{x_3^0 - x_1^0} \qquad (2.27)$$

where superscript 0 and t means initial and measuring time, respectively. Plane strain condition is assumed to calculate elastic macroscopic parameters, and Young's modulus

and Poisson's ratio were calculated according to the ISRM (International Society for Rock Mechanics) Suggested Method [14,15].

2.3.2 Uniaxial tension test

Fig.2.6(b) shows the loading condition for the simulation of uniaxial tension tests. The same rock model as the uniaxial compression test is used for the uniaxial tension test. As shown in Fig.2.6(b), particles located both top and bottom end of the model are selected, and these particles are directly moved upward or downward to reproduce the uniaxial tension test. Tensile strength is calculated from the total tensile force that acted on the selected upper particle and the width of the model.

2.3.3 Brazilian test

As shown in Fig.2.6(c), a circular rock model is used for the Brazilian test. The platen under the rock model was fixed and the upper loading platen was moved downward slowly at constant displacement rate. Tensile strength of the rock model T is calculated from the total force acts on the upper loading platen and the diameter of the model by the following equation. Because it is a two dimensional simulation, the length of the model l is assumed to be 1.

$$T = \frac{2F_{platen}}{\pi dl} \tag{2.28}$$

2.4. Calibration of microscopic parameters

2.4.1 Particle packing procedure

There are two typical methods for modeling (packing) the rock as an assembly of particles bonded with each other [2,16-20]. One is a method of dropping the particle. The particles are dropped by gravity, and accumulated. This state is assumed to be an initial state. The other is a method of setting the radius and the initial position of the particles directly by using the random number. The former has the advantage that the modeling can be done by an easy operation. However, it needs a long time for the modeling, and complex shape model cannot be modeled. On the other hands, the latter method enable us to model the complex shape model in comparatively short time though it needs a complex operation compared with the former method. In this research, the latter method is employed, and all the rock models used in the simulations are made according to the following procedures.

(a) Uniaxial compression test   (b) Uniaxial tension test

(c) Brazilian test
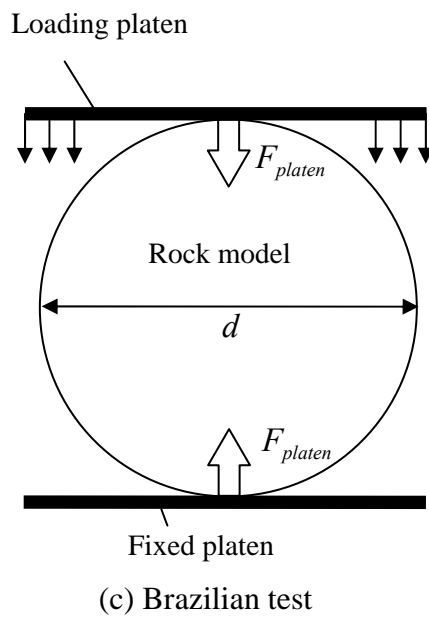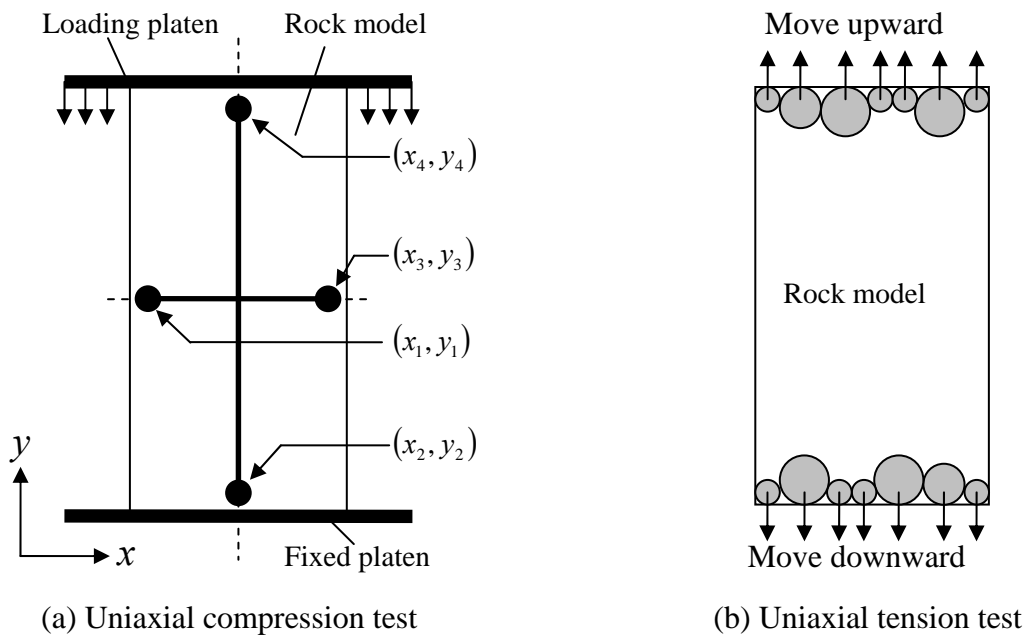
Fig.2.6   Schematic overview of the loading condition for the simulation of each rock test. (a) uniaxial compression test. The measuring points for the axial and radial strain were located slightly inside from the edge of the rock model. The distance between two measuring points is 90% of the rock model width or height. (b) uniaxial tension test. (c) Brazilian test.

The particle radius was selected following a uniform distribution between maximum and minimum radius using random number. First, four particles were arranged in the corner of the model as shown in Fig.2.7(a).

Next, particles were aligned along one side of the model as shown in Fig.2.7(b) and only the last one particle radius is decided manually to exactly contact with the particle already arranged. This process is repeated four times to enclose the model as shown in Fig.2.7(c). By this operation, every side of the model can be smoothed, and the loading stress can act on the model uniformly. As shown in Fig.2.7(d), after arraying particles along the every side of the model, the inside of the model is filled with particles. The new particle was arranged to contact with the pre-existing particles with at least three contact points. This process is repeated until a new particle with minimum radius can not be arranged.
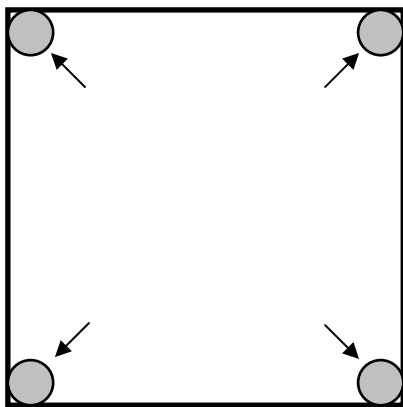
(a) Four particles are arranged
in the corner of the model.

The last one particle radius is decided to just contact with existing particles.
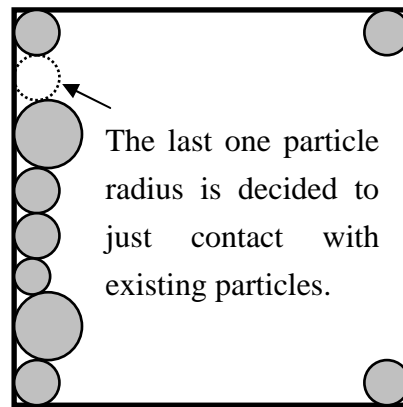
(b) Particles are aligned along
one side of the model.
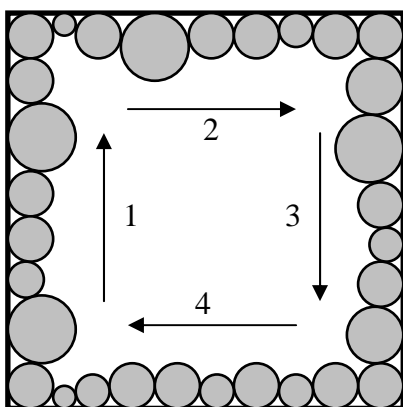
New particle

(c) Process (b) is repeated four
times to enclose the model.
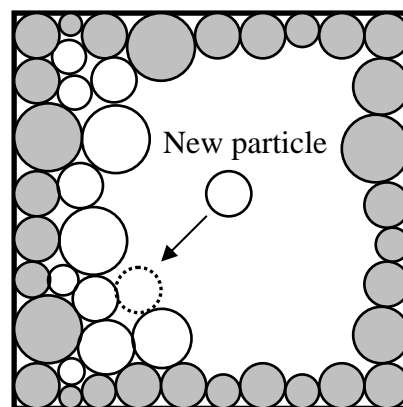
(d) Put on a new particle tangent to
the pre-existing particles.

Fig.2.7   Particle packing method.

When the number of contact points for each particle is less than three, the radius of the particle is modified and/or the position of the particle changed so that the number of contact points become at least three. Using this packing method, it is possible to generate particles in a domain with complicated geometry in relatively short time.

Although the microscopic parameters, such as Young's modulus and strength of the spring, are the same through the rock models, the stresses that act between particles are evaluated by equation (2.12) and (2.13) by using the radius of the particles. Therefore, the stress distribution in the rock models becomes heterogeneous due to the difference of the radius of each particle.

2.4.2 Calibration results

For the proper simulations using DEM, appropriate microscopic parameters should be selected. Therefore, preliminary simulations of the uniaxial compression tests, the uniaxial tension tests and the Brazilian tests were performed for the calibration of microscopic parameters, and the microscopic parameters should be adjusted to represent the macroscopic mechanical properties obtained from these rock test simulations.

The calibration is performed for four macroscopic parameters, such as the Young's modulus, the Poisson's ratio, the tensile strength and the uniaxial compressive strength (UCS) of the rock model. The UCS of the rock model is obtained from the simulation of the uniaxial compression tests, and the Young's modulus and the Poisson's ratio of the rock model is calculated from the stress-strain relations.

Since the uniaxial tension tests have been rarely carried out in the laboratory experiments, relatively easy Brazilian tests were generally conducted to obtain the tensile strength of the rock specimen. However, using the DEM, both uniaxial tension test and Brazilian test can be simulated easily. Hence, both the uniaxial tension test and Brazilian test were performed to calculate accurate tensile strength of the rock models.

Microscopic properties of the DEM model are shown in Table 2.1, and the calibration results are summarized in Table 2.2. The calibration results shown in Table 2.2 were decided by using one of the rock models that belong to Group D which will be mentioned in section 2.5.2, and the Young's modulus and the Poisson's ratio for steel was selected for the material properties of loading platens.

Although it is pointed out that the tensile strength of the rock model obtained from the calibration is larger than the experimental results when parallel-bond model that Potyondy and Cundall constructed is used [2,5], appropriate calibration results, such as not only the UCS, Young's modulus, and Poisson's ratio but also tensile strengths of the rock model were obtained [21].

Table 2.1 Rock model properties and calibration results.

ROCK MODEL DATA	
Particle density:	2500 kg/m^3
Friction coefficient of platen ($\tan\phi_w$):	0.5
Poisson's Ratio of platen (ν_w):	0.3
Young's modulus of platen (E_w):	200GPa
Friction coefficient of particle ($\tan\phi_p$):	0.3
Poisson's ratio of particle (ν_p):	0.3
TUNING PARAMETERS	
Young's modulus of particle (E_p):	145.0 (GPa)
Shear/normal spring stiffness ratio (α):	0.30
Shear strength of bonding (τ_c):	245.0 (MPa)
Tensile strength of bonding (σ_c):	60.0 (MPa)

Table 2.2 Calibration results.

-Uniaxial compression test-	**Experiment**	**Simulation**
UCS of rock model:	100 - 250 (MPa)	189.2 (MPa)
Young's modulus of rock model:	50 - 75 (GPa)	71.4 (GPa)
Poisson's Ratio of rock model:	0.1 - 0.26	0.261
-Uniaxial tension test-		
Tensile strength of rock model:		16.2 (MPa)
-Brazilian test-		
Tensile strength of rock model:	7 - 25 (MPa)	15.4 (MPa)

2.4.3 The fracturing behavior in the simulation of each rock test

Fig.2.8(a), (b) and (c) show the typical results of fracture growth pattern, transition of axial stress and the number of microcracks in the simulation of uniaxial compression, uniaxial tension and Brazilian tests, respectively. As shown in Fig.2.8(a), the microcracks generated in low stress level were widely distributed over the whole model, and the number of microcracks increases gradually as the axial stress increases. When the axial stress exceeds the peak strength, the number of microcracks increased rapidly. A macroscopic fracture had been formed by connection of many microcracks, and finally the model resulted in collapse in a very short time. Such fracturing behavior of rock model under uniaxial compression will be discussed in detail in Chapter 3.

Crack geometry

(a) Uniaxial compression test

Crack geometry

(b) Uniaxial tension test

Crack geometry
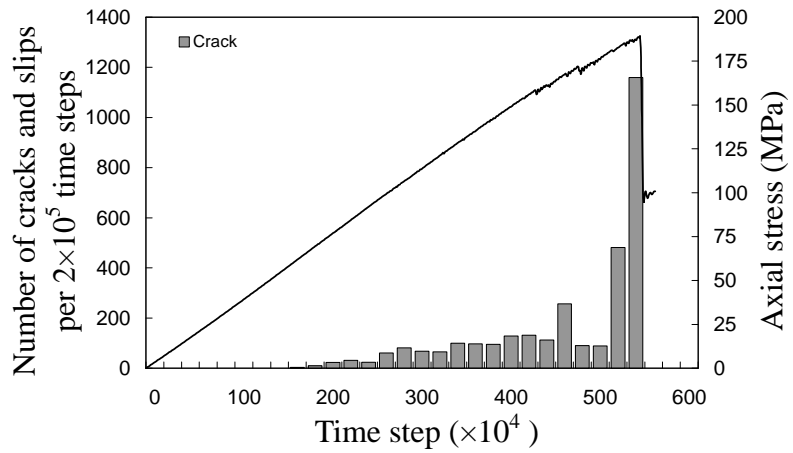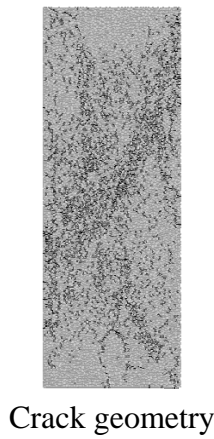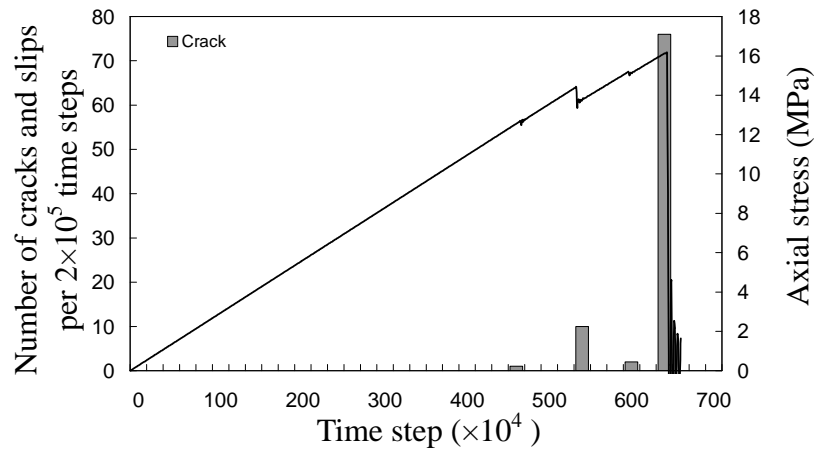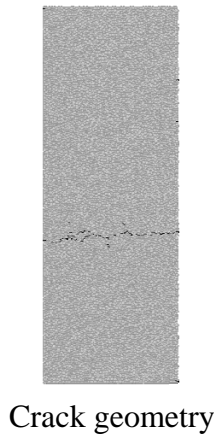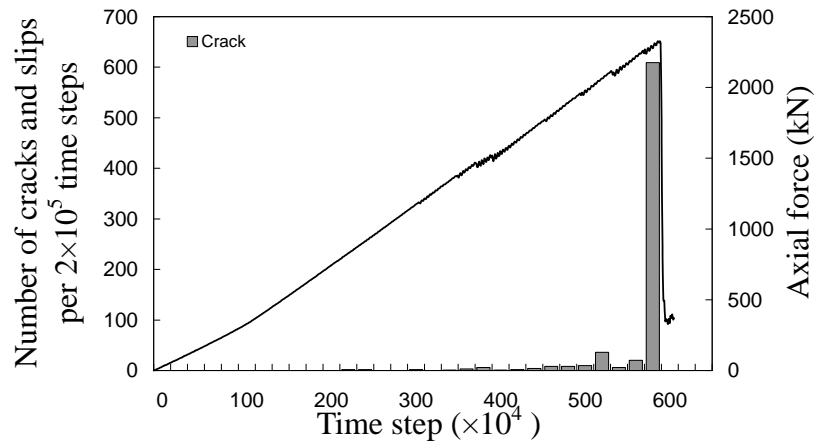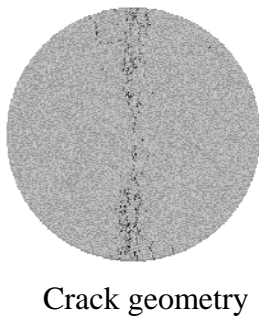
(c) Brazilian test

Fig.2.8 The features of microcrack generations in the simulation of each rock test. The left shows the spatial distribution of microcracks at the end of the simulation. The solid lines indicate the crack generations. The right shows the transition of axial stress and the number of microcracks.

As shown in Fig.2.8(b) and (c), fracturing behaviors in Brazilian test and uniaxial tension test are different from that in uniaxial compression test. Macroscopic fracture in Brazilian test and uniaxial tension test are formed by the growth of a single fracture. In Brazilian test, a macroscopic fracture propagates along the direction of the loading axis.

On the other hand, a macroscopic fracture is generated at near center of the model and develops orthogonal with the loading axis of uniaxial tension test. As shown in Table 2.2, the tensile strengths of the rock model obtained from Brazilian test and uniaxial tension test are almost the same. These fracturing behaviors obtained from the DEM simulations are well in agreement with general tendency of experimental results.

2.5. Results and discussion

2.5.1 Loading rate

In general, the loading rate for an actual rock tests must be slow enough to obtain the stable results. However, because of the limitation of the computational power and stability issues arising from the explicit time integrator that typically used in these simulations, significantly small time steps must be used in DEM. Since a number of iterations are required, DEM simulations cannot use the same loading rate as an actual rock tests. For this reason, the effect of the loading rate should be discussed at first. Therefore, a series of simulations are performed with different loading rates to decide the proper loading rate for stable and effective simulations.

Fig.2.9 shows the relation between the macroscopic mechanical parameters obtained from each rock test simulation and the reciprocal of the loading rate. The reciprocal of the loading rate is used for x-axis to make clear the relation between the macroscopic parameters and the loading rate.

Fig.2.9(a) shows the coefficients of variation of macroscopic mechanical properties. The coefficient of variation is calculated as the ratio of the standard deviation to the mean value of each macroscopic mechanical property for each group, and it is a useful statistic for evaluation of the degree of variation.

As shown in Fig.2.9(a), it is found that the coefficients of variation of macroscopic mechanical properties decrease with increase of the reciprocal of the loading rate, and that the coefficients of variation decrease sufficiently when the reciprocal of the loading rate to become ten or more. According to the former research presented by Moon *et al*. [22], when the loading rate in the DEM simulation is greater than the critical strain rate, the strength of the rock model is over estimated because of the inertial effects.
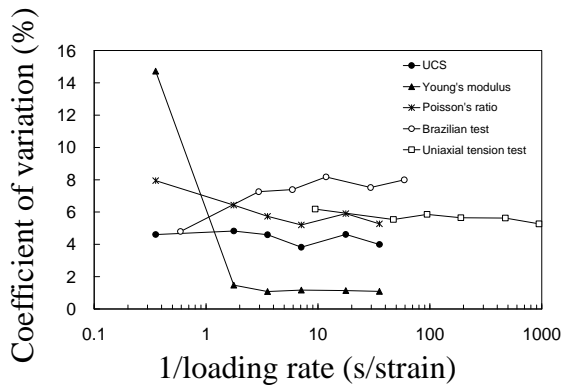
(a) Coefficient of variation
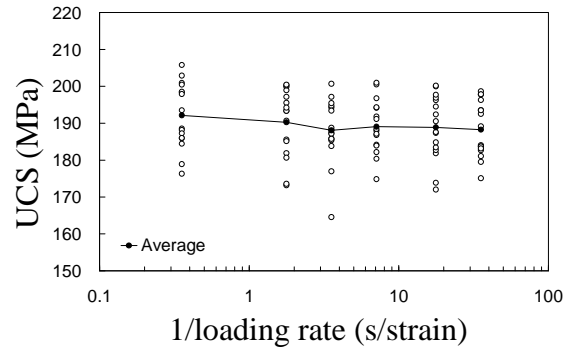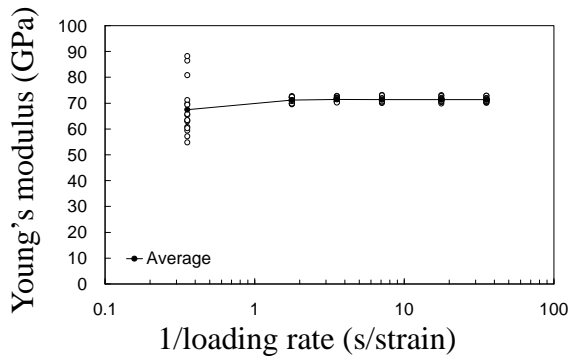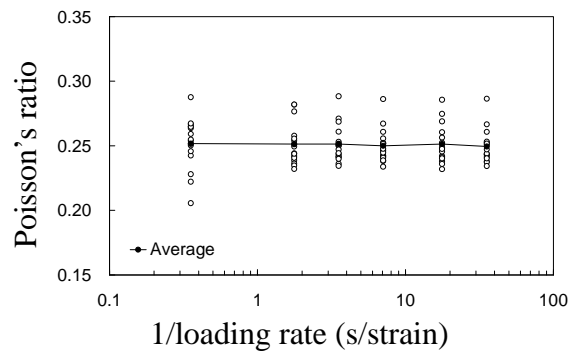
(b) Uniaxial compressive strength (UCS)

(c) Young's modulus

(d) Poisson's ratio
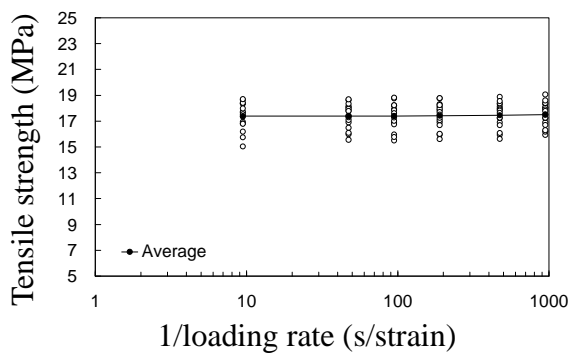
(e) Tensile strength (Uniaxial tension test)
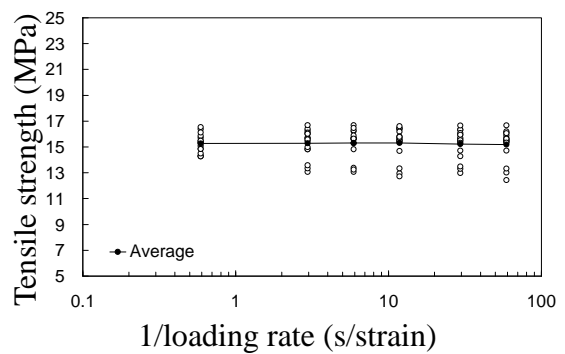
(f) Tensile strength (Brazilian test)

Fig.2.9   Relations between the reciprocal of loading rate and macro properties of rock model.

Fig.2.9(b)-(f) show the comparison of the macroscopic properties, such as UCS, Young's modulus, Poisson's ratio, uniaxial tensile strength and indirect (Brazilian) tensile strength, as a function of the reciprocal of the loading rate, respectively. As shown in Fig.2.9(b)-(f), the averages of all macroscopic mechanical properties are almost constant regardless of the reciprocal of the loading rate.

Based on these results, loading rates used in all DEM simulations are determined for the reciprocal of the loading rate to become ten or more to obtain stable and effective simulation results.

2.5.2 The number of particles

In this section, the rock models that belong to four groups (Group A, B, C and D) with different particle number were generated to discuss the influence of the number of particle on the macroscopic mechanical properties. For each group, 16 rock models were generated, and totally 64 stochastic particle models were created. The locations of particles in each model were generated randomly.

The parameters for each group are summarized in Table 2.3, and Fig.2.10 shows the close-up view of rock models for each group as examples of particle system geometry varying in the number of particles. The size of all rock models for uniaxial compression test and uniaxial tension test are 51mm in width and 143mm in height. The rock models for the Brazilian test in each group were made by the same number of particles as the rock models used in the uniaxial compression tests. For this reason, the diameter of the rock model for the simulation of Brazilian test was decided to 96mm. The ratio of maximum/minimum particle radius of all models is 2, and the average number of particles of rock models in Group A, B, C and D are about 1000, 2500, 5000 and 10000, respectively. In Table 2.3, the word "porosity" means the percentage of the void space (pore) in the rock models. The particles are closely arranged as the porosity decreases. The uniaxial compression, the uniaxial tension, and the Brazilian tests were simulated by using these rock models. Here, the same microscopic parameter shown in Table 2.1 was used for all the simulations.

Fig.2.11(a) shows the relation between the coefficients of variation of macroscopic mechanical properties and the number of particles of rock model. As shown in Fig.2.11(a), the coefficients of variation of macroscopic mechanical properties decrease with an increase of the number of rock models. In particularly, in the Group D, the coefficients of variation of all macroscopic mechanical properties are less than 10%, and stable results can be obtained.

Table 2.3   Four data sets with different number of particles.

	For uniaxial compression (tension) test			For Brazilian test	
	Width: 51mm			Diameter: 96mm	
	Height: 143mm				

	Group A	Group B	Group C	Group D
Number of particles (average):	1107	2591	5364	9444
Maximum particle radius:	1.8mm	1.16mm	0.8mm	0.6mm
Minimum particle radius:	0.9mm	0.58mm	0.4mm	0.3mm
Max/Min particle radius ratio:	2.0	2.0	2.0	2.0
Porosity of the model (average):	19.62%	19.37%	19.01%	18.80%
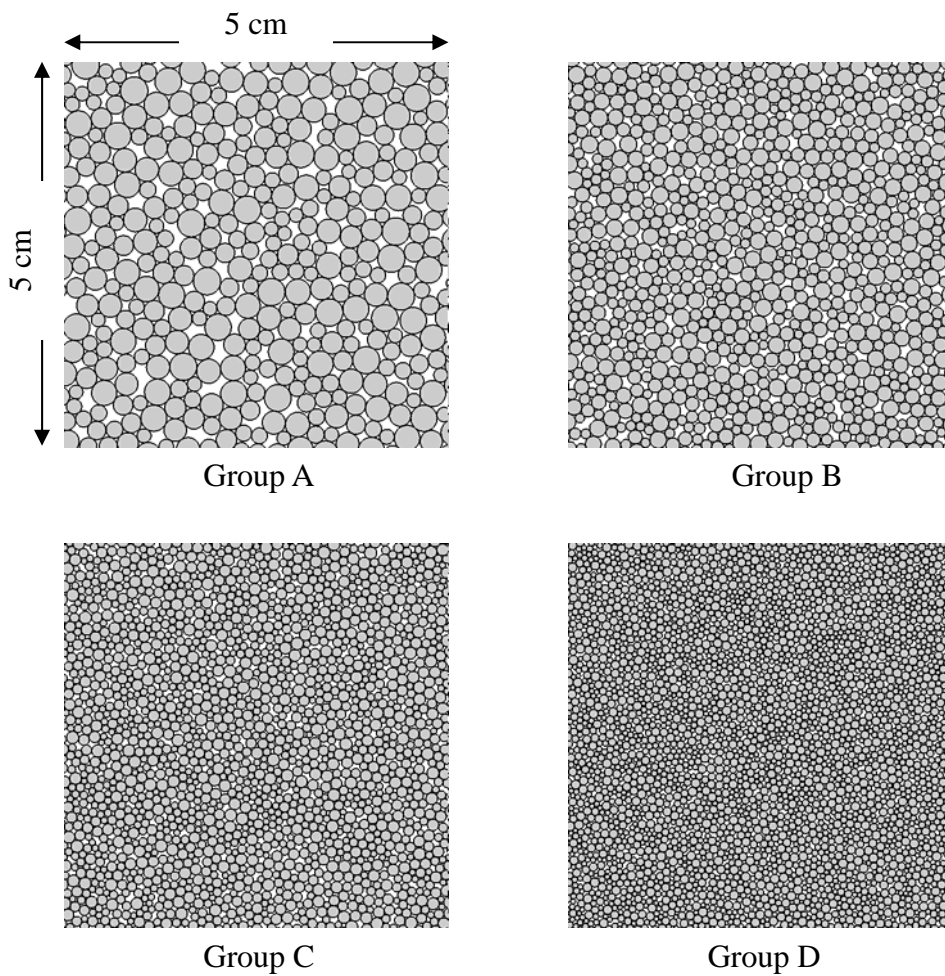
Fig.2.10   Close-up views of a rock model in group A, B, C and D. Sixteen
models are randomly generated for each group.
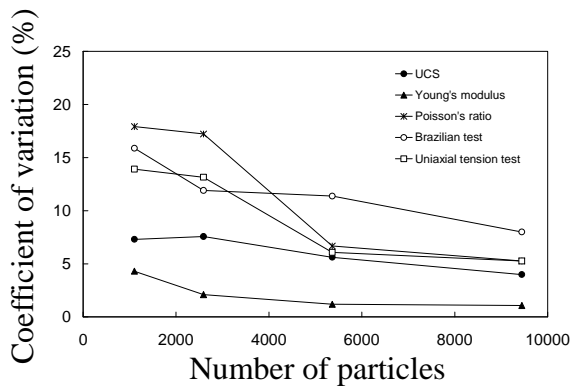
(a) Coefficient of variation
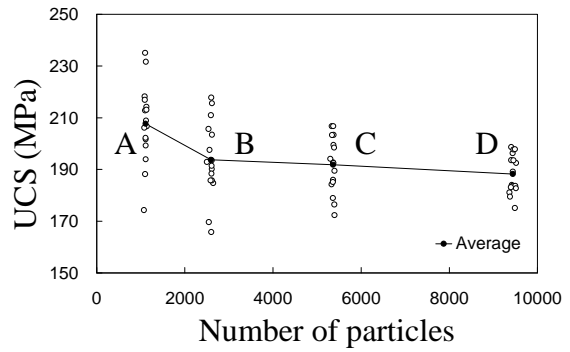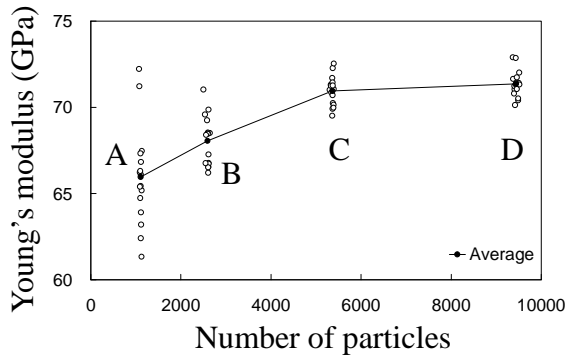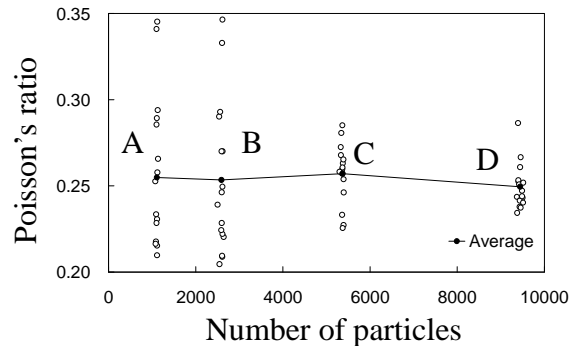
(b) Uniaxial compressive strength (UCS)

(c) Young's modulus

(d) Poisson's ratio
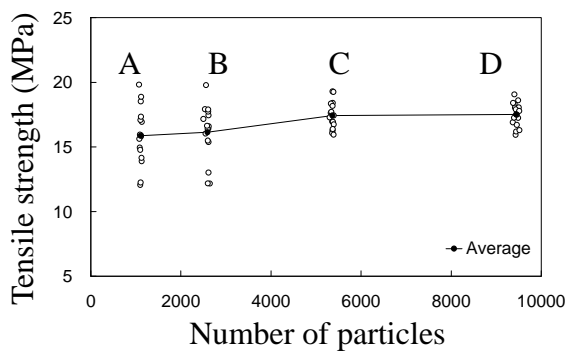
(e) Tensile strength (Uniaxial tension test)
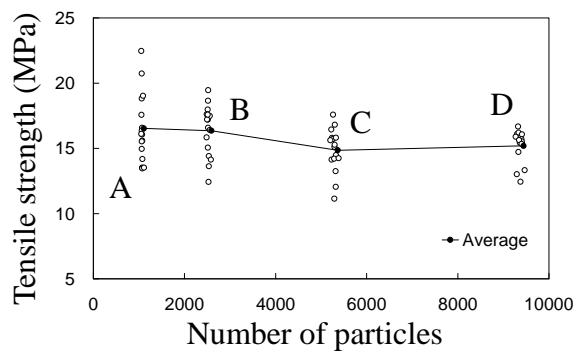
(f) Tensile strength (Brazilian test)

Fig.2.11   Relations between the number of particles and macro properties of rock model.

34

Fig.2.11(b)-(f) show the comparison of the macroscopic mechanical properties as a function of the number of particles of the rock model in each group, respectively. The solid line shows the average values of each macroscopic mechanical property.

Fig.2.11(b) shows the comparison of the UCS as a function of the number of particles of the rock model in each group. The average of the UCS decreases as the particle number increases. It is commonly agreed that rock strength decreases with increasing of specimen size in actual rock test. This is so-called "size effect". The size effect on the strength of brittle rocks can be explained by the existence of pre-existing flaws such as pores, microcracks and grain boundaries. The probability for existence of a critical defect that causes catastrophic fracture increases with increase in size of the specimen. In the DEM simulation, the number of bonds between particles increases when the number of particles increases. This also means that the number of the place where the microcracks can be generated increases as the number of particles increases because the microcrack occurs only at the bond between particles in the DEM simulation. Thus, when the number of particles increases, the probability that the rock model contains the critical points which may lead the macroscopic fracture also increases. As a result, the UCS decreases with increase in the number of particle as shown in Fig.2.11(b), and the similar effect to size effect in actual rock specimen appears in the DEM simulation.

Fig.2.11(c) shows the comparison of the Young's modulus as a function of the number of particles of the rock model for each group. Differently from the UCS, the average of the Young's modulus increases as the particle number increases. This can be explained by the porosity of the model. Since the rock model in the DEM is expressed by the assembly of circular particles, there are many void spaces (pores) in the rock model. Therefore, the Young's modulus obtained from the DEM simulations is apparent Young's modulus of void space (pore) and rock matrix (particle). As shown in Table 2.3, the porosity of the model is highest in Group A (19.62%) and lowest in Group D (18.80%), and the Young's modulus of the model is highest in Group D (71.36GPa) and lowest in Group A (65.96GPa). In many actual rocks, it is commonly assumed that the Young's modulus decreased with increasing porosity. Thus, the simulation result indicates that the relation between the Young's modulus and the porosity in DEM simulation is similar to that in actual rocks. Moreover, the coefficients of variation of Young's modulus are very small in all cases, and the highest value is about 5% in Group A. This result indicates that the particle arrangement of the model does not affect the Young's modulus of the model.

Fig.2.11(d) shows the comparison of the Poisson's ratio as a function of the number of particles of the rock model in each group. Though the coefficients of variation of the

Poisson's ratio decreases rapidly as the particle number increases, the average value is almost constant. Potyondy *et al*. [2] pointed out that the Poisson's ratio in DEM does not depend on the number of particles, and is significantly affected by the spring stiffness ratio (α). The constant Poisson's ratio shown in Fig.2.11(d) supports this indication, because all simulations in this section use the same spring stiffness ratio ($\alpha = 2$). However, the coefficient of variation of the Poisson's ratio is significantly affected by the number of particles as shown in Fig.2.11(d). As mention in section 2.3.1, the lateral strain is calculated by displacements of the two particles at the location close to the edge of the rock model. Therefore, when the rock model is generated with a few numbers of particles (the number of particles existing between the monitored particles is a few), displacement of a particle and generation of a microcrack directly affect the calculation of the lateral strain. Thus, the coefficient of variation of the Poisson's ratio is significantly affected by the number of particles.

Fig.2.11(e) and (f) show the comparison of the uniaxial tensile strength and indirect (Brazilian) tensile strength as a function of the number of particles of the rock model in each group, respectively. The tensile strengths obtained from the uniaxial tension test and the Brazilian test are almost the same, and the average values for each group in both tests are constant. However, as shown in Fig.2.11(a), the coefficient of variation of the tensile strength in the uniaxial tension test was smaller than that in the Brazilian test. In the uniaxial tension test, a microcrack occurs in the weakest point in the rock models, and a macroscopic fracture is formed by the propagation of the crack. On the other hand, in the Brazilian test, the coefficient of variation of the tensile strength is strongly affected by the particle position near the loading axis because fracture propagation is limited on the loading axis. Therefore, the coefficient of variation of indirect (Brazilian) tensile strength becomes large.

2.5.3 Particle size distribution

In this section, to discuss the influence of the particle size distribution on the macroscopic mechanical properties, the rock models belong to four groups (Group E, F, G and H) with different ranges of particle size distribution were generated as shown in Table 2.4. For each group, 16 rock models were generated, and totally 64 stochastic particle models were created in this section. The locations of the particles in each model were generated randomly. Fig.2.12 shows the close-up view of rock models in each group as examples of particle system geometry varying in the particle size distribution. As shown in Table 2.4, the minimum particle radius of all models is the same, and the

Table 2.4   Four data sets with different Max/Min radius ratios.

	Group E	Group F	Group G	Group H
Number of particles (average):	9378	9878	9375	9457
Maximum particle radius:	1.0mm	1.5mm	2.0mm	2.5mm
Minimum particle radius:	0.5mm	0.5mm	0.5mm	0.5mm
Max/Min particle radius ratio:	2.0	3.0	4.0	5.0
Porosity of the model (average):	18.89%	15.97%	14.08%	12.57%
Model width:	100mm	130mm	150mm	170mm
Model height:	200mm	260mm	300mm	340mm
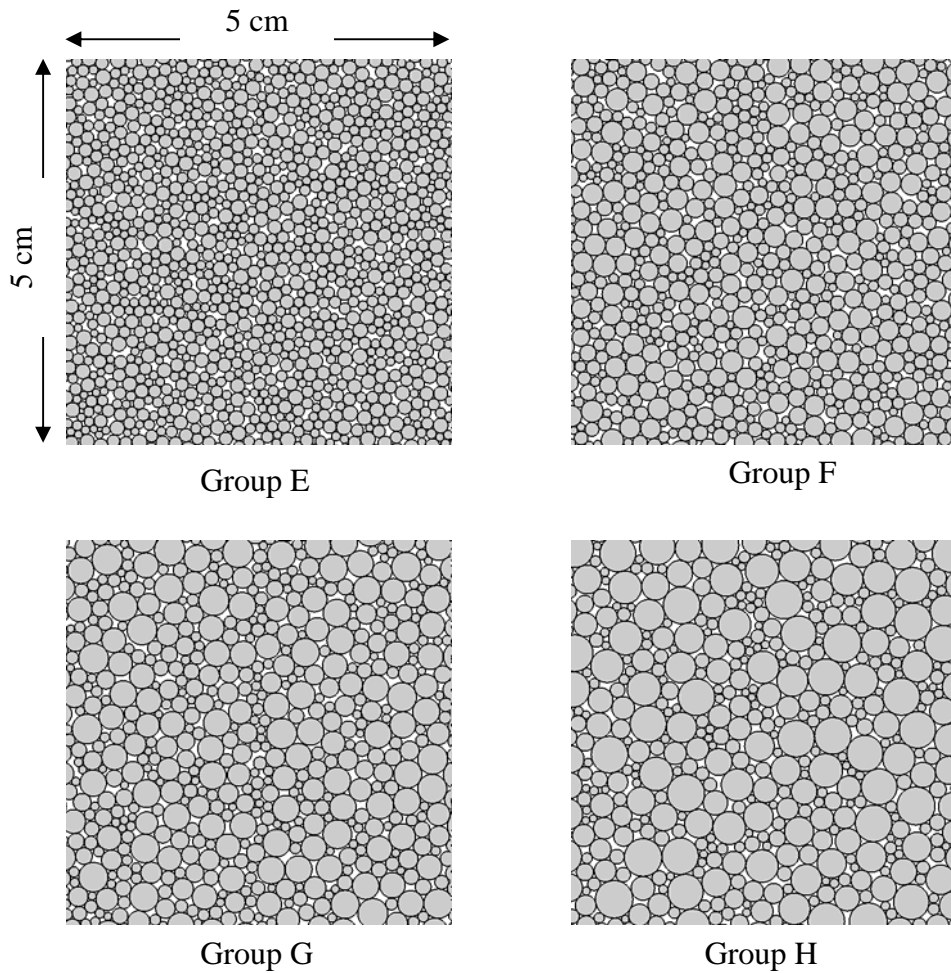
Fig.2.12   Close-up views of a rock model in group E, F, G and H. Sixteen
models are randomly generated for each group.

maximum particle radius is changed to adjust the ratio of maximum/minimum particle radius in Group E, F, G and H to 2, 3, 4 and 5, respectively. The sizes of the rock models in each group are determined so that the numbers of particles in each model will be the same.

In the previous section, it is found that the tensile strength obtained from the uniaxial tension test is more stable than that from the Brazilian test, and the uniaxial tension test can use the same rock model as that for the uniaxial compression test. For these reasons, tensile strength of the rock model is obtained only from the uniaxial tension test, and simulation of the Brazilian test is not performed in this section.

Fig.2.13(a) shows the relation between the coefficients of variation of macroscopic mechanical properties obtained from the simulation and the ratio of maximum/minimum particle radius. As shown in Fig.2.13(a), the coefficients of variation of all macroscopic mechanical properties are almost constant. This result indicates that the particle size distribution does not affect the coefficients of variation of the macroscopic properties of rock model.

Fig.2.13(b), (c) and (d) show the comparison of the UCS, the Young's modulus and the uniaxial tensile strength as a function of the ratio of maximum/minimum particle radius of the rock model for each group, respectively. The averages of the UCS, the Young's modulus and the uniaxial tensile strength increase as the ratio of maximum/minimum particle radius increases. Fig.2.13(e) shows the typical particle size cumulative curve for each group, and the number of small particles increases as the ratio of maximum/minimum particle radius increases. As mentioned in section 2.4.2, although the particle radius was selected satisfying with a uniform distribution between maximum and minimum radius using random number, particle packing process is repeated until a new particle with minimum radius can not be arranged. Therefore, a lot of small particles are required to bury the void space among large particles, and the porosity of the model significantly decreases as the ratio of maximum/minimum particle radius increases as shown in Table 2.4. When the particles were closely arranged, the displacement of the each particle is constrained by contact with surrounding particles even after the bonds between particles are broken. Moreover, the number of bonds between particles increases when the particles are closely arranged. This means that the number of bonds between particles increases as the ratio of maximum/minimum particle radius increases. When the number of bonds increases, the load can be distributed to many bonds and the stress acting on a bond decreases relatively. Therefore, the macroscopic mechanical properties increase as the ratio of maximum/minimum particle radius increases as shown in Fig.2.13(b), (c) and (d).
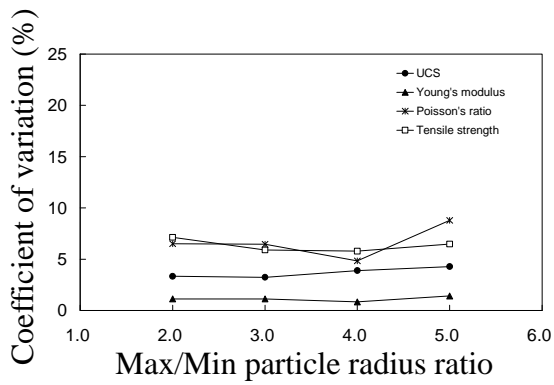
(a) Coefficient of variation
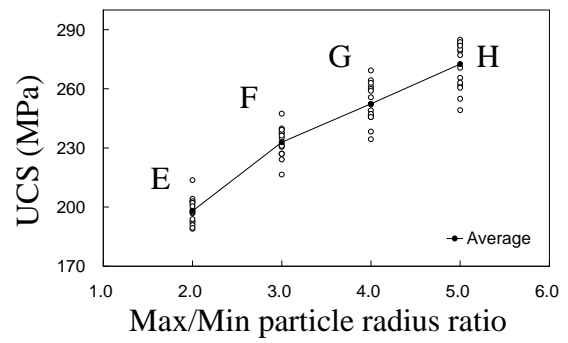
(b) Uniaxial compressive strength (UCS)
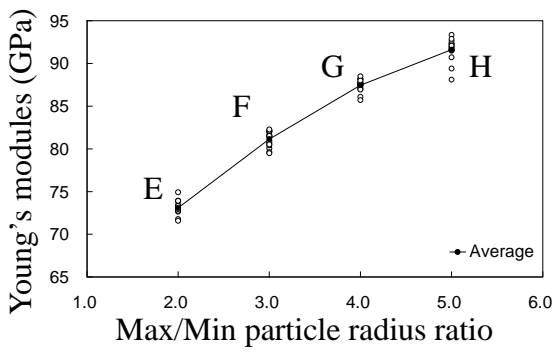
(c) Young's modules
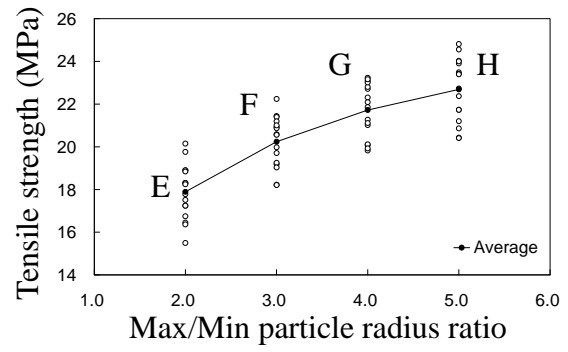
(d) Tensile strength (Brazilian test)
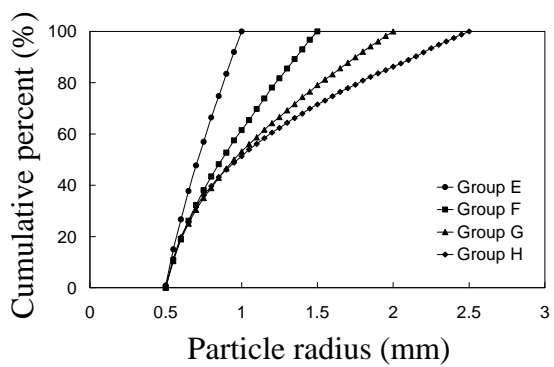
(e) Particle size cumulative curve
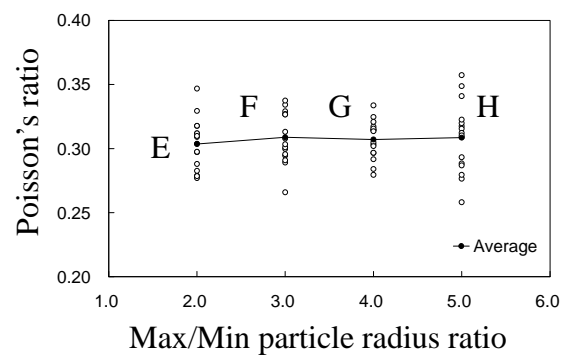
(f) Poisson's ratio

Fig.2.13   Relations between the particle radius distribution and macro properties of rock model.

In the previous section, it is found that the similar effect to size effect in actual rock specimen is caused by the number of bonds in DEM simulation, and that the UCS decreases as the number of bonds increases as shown in Fig.2.11(b). On the other hand, as shown in Fig.2.13(b), the UCS increases greatly as the ratio of maximum/minimum particle radius increases. This result may suggest that the increase in UCS of the rock model due to the decrease in porosity is much larger than the corresponding size effect in DEM.

Fig.2.13(f) shows the comparison of the Poisson's ratio as a function of the ratio of maximum/minimum particle radius of the rock model for each group. Both the coefficients of variation and the average value of the Poisson's ratio are almost constant. In addition to the result of previous section, it is found that the influence on Poisson's ratio of the number of particles and the particle size distribution is small.

2.5.4 Scale of the model

The DEM have been applied for solving many rock mechanics problems in laboratory scales. The DEM has been also used to simulate large field scale rock engineering problems such as tunnel/cavern excavation and evaluation of EDZ [23], tunnel face stability [24], design of tunnel lining [25], rock cutting, and slope stability analysis [26]. However, there is a problem to be solved to perform the DEM simulations on the field scale. Although one particle size for the field scale simulations may becomes range from several centimeters to several meters due to the limitation of the particle number, the calibration of the microscopic parameter is often performed based on laboratory scale testing results that use a small rock specimen because the rock test using a large specimen of several meters is economically difficult. Whereas, there are only a few research that consider the influence of the difference of the model scale in DEM simulation.

Hence, to reveal the influence of the model scale on the simulation results, the rock models divided into four groups (Group I, J, K and L) with different ranges of model scale as shown in Table 2.5 were generated. For each group, 16 rock models were prepared. Here, the models of Group I is almost the same as the models of Group E in the previous section, and each model of Group I is enlarged twice, five times, and ten times to create each model in Group J, K and L, respectively. The number of particles and the relative position of each particle are retained for each group.

The simulations of the uniaxial compression and tension tests are performed for each group. Loading rates for each group are adjusted as the rate of the axial strain becomes

constant. The average value of the UCS, Young's modulus, tensile strength and Poisson's ratio in each group obtained from the simulations are summarized in Table 2.6. Table 2.6 indicates that the change of the average macroscopic mechanical properties with different scale of the model is small. This result indicates that the similar macroscopic mechanical properties are obtained in DEM simulation regardless of the scale of the model when the particle arrangement and the number of particles are the same. In other words, the field scale rock mass model become relatively hard and strong when the microscopic parameters based on the laboratory scale rock test results is used because the strength of actual rock mass decreases with increasing of specimen size due to the size effect. Therefore, microscopic parameters used in the field scale DEM simulation should be calibrated with consideration of the size effect according to the scale of the application.

Table 2.5   Four data sets for different model scale.

	Group I	Group J	Group K	Group L
Number of particles (average):	9378	9378	9378	9378
Maximum particle radius:	1.0mm	2.0mm	5.0mm	10.0mm
Minimum particle radius:	0.5mm	1.0mm	2.5mm	5.0mm
Max/Min particle radius ratio:	2.0	2.0	2.0	2.0
Porosity of the model (average):	18.89%	18.89%	18.89%	18.89%
Number of models:	16	16	16	16
Model width:	100mm	200mm	500mm	1000mm
Model height:	200mm	400mm	1000mm	2000mm

Table 2.6   Average value of macro properties of rock model in each group.

	Group I	Group J	Group K	Group L
Average Young's modules (GPa):	73.1	73.2	73.1	73.1
Average Poisson's ratio:	0.30	0.30	0.30	0.30
Average UCS (MPa):	198.0	196.8	197.0	197.8
Average uniaxial tensile strength (MPa):	17.9	18.1	18.1	18.0

2.6. Conclusion

A large number of rock models have been created, and the uniaxial compression tests, uniaxial tension test and Brazilian tests are simulated by own DEM code. The simulation results are compared with the results obtained from the laboratory tests conducted by former researchers to verify the applicability of the DEM code, and the influence of the model geometry, such as model scale, the number of particles and particle size distribution are discussed in detail. As results, the followings are found.

1. It is pointed out that the tensile strength of the rock model obtained by the calibration is larger than the experimental result when parallel-bond model that Potyondy and Cundall constructed is used. However, appropriate calibration results not only the uniaxial compressive strength (UCS), Young's modulus, and Poisson's ratio but also tensile strengths of the rock model were obtained by using newly developed DEM code.

2. The averages of all macroscopic mechanical properties are almost constant regardless of the reciprocal of the loading rate, and that the coefficients of variation of macroscopic mechanical properties decrease with the increase in the reciprocal of loading rate. The coefficients of variation decrease sufficiently when the reciprocal of loading rate becomes ten or more.

3. When the sizes of the rock models are the same, the coefficients of variation of macroscopic mechanical properties, such as UCS, Young's modulus, Poisson's ratio, uniaxial tensile strength and indirect (Brazilian) tensile strength, decrease with the increase in the number of particles. By using 10000 or more particles, the coefficients of variation of all macroscopic mechanical properties are less than 10%, and stable results can be obtained.

4. The macroscopic mechanical properties are not affected by the scale of the model in DEM simulation when the particle arrangement and the number of particles are the same. On the other hand, the average of the UCS decreases as the number of particle increases. This result indicates that the similar effect to size effect in actual rock specimens is caused by change of the number of particles in DEM simulation, and not caused by the size of DEM rock model.

5. The rock model in the DEM is expressed by the assembly of circler particles and

contains many pores. This means that the Young's modulus obtained from the DEM simulations is effective Young's modulus. Therefore, the average of the Young's modulus increases as the porosity of the rock model increases.

6. The average value of the Poisson's ratio is almost constant though the coefficients of variation decreases rapidly as the particle number increases. This result is in agreement with the former results presented by other researchers [2].

7. The tensile strengths obtained from uniaxial tension tests and Brazilian tests are almost the same. However, the coefficient of variation of the tensile strength in the uniaxial tension test was smaller than that in the Brazilian test.

8. When the particles are closely arranged and the porosity of the model decreases, the displacement of the each particle is constrained by contact with surrounding particles even after the bonds between particles are broken. Moreover, by decreasing of the porosity, the load is widely distributed to the model, and the stress that acts on each bond decreases relatively. Therefore, the macroscopic mechanical properties, such as elasticity and strength, increase as the porosity of the model decreases.

References

[1] Cundall PA and Strack ODL. A discrete numerical model for granular assemblies. Geotechnique, 1979; 29(1): 47-65.

[2] Potyondy DO and Cundall PA. A bonded- particle model for rock. Int J Rock Mech Min Sci, 2004; 41: 1329-1364.

[3] Yoon J. Application of experimental design and optimization to PFC model calibration in uniaxial compression simulation. Int J Rock Mech Min Sci, 2007; 44(6): 871-889.

[4] Koyama T and Jing L. Effects of model scale and particle size on micro-mechanical properties and failure processes of rocks - A particle mechanics approach. Engineering Analysis with Boundary Elements, 2007; 31(5): 458-472.

[5] Schöpfer MPJ, Childs C and Walsh JJ. Two-dimensional distinct element modeling of the structure and growth of normal faults in multilayer sequences: 1. Model calibration, boundary conditions, and selected results. J Geophys Res, 2007; 112: B10401.

[6] Fakhimi A. Application of slightly overlapped circular particles assembly in numerical simulation of rocks with high friction angles. Engineering Geology, 2004; 74(1): 129-138.

[7] Huang H. Discrete element modeling of tool-rock interaction. Ph.D thesis, University of Minnesota, 1999.

[8] Shimizu H, Murata S and Ishida T. The applicability of distinct element modeling for rock fracture. Journal of MMIJ, 2008; 124(12): 777-784. (in Japanese).

[9] Shimizu H, Murata S and Ishida T. Distinct element analysis for rock failure under uniaxial compression. Journal of MMIJ, 2008; 125(3): 91-97. (in Japanese).

[10] Shimizu H, Koyama T, Ishida T, Chijimatsu M, Fujita T and Nakama S. Distinct element analysis for ClassII behavior of rock under uniaxial compression. Int J Rock Mech Min Sci, 2009; (in press).

[11] Kasahara K. Earthquake mechanics. Cambridge university press, 1981; 38-42.

[12] Roark RJ and Young WC. Formulas for Stress and Strain 5th Edition. McGraw-Hill Book Company, 1975.

[13] Landau LD and Lifshitz EM. Theory of Elasticity. Pergamon Press, Oxford, 1986.

[14] Fairhurst CE and Hudson JA. Draft ISRM suggested method for the complete stress-strain curve for intact rock in uniaxial compression. Int J Rock Mech Min Sci, 1999; 36: 279-289.

[15] Brown ET. Rock characterization, testing and monitoring: ISRM. suggested methods. Pergamon Press, 1981.

[16] Feng YT, Han K and Owen DRJ. Filling domains with disks: an advancing front approach. Int J Numer Meth Eng, 2003; 56: 699-713.

[17] Bagi K. An algorithm to generate random dense arrangements for discrete element simulations of granular assemblies. Granul Matter, 2005; 7: 31-43.

[18] Stoyan D. Simulation and characterization of random systems of hard particles. Image Anal Stereol, 2002; 21(Suppl. 1): 41-48.

[19] Cui L and O'Sullivan C. Analysis of a triangulation based approach for specimen generation of discrete element simulations. Granul Matter, 2003; 5: 135-45.

[20] Zsaki AM. An efficient method for packing polygonal domains with disks for 2D discrete element simulation. Computers and Geotechnics, 2008; 36(4): 568-576.

[21] Lama RD and Vutukuri VS. Handbook on Mechanical Properties of Rocks II. Translated by H.Masuda and S.Tanaka, Kokonsyoin, 1992; 289-398.

[22] Moon T, Nakagawa M and Berger J. Measurement of fracture toughness using the distinct element method. Int J Rock Mech Min Sci, 2007; 44: 449-456.

[23] Aoki K, Mito Y, Mori T, Morioka H and Maejima T. Evaluation of behavior of

EDZ around rock cavern by AE measurement and DEM simulation using bonded particle model. Proc. of the third Asian rock mechanics symposium, Mill Press, Rotterdam, 2004; 327-333.

[24] Okabe T, Haba T, Mitarashi Y, Tezuka H and Jiang Y. Study on the effect of tunnel face stabilization using the distinct element method. Proc. of the third Asian rock mechanics symposium, Mill Press, Rotterdam, 2004; 1301-1304.

[25] Tannant DD and Wang C. Thin tunnel liners modeled with particle flow code. Eng Comput, 2004; 21(2/3/4): 318-342.

[26] Wang C, Tannant DD and Lilly PA. Numerical analysis of the stability of heavily jointed rock slopes using PFC2D. Int J Rock Mech Min Sci, 2003; 40(3): 415-424.

Chapter 3
Distinct element analysis for rock failure
considering AE events generated by the slip at crack surfaces

3.1. Introduction

In order to understand the mechanism of microcracking in brittle rock samples, considerable amount of experiment has been carried out by various methods in the past few decades. Among them, one approach is monitoring acoustic emission (AE) events caused by microcracking activity. Using the recently developed high speed, multichannel waveform recording device, many waveforms of AE events can be recorded with fracturing process in a stressed rock specimens with high resolution. Thus, the measurement of the AE is effective technique to study the dynamics of microcracks [2-5].

However, even at present, it is still difficult to record the waveform of all AE events generated in the experiments due to the limitation of storage capacity and recording speed of measuring device, and the influence of the noise. In particular, when the catastrophic fracture is formed in a rock specimen, there is a burst of AE events in a very short time. Therefore, sufficient AE waveform data cannot be recorded by most experimental systems. In addition, though generation of new cracks and propagation of existing cracks are seems to be the dominant mechanisms of AE events, slipping at the crack surface should also generate AE events. However, it is difficult to distinguish AE events caused by slip at pre-existing crack surfaces.

In this chapter, as a fundamental research for the rock fracturing, the uniaxial compression test of rock have been simulated by newly developed DEM code that can model the AE events generated by the slip at pre-existing crack surfaces. The DEM can represent grain-scale microstructural features directly by considering each grain in actual rock as a DEM particle. The grain-scale discontinuities in the DEM model induce complex macroscopic behaviors without complicated constitutive laws [6,7]. The mechanical behavior in a brittle rock including not only generation of microcracks but also slip occurrence at existing crack surfaces can be discussed in detail. The simulation results are compared with the fracturing process deduced from the laboratory AE measurements conducted by previous researchers in order to discuss the process in which microcracks are induced inside a rock and result in a macroscopic fracture.

3.2. Consideration of the slip AE

Hazzard *et al*. [8,9] have reported the DEM modeling for AE activity. They presented a technique to simulate AE behavior in brittle rock under uniaxial compression using the commercially available DEM code (particle flow code: PFC [7]) by considering the kinetic energy released when the bonds break. However, one of inaccuracy with the AE produced by their PFC model is the narrow range in observed magnitudes and consequently low b-values. According to their results, the magnitude of smallest AE events produced by their model is about an order larger than the corresponding actual AE monitoring. One possible solution for this problem is to somehow consider re-activation of cracks such that seismicity could occur on the contacts where bonds had already broken [8,9].

In actual AE measurements in the laboratory, the AE hypocenter can be calculated by the arrival time of the P-wave first motion and focal mechanisms of AE events are determined from the spatial distribution of P-wave first motion polarities [10]. Therefore, the crack modes in the DEM simulation are classified by shear-tensile stress ratio $|\tau/\sigma|$ regardless of broken spring type (normal spring or shear spring) as mentioned in section 2.2.2. In this research, these classified shear and tensile crack generation are assumed to be the shear AE and the tensile AE, respectively [11,12].

In addition to the shear AE and the tensile AE, the classification and the failure criterion for the slip AE was introduced in the DEM code by extending conventional concept of the DEM [13]. When the frictional force acting at the contact points exceeds the critical value, the slip occurs as mentioned in section 2.2.3. It is thought that such a slip occurring at the crack surface should also generate AE events. Thus, the slip at crack surfaces is added to the bond breakage as a possible mechanism of AE event occurrence. Consequently, AE events in the DEM simulation are classified by their source mechanisms as follows.

- Generation of new tensile cracks $\longrightarrow$ Tensile AE
- Generation of new shear cracks $\longrightarrow$ Shear AE
- Slip occurrence at the crack surface $\longrightarrow$ Slip AE

When a new microcrack is generated, the strain energy stored in both normal and shear springs at the contact point is released. The strain energy E_k calculated using equation (2.14) is assumed to be the energy corresponding to the magnitude of tensile and shear AE event.

On the other hand, when a slip occurs, frictional force will be replaced by the critical

value calculated using the equation (2.25) which represents the Coulomb's frictional law. During this process, the strain energy stored in springs at the contact point is partly released. The released strain energy E_{slip} is given by

$$E_{slip} = E_{kafter} - E_{kbefore} \tag{3.1}$$

where $E_{kbefore}$ and E_{kafter} are the strain energy calculated by equation (2.14) at the time step before and after slip occurrence, respectively. The released strain energy E_{slip} is assumed to be the energy corresponding to the magnitude of slip AE.

3.3. Rock specimen model for the simulation

As shown in Fig.3.1, the rock model which was 10cm in width and 20cm in height was used to simulate the uniaxial compression test. The rock model is expressed by the assembly of particles bonded with each other. The particle radius was chosen to have a uniform distribution between maximum radius and minimum radius. The number of particles was 9319. The particles were irregularly arranged in positions by using a random number.
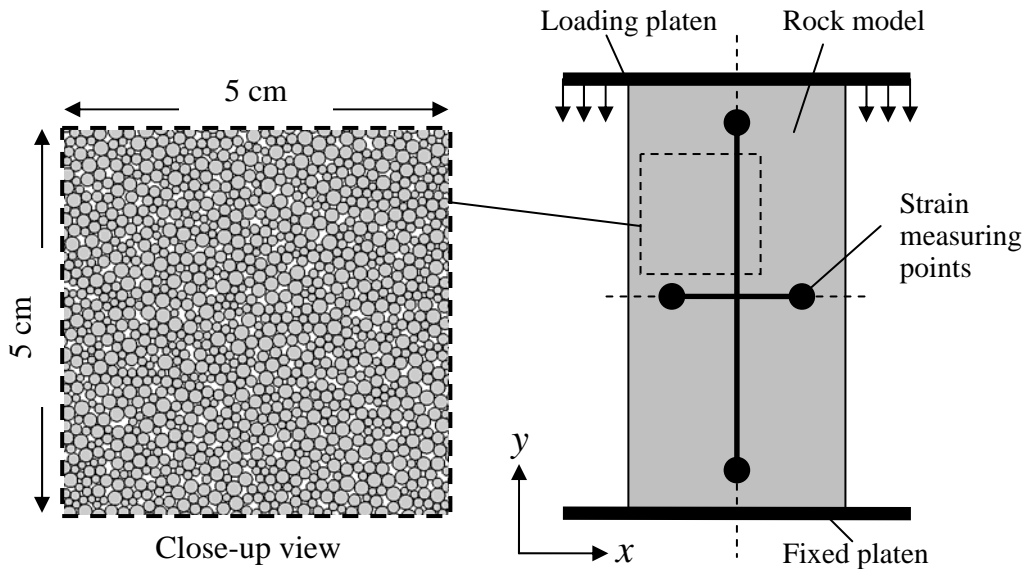
Fig.3.1   Loading condition for the simulation of uniaxial compression tests. The monitored particles for the axial and radial strain were located slightly inside from the edge of the rock model. The distance between two measuring points is 90% of the rock model width or height.

The platen under the rock model was fixed and the upper loading platen was moved downward slowly to reproduce the uniaxial compression test. At this time, frictional force was acting between the rock model and the platens.

The axial stress applied to the rock model during the compression test was calculated from width of the model and total force acting on the upper loading platen from particles. The strain is calculated from the displacement of the four monitored particles as shown in Fig.3.1.

Table 3.1　Rock model properties and calibration results.

ROCK MODEL DATA

Width of the Rock model:	100mm
Height of the Rock model:	200mm
Number of particles:	9319
Maximum particle radius:	1.0mm
Minimum particle radius:	0.5mm
Particle density:	2620 kg/m^3
Friction coefficient of platen ($\tan \phi_w$):	0.5
Poisson's Ratio of platen (v_w):	0.3
Young's modulus of platen (E_w):	200GPa
Friction coefficient of particle ($\tan \phi_p$):	0.3
Poisson's Ratio of particle (v_p):	0.3

TUNING PARAMETERS

Young's modulus of particle (E_p):	87.0 (GPa)
Shear/normal spring stiffness ratio (α):	0.54
Shear strength of bonding (τ_c):	235.0 (MPa)
Tensile strength of bonding (σ_c):	26.0 (MPa)

CALIBRATION RESULTS

	Experiment	Simulation
UCS of rock model (MPa):	200	200.63
Young's modulus of rock model (GPa):	70.0	69.25
Poisson's Ratio of rock model:	0.250	0.244
Tensile strength of rock model (MPa):	10.0	10.2

For proper simulation using DEM, appropriate microscopic parameters should be selected. Therefore, preliminary simulations of the uniaxial compression test and the Brazilian test was repeated beforehand, and the microscopic parameters should be adjusted to represent a certain macroscopic mechanical properties. In this study, macroscopic mechanical properties of Kurokamijima granite are used to calibrate the microscopic parameters. The microscopic parameters and calibration results are shown in Table 3.1.

3.4. Simulation Results

3.4.1 Stress-strain curves

Fig.3.2 shows the stress-strain curves obtained from the DEM simulation. Though actual deformation is three-dimensional, this simulation is two-dimensional, and the strain in the direction of depth is not considered. Therefore, the volumetric strain ε_v in this simulation is defined by using the axial strain ε_1 and lateral strain ε_2. The volumetric strain ε_v is defined as the following equation. The stress and the strain are positive in compression.

$$\varepsilon_v = \varepsilon_1 + 2\varepsilon_2 \tag{3.2}$$
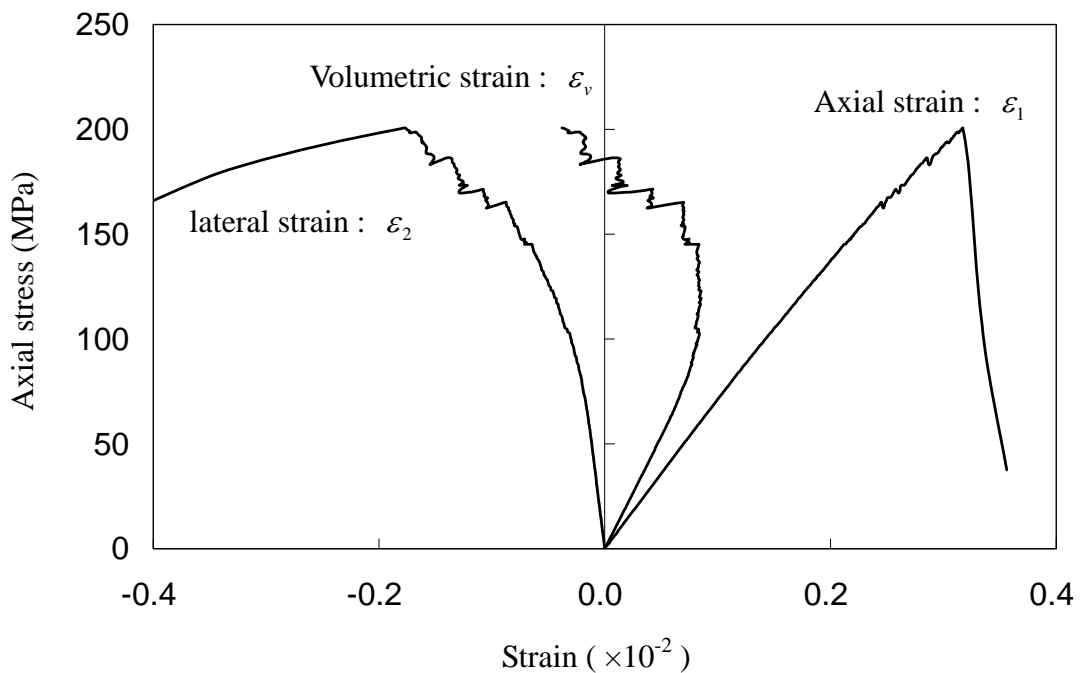
Fig.3.2   Stress strain curves.

Fig.3.3 shows the relation between the axial stress and the number of AE events. The solid line in Fig.3.3 shows evolution of the axial stress. The open, closed and hatched bar diagrams in the figure express the number of tensile AE, shear AE and slip AE, respectively. As shown in Fig.3.3, the number of total AE event increases gradually as the axial stress increases. This result agrees well with the typical tendency observed in actual rock fracturing under compression [14].

Fig.3.4 shows the close-up view of the dotted rectangle in Fig.3.3 to clarify the activities of shear and tensile AE. The solid line in Fig.3.4 shows evolution of the volumetric strain. The volumetric strain increases (volume of the model decreases) constantly in the initial stage of the loading, and gradually changes into nonlinear behavior as the axial stress increases.

It is well known that the dilatancy in an actual rock is caused with the growth and opening of microcracks. When a shear crack is generated and slip occurs at the existing crack surface, the tensile cracks develop from both ends of the shear crack with large opening of tensile crack [15,16]. Then, the volume of the model increases, and the dilatancy occurs. As shown in Fig.3.4, the volumetric strain curve begins to change when generation of shear AE begins, and decreases (volume of the model increases) with increasing in shear AE and slip AE. This result indicates that occurring of the dilatancy observed in an actual uniaxial compression test can be appropriately reproduced by the DEM simulation.

3.4.2 Transition of the number of AE events and AE source mechanism

As shown in Fig.3.3 and 3.4, the rock fracturing process under uniaxial compression can be divided into three phases according to the AE activities as follows [5].

- Phase I   (Time Step 1 - 190×10^4): Tensile AE is dominant.
- Phase II   (Time Step 190×10^4 - 320×10^4): Slip AE increases.
- Phase III   (Time Step 320×10^4 - 360×10^4): Catastrophic fracture is formed.

Fig.3.5(a), (b) and (c) show the spatial distribution of the tensile and the shear AE events in each phase, respectively. The tensile and shear AE are classified and expressed as closed and open circles, respectively. The diameters of each circle correspond to respective magnitude of tensile and shear AE obtained by equation (2.14). On the other hand, Fig.3.6(a), (b) and (c) show the spatial distribution of the slip AE in each phase, respectively. The diameters of the circle correspond to respective magnitude of slip AE obtained by equation (3.1). The AE activities in each phase are described as follows.
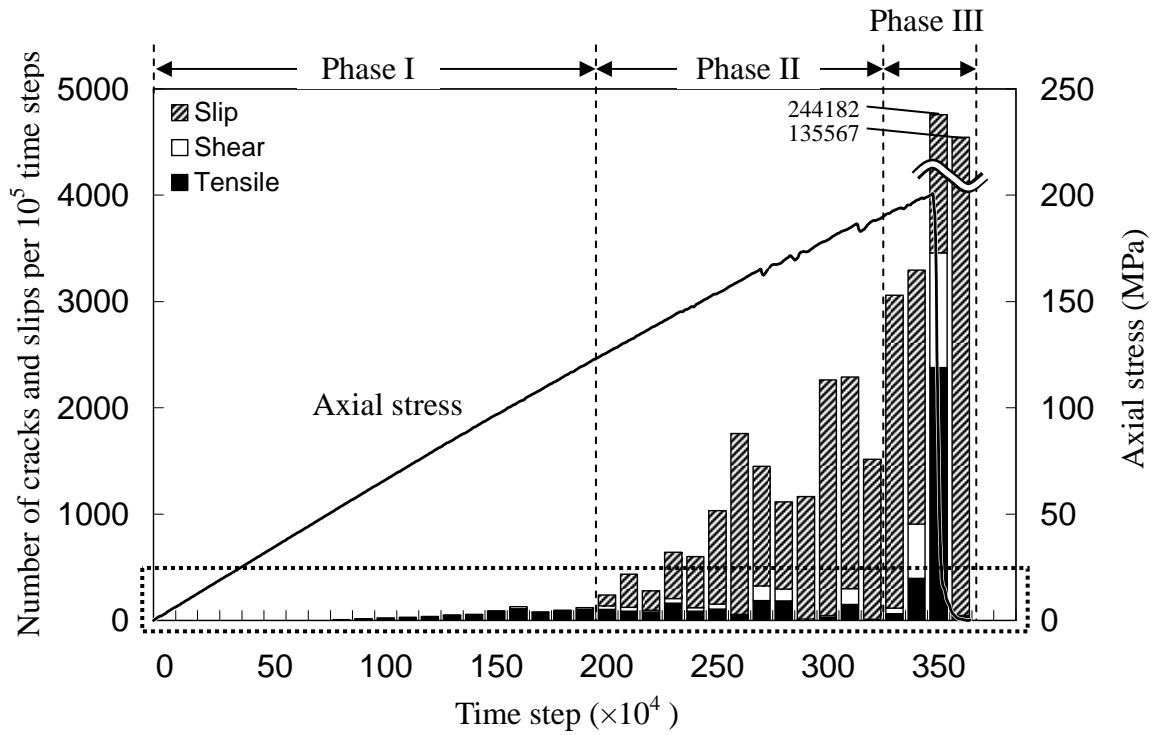
Fig.3.3   Transition of the number of cracks and slip with the evolution
of the axial stress.
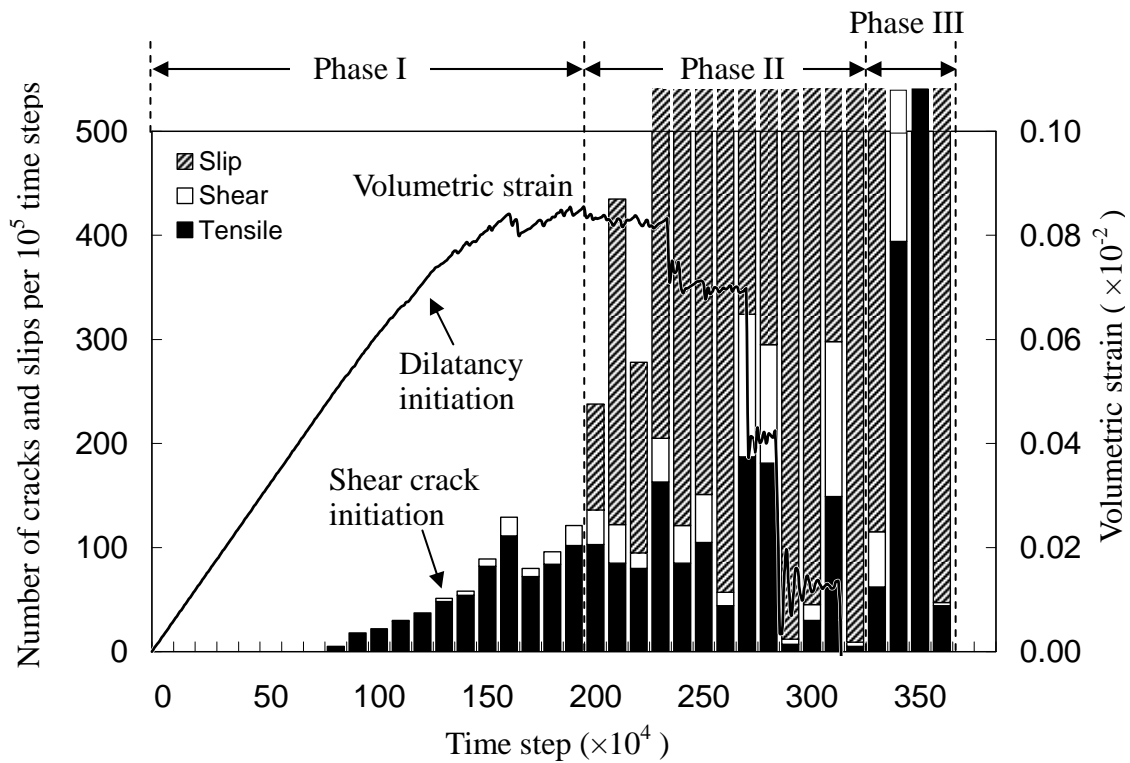
Fig.3.4   Close-up view of the transition of the number of shear and tensile AE
(dotted rectangle in Fig.3.3) with the evolution of the volume strain.

53

(a) Phase I

[Step1-190 ($\times 10^4$)]

(b) Phase II

[Step190-320 ($\times 10^4$)]

(c) Phase III

[Step320-360 ($\times 10^4$)]
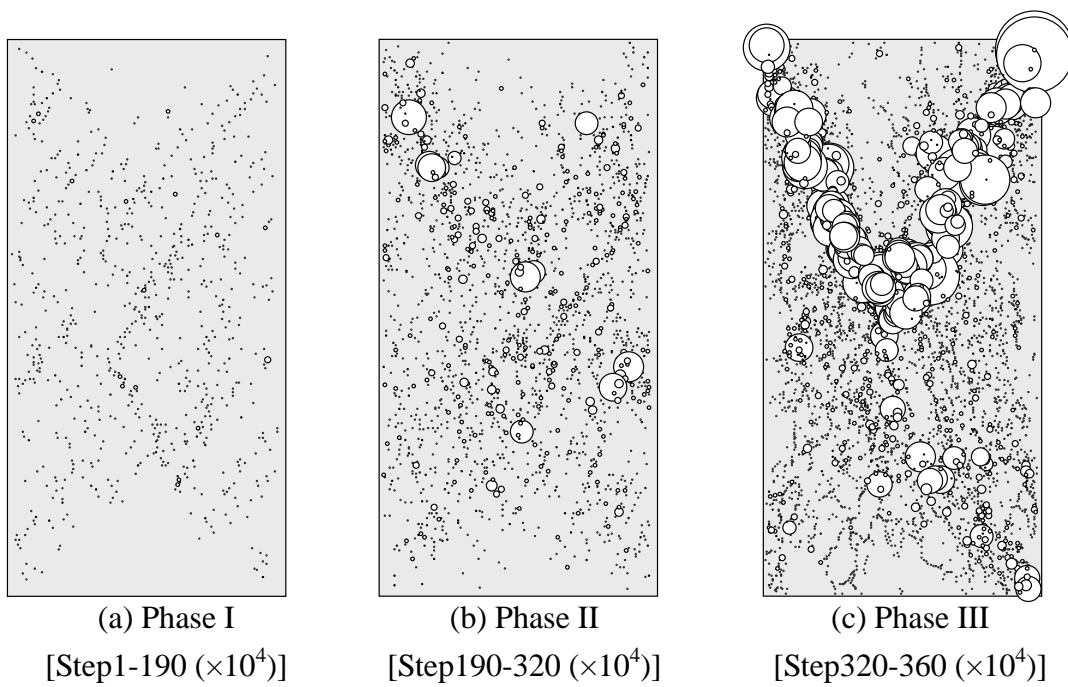
Fig.3.5 Spatial distribution of the tensile and the shear AE events generated in each phase. Tensile and shear cracks are expressed as closed and open circles, respectively. The diameters of each circle correspond to their respective magnitudes of energy.

(a) Phase I

[Step1-190 ($\times 10^4$)]

(b) Phase II

[Step190-320 ($\times 10^4$)]

(c) Phase III

[Step320-360 ($\times 10^4$)]
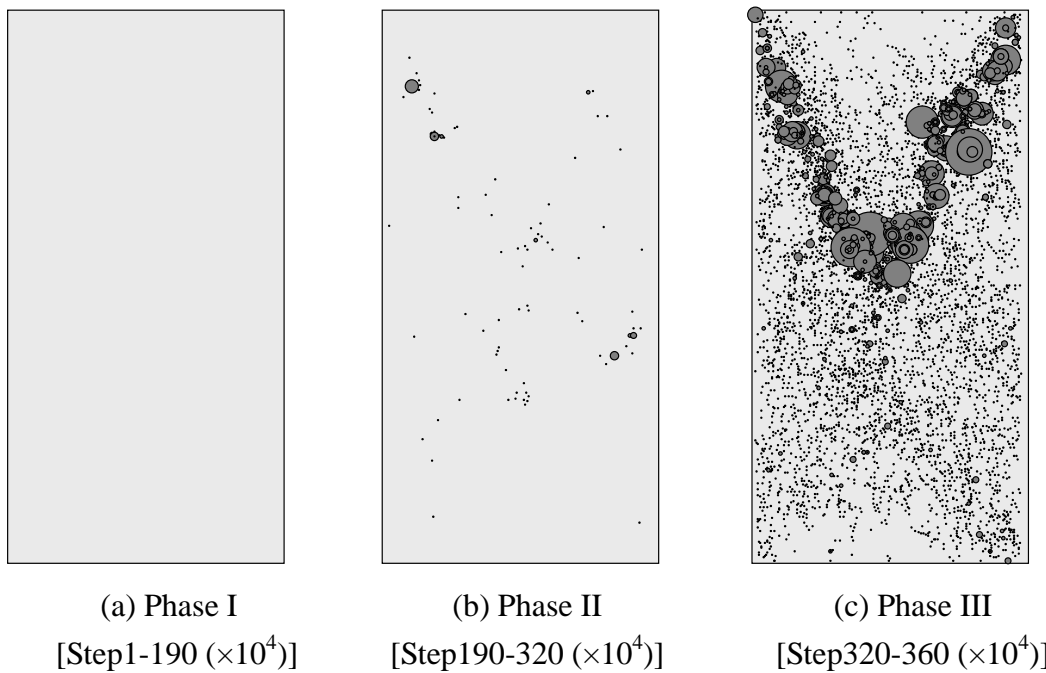
Fig.3.6 Spatial distribution of the slip AE events generated in each phase. The diameters of each circle correspond to their respective magnitudes of energy.

In the Phase I, tensile AE initiated at a stress level about 35% of the uniaxial strength. As the axial stress increases, the number of AE events increases gradually and shear AE also initiated. As shown in the bar diagram in Fig.3.3 and 3.4, dominant mechanism of the AE events in low stress level was new tensile crack generation.

As shown in Fig.3.5(a), energy of AE events generated in the Phase I was very small. Although these AE events were widely distributed over the whole model, the density of AE events decreased from the center toward the loaded ends of the rock model. On the other hand, slip AE was not generated in the Phase I as shown in Fig.3.6(a). After the tensile crack generation, these tensile cracks opened immediately due to the tensile stress acting perpendicular to the loading axis. Thus, the surface of open crack never contact mutually, and slip did not occur.

In the Phase II, in addition to the tensile and the shear AE, the slip AE began to be generated. As the axial stress increases, the number of slip AE increased more. This result suggests that the dominant mechanism of the AE occurrence changes from new crack generation to slip occurrence. As shown in Fig.3.4, burst of microcracking observed in this phase, and the number of microcracking extremely decreased after each burst of AE. By comparing the AE magnitudes and location shown in Fig.3.5(b) and Fig.3.6(b), a few shear AE which releases comparatively large energy were generated in this phase, and the slip AE were generated at the same position as such the shear AE that release large energy.

In the Phase III, the number of AE events increased rapidly. A macroscopic fracture was formed in a very short time, and the model resulted in collapse. The macroscopic fracture grows toward upper left and right from the center of the model. At this time, 95% of AE events were caused by the slip occurrence. As shown in Fig.3.5(c), the shear and tensile AE concentrated near the center of the model and progressed to both the upper left and upper right of the model along the macroscopic fracture. These AE events were the shear AE and released remarkably large energy compared with other AE. Moreover, the slip AE events that release remarkably large energy were also generated along the macroscopic fracture as shown in Fig.3.6(c).

3.4.3 b-value

The b-value is defined as the log-linear slope of the frequency–magnitude distribution of AE [17,18]. It represents the scaling of magnitude distribution of AE, and is a measure of the relative numbers of small and large AE which are indicator of localized failures in materials under stress. A high b-value arises due to relatively large number of small AE events compared with the number of AE events with relatively large

amplitude. On the other hand, a low b-value arises in the contrary case. The b-value is calculated by the Gutenberg–Richter relation [19], which is widely used in seismology. The equation is as follows.

$$\log n = a - bM \tag{3.3}$$

where M is the magnitude of AE event, n is the number of AE events of magnitude M or greater, a is a constant and b is the seismic b-value.

In this simulation, the magnitude M of an AE event is calculated by following equation (3.4) as logarithm of the energy obtained by equation (2.14) and (3.1), and the b-value was calculated by equation (3.5) [20,21].

$$M = \log(E_k) \tag{3.4}$$

$$b = \frac{0.4343n}{\sum_{i=1}^{n} M_i - nM_m} \tag{3.5}$$

where M_m is the minimum magnitude of AE event.

Note that, the energy of most slip AE is extremely smaller than that of tensile and shear AE. Such too small AE are hardly observed in an actual AE measurement experiment. For this reason, slip AE which energy is smaller than the minimum energy of tensile and shear AE is excluded from the calculation of the b-value. Hence, the minimum magnitude of AE event for the calculation of the b-value is about -3.0 in this simulation.

Fig.3.7 shows the relation between the magnitude of AE events and cumulative number of AE events with the b-value in each phase. In the Phase I, since all AE events generated in this phase are very small, b-value is relatively high, 1.01. Whereas, the b-value is decreasing as the axial stress increases, and the b-value becomes minimum value, 0.59, in Phase III. This result is well in agreement with the tendency of actual AE measurement experiment conducted by Lei et al. [4,5,22].

The strain energy given by equation (2.14) or (3.1) is released from the model when a bond breaks or a slip occurs. This produces force imbalance, and subsequent stress redistribution induces an AE event. Therefore, logarithm of the energy given by equation (3.4) does not directly express the magnitude of AE event. However, as shown in Fig.3.7, the relation between the magnitudes calculated from equation (3.4) and the number of AE events appropriately represents the tendency of an actual AE

measurement. This result suggests that the strain energy given by equation (2.14) and (3.1) is at least qualitatively valid as a value that corresponds to the magnitude of AE. Moreover, several researchers pointed out that the b-value depends on the heterogeneity of the rock [4,5,17,18]. Therefore, the DEM simulations with various heterogeneous rock models will be effective to discuss the influence of the heterogeneity on the fracturing process of rock that is difficult to be observed in an experiment.

3.5. Discussion

3.5.1 Generation of tensile AE at lower stress level

During the Phase I, the tensile AE events were dominant and were widely distributed over the whole model. This result agrees well with the experimental results. According to the experimental results, the major mechanism of the AE events at lower stress level is the tensile cracks associated with the initial rupture of pre-existing flaws [4,5]. This indicates that the DEM can successfully represent the grain-scale microstructures such as pores, microcracks and grain boundaries directly by considering each grain as a DEM particle.
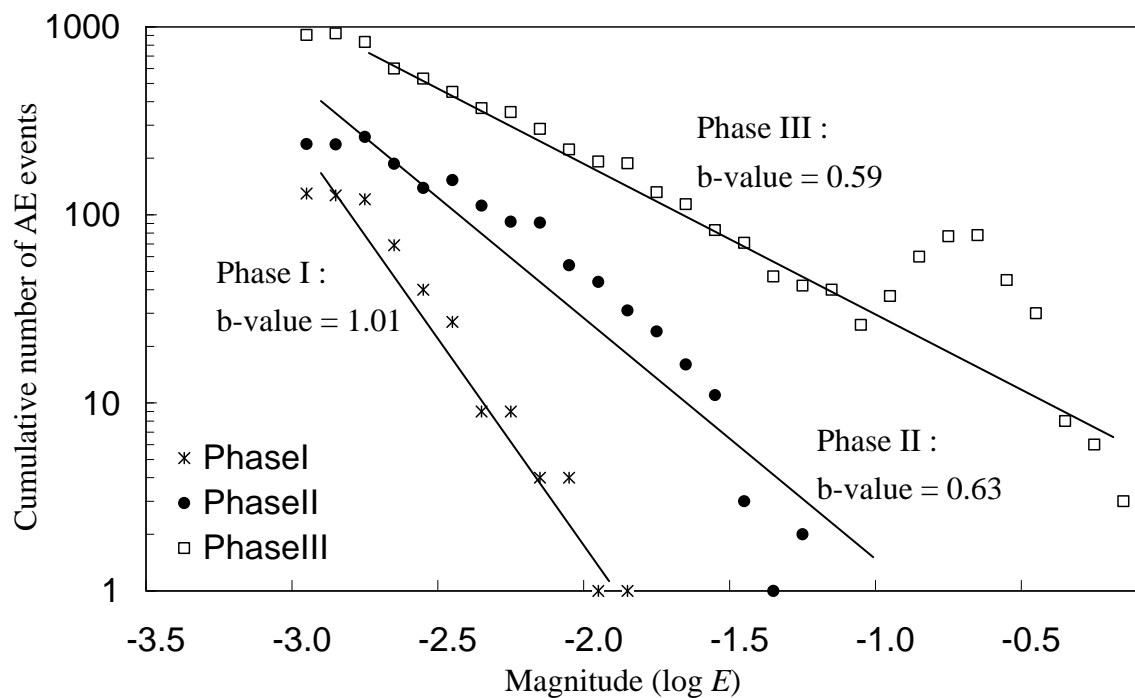
Fig.3.7   Energy-frequency distributions and temporal variations in b-value.

Fig.3.8(a), (b), and (c) show the distribution of maximum principal stress, the minimum principal stress, and the maximum shear stress in the model at time step 71×10^4. The stress is positive in compression. The calculation procedure for the stress distribution in DEM model is described in APPENDIX.

As shown in Fig.3.8 (a), (b) and (c), the stress distribution in the rock model is not entirely uniform. This is because the stresses that act between particles are evaluated by using the radius of the particles. The particle radius and the position are irregularly given by the random number though the microscopic parameters, such as Young's modulus and strength of the spring, are constant. Therefore, the transmission of force becomes irregular and local; as a result, the stress distribution in the rock models becomes heterogeneous.

As shown in Fig.3.8(b), there are some regions where a relatively large tensile stress were acting on. The tensile AE were dominantly generated in such regions because the tensile strength of the spring that connects between particles is small compared with the shear strength as shown in Table 3.1. However, the tensile cracks are widely distributed in the rock model and the number of cracks is few at Phase I. Each microcrack does not influence each other, and such the tensile cracks did not grow any more.

(a) Maximum principal stress (b) Minimum principal stress (c) Maximum shear stress
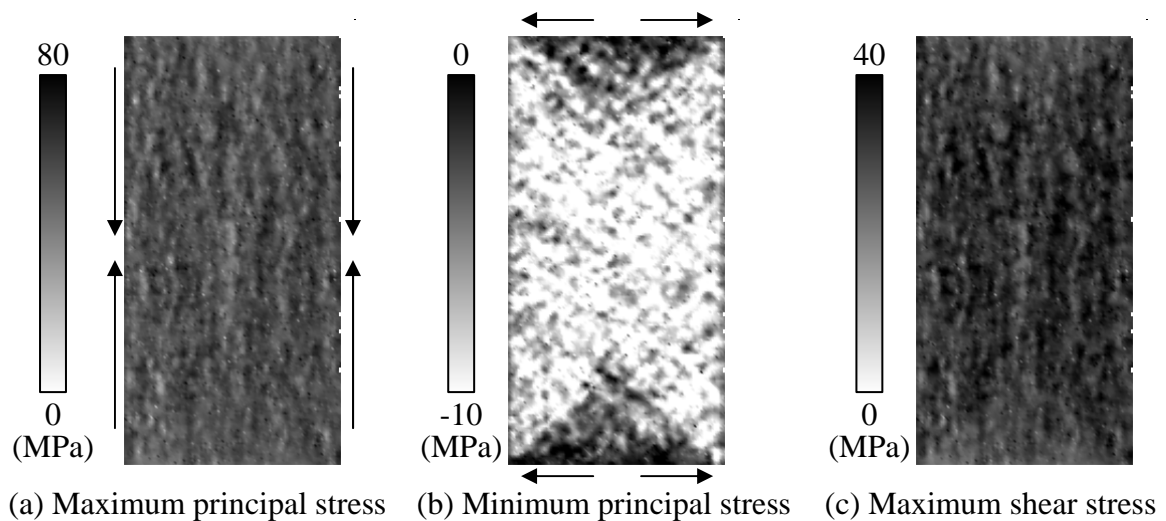
Fig.3.8   Stress distribution at time step 71×10^4. Cracks initiate at this time step. (a) maximum principal stress, (b) minimum principal stress and (c) maximum shear stress. The arrows in (a) and (b) indicate the direction of maximum and minimum principal stress, respectively. The stresses are positive in compression.

Fig.3.8(b) also indicates that the tensile stress at the loaded ends of the rock model is relatively lower than the other region. According to the stress distribution, the density of AE events decreases from the center toward the loaded ends of the rock model. This is due to the frictional restraints between the rock model and the loading platen interfaces [23].

3.5.2 AE clustering

In the Phase II, a few shear AE that release comparatively large energy generated, and slip AE were generated at the same position with such shear AE as shown in Fig.3.5(b) and Fig.3.6(b).

Fig.3.9 shows the cumulative distribution of all AE events (tensile, shear and slip AE) in the Phase II. The size of each symbol corresponds to the number of the overlapping of AE events. The place where AE has been intensely generated is expressed by large symbol. We can find that occurrence of AE events became active at several points of the model in this phase. Such concentration of AE events is called "clustering".

⬤ 1935
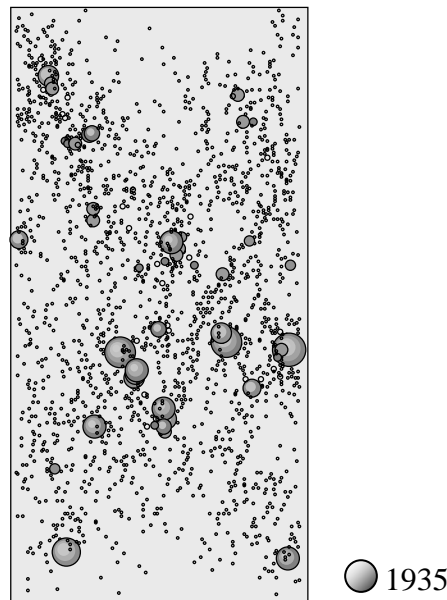
Fig.3.9　Spatial distribution of all AE events (Tensile, Shear and Slip AE) in Phase II. The size of each symbol corresponds to the number of the overlapping of AE events. The place where AE has been intensely generated is expressed by large symbol.

The total number of microcracks increases and the dense microcracking intensifies the interaction between microcracks in the Phase II. Once the interaction becomes strong enough within a certain region, an enhancement of the local stress concentration will be caused, as a result, new microcracks are generated one after another in the region and an AE cluster is formed [2,24]. Such a concentration of microcrack generation releases local stress. When stress has been sufficiently released in the previous region, a new microcrack does not occur because the microcrack occurs in the region on which the stress strongly concentrated. After an AE cluster is formed, migration of microcracking activity might proceed to new clustering regions, and many small AE clusters are formed [2]. Thus, burst of microcracking are observed temporarily in the Phase II with the formation of many small AE clusters, and the number of microcracking might have extremely decreased after each clustering of AE as shown in Fig.3.4.

3.5.3 Formation of the catastrophic fracture

In the Phase III, a catastrophic fracture was formed and the model resulted in collapse within a very short time. Fig.3.10 shows the propagation process of the macroscopic fracture in the four periods of the Phase III. The solid lines express the fracture which is represented by the connection of largely opened microcracks. To clarify the macroscopic fracture, small and discrete microcracks are ignored in these figures.

(a) Step 339×10^4 (b) Step 340×10^4 (c) Step 341×10^4 (d) Step 342×10^4
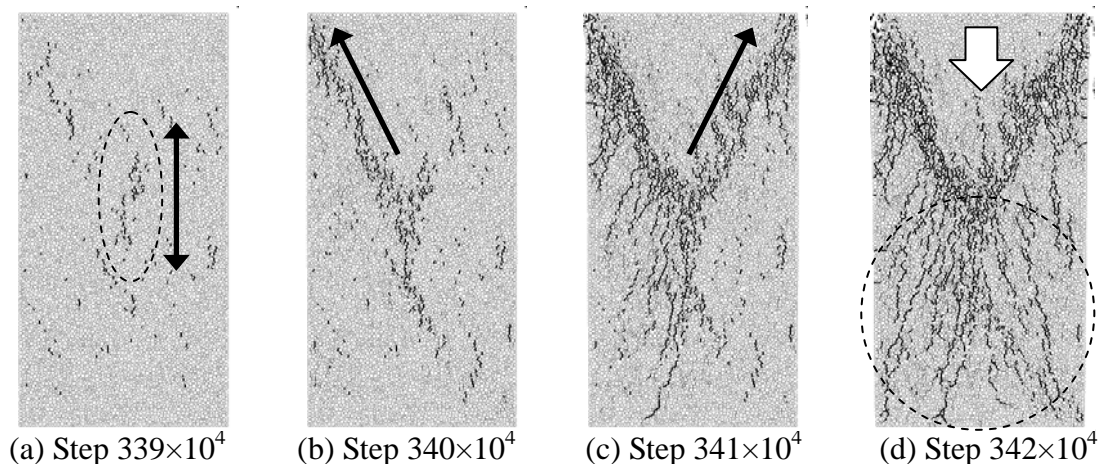
Fig.3.10   Propagation process of the macroscopic fractures at the four time steps of the Phase III. The solid lines express the fracture which is represented by the connection of largely opened microcracks. To clarify the macroscopic fracture, small and discrete microcracks are ignored in these figures.

As shown in Fig.3.10(a), microcracks concentrated near the center of the model in the region surrounded by the dotted ellipse at first. Most of the microcracks shown in Fig.3.10(a) are tensile cracks, and these microcracks propagate stably in the direction of loading axis.

However, at the time step 340×10^4, microcracks are connected again and again by sliding and the fracture grows rapidly toward upper left from the center of the model as shown by an arrow in Fig.3.10(b). In addition to this, fracture also grows toward upper right from the center of the model as shown by an arrow in Fig.3.10(c). Most of the microcracks generated in time step 340×10^4 and 341×10^4 were shear cracks, and these cracks released remarkably large energy as shown in Fig.3.5(c). Such concentration of shear cracks is called "shear band". This result suggests that the formation of shear bands is guided by development of a process zone where the tensile cracks have encompassed though shear cracks are the dominant mechanism in this phase [2,5].

Finally, as shown in Fig.3.10(d), a large wedge-shaped block is separated from the rock model by the formation of shear bands. The wedge-shaped block moves downward by the loading in the direction as shown by an open arrow, and many tensile fractures are propagate toward the bottom of the rock model in the region surrounded by the dotted circle in Fig.3.10(d).

A number of slips occurred at the existing crack surface due to the impact from the formation of shear band, and quite a lot of slip AE occurs. Moreover, the slip AE events that release remarkably large energy were generated between the wedge-shaped block the rock model as shown in Fig.3.6(c). This result suggests that the burst of AE events when the rock model resulted in collapse was governed by the slip of pre-existing cracks.

A lot of microcracks are overcrowded in this phase. Thus, the interaction during the microcracks is so strong, and the local stress concentration is very intense compared with the other two phases. Therefore, this phase is very unstable. Hence, once a catastrophic fracture initiated at one key location, microcracks are connected again and again by sliding until the rock model is completely collapsed [2,4,5]. This process is similar to the AE clustering process in the Phase II. In the Phase II, the stress level is relatively lower and the interaction during microcracks is not so strong compared with the Phase III. Therefore, each AE cluster can not sufficiently grow large. On the other hand, generation and development of the AE cluster continue and become intensely in the Phase III, and an especially large scale cluster among them takes part in the formation of the macroscopic fracture.

Since extremely a lot of AE occurs during the formation of shear bands, smaller AE

wave may be hidden by larger AE wave. Therefore, it is difficult to evaluate the source location of all AE correctly in an experiment. On the other hand, the forming processes of the cluster and the shear band that is difficult to be measured in actual experiments were able to be discussed in detail by using the DEM.

3.5.4 Comparison of the energy

The conventional theories suggest that tensile cracks cause AE events because the number of accumulated AE events is positively related to the amount of the dilatancy, and the tensile strength of rock is obviously small compared with compressive strength [25]. Moreover, the microscopic observations revealed that there are a lot of tensile cracks in the rock specimen under uniaxial compression, and the shear crack is few [26]. This result also indicates that the dominant mechanism of AE is tensile crack.

Fig.3.11(a) expresses spatial distribution of all the cracks generated during this simulation. The diameter of all the circles is the same. As shown in Fig.3.11(a), many tensile cracks are generated in this simulation. In fact, 72% of all cracks that generated in the Phase I and II were tensile cracks. This result is in accord with the conventional theories and microscopic observations.
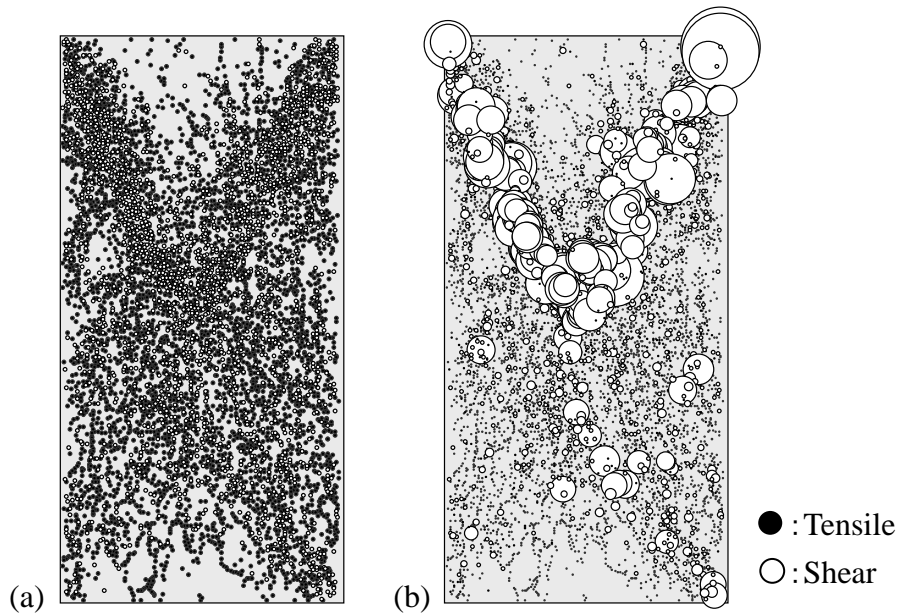
Fig.3.11   Spatial distribution of all the cracks obtained during this simulation. A tensile crack is expressed with a closed circle and a shear crack is expressed with an open circle. In the left figure (a), the diameter of all the circles is the same. In the right figure (b), the diameters of the circles correspond to their respective magnitudes of energy.

However, in an AE measurement experiment, many of observed AE events originated in the generation of the shear crack [2,27,28]. Thus, there is an inconsistency between the conventional theory and the AE measurement result. Nevertheless, this simulation has clarified that the inconsistency can be resolved by considering the energy of AE.

Fig.3.11(b) expresses spatial distribution of all the cracks, and the diameters of the circles correspond to their respective magnitudes of energy. It turns out that the energy released from a tensile crack is so small compared with a shear crack. It is theoretically indicated that the energy emitted from a tensile crack is small compared with that from a shear crack [29,30]. The results of this simulation are consistent with the theory.

Although the tensile cracks are dominantly generated in the simulation, the energy released from a tensile crack becomes small because the tensile strength of rock is obviously small. Such an AE which emits small energy is easily buried in a noise and hard to be measured in an experiment. Lei at al. [2] recorded several thousands of AE events with waveforms and more than 50% of the recorded events were located appropriately. However, only 10% among the located events have clear P-wave first motions and is possible to obtain reliable focal mechanism solutions from their radiation pattern. It is difficult to make clear assignments of the focal mechanisms for other events since some of polarities of the first motions cannot be determined due to their vague first motions.

Therefore, in AE measurement experiments, a shear AE with large energy that can be easily recorded with clear waveform is dominantly observed.

3.5. Conclusion

The uniaxial compression test of rock was simulated by newly programmed DEM code considering AE events generated by the slip at crack surfaces. As the results, the followings were found.

1. The volumetric strain increases constantly in the first stage of the loading, and gradually changes into nonlinear behavior as the axial stress increases. In addition, the volumetric strain curve began to change when generation of shear AE begins. This result indicates that occurring of the dilatancy observed in an actual uniaxial compression test can be appropriately reproduced by the DEM simulation.

2. Since extremely a lot of AE occurs during the formation of shear bands, smaller AE wave may be hidden by larger AE wave. Therefore, it is difficult to locate all AE

sources correctly in an experiment. On the other hand, the forming processes of cluster and shear band that is difficult to be measured in the experiment were able to be discussed in detail by using the DEM.

3. At first, dominant mechanism of AE events under low stress level in the beginning of a uniaxial compression test were new tensile cracks. As the axial stress increases, the dominant mechanism of AE changed from the new crack initiation to the slip occurrence at the existing crack surface.

4. The burst of AE events when the rock model resulted in collapse was governed by the slip occurrence at the existing crack surface.

5. The simulation result indicates that the rock fracturing process is characterized by three typical phase. In the Phase I, tensile cracks are dominant. The microcracking in this phase is governed by microstructures of rock such as pores, microcracks and grain boundaries. In the Phase II, the number of cracks increases and the interaction between the cracks becomes stronger gradually. This induces coalescence of neighboring cracks and results in clustering of microcracks. In the Phase III, once a catastrophic fracture initiated at one key location, it grows again and again within a very short time. The catastrophic fracturing is guided by development of a process zone encompassing tensile cracks.

6. The b-value at the beginning of loading (Phase I) is relatively high because all AE events generated in this phase was very small. Whereas, the b-value is decreasing as the axial stress increases, and the b-value becomes minimum value in the stage of collapse (Phase III). This result is well in agreement with the tendency of actual AE measurement experiment. Since the b-value depends on the heterogeneity of the rock, the DEM simulations are effective to discuss the influence of the heterogeneity on the fracturing process of the various heterogeneous rocks that is difficult to be observed in an experiment.

7. The conventional theories and the microscopic observations suggest that tensile cracks cause AE events. However, in an AE measurement experiment, many of observed AE originated in the generation of the shear crack. Nevertheless, this inconsistency can be resolved by considering the energy of AE. Although the tensile cracks are dominantly generated during the rock fracturing under uniaxial

compression, the energy released from a tensile crack becomes small because the tensile strength of rock is obviously small. Such a small AE is easily buried in a noise and hard to be measured in an experiment. Therefore, in AE measurement experiments, shear AE with large energy is dominantly observed.

The results of the DEM simulation could explain time-space distribution of AE activity in the course of a uniaxial compression test, and were well in agreement with the fracturing process deduced from AE measurements in the laboratory experiments conducted by previous researchers. This indicates that DEM is an effective numerical analysis technique for studying the dynamics of microcracking in brittle materials like rock.

References

[1] Ashby MF and Sammis CG. The damage mechanics of brittle solids in compression. Pure and Applied Geophysics, 1990; 133(3): 489-521.

[2] Lei X-L, Nishizawa O, Kusunose K and Satoh T. Fractal Structure of the Hypocenter distribution and Focal Mechanism Solutions of AE in Two Granites of Different Grain Size. J Phys Earth, 1992; 40: 617-634.

[3] Lei X-L, Kusunose K, Rao MVMS, Nishizawa O and Satoh T. Quasi-static fault growth and cracking in homogeneous brittle rocks under triaxial compression using acoustic emission monitoring. J Geophys Res, 2000; 105(B3): 6127-6139.

[4] Lei X-L, Masuda K, Nishizawa O, Jouniaux L, Liu L, Ma W, Satoh T and Kusunose K. Detailed analysis of acoustic emission activity during catastrophic fracture of faults in rocks. J Struct Geol, 2004; 26: 247-258.

[5] Lei X-L. Typical phases of pre-failure damage in granitic rocks under differential compression. Fractal Analysis for Natural Hazards. Geological Society, London, Special Publications, 2006; 261: 11-29.

[6] Cundall PA and Strack ODL. A discrete numerical model for granular assemblies. Geotechnique, 1979; 29(1): 47-65.

[7] Potyondy DO and Cundall PA. A bonded- particle model for rock. Int J Rock Mech Min Sci, 2004; 41: 1329-1364.

[8] Hazzard JF and Young RP. Dynamic modeling of induced seismicity. Int J Rock Mech Min Sci, 2004; 41(8): 1365-1376.

[9] Hazzard JF and Young RP. Simulating acoustic emissions in bonded-particle models of rock. Int J Rock Mech Min Sci, 2000; 37(5): 867-872.

[10] Kasahara K. Earthquake mechanics. Cambridge university press, 1981; 38-42.

[11] Shimizu H, Murata S and Ishida T. Distinct element analysis for rock failure under uniaxial compression. Journal of MMIJ, 2008; 125(3): 91-97. (in Japanese).

[12] Shimizu H, Koyama T, Ishida T, Chijimatsu M, Fujita T and Nakama S. Distinct element analysis for ClassII behavior of rock under uniaxial compression. Int J Rock Mech Min Sci, 2009; (in press).

[13] Shimizu H, Murata S and Ishida T. Distinct element analysis for rock failure considering AE events generated by the slip at crack surfaces. Proc. 19th International AE Symp, 2008; 407-414.

[14] Lei X-L, Kusunose K, Nishizawa O, Cho A and Satoh T. On the Spatio-temporal Distribution of Acoustic Emissions in Two Granitic Rocks Under Triaxial Compression: the Role of Pre-existing Cracks. Geophys Res Lett, 2000; 27(13): 1997-2000.

[15] Brace WF and Bombolakis EG. A note on brittle crack growth in compression. J Geophys Res, 1963; 68: 3709-3713.

[16] Brace WF, Paulding BM and Scholz C. Dilatancy in the fracture of crystalline rocks. J Geophysical Res, 1966; 71(16): 3939-3953.

[17] Mogi K. Magnitude–frequency relation for elastic shocks accompanying fracture of various materials and some related problems in earthquakes. Bull. Earthquake Res Inst, Tokyo University, 1962; 40: 831-853.

[18] Scholz CH. The frequency–magnitude relation of microfracturing and its relation to earthquakes. Bull Seismol Soc Am, 1968; 58: 399-417.

[19] Gutenberg B. and Richter CF. In Seismicity of the Earth and Associated Phenomena. Princeton University Press, Princeton, NJ, USA, 1954; 2nd edn.

[20] Aki K. Maximum likelihood estimates of b in the formula $\log N = a - bm$ and its confidence limits. Bull Earthquake Res Inst, Tokyo University, 1965; 43: 237-239.

[21] Utsu T. A method for determining the value of b in formula $\log n = a - bM$ showing the magnitude-frequency relation for earthquakes. Geophys bull of the Hokkaido University, 1965; 13: 99-103.

[22] Lei X-L and Satoh T. Indicators of critical point behavior prior to rock failure inferred from pre-failure damage. Tectonophysics, 2007; 431: 97-111.

[23] Wawersik WR and Fairhurst C. A Study of brittle rock fracture in laboratory compression experiments. Int J Rock Mech Min Sci, 1970; 7(5): 561-575.

[24] Yanagidani T, Ehara S, Nishizawa O, Kusunose K and Terada M. Localization of Dilatancy in Ohshima granite under constant uniaxial stress. J Geophys Res, 1985; 90: 6840-6858.

[25] Kusunose K, Yamamoto K and Hirasawa T. Analysis of Acoustic Emissions in Granite under Uniaxial Stresses for the Size Relation between Microcracks and Grains. Journal of the Seismological Society of Japan, 1979; 32: 11-24.

[26] Kranz RL. Crack Growth and Development During Creep of Barre Granite. Int J Rock Mech Min Sci Geomech Abstr, 1979; 16: 23-35.

[27] Kusunose K, Nishizawa O, Ito H, Ishido T and Hasegawa I. Source Mechanism of Acoustic Emission in Rocks under Uniaxial Compression. Journal of the Seismological Society of Japan, 1981; 34: 131-140. (in Japanese).

[28] Idehara O, Satoh T, Nishizawa O and Kusunose K. Hypocenter Distribution and Focal Mechanisms of AE Events under Triaxial Compression Focal Mechanisms of AE Events in Yugawara Andesite. Journal of the Seismological Society of Japan, 1986; 39: 351-360. (in Japanese).

[29] Hayashi K, Nishimura H. Consideration on Field AE Data Based on Theoretical Studies of Elastic Waves Due to Sudden Movement of a Subsurface Reservoir Crack. Progress in Acoustic Emission III, NDI Japan, 1986; 742-749.

[30] Hayashi K, Motegi S. Characteristics of Energy of Elastic Waves Due to Sudden Growth of Subsurface Reservoir Cracks for Geothermal Heat Extraction. Progress in Acoustic Emission IV, NDI Japan, 1988; 265-272.

Chapter 4
Distinct element analysis
for Class II behavior of rocks under uniaxial compression

4.1. Introduction

The brittle fracture of rocks is the most studied issue in rock mechanics fields and especially the post-peak behavior of rocks is important for rock mechanics problems. The post-failure behavior is considered to be closely related to the stability of mine pillar, rib wall, tunnel and many other underground structures because it directly influences the sudden and violent fracture of rock that known as a rockburst.

For the better understanding such a mechanical behavior of brittle rocks, many laboratory experiments have been performed. In the 1960's, many uniaxial compression tests using high stiff testing machine were carried out to understand the failure mechanism of brittle rocks, and they enable to obtain the post-peak behavior of rocks such as complete stress-strain curves. Wawersik [1,2] obtained successfully the complete stress-strain curves for various rocks using a stiff testing machine, and classified rock mechanical behavior under uniaxial compression into Class I and Class II according to complete stress-strain curves. As shown in Fig.4.1, for Class I behavior, axial strain keeps stable even though the axial stress exceeds the peak strength, and the stress-strain curve monotonically increases in axial strain.
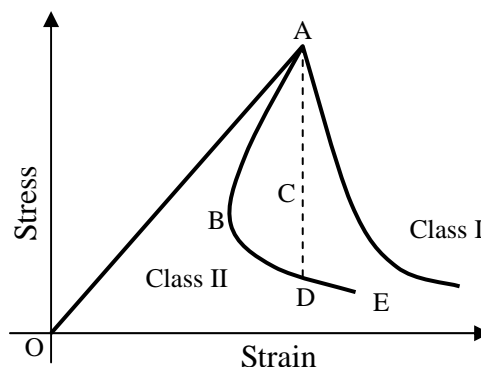
Fig.4.1 Representative figures for stress-strain curves of class I and class II behavior of rock failure under uniaxial compression.

On the other hand, for the Class II behavior, it suddenly falls into uncontrolled when the axial stress exceeds the peak strength and the curve does not monotonically increase in axial strain. It is necessary to control violent collapse of the specimen to obtain the Class II complete stress-strain curve illustrated as the curve OABDE in Fig.4.1 [3]. Therefore, even if the recently developed servo-controlled testing machine is used, there are still difficulties to obtain complete stress-strain curve of brittle rocks in the laboratory experiments, and the Class II post-peak behavior has not been sufficiently clarified.

Moreover, some researchers tried to simulate the Class II behavior [4,5] using various loading control methods. However, it is still difficult to simulate the Class II post-peak behavior by any numerical analysis technique including the DEM, and realistic simulation of the Class II behavior of rock under uniaxial compression has not been achieved actually [6]. Therefore, a new DEM code was developed and Class II behavior of rock was simulated. The objective of this paper is to simulate the uniaxial compression test with radial strain control using a newly developed DEM code, and investigate the Class II post-peak behavior of rocks in detail.

4.2. DEM simulations for Class II behavior

4.2.1 Experimental data for the simulations

The uniaxial compression tests and Brazilian tests for Äspö diorite were carried out at the Äspö Hard Rock Laboratory (ÄHRL, Sweden) [7]. These experiments were performed using the MTS 815 rock mechanics testing system according to the ISRM (International Society for Rock Mechanics) Suggested Method [8].

Elastic macroscopic parameters, such as Young's modulus and Poisson's ratio were calculated as secant values between axial stress levels at -0.01% of radial strain and 50% of peak strength. In the uniaxial compression tests, the loading rate was controlled so that the radial strain rate becomes constant.

The complete stress-strain curve obtained from the radial strain controlled uniaxial compression tests is presented in Fig.4.2 and the testing results are summarized in Table 4.1. As shown in Fig.4.2, the stress-strain curve obviously shows the Class II behavior.

In this study, the radial strain controlled uniaxial tests performed at the ÄHRL were simulated using newly developed DEM code. The microscopic parameters for simulations were carefully calibrated from the laboratory experimental data.
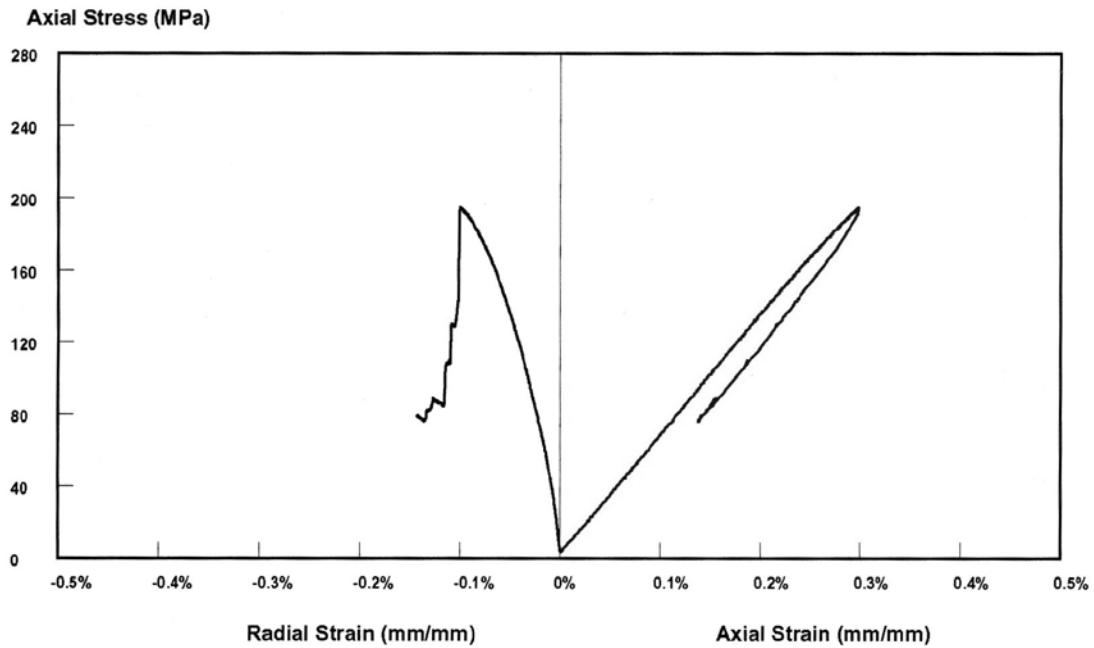
Axial Stress (MPa)

Fig.4.2 Complete stress-strain curve obtained by using the radial strain controlled loading method [7].

Table 4.1 Laboratory tests and testing results.

TEST DATA

Client:	SKB	Loading Control:	Radial Strain Rate
Test:	Uniaxial	Equivalent Loading Rate:	0.75 MPa/s
Equipment:	MTS 815	Confining Stress:	0 MPa
Test Date:	2003-06-10		

SPECIMEN DATA

Site:	Äspö Rock	Diameter:	50.9 mm
Type:	Diorite	Length/Diameter:	2.80
Hole:	KA3376B01	Density:	2742 kg/m^3
Depth:	33.32 m		

TEST RESULTS

Peak Strength:	195.1 MPa	Young's Modulus:	67.4 GPa
Tensile Strength:	15.5 MPa	Poisson's Ratio:	0.27

4.2.2 Radial strain controlled uniaxial compression tests

Fig.4.3 shows the rock model and the loading condition for the simulation of uniaxial compression tests. The platen under the rock model was fixed and the upper loading platen was moved downward slowly at a certain displacement rate to simulate the uniaxial compression tests. Frictional force was acting between the rock model and the platens. The confining wall was not set along the side of the rock model.

The most common control method for the uniaxial compression test is axial strain control. The axial strain controlled uniaxial compression tests can be easily reproduced in DEM models by moving the upper loading platen downward slowly with constant displacement rate. On the other hands, in the radial strain controlled uniaxial compression tests, loading rate for upper platen should be controlled to keep the radial strain rate constant. Therefore, it is necessary to introduce a special operation for the upper loading platen in DEM models. As shown in Fig.4.4, the ideal radial strain rate is manually set firstly, and the error of actual radial strain from ideal value is calculated every loading steps. If the error exceeds the maximum value, the simulation returns to the previous time step, and the simulation is restarted with updated loading rate. This process is repeated until the error becomes within ±5%, in this study.
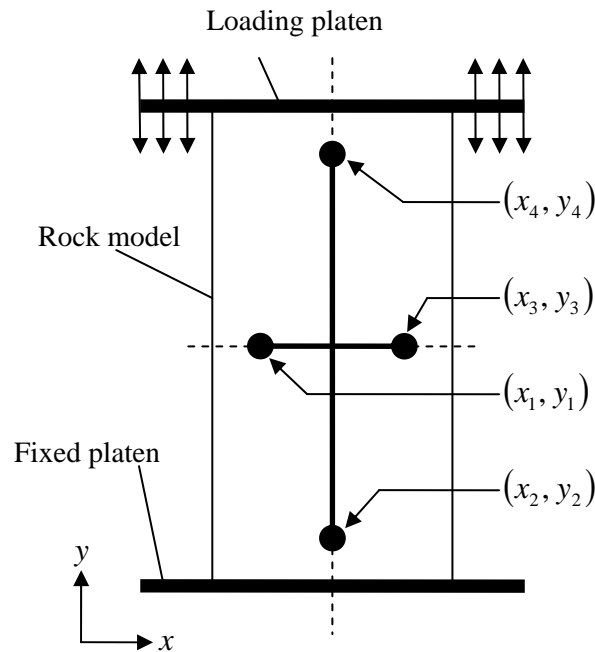
Fig.4.3   Loading condition for the simulation of uniaxial compression tests. The measuring points for the axial and radial strain were located slightly inside from the edge of the rock model. The distance between two measuring points is 90% of the rock model width or height.
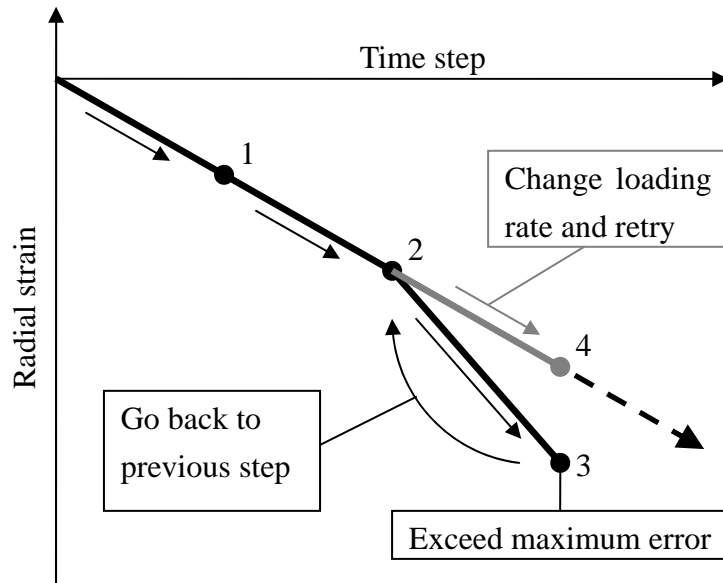
Fig.4.4 Simulation procedure for radial strain controlled uniaxial compression test.

Since one particle influences only the adjacent particles in the DEM simulations, some time steps are required to modify the radial strain by changing the loading rate. For this reason, the modification of the loading rate should be done at some time interval. If the modification interval is too small, too many calculation steps are required and as a result, it becomes almost impossible to control radial strain with good accuracy. On the other hand, if the modification interval is too large, it is difficult to control sudden increase and/or decrease of the radial strain. Therefore, the modification of the loading rate is done every 20000 time steps in this study.

4.3. Rock model for the simulation and the results

4.3.1 DEM model for Rock specimen and simulation of laboratory tests

Microscopic properties of the DEM model for rock specimen are summarized in Table 4.2. As mention above, tuning parameters are determined from calibrations using laboratory testing results (UCS, tensile strength, Young's modulus and Poisson's ratio). The other microscopic parameters, such as the shape of the rock model, were the same as the rock specimen used in the laboratory experiments. The size of rock specimen is 5.1cm in width and 14.3cm in height. The number of particles is about 10,000 with the maximum and minimum radiuses are 0.6mm and 0.3mm, respectively. Young's modulus and the Poisson's ratio values for steel was selected for the wall material properties.

Table 4.2 Rock model properties.

ROCK MODEL DATA	
Rock model for simulation of uniaxial compression (tension) test	
Width:	51mm
Height:	143mm
Number of particles:	9457
Rock model for simulation of Brazilian test	
Diameter:	96mm
Number of particles:	9401
Maximum particle radius:	0.6mm
Minimum particle radius:	0.3mm
Particle density:	2742 kg/m^3
Friction coefficient of particle:	0.5
Friction coefficient of wall:	0.3
Young's modulus of wall (E_w):	200GPa
Poisson's Ratio of wall (ν_w):	0.3
TUNING PARAMETERS	
Young's modulus of particle (E_p):	146.0 (GPa)
Poisson's Ratio of particle (ν_p):	0.2
Shear strength of bonding (τ_c):	245.0 (MPa)
Tensile strength of bonding (σ_c):	60.0 (MPa)

For the simulations of the Brazilian tests, a circular shaped rock model was used. Since the number of particles affects significantly the mechanical properties in DEM, the DEM models of rocks for the Brazilian test was made by the same number of particles and the same distribution of particle radius as the rock model used in the uniaxial compression tests. For this reason, even though the rock specimen used in the actual Brazilian test was 50.9mm in the diameter, the diameter of the rock model for the simulation of Brazilian test was 96mm.

Although the actual uniaxial compression tests were performed with radial strain control in Äspö HRL, the DEM model calibration was performed under axial strain control because the radial strain controlled uniaxial compression tests require more

computer power and calculation time due to the iterative computation for the modification of the loading rate for the upper platen. For this reason, microscopic parameters were determined from the axial strain controlled uniaxial compression tests, and the radial strain controlled uniaxial compression tests were simulated using the same microscopic parameters. The calibration process is summarized in Fig.4.5.

The calibration results are summarized in Table 4.3. The macroscopic parameters of the rock model show good agreement with the experimental results. The calculated values of mechanical properties obtained from the radial strain controlled uniaxial compression tests were close to the values obtained from the axial strain controlled uniaxial compression tests.
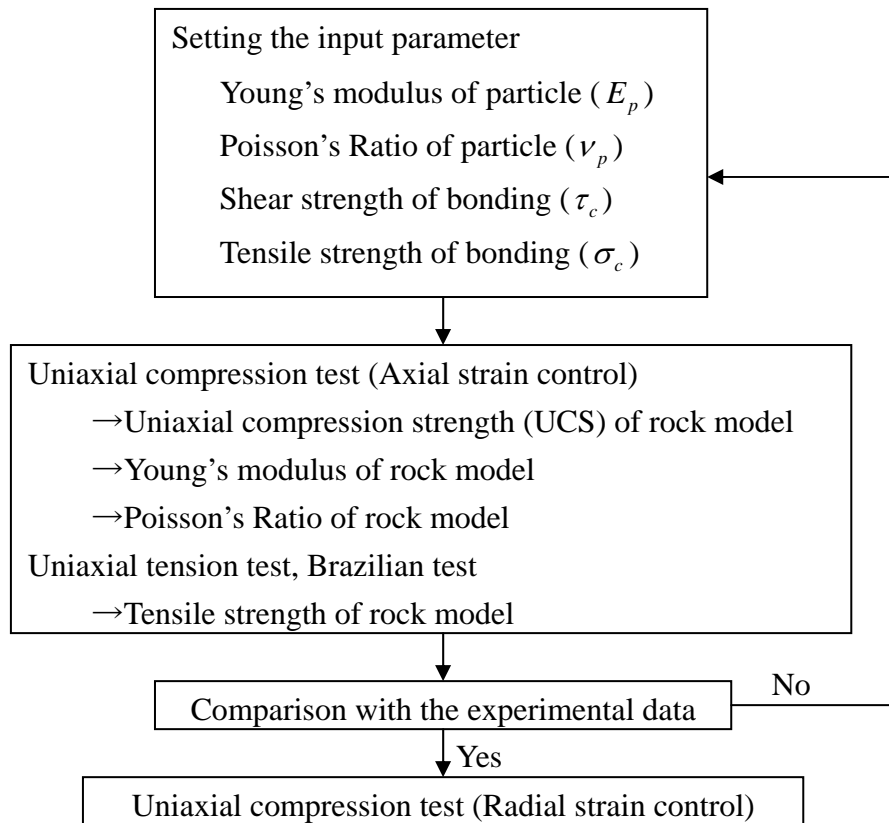
Fig.4.5   Calibration process.

Table 4.3 Calibration result.

Loading control:	Experiment	Simulation	
	Radial	Axial	Radial
UCS of rock model (MPa):	195.10	195.47	200.65
Young's modulus of rock model (GPa):	67.40	67.63	67.55
Poisson's Ratio of rock model:	0.270	0.276	0.286
Tensile strength of rock model (MPa)			
Brazilian test:	15.50	15.51	
Uniaxial tension test:	-	16.05	

4.3.2 Difference of post-peak behavior by load control method

The complete stress-strain curve obtained from the simulation with axial strain controlled uniaxial compression tests is shown in Fig.4.6(a). It is found that the axial strain increase monotonically in the post-peak region, and the stress-strain curve shows clearly the Class I behavior. The complete stress-strain curve obtained from the axial strain controlled uniaxial compression tests can not follow the curve OABDE in Fig.4.1 because any special axial loading control was not applied. If rock specimens showing Class II behavior are tested with axial strain control, rock specimens will suddenly break as soon as the axial stress exceeds the peak strength and fall into uncontrolled. The complete stress-strain curve will follow the curve OACDE in Fig.4.1.

On the other hand, Fig.4.6(b) shows the stress-strain curve obtained from the simulation of the radial strain controlled uniaxial compression tests. As shown in Fig.4.6(b), the axial strain decreases in the post-peak region to keep the radial strain constant. The complete stress-strain curve shows the Class II behavior and good agreement with the experimental result shown in Fig.4.2.

These simulation results show that DEM can reproduce the Class II behavior of brittle rock successfully. Moreover, it was found that only loading control methods affect significantly the post-peak behavior of rocks. It should be noted that the same rock models with same geometry and microscopic parameters were used for both simulations. This indicates that the loading control methods play important roles for the failure mechanisms and their processes of rocks under uniaxial compression (Class I and II). The microscopic parameter set determined here will be named "Case 1" later.
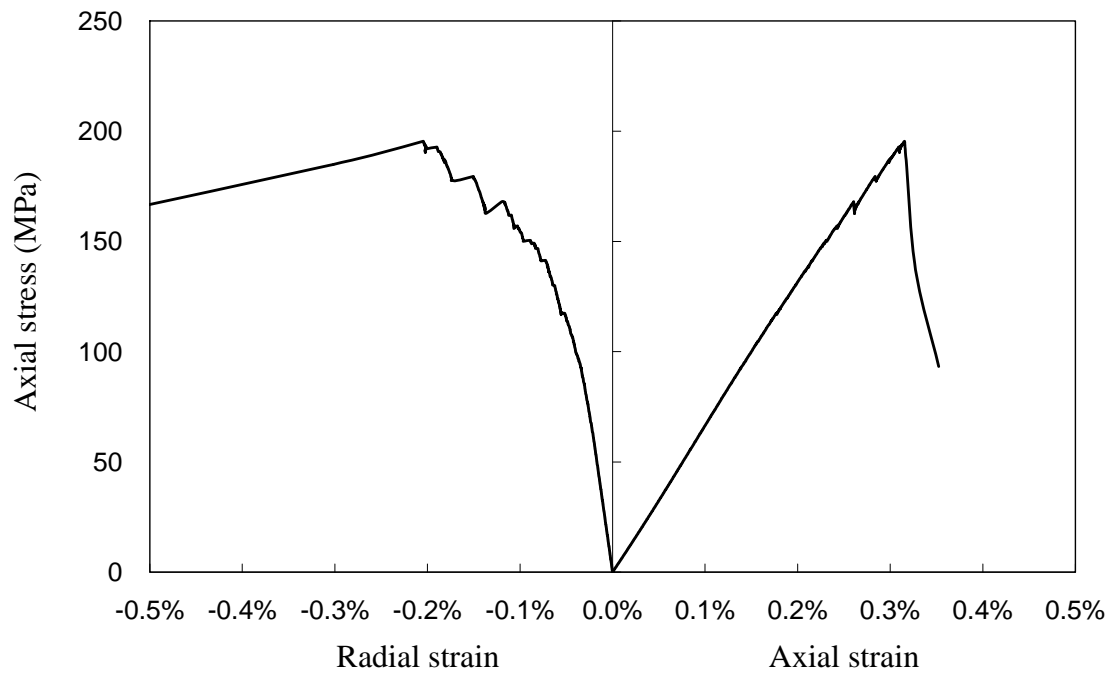
(a) Axial strain control.
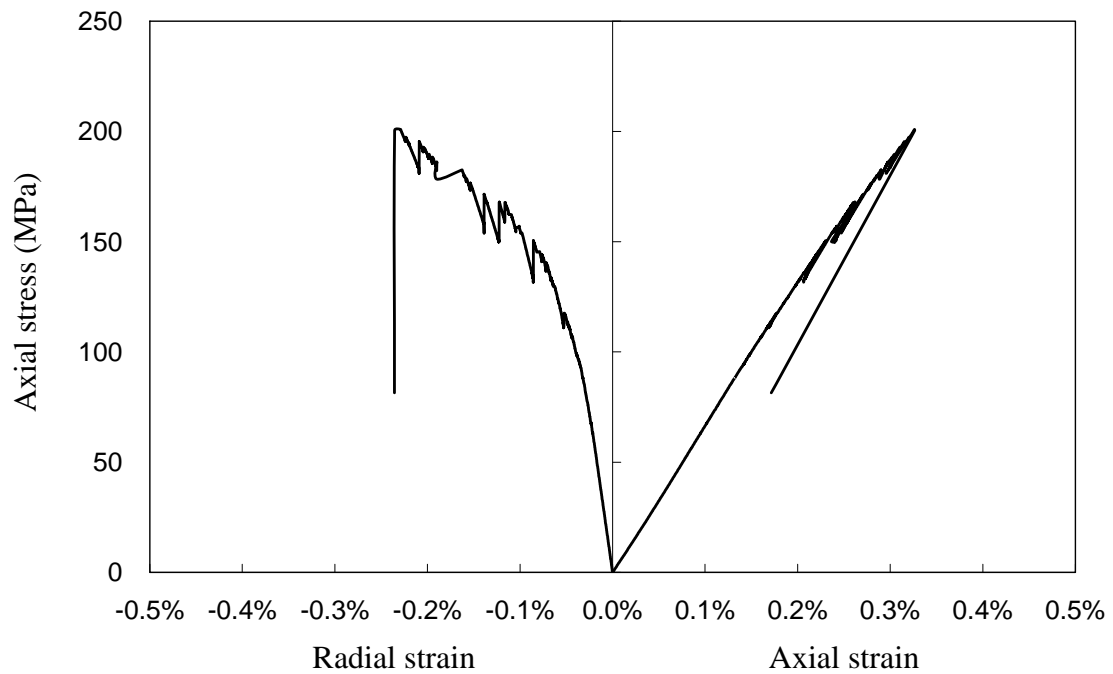
(b) Radial strain control.

Fig.4.6   Complete stress-strain curves obtained from the simulation with different controlling methods.

4.4. Discussion

4.4.1 Difference of crack patterns by load control methods

In the previous section, the loading control methods significantly affect on the mechanical behavior of rocks under uniaxial compression. A more detailed discussion will be given in this section mainly focusing on the effects of the loading control methods on the crack generation and propagation, since complex macroscopic behaviors, such as fracture propagation and failure, are strongly controlled by generated microcracks.

Fig.4.7(a) and (b) show the spatial distribution of microcracks for Case 1 with axial and radial strain controlled uniaxial compression tests, respectively. In this figure, tensile and shear cracks are expressed as filled and open circles, respectively. The diameter of the circle corresponds to respective magnitude of AE energy obtained by equation (2.14). For both control methods, the crack generation pattern in the pre-peak region was similar and most microcracks generated in low stress level were tensile cracks. As the axial stress increases, the number of microcracks increases gradually, and shear cracks starts generating. The detailed discussion on the pre-peak behavior is also seen in Chapter 3.

As shown in Fig.4.7(a), many shear cracks with relatively large energy were connected along a line in the post-failure region, which is called "shear band". On the other hand, although a several microcracks were generated and released relatively large energy at the center of the model, shear bands does not appear for the radial strain controlled uniaxial compression tests as shown in Fig.4.7(b). As shown in Fig.4.6(a), radial strain increases rapidly when the axial stress exceeds the peak strength for the axial strain controlled uniaxial compression tests. For the radial strain control, on the other hand, to keep the radial strain constant even in the post-peak region, axial loading control was applied and axial load was reduced. As a result, strain energy accumulated in the rock specimen was reduced. Therefore, the cracks released small energy and the formation of the shear band can not grow sufficiently under radial strain control.

Consequently, these simulation results clearly show that the formation of shear bands in the rock specimen plays important roles on post-peak Class I and II behaviors.

4.4.2 Influence of the rock model properties

In this section, to investigate the effect of microscopic parameters for DEM (the shear and tensile strength of the particles) on the mechanical behavior of rocks under uniaxial compression, especially post-peak Class I and II behaviors, a series of simulations using different values for microscopic parameters were performed.

| | Pre-failure | Post-failure | Pre-failure | Post-failure |

(a) Axial strain control.   (b) Radial strain control.
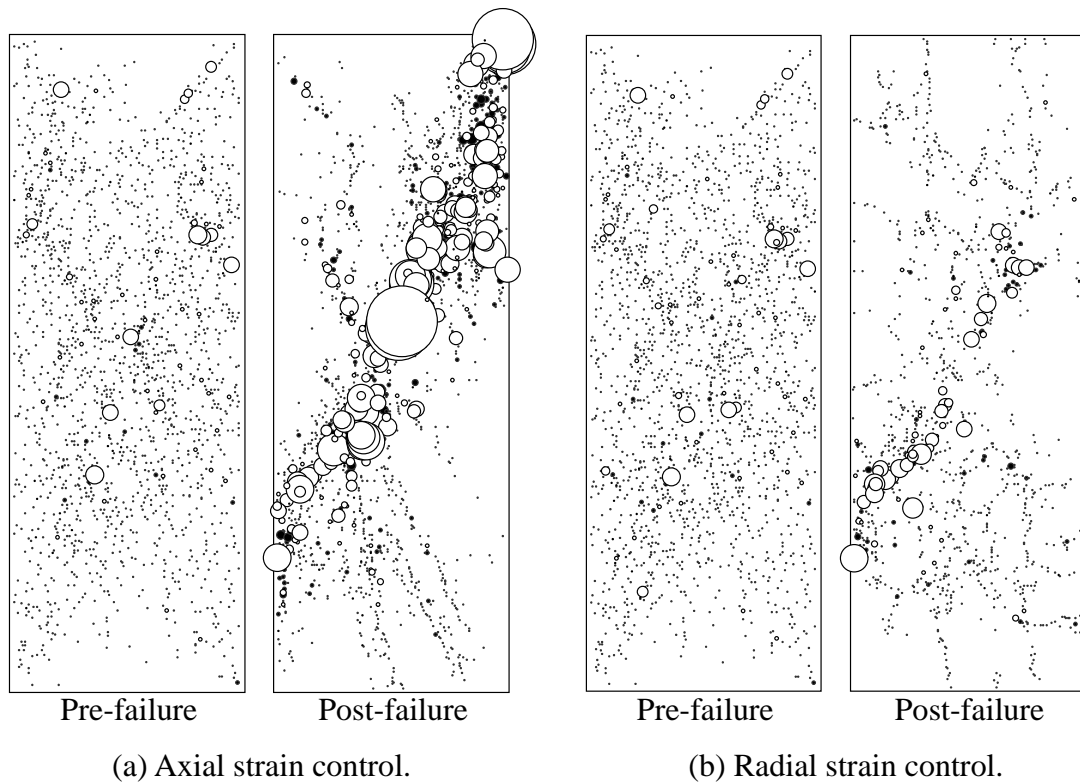
Fig.4.7   Spatial distribution of all the cracks for Case 1 in pre-failure region (left) and post-failure region (right). (a) axial strain control and (b) radial strain control. Tensile and shear cracks are expressed as filled and open circles, respectively. The diameters of each circle correspond to their respective magnitudes of energy.

Among the microscopic parameters, the shear and tensile strength of the particles significantly affect the microcrack generation. Therefore, the different shear-tensile strength ratio was given for each case. The microscopic parameters and calculated material properties of four rock models are listed in Table 4.4. The microscopic parameters were calibrated using the uniaxial compressive strength and Young's modulus obtained from the laboratory experiments. Note that the model geometry (particle location and radius) is the same as the one used in Case 1.

The DEM simulations for uniaxial compression tests with both axial and radial strain controls were performed, and the complete stress-strain curves were obtained for each case and are shown in Fig.4.8. As shown in Fig.4.8, for all cases, the Class I behavior was observed only for the axial strain control, and the Class II behavior was observed in the uniaxial tests with the radial strain control.

Fig.4.9(a) and (b) shows the microcrack distributions obtained from both axial and radial strain controlled uniaxial compression tests, respectively.

As shown in Fig.4.9(a), microcrack generation was different for each case. When tensile strength is small (Case 2), a lot of tensile cracks had been generated in the whole rock specimen. On the other hand, when the tensile strength is large (Case 5), the generation of tensile cracks was controlled and fewer tensile cracks were generated. However, clear shear bands appear for all cases when the axial strain controlled method was applied. As shown in Fig.4.9(b), these shear bands were not observed when the radial strain controlled method was applied.

From these simulation results, the microscopic parameters (in this case the tensile and shear strength) affect only tensile/uniaxial strength of the rock specimen but do not affect significantly the post-peak Class I and II behaviors. Again the loading conditions (controlled axial and/or radial strain) affect the post-peak behaviors and the formation of shear bands will be key issue.

Table 4.4 Four data sets with different values for microscopic parameters.

-Input parameters-	Case 2	Case 3	Case 4	Case 5
Shear strength of bonding (σ_c MPa):	320	255	198.5	162.5
Tensile strength of bonding (τ_c MPa):	32	51	99.25	162.5
Shear/Tensile strength ratio	10	5	2	1
Young's modulus of particle (E_p GPa):	170.0	150.0	140.0	142.0
Poisson's Ratio of particle (ν_p):	0.2	0.2	0.2	0.2
-Results (Axial strain control)-				
UCS of rock model (MPa):	195.93	196.08	194.97	194.66
Young's modulus of rock model (GPa):	67.83	67.52	67.06	67.96
Tensile strength of rock model (MPa):	8.59	13.69	26.56	43.50
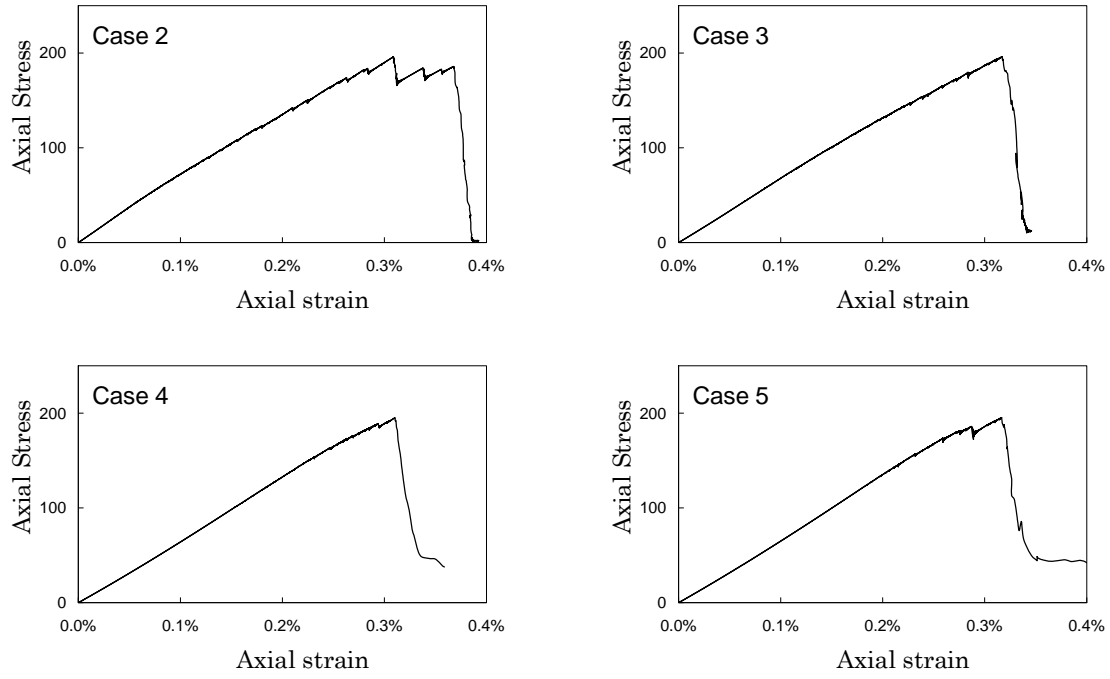
(a) Axial strain control.
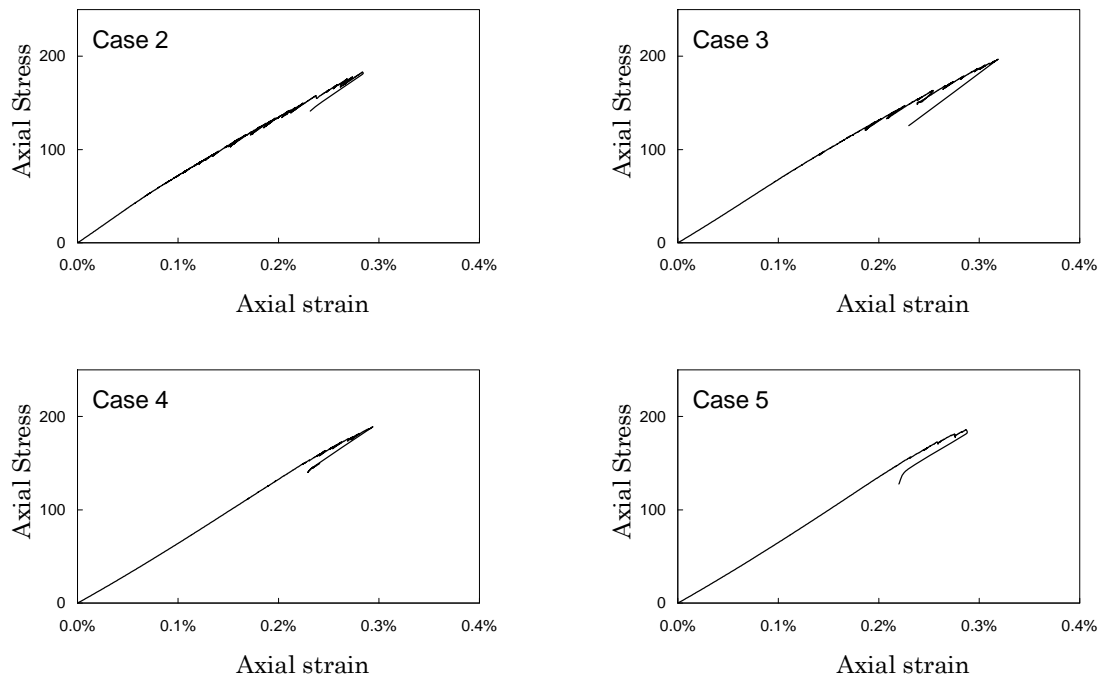
(b) Radial strain control.

Fig.4.8   Complete stress-strain curves obtained from each case.

Case 2　　　　Case 3　　　　Case 4　　　　Case 5

(a) Axial strain control.

Case 2　　　　Case 3　　　　Case 4　　　　Case 5

(b) Radial strain control.
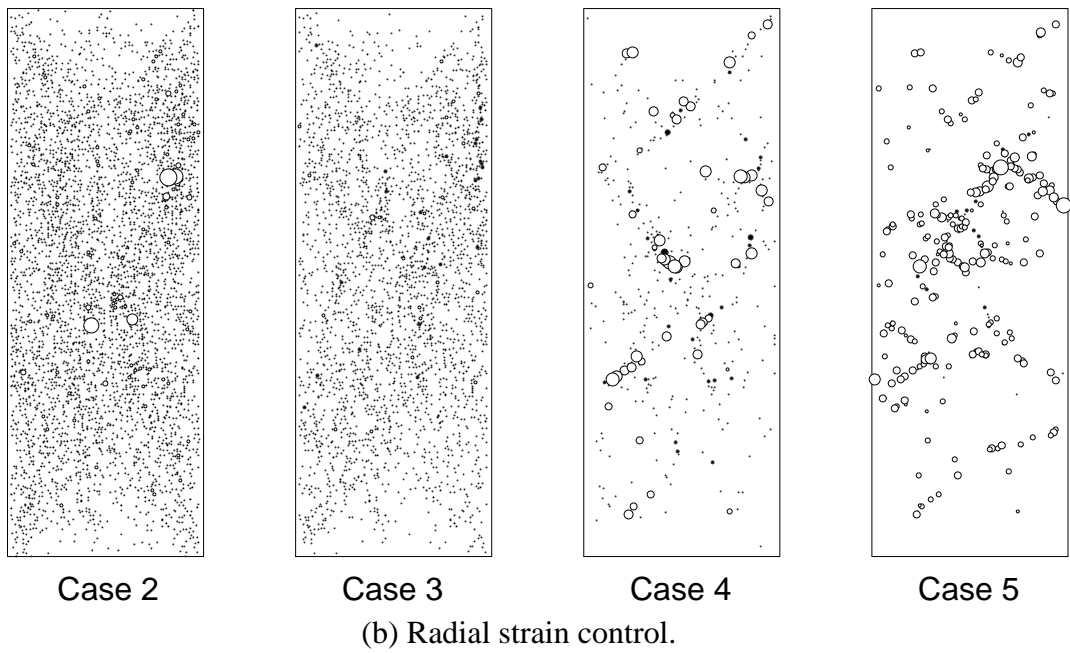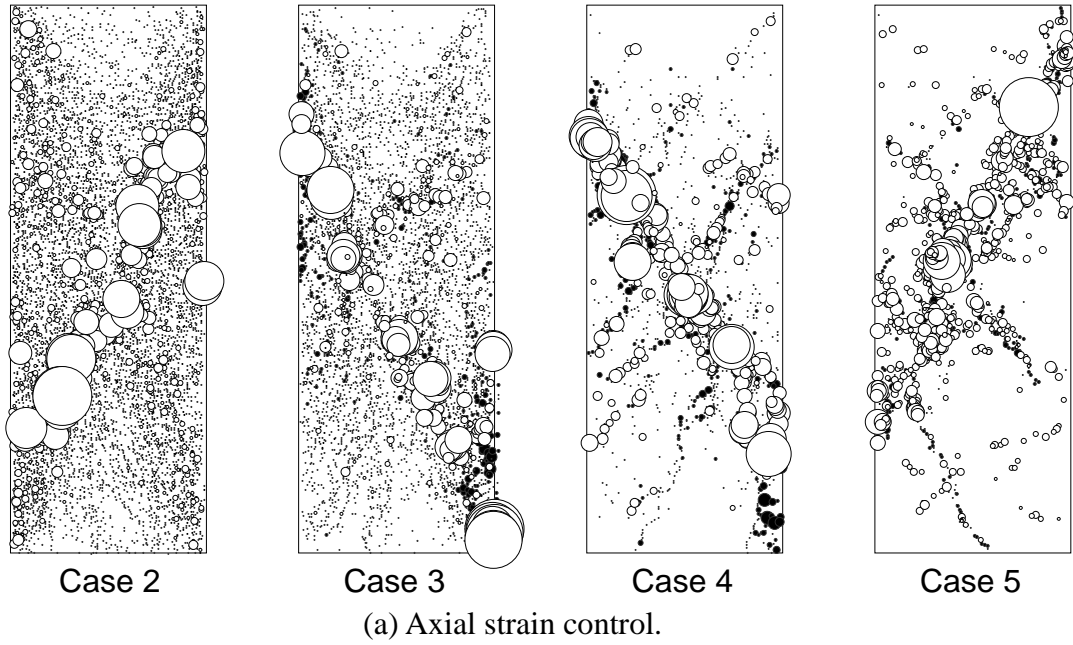
Fig.4.9　Spatial distribution of all the cracks for each cases. (a) axial strain control and (b) radial strain control. These figures are obtained from axial strain controlled uniaxial compression tests. Tensile and shear cracks are expressed as closed and open circles, respectively. The diameters of the circles correspond to their respective magnitudes of energy.

4.4.3 Local strain distribution

The DEM simulation results show that the key to understand the Class II behavior is the localized deformation along the shear bands. Hudson *et al.* mentioned in Ref 7 that ". . . as one region of the specimen is loaded and fails, the rest of the specimen remains intact and is elastically loaded and unloaded." This statement implied that the failure localization and non-uniform failure in rock specimen probably causes the class II behavior. However, the mechanism of non-uniform failure was not sufficiently investigated.

For further discussions, the inside of the rock model was divided into nine local small regions as shown in Fig.4.10, and local axial strain in each region was measured. The microscopic parameters of Case 1 were used for this calculation. Four particles are selected in each region to calculate the local axial strain. The radial and axial strain was calculated from the displacement of selected particles.

Fig.4.11(a) shows the relation between a local axial strain for each region and the loading stress obtained from the axial strain controlled uniaxial compression tests. The numbers in Fig.4.11 represent the region number shown in Fig.4.10. As shown in Fig.4.11(a), although the local axial strain recovers in most regions after passing the peak, a significant increase of the axial strain observed in the region No.5.
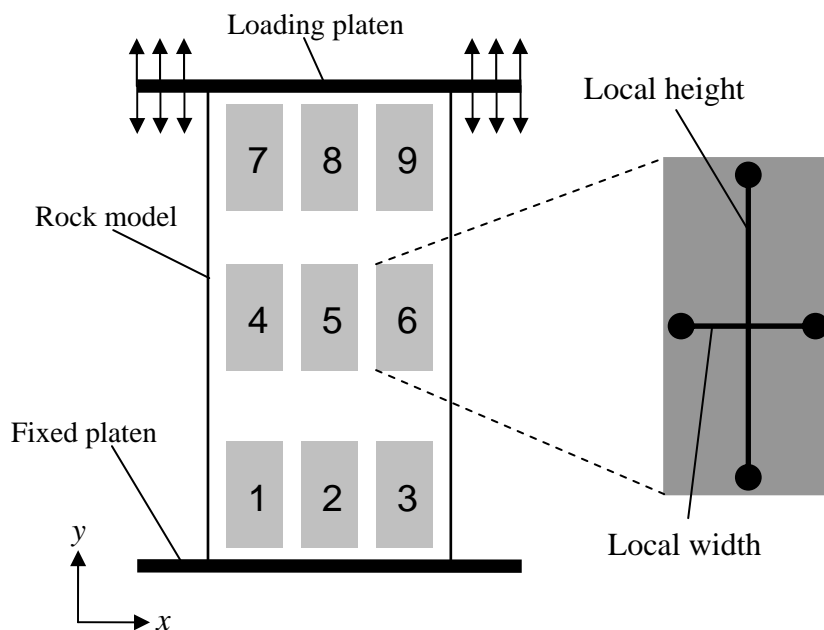
Fig.4.10   Local strain monitoring procedure in each region.
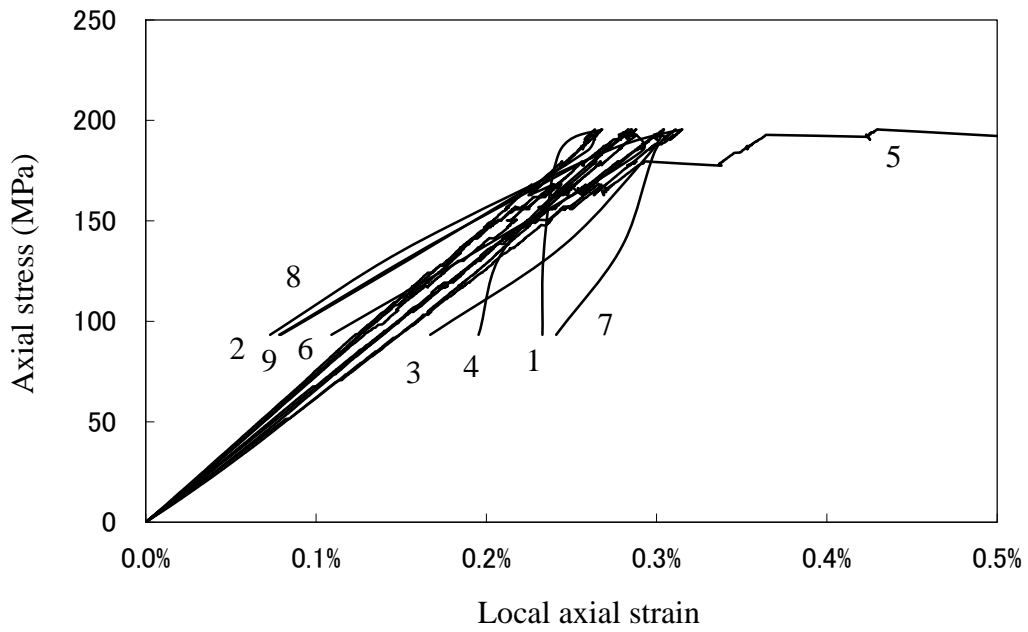
(a) Axial strain control.
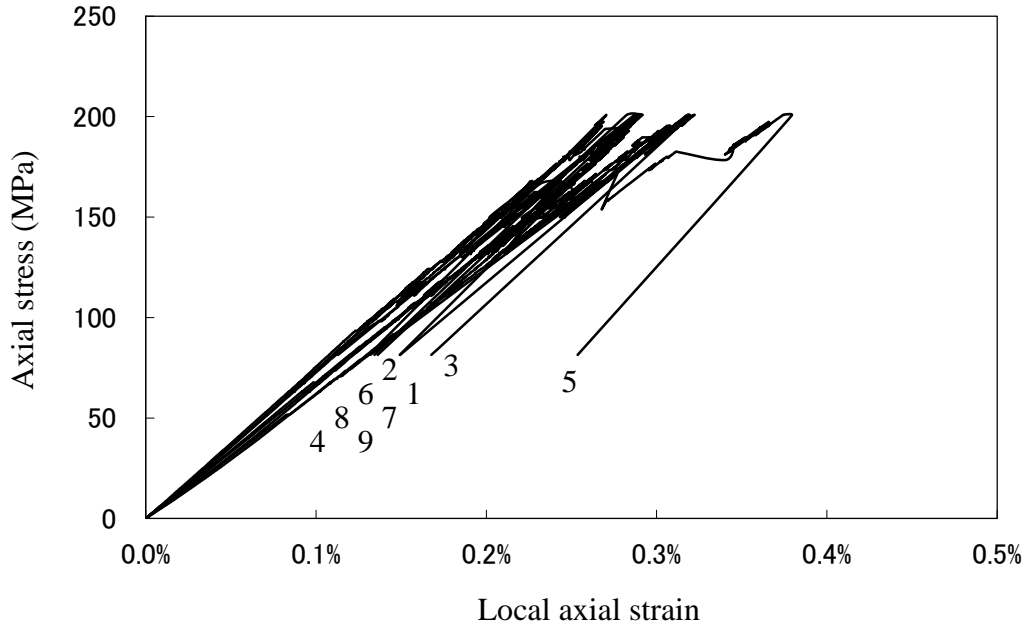
(b) Radial strain control.

Fig.4.11　Local stress-strain curves in each region. The numbers in
the figure represent the region number shown in Fig.4.10.

84

As shown in Fig.4.7(a), shear bands clearly appear in the axial strain controlled uniaxial compression tests, and the shear bands pass the small region No.5 in Fig.4.10. This means that an increase of local axial strain in the region No.5 which was caused by the crack surface slips along the shear bands dominates the mechanical behavior of whole rock specimen and as a result, the complete stress-strain curve shows the Class I behavior.

On the other hand, Fig.4.11(b) shows the relation between a local axial strain in each region and the loading stress obtained from the radial strain controlled uniaxial compression tests. As shown in Fig.4.11(b), the axial strain recovers in all local small region of rock specimen after the peak stress. This is because the formation of shear band does not grow due to the axial strain control was applied after the peak stress to keep the radial strain constant. Since shear bands were not formed clearly for the radial strain controlled uniaxial compression tests, all local small regions of rock specimen still keep elastic behavior, and as a result, the complete stress-strain curve of rock specimen showed the Class II behavior.

4.5. Conclusion

A new DEM code for the uniaxial compression tests with radial strain control was developed and Class II behavior of rock was simulated in this study. The simulation results show good agreement with the complete stress-strain curve obtained from the laboratory experiment. These results suggest that the DEM can reproduce the Class II behavior of the rock successfully. In addition, the mechanism of the Class II behavior was discussed in detail from the microscopic point of view. The findings obtained from this study can be summarized as follows.

1. Although the same rock model and the same microscopic parameters were used, Class I behavior was obtained in the axial strain controlled uniaxial compression tests and Class II behavior was obtained from the radial strain controlled uniaxial compression tests. This indicates that the loading control methods significantly affect on the mechanical behavior of rocks with uniaxial compression (Class I and II).

2. The pre-peak behavior was almost the same for both loading control methods. However, the mechanical behavior in post-peak region is different between two different loading control methods and the formation of shear bands play important

roles in the post-peak region. The shear bands appear clearly in the axial strain controlled uniaxial compression tests. On the other hand, clear shear band does not appear in the radial strain controlled uniaxial compression tests. This is caused by the fact that the formation of shear bands does not grow rapidly due to the axial loading control (unloading) to keep constant radial strain.

3. A series of simulations using different values for microscopic parameters were also carried out and simulation results clearly show that the microscopic parameters do not affect significantly the post-peak Class I and II behaviors. Hence, the key to understand the Class II behavior of brittle rocks is the localized deformation, such as the formation of a shear band.

4. A clear shear bands appear in the axial strain controlled uniaxial compression tests and a significant increase of the axial strain occurs in some small regions of the rock specimen following the crack surface slips along the shear bands. As a result, the stress-strain curve of the entire rocks will show the Class I behavior. On the other hand, since clear shear band is not formed during the radial strain controlled uniaxial compression tests, most local small regions of rock specimen still keep elastic behavior, and as a result, the complete stress-strain curve of the whole rock specimen shows the Class II behavior.

The post-peak behavior of the rocks was discussed in detail by using newly developed DEM code. The DEM model may be a strong tool to analyze and understand the failure mechanisms and their processes of rocks such as Class II behavior.

Even though the uniaxial compression tests with radial strain control was simulated in this study, many other experimental techniques to obtain the complete stress-strain curves including Class II behavior using various measuring values as the feedback signal to control the loading conditions [9-12]. It is very interesting to simulate and discuss these experimental techniques using DEM. Moreover, it is well-known that the geometry and size of the rock specimen also affect significantly the mechanical behavior in the post-peak region of the rocks [13], which was not investigated in this study. Investigating these issues in detail using DEM will be the future works.

References

[1] Wawersik WR. Detailed analysis of rock failure in laboratory compression tests. Ph.D thesis, University of Minnesota, 1968.

[2] Wawersik WR and Brace WF. Post-failure behavior of a granite and diabase. Rock Mechanics, 1971; 3: 61-85.

[3] Wawersik WR and Fairhurst C. A Study of brittle rock fracture in laboratory compression experiments. Int J Rock Mech Min Sci, 1970; 7(5): 561-575.

[4] He C, Okubo S and Nishimatsu Y. A study on the Class II behavior of rock. Rock Mech and Rock Eng, 1990; 23: 261-273.

[5] Pan P-Z, Feng X-T and Hudson JA. Numerical simulations of Class I and Class II uniaxial compression curves using an elasto-plastic cellular automaton and a linear combination of stress and strain as the control method. Int J Rock Mech Min Sci, 2006; 43(7): 1109-1117.

[6] Bäckström A, Antikainen J, Backers T, Feng X-T, Jing L, Kobayashi A, Koyama T, Pan P-Z, Rinne M, Shen B and Hudson JA. Numerical modelling of uniaxial compressive failure of granite with and without saline porewater. Int J Rock Mech Min Sci, 2008; 45(7): 1126-1142.

[7] Staub I, Andersson JC and Magnor B. Äspö Pillar Stability Experiment, geology and mechanical properties of the rock mass in TASQ. SKB report R-04-01, Stockholm, 2004; 81-84.

[8] Brown ET. Rock characterization, testing and monitoring: ISRM. suggested methods. Pergamon Press, 1981.

[9] Sano O, Terada M and Ehara S. A Study of the time-dependent microfracturing of oshima granite. Tectonophysics, 1982; 84: 343-362.

[10] Terada M, Yanagidani T and Ehara S. A. E. rate controlled compression test of rocks. In: Proceedings of the 3rd conference on acoustic emission microseismic activity in geologic structures and materials. Trans-Tech, Clausthal, 1984; 159-171.

[11] Okubo S. Uniaxial compression testing using a linear combination of stress and strain as the control variable. Int J Rock Mech Min Sci, 1985; 22(5): 323-330.

[12] Okubo S, Nishimatsu Y and He C. Loading rate dependence of class II rock behaviour in uniaxial and triaxial compression tests—an application of a proposed new control method. Int J Rock Mech Min Sci Geomech Abstr, 1990; 27: 559-562.

[13] Labuz JF and Biolzi L. Class I vs class II stability: A demonstration of size effect. Int J Rock Mech Min Sci, 1991; 28: 199-205.

Chapter 5
The distinct element analysis for hydraulic fracturing in hard rock considering fluid viscosity and particle size distribution

5.1. Introduction

To better understand the mechanics of hydraulic fracturing, a considerable amount of research has been carried out in the past few decades. According to the conventional theory, hydraulic fracturing is formed by tensile crack generation [1].

On the other hand, the shear type mechanisms was observed in most of the acoustic emission (AE) events recorded during the laboratory and field hydraulic fracturing experiments [2-5]. Ishida *et al*. carried out a laboratory hydraulic fracturing experiments using low viscous water and high viscous oil. The source mechanisms of AE events indicates that shear type mechanisms are dominant when low viscous fluid is injected, and both shear and tensile type mechanisms are observed when high viscous fluid is injected [6].

In addition, Matsunaga *et al*. conducted hydraulic fracturing experiments for various rocks and acrylic resin, and predicted that texture of rock, such as grain size, affects the hydraulic fracturing mechanism [7]. Ishida *et al*. extended this work and the hydraulic fracturing experiments were conducted for four different types of granitic rock specimens with different grain size in order to investigate the influence of grain size on induced crack geometry and fracturing mechanism [8-10]. The fault plane solutions of AE indicated that the dominant micro-fracturing mechanism becomes tensile rather than shear with decreasing grain size. Their experimental results indicate that texture of rock like grain size of granitic rocks considerably affects the geometry, surface roughness and microcracking mechanism of hydraulically induced cracks.

To give the rational explanation for such disagreement between conventional theory and AE monitoring and to better understand the hydraulic fracturing mechanism, various numerical analysis techniques have been developed. The FEM and the BEM have been commonly used to simulate hydraulic fracturing in complex three-dimensional structures [11,12]. Al-Busaidi *et al*. performed the simulation of hydraulic fracturing in granite by using the DEM, and the results were compared with the AE data from the experiment. However, the simulation results showed that the disagreement mentioned above was not solved successfully. Thus, the hydraulic fracturing mechanism has not been sufficiently clarified [13].

In this section, the fluid flow algorithm that can consider the fluid viscosity and

permeability is introduced into the DEM program to reproduce the hydraulic fracturing. A series of simulations for hydraulic fracturing in hard rock was performed by using the flow-coupled DEM code to discuss the influence of the fluid viscosity and the particle size distribution, and to obtain insights that gave the rational explanation to the disagreement between conventional theory and the AE monitoring results.

5.2. Flow-coupled DEM

5.2.1 Fluid flow algorithm

The fluid flow algorithm that can consider the fluid viscosity and permeability is introduced into the DEM program to reproduce the hydraulic fracturing [13-16]. In the fluid flow algorithm, as shown in Fig.5.1, the aperture between the adjoining particles is assumed to be a flow channel, and a series of enclosed domain is created by connecting the centers of adjoining particles.

As shown in Fig.5.2, each channel is assumed to be a set of parallel plates with some aperture, and the fluid flow in the channel is modeled by the Poiseuille equation. Therefore, the volumetric laminar flow is given by

$$Q = \frac{w^3}{12\mu} \frac{\Delta P}{L_p} \tag{5.1}$$
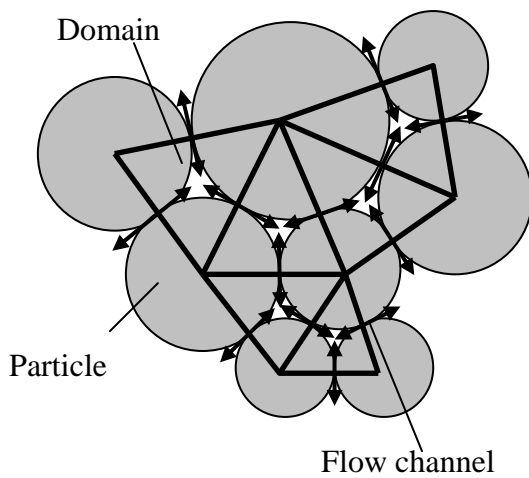
Fig.5.1 Channel - Domain model.
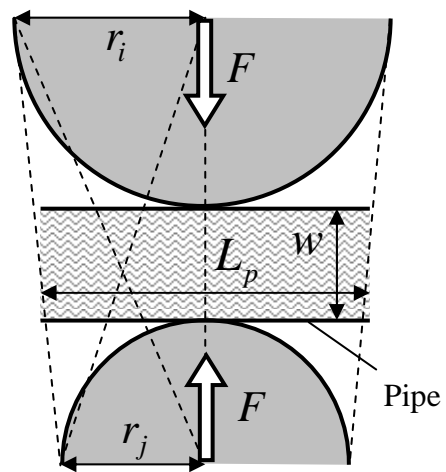
Fig.5.2 Channel width and length.

where w is the aperture, L_p is the length of the channel. L_p is assumed to be obtained from harmonic mean of the radius of two particles r_i and r_j, and given by

$$L_p = 2 \cdot \frac{2 r_i r_j}{r_i + r_j} \tag{5.2}$$

ΔP is the difference in pressure across a channel and μ is the viscosity of the fluid. Because the model is 2-D, an out of plane thickness is assumed to be a unit.

According to equation (5.1), fluid flow never occur when the two particles are in contact ($w=0$). To avoid this, the w will be given by equation (5.3) relating to the compressive normal force F at the contact.

$$w = \frac{w_0 F_0}{F + F_0} \tag{5.3}$$

where w_0 is assumed initial aperture for particles that are just touching and F_0 is the normal force at which the channel aperture decreases to half of its initial aperture. Since flow rate Q in equation (5.1) is microscopic flow rate in one flow channel and the fluid flow in a rock model is expressed by assembly of many flow channels, the permeability of the entire rock model cannot be calculated directly from equation (5.1). Therefore, the value of w_0 is determined as the permeability of the entire rock model obtained by simulating the permeability test correspond to the value of an actual specimen. This implies that the permeability of the entire rock model can be adjusted by tuning the value of w_0, and particle displacement updates the porosity and permeability of the rock model.

Each domain accumulates the fluid pressure acting on the surface of surrounding particles, and the fluid pressure is updated during the fluid flow calculation. The change of fluid pressure dP is given as the following equation by the continuity equation

$$dP = \frac{K_f}{V_r} \left(\sum Q dt - dV_r \right) \tag{5.4}$$

where $\sum Q$ is total flow rate for one time step from the surrounding channels, dt is duration in one time step, K_f is the fluid bulk modulus, V_r is the apparent volume of the domain and dV_r is the change of the volume in the domain.

5.2.2 Fluid flow and fluid pressure

The fluid flow in the channel is assumed to be the two-dimensional poiseuille flow. Therefore, the laminar flow between two parallel plates extending in x-directions, as shown schematically in Fig.5.3 will now be considered. The plates are at the planes $y = 0$ and $y = w$, and the flow is in the x-direction, hence there is no velocity component in y-direction. The velocity distribution u for laminar flow between parallel plates is a function of y only, and given by

$$u = \frac{w^2}{2\mu}\left\{\frac{y}{w} - \left(\frac{y}{w}\right)^2\right\}\frac{\Delta P}{L_p} \tag{5.5}$$

Viscous fluid flow along solid boundary will incur a shear stress on that boundary. The shear stress at a surface element parallel to a plate, at the point y, is given by

$$\tau_f = \mu\frac{du}{dy} = \left(\frac{w}{2} - y\right)\frac{\Delta P}{L_p} \tag{5.6}$$

Especially, the wall shear stress is defined as

$$\tau_{f0} = \frac{w}{2}\frac{\Delta P}{L_p} \tag{5.7}$$

Therefore, total force acting on a plate is given by

$$f_c = L_p \cdot \tau_{f0} = \frac{w}{2}\Delta P \tag{5.8}$$

where L_p is the length of the channel. As shown in Fig.5.3, total force f_c is given to particles as a shear force that acts on the surface of two particles that form channels.

Each domain accumulates the fluid pressure, and the fluid pressure acts on the surface of surrounding particles as shown in Fig.5.4. When fluid pressure P acts on a particle whose radius is r, the total force f_d that acts on the center of a particle is given by

$$f_d = \int_{-\varphi}^{\varphi} P\cos\theta \cdot rd\theta \tag{5.9}$$

where φ is corner half-angle of a domain.

Consequently, by introducing fluid flow algorism, the shear stress caused by fluid flow and fluid pressure accumulated in each domain are acting on particles.
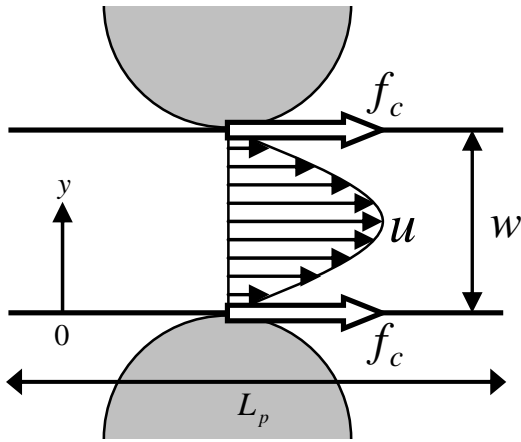
Fig.5.3   Flow velocity and viscous forces.
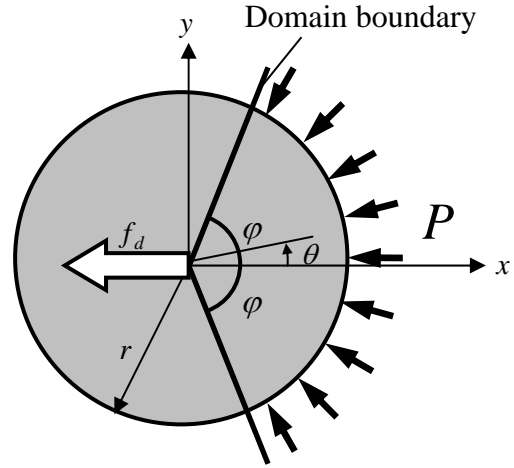
Fig.5.4   Fluid pressure acting on the particle.

5.2.3 Saturation

Fluid flow algorithm presented in Ref.13-16 assumed that the entire model is always filled with the fluid (consider only saturated condition). However, the specimen might not always be saturated in actual laboratory experiments. Such a condition with different saturation (saturated-unsaturated condition) might influence the simulation results. Therefore, to consider the unsaturated conditions, fluid flow algorithm is further improved, and the saturation factor in each domain is introduced. The saturation factor in each domain is defined as

$$S_t = \frac{V_f}{V_r \cdot po} \tag{5.10}$$

where V_r is the volume of domain as shown in Fig.5.5, V_f is the volume of fluid that exists in the domain, and *po* is assumed porosity of the model. For $1 < S_t$ the domain is filled with fluid, while as $1 > S_t$ the domain is unsaturated. When the unsaturated condition is considered, fluid pressure is assumed to be the same value as the atmospheric pressure (0MPa in this research) in the unsaturated domain, and increases only after the domain is saturated. Fig.5.6 shows the relation between the saturation factor and the fluid pressure.

Since the saturation factor of each domain is calculated with the volume of the domain, transmission of fluid pressure significantly depends on porosity of the model.

True pore volume (V_{pore})
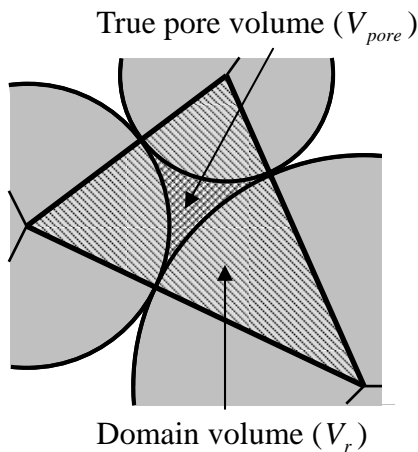
Domain volume (V_r)

Fig.5.5   Domain volume and pore volume.
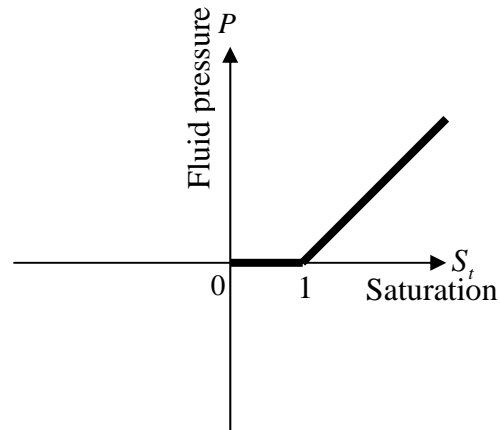
Fig.5.6   Relationship between saturation of the domain and fluid pressure.

However, in the DEM simulation, it is difficult to reproduce the porosity of an actual rock and the unconsolidated sands accurately because the DEM model is expressed by the assembly of circular particles. Therefore, the true pore volume of the domain, V_{pore}, can not used for the calculation of saturation factor. Therefore, the apparent pore volume of the domain obtained from the entire volume of the domain, V_r, and assumed porosity, *po*, is used in equation (5.10).

Incidentally, in equation (5.4), the change in fluid pressure caused by volume change is calculated by using the entire volume of the domain. This means the bulk modulus used for equation (5.4) is apparent bulk modulus of elasticity of the pore fluid and particle.

5.3. Simulation condition
5.3.1 Rock specimen model and loading condition

Fig.5.7(a) illustrates the rock model and loading condition for the hydraulic fracturing. The rock model is expressed by the assembly of particles bonded with each other. The size of rock specimen is 20cm in width and 20cm in height. A borehole for fluid injection is created at the center of the rock model. The rock model is surrounded by the four confining walls. The left and under walls are fixed and the right and upper walls can move to apply the constant confining pressure. Two confining pressures, 10MPa in the *x*-direction and 5MPa in the *y*-direction, were applied to the rock model. Frictional force has not acted between the model and the confining walls. The rock models used in

the simulations were made according to the following procedures.

At first, particles were aligned along one edge of the model as shown in Fig.5.8. The particle radius was selected following a uniform distribution between maximum and minimum radius using random number. In addition, particles that have the same radius are arranged in the circular form at the center of the model to form the inner wall of the borehole. During this process, the edge of the model and the surface of borehole can be smoothed, and unnecessary stress concentration that originates in the model geometry can be avoided. The other parts of the model are filled with particle according to the procedure mentioned in the section 2.4.1.

(a) Rock specimen model and loading condition

(b) Model A (Heterogeneous).   (c) Model B (Homogeneous).
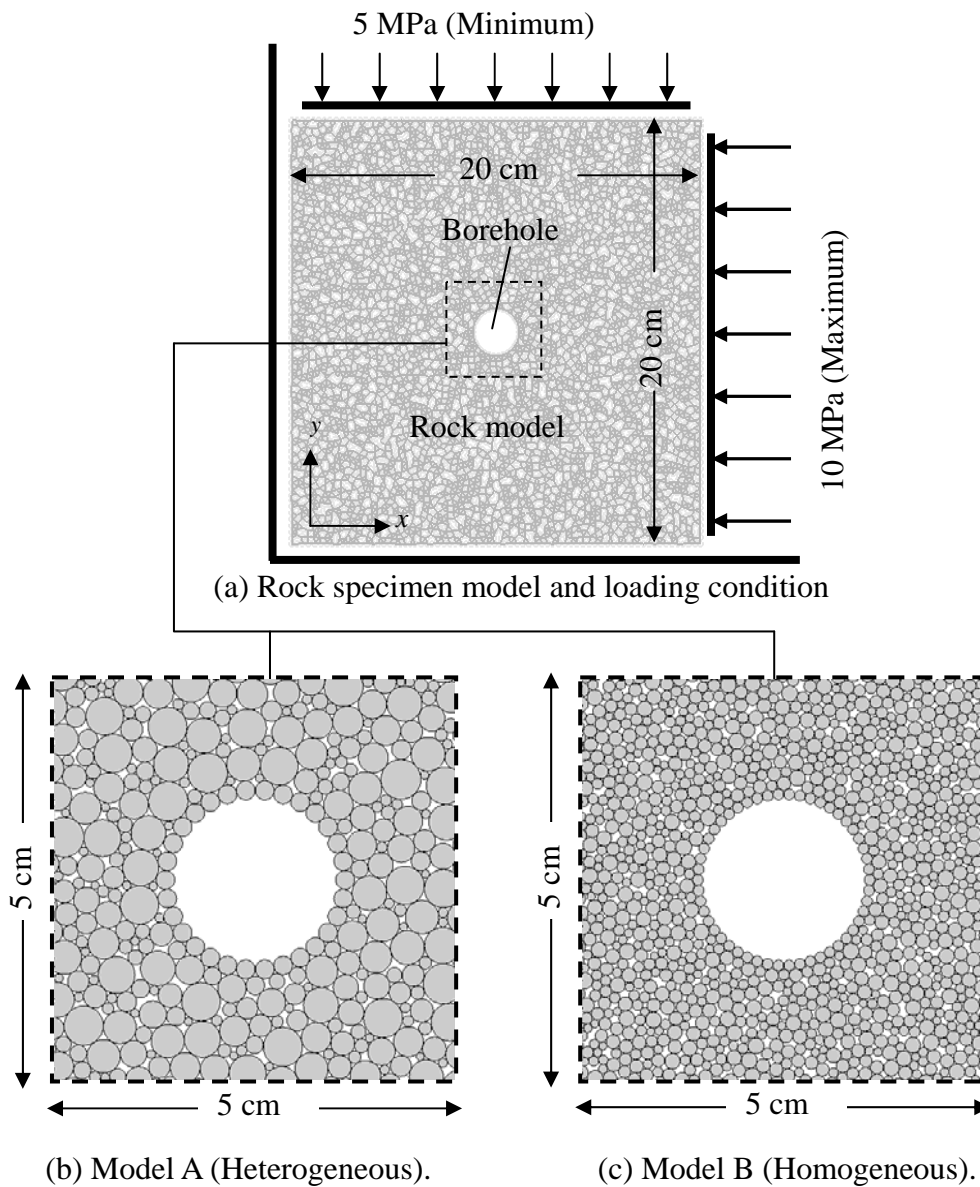
Fig.5.7   Rock specimen model and loading condition.

As shown in Fig.5.7(b) and (c), to investigate the influence of the particle size distribution on the hydraulic fracturing behavior, two types of rock models (heterogeneous and homogeneous model) with different ranges of particle radius were considered. In this study, heterogeneous model is called as "Model A" and homogeneous model is called as "Model B". The number of particles for model A is about 6,500 with the particle radius range from 0.5mm to 2.5mm, and the number of particles for model B is about 18,000 with the particle radius range from 0.5mm to 1.0mm. Fig.5.9 shows the particle size cumulative curve for each model.

In addition, to investigate the influence of the fluid viscosity on the hydraulic fracturing behavior, low viscous fluid ($0.1\,\text{mPa}\cdot\text{s}$) and high viscous fluid ($100\,\text{mPa}\cdot\text{s}$) are used as the fracturing fluid. Fracturing fluid was injected at constant pressurizing rate.
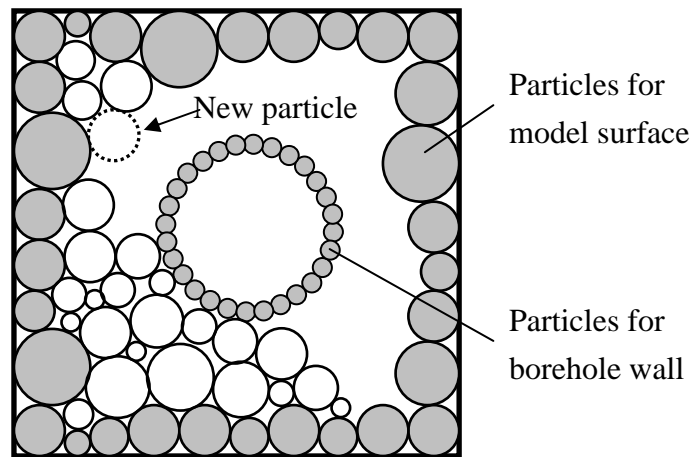
Fig.5.8 Particle packing method.
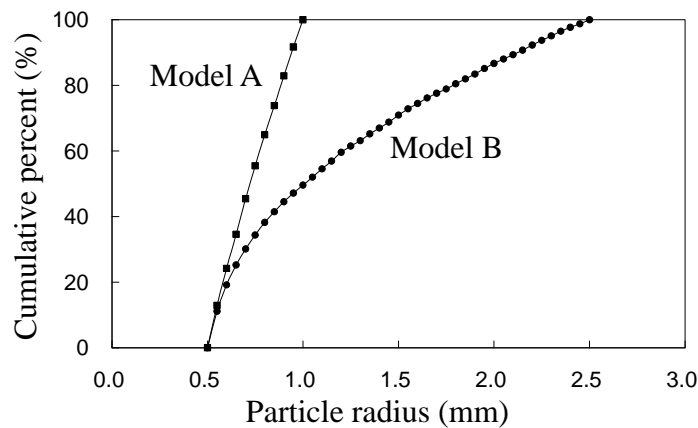
Fig.5.9 Particle size cumulative curve.

5.3.2 Calibration

The microscopic mechanical parameters used in this simulation were calibrated by preliminary simulations of uniaxial compression and Brazilian tests. In this study, macroscopic mechanical properties of Kurokamijima granite were used to calibrate the microscopic parameters, such as the Young's modulus, the Poisson's ratio, the tensile strength and the uniaxial compressive strength (UCS) of the rock model. The confining wall is assumed to be the steel. The microscopic mechanical parameters used in this simulation and the calibration results are summarized in Table 5.1. The macroscopic parameters of both rock models show good agreement with the experimental results.

As mentioned above, since the permeability of the rock model cannot be determined directly, the value of w_0 is calibrated as the permeability of the entire rock model obtained by simulating the permeability test. As shown in Fig.5.10, the rock model with 20cm in width and 10cm in height was used for the permeability test. Fluid flow was established through the model by maintaining the fluid pressure P_{in} on the left side of the model at 0.2 MPa and the fluid pressure P_{out} on the right side of the model at 0.1 MPa. This pressure difference causes fluid flow only through the existing network of flow channels, and fluid flow does not occur between the rock model and the wall. The simulation of the permeability test is continued until the inflow Q_{in} equals outflow Q_{out} and a steady flow state is achieved ($Q = Q_{in} \cong Q_{out}$).
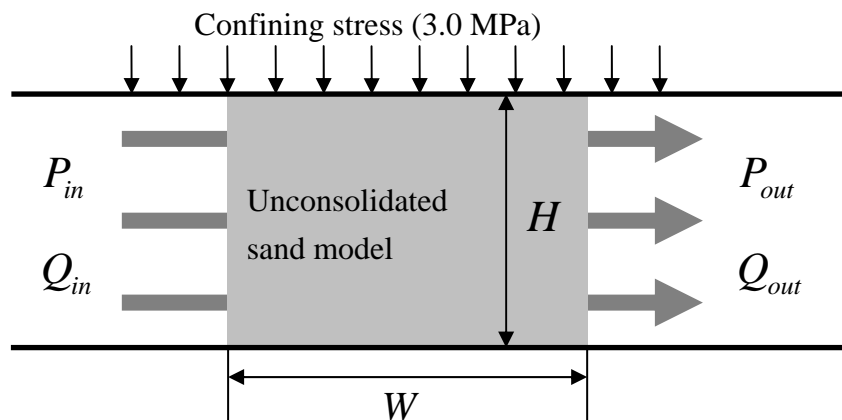
Fig.5.10   Simulation of permeability test.

Table 5.1   Rock model properties and input parameters.

-Microscopic parameters-	Heterogeneous	Homogeneous
Number of particles:	6407	18505
Maximum particle radius:	2.5 mm	1.0 mm
Minimum particle radius:	0.5 mm	0.5 mm
Porosity of the model:	12.5 %	18.5 %
Width:	200 mm	200 mm
Height:	200 mm	200 mm
Borehole radius:	10mm	10 mm
Particle density:	2620 kg/m^3	2620 kg/m^3
Young's modulus of wall (E_w):	200 GPa	200 GPa
Friction coefficient of wall ($\tan \phi_w$):	0.0	0.0
Poisson's Ratio of wall (v_w):	0.3	0.3
Young's modulus of particle (E_p):	66 GPa	84 GPa
Friction coefficient of particle ($\tan \phi_p$):	0.5	0.5
Poisson's Ratio of particle (v_p):	0.25	0.25
Shear/normal spring stiffness ratio (α):	0.55	0.7
Shear strength of bonding (τ_c):	157.5 MPa	249 MPa
Tensile strength of bonding (σ_c):	15.8 MPa	21 MPa
Assumed porosity of the model (po):	0.2 %	0.2 %
Initial saturation (S_t):	10 %	10 %
Initial aperture (w_0):	7.028×10^{-7} m	5.775×10^{-7} m
Bulk modulus of the fracturing fluid (K_f):	2.0 GPa	
Fluid viscosity for low viscous fluid (μ)	0.1 mPa$\cdot$s	
Fluid viscosity for high viscous fluid (μ)	100 mPa$\cdot$s	

-Calibration results-	Experiment	Simulation	
	Kurokamishima-granite	Heterogeneous	Homogeneous
UCS of rock model (MPa):	200.0	199.5	199.9
Tensile strength (MPa):	10.0	10.2	10.2
Young's modulus (GPa):	70.0	70.3	70.2
Poisson's Ratio:	0.250	0.254	0.248
Permeability (m^2):		1.0×10^{-17}	1.0×10^{-17}

Assuming the rock model as an isotropic medium and according to the Darcy's low, the steady flow rate Q_{steady} is given as follows.

$$Q_{steady} = \frac{kH}{\mu} \frac{(P_{in} - P_{out})}{W}$$

(5.11)

where μ and k are the viscosity of the fluid and the macroscopic permeability of the rock model. Thus the permeability of the rock model can be calculated by equation (5.11) as

$$k = \frac{Q_{steady} \mu W}{H(P_{in} - P_{out})}$$

(5.12)

5.4. Summary of the simulation results

As shown in Table 5.2, four hydraulic fracturing simulations called Case A1, A2, B1 and B2 with different combination of rock model and fracturing fluid were performed. For Case A1 and A2, the same heterogeneous rock model (Model A) was used, and for Case B1 and B2, the same homogeneous rock model (Model B) was used. For Case A1 and B1, the low viscous fluid ($0.1\,\mathrm{mPa \cdot s}$) was used, and for Case A2 and B2, the high viscous fluid ($0.1\,\mathrm{mPa \cdot s}$) was used. In all cases, two confining pressures, 10MPa in the x-direction and 5MPa in the y-direction, were applied to the rock model.

The conventional theory showed that hydraulic fracture is created by tensile crack and extend along the direction of maximum compressive principal stress [1]. Fig.5.11 illustrates the geometry of the fracture formed in each case. Location of a microcrack is expressed by a solid line. For all cases, the orientation of the hydraulic fractures will be parallel to the direction of maximum compressive principal stress in theory. This result indicates that the effect of the confining stress was appropriately expressed in the DEM simulations.

Fig.5.12(a), (b), (c) and (d) show the location of x-coordinates of the cracks versus time step. The crack mode is identified based on the criterion described in the section 2.2, and a tensile crack is expressed with a closed circle and a shear crack is expressed with an open circle. Fig.5.12(e) shows the evolution of the fluid pressure in the borehole. Hydraulic fracturing has been initiated before the breakdown (peak) pressure in all cases. This result agrees well with the hydraulic fracturing process deduced from AE measurements in the laboratory experiments conducted by some researchers [17,18].

Table 5.2   Simulation condition for four cases.

	Rock model	Fracturing fluid	Confining stress
Case A1	Model A (Heterogeneous)	Low viscosity (0.1 mPa · s)	*x*-direction
Case A2	Model A (Heterogeneous)	High viscosity (100 mPa · s)	10 MPa
Case B1	Model B (Homogeneous)	Low viscosity (0.1 mPa · s)	*y*-direction
Case B2	Model B (Homogeneous)	High viscosity (100 mPa · s)	5 MPa
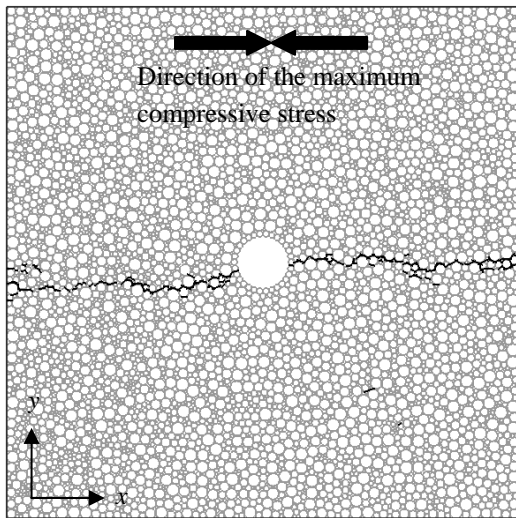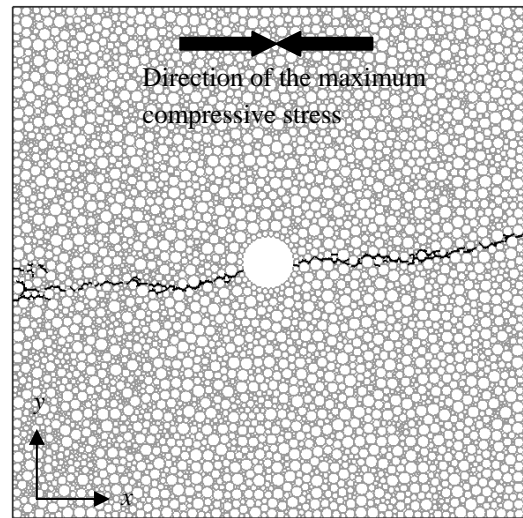
(a) Case A1
(Heterogeneous, Low viscosity)

(b) Case A2
(Heterogeneous, High viscosity)
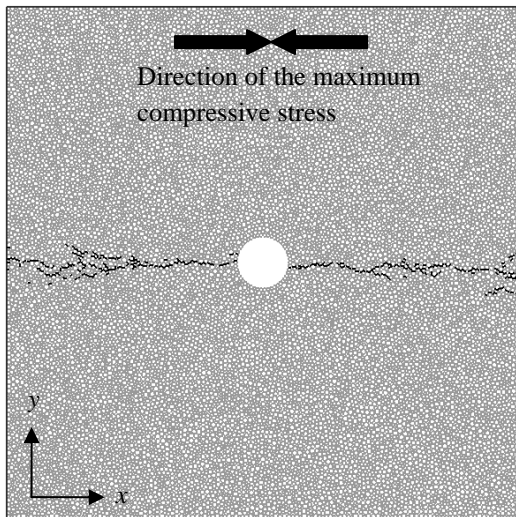
(c) Case B1
(Homogeneous, Low viscosity)
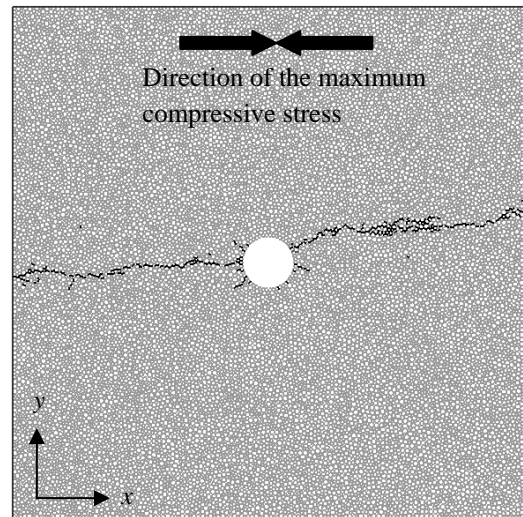
(d) Case B2
(Homogeneous, High viscosity)

Fig.5.11   Spatial distribution of all the cracks obtained from each case. The solid
lines indicate the crack generations.
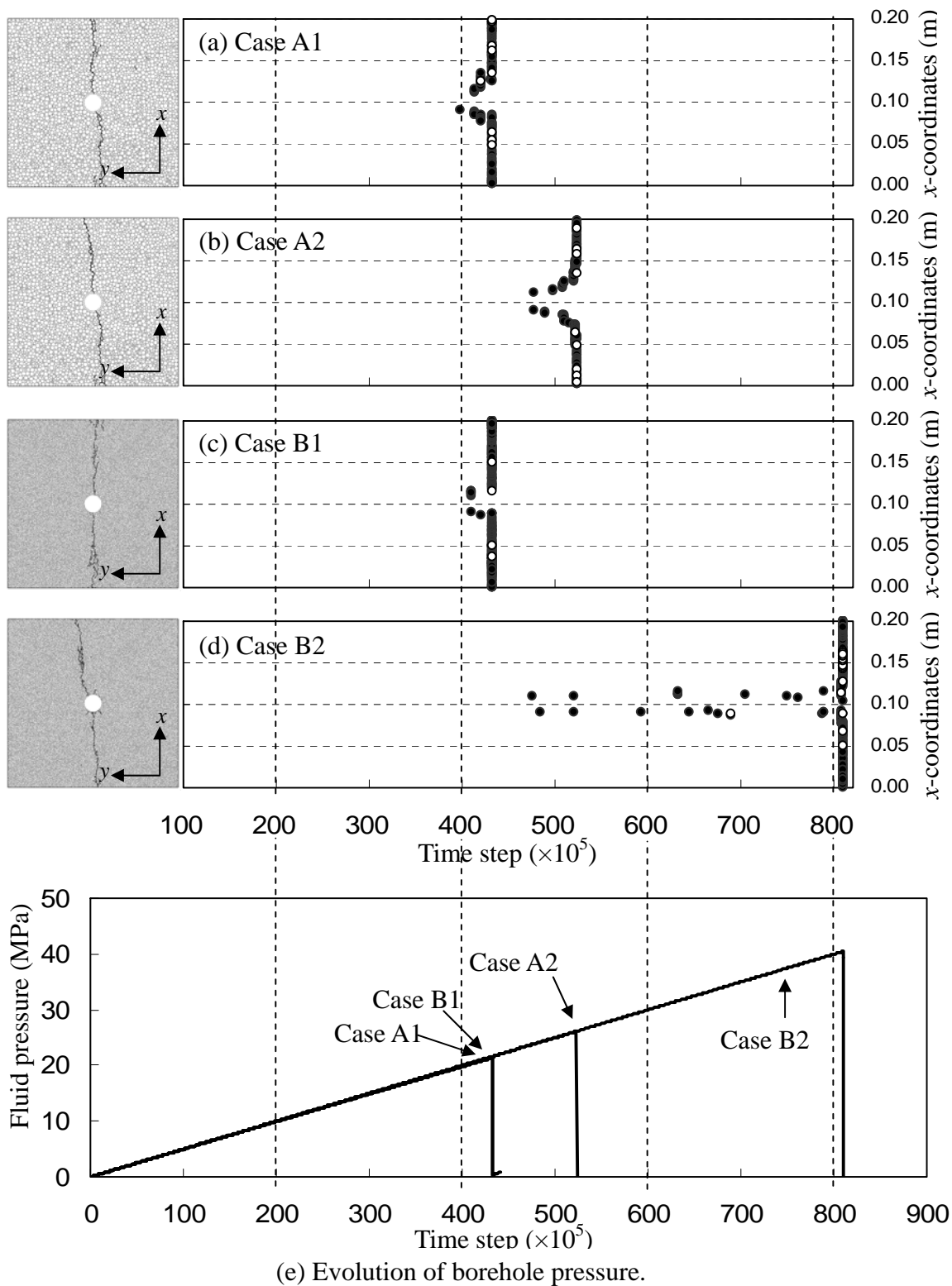
Fig.5.12   Results of the hydraulic fracturing simulation. (a), (b), (c) and (d)
Time-space distribution of cracks generated in each cases. (e) Evolution of
borehole pressure.

Table 5.3   Summary of the simulation results.

	Crack initiation pressure (MPa)	Breakdown pressure (MPa)	The number of microcracks	
			Tensile crack (%)	Shear crack (%)
Case A1	19.73	21.40	151 (93.8%)	10 (6.2%)
Case A2	23.84	26.09	144 (94.1%)	9 (5.9%)
Case B1	20.26	21.34	261 (98.5%)	4 (1.5%)
Case B2	23.84	40.42	258 (91.2%)	25 (8.8%)

Simulation results, such as crack initiation pressure, breakdown pressure and the number of microcracks generated during the simulation, are summarized in Table 5.3. As shown in Table 5.3, when the high viscous fluid was used, the crack initiation pressure and the breakdown pressure becomes higher than that with low viscous fluid regardless of the rock model. Especially, breakdown pressure in Case B2 (homogeneous model and high viscous fluid) was remarkably higher than that in other cases.

Since the number of particles of Model B is larger than that of Model A, the number of bonds between particles of Model B is also larger than that of Model A. Therefore, when the model B was used (Case B1 and B2), total number of microcrack generation becomes larger as shown in Table 5.3. In all cases, percentage of tensile crack generation is 90% or more. Percentage of shear crack generation is smallest in Case B1 (1.5%), and largest in Case B2 (8.8%). Thus, even though a few shear cracks were generated, tensile cracks were dominant in all cases as expected in theory.

5.5. Crack initiation pressure

As shown in Table 5.3, when the low viscous fluid was used, the crack initiation pressure and the breakdown pressure were lower than those with high viscous fluid. For Case A1 and B1 (low viscous fluid was used), the crack initiation pressure is almost the same (around 20 MPa). On the other hand, the crack initiation pressure is about 24 MPa for Case A2 and B2 with high viscous fluid.

This result can be explained by the effect of fluid infiltration and pore pressure gradient around the borehole. There is large number of small pores inside of rocks. When the borehole pressure increases with fluid injection, fracturing fluid penetrates into the interconnected pores of a rock from borehole wall. The fluid penetration causes an additional pore pressure around the borehole. The pore pressure reduces the effective stress of rock around the borehole, and makes it easy to generate tensile cracks [19].

To investigate the effect of fluid infiltration on the tensile rupture of permeable rock, Haimson [20,21] developed a sophisticated model theoretically to consider the fluid penetration. Moreover, Ito *et al*. [22,23] developed a new theory based on the point stress criterion, the theory assumes that the fracture initiation occurs when the maximum tensile effective stress reaches the tensile strength of a rock at a point not on the wellbore surface but inside of the rock.

Fig.5.13 shows close-up view of the rock model around the borehole for each case at the time step just before the crack initiation. The solid lines indicate the fluid penetration (saturated) area and the shade of each domain indicates the fluid pressure. As mentioned in section 5.2.3, saturated area is judged by the saturation factor, S_t. S_t is calculated by equation (5.10). For $1 < S_t$ the domain is assumed to be saturated. When low viscous fluid was used (Case A1 and B1), fracturing fluid widely infiltrated into the rock model from borehole wall and fluid pressure around the borehole increased. According to equation (5.3), the flow rate between particles is affected by the compressive normal force at the contact point. When the compressive normal force increases, the aperture of the channel, w, decreases. Therefore, since the maximum confining pressure is 10MPa in the x-direction, fluid flow perpendicular to x-axis decreases. Thus, the fluid saturation area is not a circle but an oval shape. On the other hand, fracturing fluid did not infiltrate into the rock model when high viscous fluid was used (Case A2 and B2).

Fig.5.14(a) shows the spatial distribution of the maximum principal stress at the initial step. Fig.5.14(b) and (c) show the spatial distribution of the maximum principal stress in Case B1 and B2 at the time step just before the crack initiation, respectively. The calculation procedure for the stress distribution in DEM model is described in APPENDIX. The distribution of the principal stresses is calculated based on the forces acting on the particles. In a word, Fig.5.14 shows the distribution of the effective stress.

At the initial step (borehole pressure is 0MPa), maximum principal stress at the borehole surface across y-axis is highest as shown in Fig.5.14(a). This is in agreement with conventional elastic theory.

However, as shown in Fig.5.14(b), the maximum principal stress around the injection hole decreases when the low viscous fluid was used. On the other hand, when the high viscous fluid was used, such a decrease in stress is not observed and maximum principal stress around the borehole increases due to the borehole pressure as shown in Fig.5.14(c). This result indicates that decrease in the crack initiation pressure in case which uses low viscous fluid is caused by decrease in effective stress due to the rise of fluid (pore) pressure around the borehole.

In actual hydraulic fracturing experiments, it is difficult to observe the infiltration behavior of fluid and change of stress distribution due to the fluid injection directly. On the contrary, the DEM can directly represent grain-scale microstructural features of rock, such as pre-existing flaws, pores, microcracks and grain boundaries by considering each grain as a DEM particle without complicated constitutive laws. The effect of fluid infiltration on the tensile rupture of permeable rock can be successfully reproduced by the coupled fluid flow and the DEM. This suggests that the DEM model may be a strong tool to understand the fracture behavior of permeable rock.

(a) Case A1
(Heterogeneous, Low viscosity)

(b) Case A2
(Heterogeneous, High viscosity)

(c) Case B1
(Homogeneous, Low viscosity)

(d) Case B2
(Homogeneous, High viscosity)

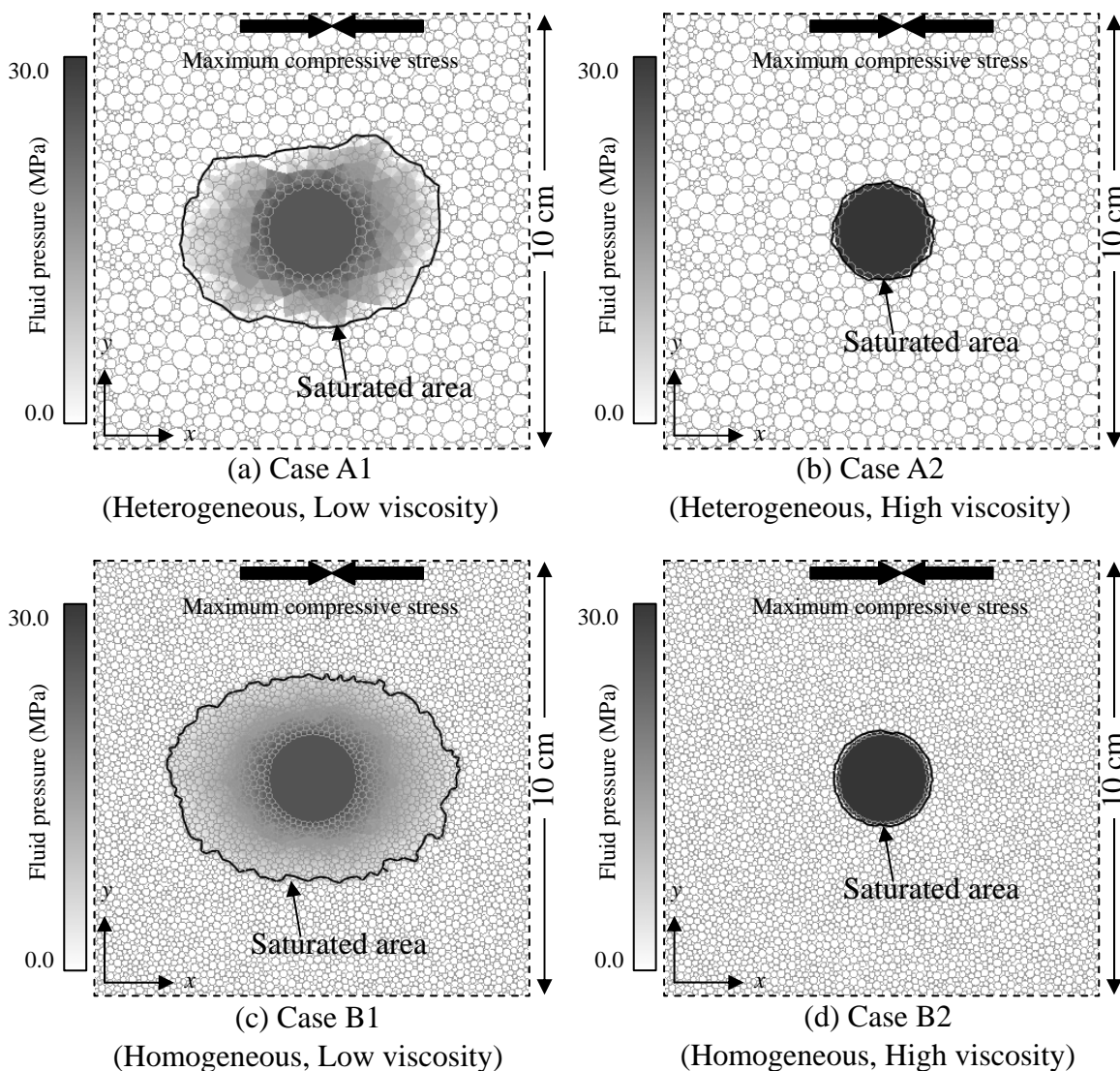Fig.5.13   Close-up view of the rock model around the borehole in each case at the time step just before the crack initiation. The solid lines indicate the fluid penetration (saturated) area and the shade of each domain indicates the fluid pressure.
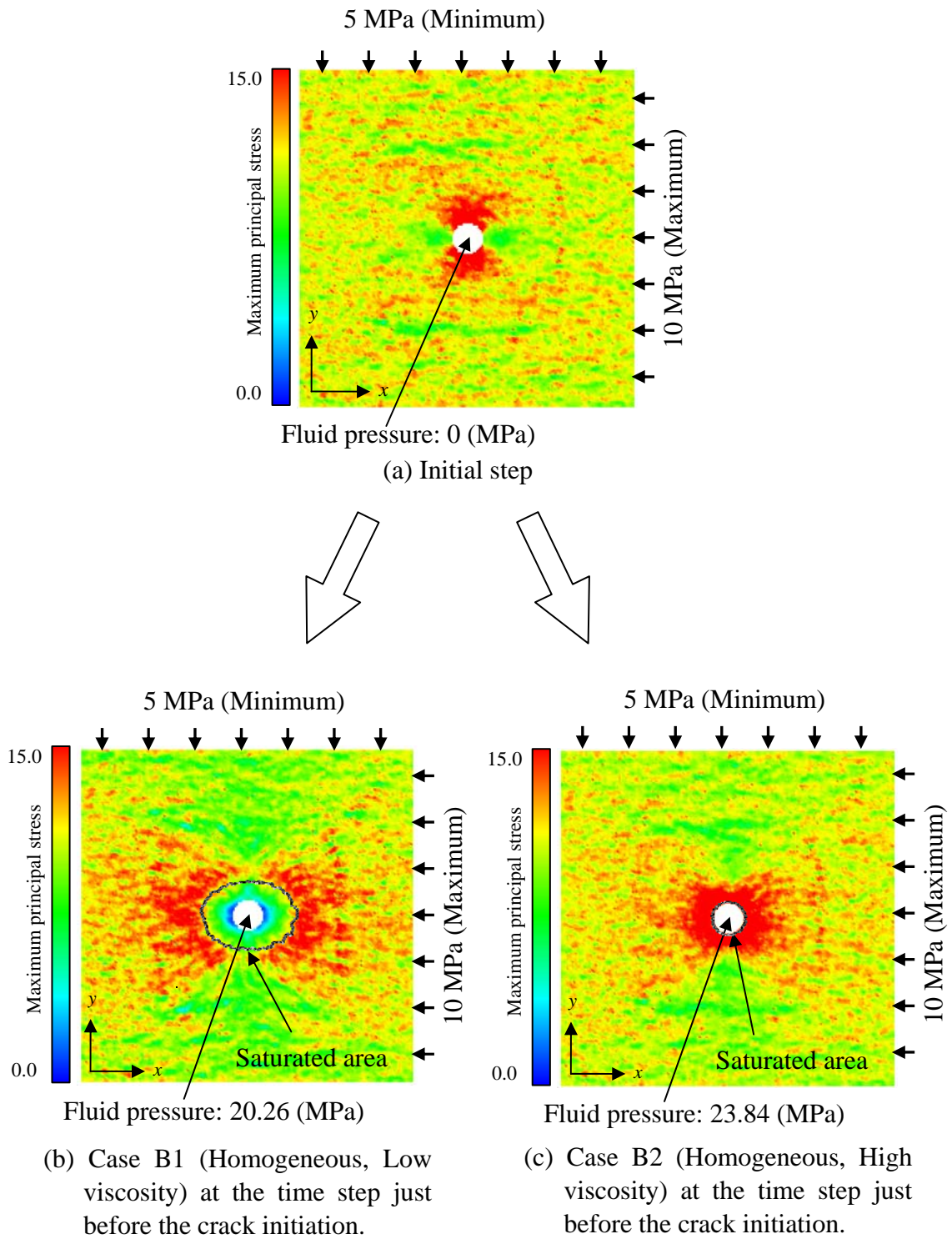
Fig.5.14 Spatial distribution of magnitude of the maximum principal stress at the initial step and at the time step just before the crack initiation.

5.6. Breakdown pressure

As shown in Table 5.3, when the high viscous fluid was used, the breakdown pressure was markedly higher than that with low viscous fluid. This result agree well with the theory [17,24], and can be explained by comparison between simulation result of hydraulic fracturing by DEM and fracturing process led by Linear Elastic Fracture Mechanics (LEFM).

In general, LEFM is often used as an analytical technique for the propagation of the fracture in the rock like materials. LEFM is a theory that assumes application to the continuum.

On the other hand, DEM is basically a discontinuity analysis technique for granular material. Therefore, the breakage of individual bonds that connect particles in DEM can not be compared with LEFM directly.

However, by assuming the connection of individual microcracks in DEM as a propagation of one macroscopic fracture, the simulation result by DEM can be interpreted by LEFM. Such a research has already been reported and it is shown that the fracture strength calculated from macroscopic fracture in DEM agree well with the one lead from LEFM [25-27].

Fig.5.15(a) and (b) show the fluid pressure acting on the inside of hydraulic fractures during low viscous fluid and high viscous fluid injection, respectively. The solid lines indicate the crack generations and the shade of each domain indicates the fluid pressure. As shown in Fig.5.15(a), when low viscous fluid was used, the fluid was infiltrated into the fracture instantaneously and the fluid pressure was applied throughout the fracture surface. On the other hand, when high viscous fluid was used, only the fracture elongated first and then the fluid was infiltrated slowly into the fracture and fluid pressure was applied only a part of the fracture surface.

Newman theoretically derived stress intensity formulae for the cases mentioned above [28]. Fig.5.16 illustrates the normalized stress intensity factor at the crack tips as a function of the crack length for two cracks propagating symmetrically from a borehole in an infinite medium, and the borehole radius R is adjusted to that used in the simulation. According to Fig.5.16, in case of $\lambda = 1$ (pressure acts all over the fracture surface), stress intensity factor monotonically increases with crack length. Thus, fracture never stops once it grows. On the other hand, in case of $\lambda = 0$ (pressure acts only in the borehole), stress intensity factor slowly decreases with crack length. Therefore, when high viscous fluid was used as the fracturing fluid, the fracture never extends without an additional pressure.
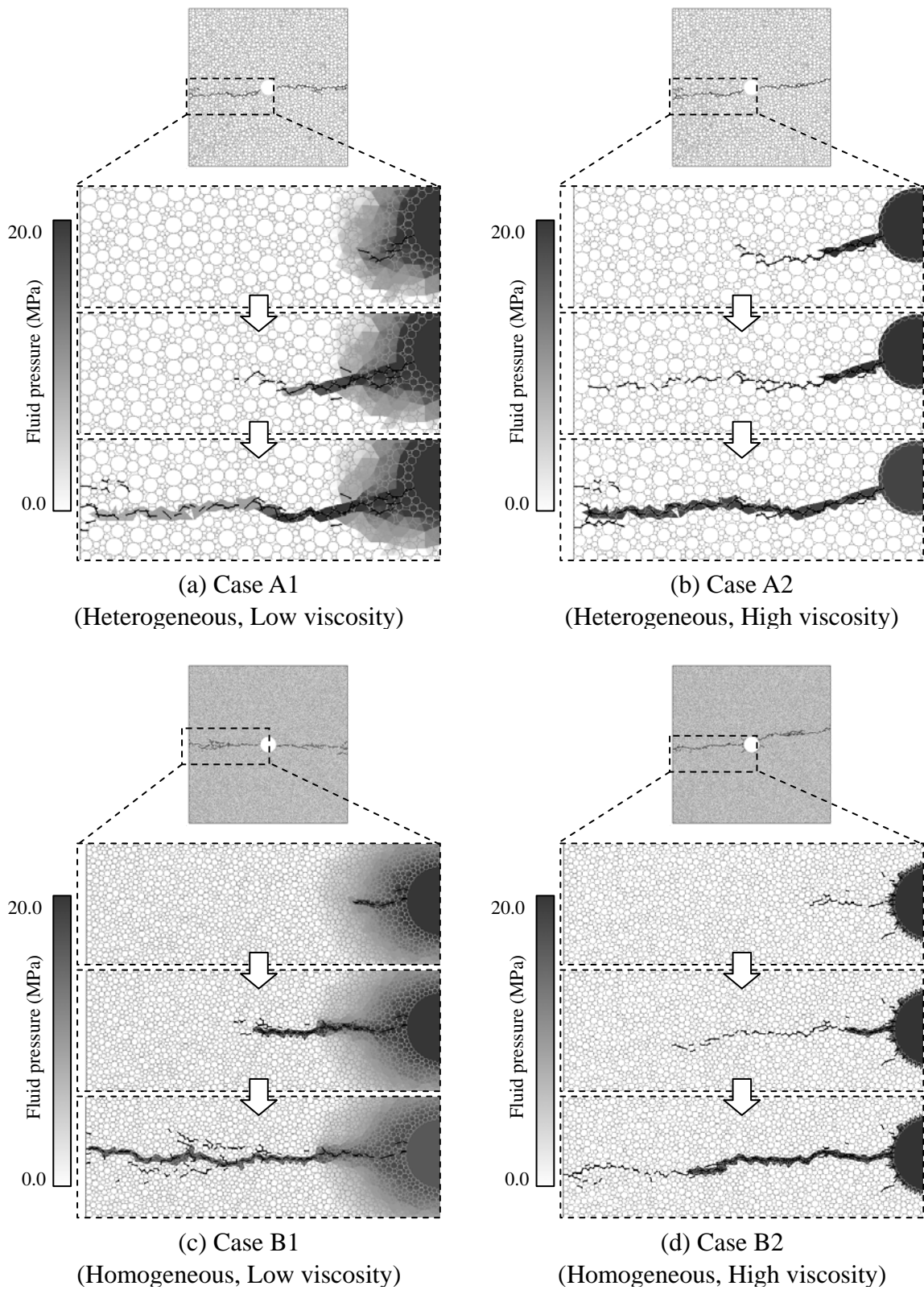
Fig.5.15 Fracture propagation and fluid infiltration behavior. The solid lines indicate the crack generations and the shade of each domain indicates the fluid pressure.

Thus, simulation result of hydraulic fracturing by DEM show good agreement with fracturing process explained by LEFM, and the effect of fluid viscosity on the breakdown pressure was discussed.

Moreover, as shown in Table 5.3, the breakdown pressure in Case B2 (homogeneous model and high viscous fluid) was remarkably higher than that in Case A2 (heterogeneous model and high viscous fluid). The similar results were obtained from the laboratory hydraulic fracturing experiment conducted by Ishida *et al.* and Matsunaga *et al.* Their experimental results indicate that the breakdown pressure decreased with increasing grain size of the rock specimen [7-10].

One possible explanation for such an effect of particle size distribution is given as follows. As the difference between maximum and minimum grain size in rock specimen increases, the defects between the grains become larger, and such defects become triggers for the propagation of the fractures. Therefore, breakdown pressure in Case B2 that use homogeneous model was remarkably higher than that in Case A2 that use heterogeneous model even though the same fracturing fluid was used.

In actual hydraulic fracturing experiments, since the development of the fracture is completed in very short time, it is difficult to observe the behavior of the fracturing fluid during the fracture growth. However, by using DEM, hydraulic fracturing process that is hard to be observed in an experiment can be discussed in detail.
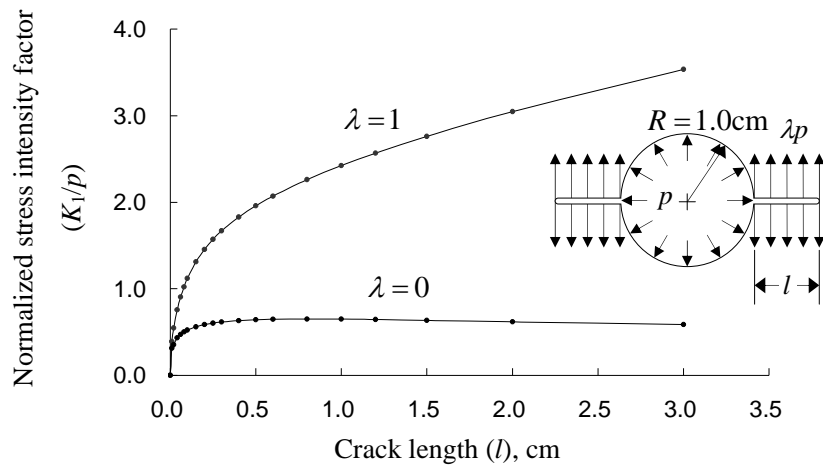
Fig.5.16   Normalized stress intensity factor as a function of
crack length for two radial cracks emanating from a
circular hole in an infinite medium [28].

108

5.7. Geometry and micro cracking mechanism of hydraulic fracturing

5.7.1 Hydraulic fracturing in heterogeneous model

Fig.5.17 (a) and (b) show the spatial distribution of all the microcracks generated during the hydraulic fracturing simulations in Case A1 and A2, respectively. The closed circle indicates a location of tensile crack and the open circle indicates that of shear crack. The diameter of the circle corresponds to respective magnitude of energy obtained by equation (2.14). The fracture path is almost the same for both cases. However, tendency of the microcrack generation is different due to the difference of fluid viscosity.

(a) Case A1 (Heterogeneous, Low viscosity)

(b) Case A2 (Heterogeneous, High viscosity)

Fig.5.17   Crack types and magnitude of energy emitted from the cracks in Case A1 and A2 (Heterogeneous model). The diameter of the circle corresponds to the magnitude of crack energy.

As shown in Fig.5.17(a), when the low viscous fluid was used, the energy emitted from the shear crack is larger than that from the tensile crack. This result agrees well with the fact proved in theory [29].

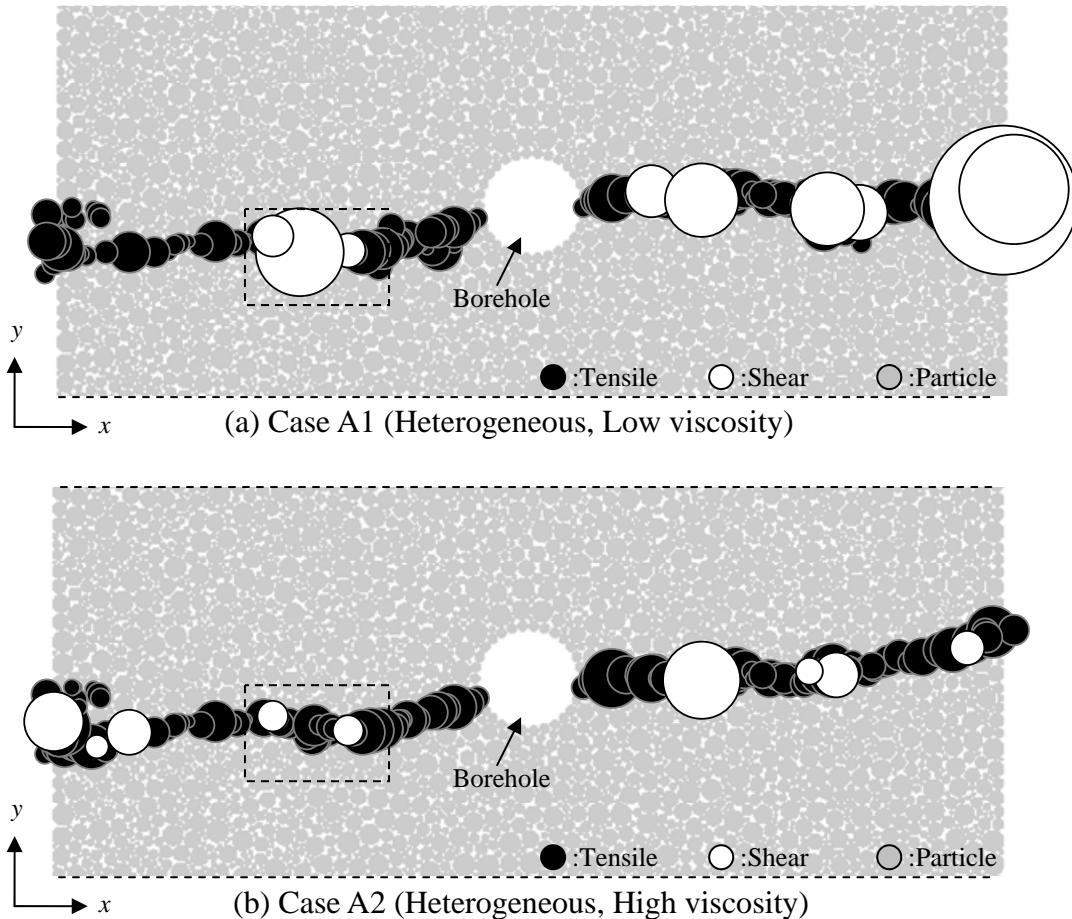When the low viscous fluid was used, shear cracks emitting significantly large energy were generated in the region enclosed by a dotted line square in Fig.5.17(a). On the other hand, when the high viscous fluid was used, the energy emitted from the shear crack is relatively small as shown in Fig.5.17(b), and such a shear crack emitting large energy did not generated at the same position (see dotted line square in Fig.5.17(b)) even though the same rock model was used. This result is caused by the difference of the fracturing process due to the difference of fluid viscosity.

Fig.5.18(a) illustrates a close-up view of the fracture propagation and fluid infiltration behavior in Case A1. Tensile and shear cracks are expressed as thick solid lines and open ellipses respectively. As shown in Fig.5.18(a), when low viscous fluid was used, the fracture propagated in the direction of maximum compressive stress and the fluid was infiltrated into the fracture instantaneously. At this time, fracture is mainly formed by tensile microcracks. However, when a large particle exists on the course of the fracture growth, propagation of the fracture is obstructed and the fluid pressure was applied throughout the fracture surface. Beyond the obstructing particle, tensile cracks are generated in front of the fracture tip due to the fluid pressure acting on the fracture surface because the tensile strength of bond is obviously small compared with the shear strength. Finally, when the fluid pressure acting on the fracture tip sufficiently increase, shear cracks emitting significantly large energy are formed to connect these tensile cracks. This fracturing process is similar to the Hill's model which is originally proposed for volcanic earth quake swarms [30].

On the other hand, Fig.5.18(b) illustrates a close-up view of the fracture propagation and fluid infiltration behavior in Case A2. When high viscous fluid was used, only the fracture propagated first. At this time, microcrack geometry is similar to that in Case A1. However, fracturing fluid can not infiltrate into the fracture because the fluid viscosity is high. Therefore, fluid pressure was applied the borehole and only a part of the fracture surface. In this research, the microscopic parameters given to the bonds between particles, such as Young's modulus and strength, are constant. However, since the stiffness of the bonding springs and the stress acting on the bonds are given as a function of the particle radius by equation (2.9) - (2.13), the strain energy given by equation (2.14) becomes the function of the particle radius.

Maximum compressive stress

Maximum compressive stress

Fluid pressure (MPa)
0.0   30.0
———— :Tensile
⬯ :Shear

Fluid pressure (MPa)
0.0   30.0
———— :Tensile
⬯ :Shear

(a) Case A1
(Heterogeneous, Low viscosity)

(b) Case A2
(Heterogeneous, High viscosity)

Fig.5.18   Close-up view of the fracture propagation and fluid infiltration behavior.

Hence, the local strength of rock model and energy emitted along with microcrack generation are irregularly distributed according to the distribution of the particle radius of the rock model. The microcracks are likely to be generated between small particles and the energy emitted from such microcracks become small. Therefore, as borehole pressure increases, a number of microcracks are generated between small particles without fluid infiltration. When these microcracks are connected and one straight fracture is formed, fracture width gradually increases due to the borehole pressure. Finally, high viscous fluid infiltrate into the existing fracture when the fracture width sufficiently increased. As a result, the fracture becomes thick planar with few branches when high viscous fluid was used, and the shear crack emitting large energy observed in Case A1 was not generated in Case A2.

Fig.5.18(b) indicates that the macroscopic fracture is mainly formed by tensile cracks. However, a few shear cracks are generated even when high viscous fluid was used and the fracturing fluid did not infiltrated into the fracture. The macroscopic fracture seems to develop straight. However, individual microcracks are generated in various directions along the direction of the particle boundary. When the particle boundary located diagonally across the direction of maximum confining stress, confining stress and borehole pressure act on the particle boundary as shear stress. Hence, the shear cracks were generated along the grain boundaries that diagonally across the direction of maximum confining stress.

According to the microscopic observation in laboratory experiments [6,7], hydraulic fracture mainly located at the grain boundary. They also pointed out that the fracture induced by high viscous oil injection could be observed very clearly because of their large widths, whereas fracture induced by low viscous water injection could only be detected after careful and close observation because they were extremely thin. In addition, high viscous oil tends to generate thick planar fracture with few branches, while low viscous water tends to generate thin and wavelike cracks with many secondary branches. By considering the particles in DEM as the mineral grains, the fracture propagation process in the DEM simulations mentioned above give the rational explanation for the hydraulic fracturing behavior observed in the experiment.

As shown in Table 5.3, tensile cracks were dominant in all cases though a few shear cracks were generated. This result is not in agreement with the result obtained from the laboratory AE measurement experiments conducted by Ishida *et al*. [6]. Recorded AE waveforms in their hydraulic fracturing experiment indicate that the shear type fracturing seemed to be dominant in slick water injection and both tensile and shear AE are recorded in viscous oil injection. This disagreement between the results obtained

from the simulation and experiment can be explained by considering the energy of microcracks.

When low viscous fluid is used as the fracturing fluid, low viscous fluid can easily infiltrate into the pores, defects and generated microcracks, and the fracture windles according to the boundary of the mineral grain. When the fluid pressure acting on the fracture tip increase sufficiently, shear cracks that emit large energy are formed to connect pre-existing microcracks. Since the tensile strength of rock is obviously small compared with the compressive strength, the energy emitted from a tensile crack is small compared with that from a shear crack. Such a small AE is easily buried in a noise and hard to be measured in the experiments. In fact, several hundreds of AE sources were located during hydraulic fracturing conducted by Ishida *et al*. However, only a few percent of the located AE events showed clearly the first motions of the P-wave and are possible to obtain reliable mechanism solutions. Hence, only for about five events in each specimen, their fracturing mechanisms could be examined based on the polarities of P-wave first motions [6,10]. Therefore, the shear type AE with large energy is dominantly observed in AE measurement experiments.

On the other hand, when the high viscous fluid is used, fracturing fluid cannot infiltrated into the microcracks, and one straight fracture is formed according to the stress state in the rock due to the increase in the borehole pressure. Although the fracture is mainly formed by tensile cracks, a few shear cracks are generated along the grain boundaries that diagonally across the direction of maximum confining stress. The fracturing fluid will infiltrate along existing straight fracture after enough opening of the fracture due to the borehole pressure. However, the energy emitted from these shear cracks are not so large as shown in Fig.5.17(b) because such microcracks are mainly generated between small particles. Therefore, very few shear cracks emitting large energy observed when the high viscous fluid is used. In addition, when the high viscous fluid is infiltrated into the fracture, fluid pressure becomes very high. Thus, in an actual hydraulic fracturing, highly pressurized fluid causes large fracture opening, and tensile AE with large energy may be generated. Therefore, both tensile and shear AE can be observed during the injection of high viscous fluid in an actual AE monitoring.

5.7.2 Hydraulic fracturing in homogeneous model

Fig.5.19(a) and (b) show the spatial distribution of all the microcracks generated during the hydraulic fracturing simulation in Case B1 and B2, respectively. The energy emitted from the microcrack generation in Model B is relatively small compared with that in Model A as shown in Fig.5.17.

As mentioned in the section 5.7.1, the local strength of rock model and energy emitted along with microcrack generation are irregularly distributed according to the distribution of the particle radius of the rock model. Microcracks are hardly to be generated between large particles and the energy emitted from such microcrack become large. For this reason, the energy emitted from the microcrack generation in Model B consisting of small particles is relatively small compared with that in Model A including many large particles. This tendency agree well with the results of the uniaxial experiments conducted by Eberhardt [31] and the results of laboratory hydraulic fracturing experiment conducted by Ishida *et al.* [10]. Their experimental results showed that the number of detected AE events decreases markedly with decreasing grain size.

(a) Case B1 (Homogeneous, Low viscosity)

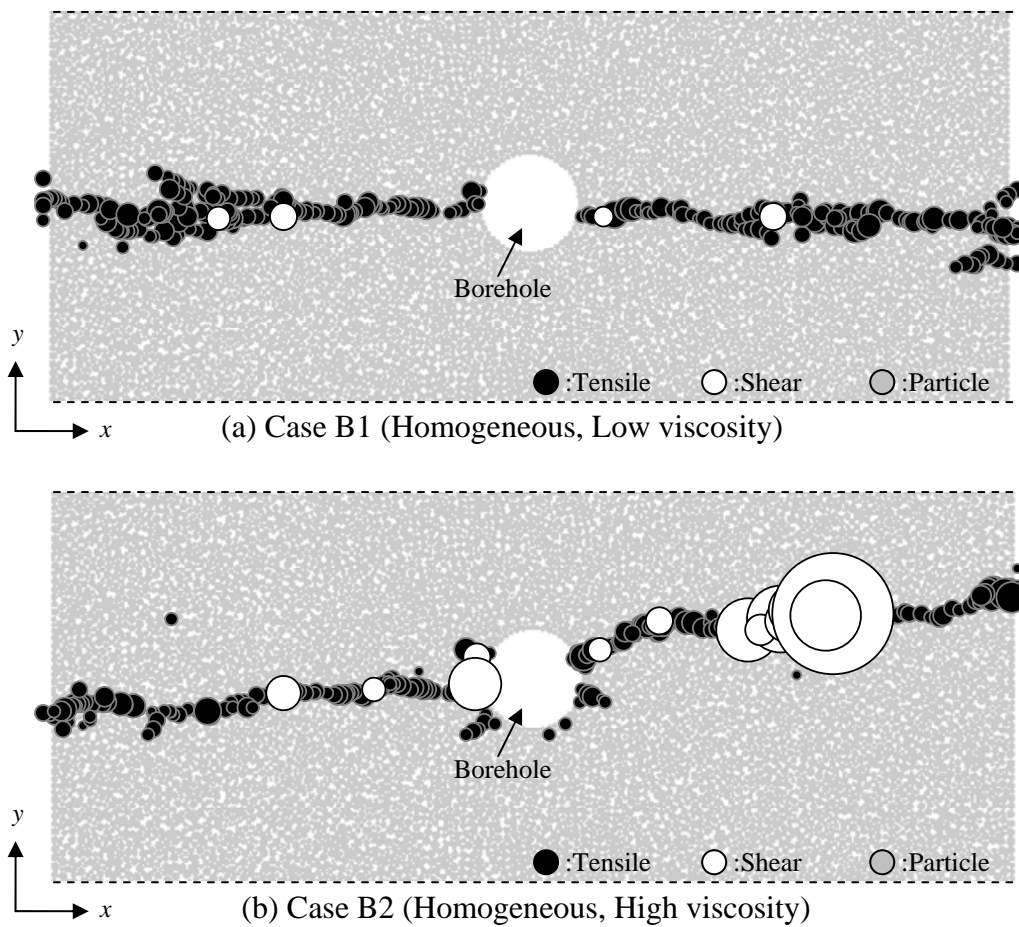
(b) Case B2 (Homogeneous, High viscosity)

Fig.5.19   Crack types and magnitude of energy emitted from the cracks in Case B1 and B2 (Homogeneous model). The diameter of the circle corresponds to the magnitude of crack energy.

By comparing Fig.5.19(a) with (b), many small branching cracks were generated when the low viscosity fluid was used. On the other hand, when the high viscosity fluid was used, such a branching crack was not generated. This result supports the consideration related to the influence of the viscosity of the fracturing fluid discussed in the previous section.

As shown in Fig.5.19(a), only a few shear cracks were generated in Case B1 (Homogeneous, Low viscosity). Percentage of shear crack generation in Case B1 is smallest, 1.5%. This tendency agrees with the experimental results. The fault plane solutions of AE implied shear type fracturing in the specimens with large grain, while they implied tensile fracturing in the specimen with small grain [7,10]. In addition, in hydraulic fracturing in an acrylic resin block, all recorded AE events indicated tensile fracturing mechanisms [7]. The acrylic resin is impermeable and could be considered to be an extremely homogeneous material. These results clearly indicate that, with decreasing grain size, the dominant micro fracturing mechanism becomes tensile rather than shear. This result can be explained by particle size distribution of the model. As mentioned in the previous section, when the particle radius is widely distributed and relatively large particles are contained in the rock model, shear cracks generated along the grain boundaries that diagonally across the direction of maximum confining stress. On the other hand, when all particles in the rock model are small, the hydraulic fracture can develop straight in the direction of the maximum confining stress. Therefore, shear cracks which emit large energy are hardly to be generated in homogeneous rock model as shown in Fig.5.19(a).

However, as shown in Fig.5.19(b), when high viscous fluid was used, many shear cracks that emit large energy were generated even though homogeneous model (Model B) was used. Fig.5.20 shows a close-up view of the time-space distribution of cracks generated in Case B2 (Homogeneous, High viscosity) from time step 807 to 811 ($\times 10^5$). As shown in Fig.5.20, the fracture does not develop smoothly but develops stepwise, and such stepwise development of the fracture may be lead by the generation of shear cracks. Moreover, as indicated in the region enclosed with dotted circle in Fig.5.20, the shear cracks that emit significantly large energy generated when the fluid was injected into the fracture after the fracture development.

In the actual AE measurement during hydraulic fracturing using low viscous water and high viscous oil injection, AE events spread from the hole throughout the specimen, within short periods corresponding to the respective pressure drops. In particular, when the fracturing fluid is not allowed to penetrate the fracture, AE sources spread stepwise [6]. The DEM simulation results are well in agreement with these AE behaviors. The

macroscopic fracture seems to be straight. However, the fracture is microscopically winded due to the particle arrangement even when homogeneous model is used. When the fracture grows diagonally across the direction of maximum confining stress, the higher fluid pressure is required to extend the fracture because a part of the confining stress and the borehole pressure act on the fracture tip as the shear stress. Thus, the fracture develops stepwise accompanied with the shear crack generation, and the breakdown pressure in Case B2 was remarkably higher than that for other cases as shown in Table 5.3.

Since the fracture is microscopically winded due to the particle arrangement, there exists the region where fracture width was narrowed locally. Therefore, when the highly pressurized fracturing fluid is infiltrated into the fracture, extremely large pressure suddenly acts on such region and many new microcracks including the shear crack generated due to the impact of fluid infiltration as shown in the dotted circle in Fig.5.20. However, such shear cracks that emitted significantly large energy was not seen in Case A2 though the highly viscous fluid was used. This is because the particle number of Model A is about 1/3 of the particle numbers of Model B, and the region where fracture width was narrowed partially as mentioned above did not appear since the number of particles is small. Therefore, the phenomenon similar to Case B1 possibly occurs when the model A with different particle arrangement is used. Since these shear cracks emit significantly large energy, AE that occurs from such large shear cracks would be observed even in field scale AE measurement as reported by Baria *et al*. [2] and Talebi *et al*. [3]. To validate this phenomenon, more detailed analysis, such as field scale simulation, would be required.
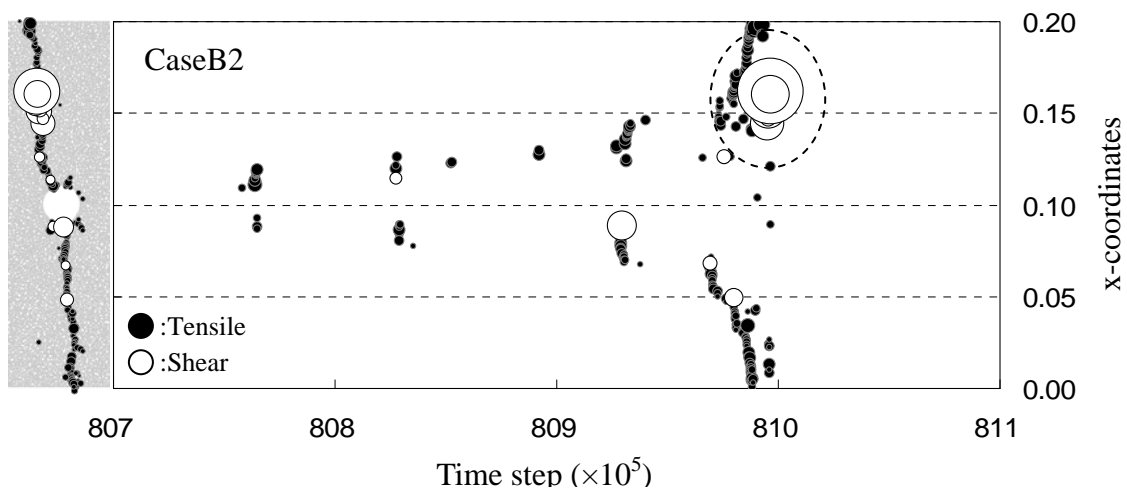

Fig.5.20   Time-space distribution of cracks generated in Case B2 (Homogeneous, High viscosity). Close-up view of the time step 807 to 811 ($\times 10^5$).

5.8. Conclusion

A series of simulations for hydraulic fracturing in hard rock was performed by using the flow-coupled DEM code to discuss the influence of the fluid viscosity and the particle size distribution. The simulation results show good agreement with the actual experimental results including the AE measurement data. The findings obtained from this study are summarized as follows.

1. For all cases, the orientation of hydraulic fractures is parallel to the direction of maximum compressive principal stress. This result indicates that the effect of the confining stress was appropriately expressed in the DEM simulations.

2. When the low viscous fluid was used, crack initiation pressure and breakdown pressure were lower than those for high viscous fluid. When the low viscous fluid was used, fracturing fluid easily penetrates through the interconnected pores into a rock from borehole wall. The fluid penetration causes pore pressure increase around the borehole. Such an increase in pore pressure reduces the effective stress around the borehole, and makes it easy to generate tensile cracks. In an actual hydraulic fracturing experiment, it is difficult to observe the infiltration behavior of fluid and change of effective stress distribution due to the fluid injection directly. On the contrary, the effect of fluid infiltration into the tensile rupture of permeable rock can be successfully reproduced by the DEM.

3. When the low viscous fluid is used, the fluid is infiltrated into the fracture instantaneously and the fluid pressure was applied throughout the fracture surface. Hence, once it grows, fracture never stops because the stress intensity factor at the fracture tip monotonically increases with crack length. On the other hand, when the high viscous fluid is used, fluid pressure was applied only a part of the fracture surface. Therefore, the fracture never extends without an additional pressure. For this reason, when the high viscous fluid was used, breakdown pressure was markedly higher than that with low viscous fluid.

4. Although most of cracks in all cases were tensile cracks as theoretically expected, a few shear cracks are generated during the fracture propagation. When the fluid pressure acting on the fracture tip increase sufficiently, shear cracks that emit significantly large energy are formed to connect these tensile cracks. This fracturing process is similar to the Hill's model originally proposed for volcanic earth quake

swarms. In addition, shear cracks are also generated even when the fracturing fluid did not infiltrated into the fracture due to the following reason. Although the macroscopic fracture seems to develop straight, individual microcracks are generated in various directions along the direction of the particle (grain) boundary. When the particle boundary located diagonally across the direction of maximum confining stress, confining stress and borehole pressure act on the particle boundary as shear stress. Thus, shear cracks generated along the grain boundaries that diagonally across the direction of maximum confining stress.

5. Although the tensile cracks are dominantly generated in the simulation, the energy released from a tensile crack becomes small because the tensile strength of rock is obviously small compared with the compressive strength. Such a small AE is easily buried in a noise and hard to be measured in an experiment. Therefore, in AE measurement experiments, shear type of AE with large energy is dominantly observed.

References

[1] Hubbert MK and Willis DG. Mechanics of hydraulic fracturing. Trans AIME, 1957; 210: 153-166.

[2] Baria R and Green ASP. Seismicity induced during a viscous stimulation at the Camborne School of Mines Hot Dry Rock geothermal project in Cornwall, England. Proc Progress in Acoustic Emission III, Japanese Soc NDI; 407-429.

[3] Talebi S and Cornet FH. Analysis of the microseismicity induced by a fluid.injection in a granitic rock mass. Geophys Res Lett, 1987; 14(3): 227-230.

[4] Falls SD, Young RP, Carlson SR and Chow T. Ultrasonic tomography and acoustic emission in hydraulically fractured Lac du Bonnet grey granite. J Geophys Res, 1992; 97(B5): 6867-6884.

[5] Urbancic TI, Shumila V, Rutledge JT and Zinno RJ. Determining hydraulic fracture behavior using microseismicity. Proc 37th US Rock Mech Symp, 1999: 991-997.

[6] Ishida T, Chen Q, Mizuta Y and Roegiers JC. Influence of fluid viscosity on the hydraulic fracturing mechanism. Transactions of the ASME, Journal of Energy Resource Technology, 2004; 126: 190-200.

[7] Matsunaga I, Kobayashi H, Sasaki S and Ishida T. Studying hydraulic fracturing mechanism by laboratory experiments with acoustic emission monitoring. Int J Rock Mech Min Sci Geomech Abstr, 1993; 30(7): 909-912.

[8] Ishida T, Mizuta Y, Matsunaga I, Sasaki S and Chen Q. Effect of grain size in granitic rock on crack extension in hydraulic fracturing. Proc. of 4th North American Rock Mechanics Symposium, Seattle, 2000; 1105-1111.

[9] Ishida T, Sasaki S, Matsunaga I, Chen Q and Mizuta Y. Effect of grain size in granitic rocks on hydraulic fracturing mechanism. Trends in Rock Mechanics (Proc. of Sessions of Geo-Denver 2000), Geotechnical Special Publication, 2000; 102, ASCE: 128-139.

[10] Ishida T. Acoustic emission monitoring of hydraulic fracturing in laboratory and field. Construction and Building Materials, 2001; 15: 283-295.

[11] Shah KR, Carter BJ and Ingraffea AR. Hydraulic fracturing simulation in a parallel computing environment. Int J Rock mech Min Sci, 1997; 34(3-4): Paper No.282.

[12] Vandamme L and Curran JH. A threedimensional hydraulic fracturing simulator. Int J Numer Methods Eng, 1989; 28: 909-27.

[13] Al-Busaidi A, Hazzard JF and Young RP. Distinct element modeling of hydraulically fractured Lac du Bonnet granite. J Geophys Res, 2005; 110(B6): B06302.

[14] Kiyama H, Nishimura T and Fujimura H. An advanced distinct element model coupling with pore water. J Geotech Eng, 1994; 499(III-28): 31-39.

[15] Bruno MS. Micromechanics of stress-induced permeability anisotropy and damage in sedimentary rock. Mechanics of Materials, 1994; 18: 31-48.

[16] Thallak S, Rothenburg L and Dusseault M. Simulation of multiple hydraulic fractures in a discrete element system. Proc 32nd US Symposium on Rock Mechanics, 1991; 271-280.

[17] Zoback MD, Rummel F, Jung R and Raleigh CB. Laboratory hydraulic fracturing experiments in intact and pre-fractured rock. Int J Rock Mech Min Sci Geomech Abstr, 1977; 14: 49-58.

[18] Zhao Z, Kim H and Haimson B. Hydraulic fracturing initiation in granite. Proc of the 2nd North American Rock Mech Symp, 1996; 1231-1235.

[19] Schmitt DR and Zoback MD. Infiltration effects in the tensile rupture of thin walled cylinders of glass and granite: Implications for the hydraulic fracturing breakdown equation. Int J Rock Mech Min Sci, 1993; 30(3): 289-303.

[20] Haimson BC. Hydraulic fracturing in porous and nonporous rock and its potential for determining in-situ stresses at great depth. Ph.D thesis, University of Minnesota, 1968.

[21] Haimson BC and Fairhurst C. Initiation and Extension of Hydraulic Fracture in

Rocks. Soc Petr Engrs J, 1967; 310-318.

[22] Ito T. Effect of pore pressure gradient on fracture initiation in fluid saturated porous media: Rock. Engineering Fracture Mechanics, 2008; 75(7): 1753-1762.

[23] Ito T and Hayashi K. Physical background to the breakdown pressure in hydraulic fracturing tectonic stress measurements. Int J Rock Mech Min Sci, 1991; 28(4): 285-293.

[24] Zoback MD and Pollard DD. Hydraulic fracture propagation and the interpretation of pressure time records for in-situ stress determination. Proc. 19th US Rock Mech Symp, 1978; 19th: 14-22.

[25] Potyondy DO and Cundall PA. A bonded- particle model for rock. Int J Rock Mech Min Sci, 2004; 41: 1329-1364.

[26] Huang H. Discrete element modeling of tool-rock interaction. Ph.D thesis, University of Minnesota, 1999.

[27] Moon T, Nakagawa M and Berger J. Measurement of fracture toughness using the distinct element method. Int J Rock Mech Min Sci, 2007; 44: 449-456.

[28] Newman JC. An improved method of collocation for the stress analysis of cracked plates with various shaped boundaries. NASA tech Note, 1971: D-6373.

[29] Hayashi K, Motegi S. Characteristics of Energy of Elastic Waves Due to Sudden Growth of Subsurface Reservoir Cracks for Geothermal Heat Extraction. Progress in Acoustic Emission IV, NDI Japan, 1988; 265-272.

[30] Hill D. A model for earthquake swarms. J Geophys Res, 1977; 82: 1347-1352.

[31] Eberhardt E, Stimpson B and Stead D. Effect of grain size on the initiation and propagation thresholds of stress-induced brittle fractures. Rock Mech and Rock Eng, 1999; 32(2): 81-99.

Chapter 6
The distinct element analysis
for hydraulic fracturing in unconsolidated sands

6.1. Introduction

The methane hydrate is expected as a new energy resource that takes the place of oil and gas [1]. The hydraulic fracturing is expected as an effective technique to stimulate and produce the methane hydrate [2].

A considerable amount of theoretical and experimental research has been carried out in the past few decades to better understand the mechanics of hydraulic fracturing. These works are mainly assuming the hydraulic fracturing in consolidated hard rock, such as sandstone and granite.

However, the methane hydrate mainly exists in an unconsolidated sedimentary layer under a sea bottom, and it takes neither a form of gas nor liquid but ice-like solid. There are only a few reports that investigate the hydraulic fracturing mechanism in unconsolidated sands [3-7], and it is unclear whether fracture-like structure is formed or not by high fluid pressure applied to the sediments in hydraulic fracturing procedure. To clarify the hydraulic fracturing behavior in unconsolidated sands, and to design it effectively, a new approach different from the past theoretical model for the consolidated rock is required.

Therefore, Igarashi *et al*. performed the laboratory hydraulic fracturing experiment under true triaxial compression with unconsolidated sand specimen, and discussed the hydraulic fracturing behavior [8,9]. As a result, it is found that the hydraulic fracturing behavior is strongly affected by the viscosity of fracturing fluid, the pressurization rate and the permeability of the specimen. However, the detail of the mechanism that causes such hydraulic fracturing behavior has not been sufficiently clarified.

In this research, a new DEM code applicable to unconsolidated sand was developed, and the mechanism of the hydraulic fracturing in the unconsolidated sands was discussed in detail by simulating the hydraulic fracturing. As a result, the suggestion that gave the rational explanation to the hydraulic fracturing behavior observed in the existing laboratory experiment was found.

6.2. Outline of the experimental study

6.2.1 Unconsolidated sand specimen and experimental set up

Fig.6.1 shows the photograph of the specimen used for the hydraulic fracturing experiment that was conducted by Igarashi *et al*. [8,9]. The cubic specimen (200mm×200mm×200mm) is made from a mixture of a small amount of kaolin with the quartz sand, and a cube of 200mm in width. By adding small quantity of water, the specimen can keep shape without confining pressure. The water content has been adjusted to 10%.

A casing pipe has been inserted in the center of the specimen. This casing pipe corresponds to the casing in an actual wellbore and prevents the borehole from collapsing in the compressive stress field. The casing pipe is a stainless steel pipe whose length is 220mm, internal diameter is φ20mm and 2mm in the thickness. A rectangular slit of 0.5mm in width and 40mm in length is installed at the center of the casing. The fracturing fluid flows throughout this slit. Since the slit is a long rectangle parallel to the casing axis, the fluid pressure distribution around the casing becomes two-dimensional and the breakdown phenomena can be simplified.
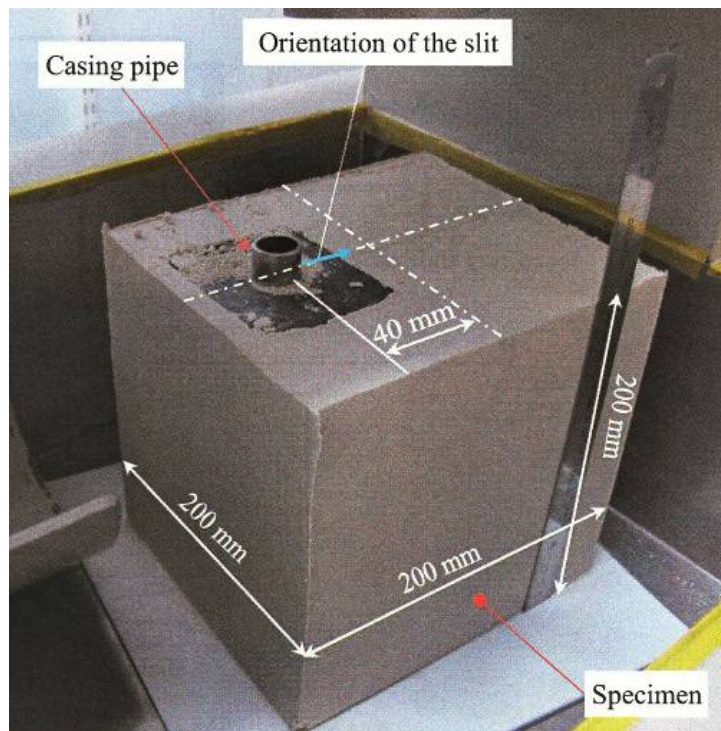
Fig.6.1   Unconsolidated sand specimen [8,9].

122

Jack type true triaxial compression test apparatus was used for the experiment. As shown in Fig.6.2, compressive stress of 3.0MPa is vertically loaded and 2.0MPa, 3.0MPa is horizontally loaded into the specimen as a tectonic stress. The casing has been inserted 40mm offset from the center of the specimen to prevent the piston of hydraulic jack and the casing from interfering. Moreover, it is expected that the fracture develops in the direction of the maximum compressive stress from the position of the slit during the hydraulic fracturing. Therefore, the position of the casing was moved in the direction of the maximum compressive stress, and the slit was located in the opposite direction to the moving direction of casing. The region where the fracture develops can be enlarged by this operation.
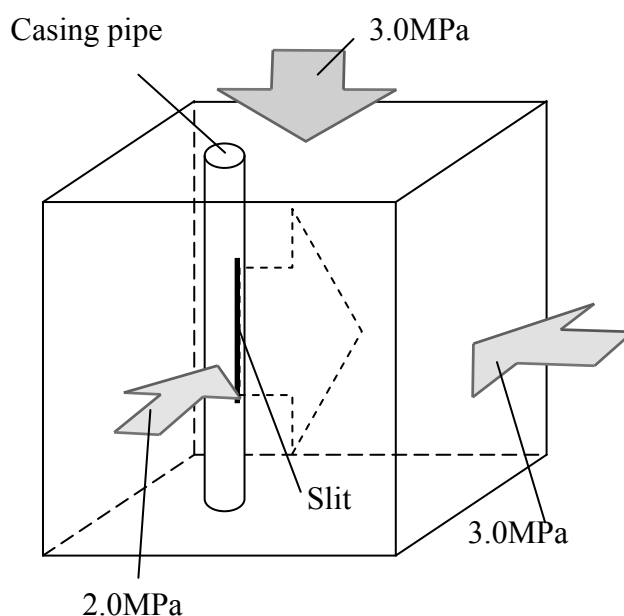
Fig.6.2   Loading condition for the experiment [8,9].

6.2.2 Summary of the experimental results

The hydraulic fracturing experiment that Igarashi *et al.* had conducted revealed that the hydraulic fracturing behavior is strongly affected by the viscosity of fracturing fluid, the pressurization rate and the permeability of the specimen. Fig.6.3 illustrates the five typical fracture growth patterns observed in the hydraulic fracturing experiment with unconsolidated sands. In this experiment, red dyestuff was added to the fracturing fluid to color the sand particle in the region where the fracturing fluid flows. The region where the fracturing fluid flows and the fracture growth pattern can be observed from the color of the sand particle. Each fracture growth pattern has following features [8,9].

(a) No Fracture (NF): The fracturing fluid widely infiltrates into the specimen, and no clear fracture occurred.

(b) Shear Fracture (SF): The small fractures with the length of the borehole radius occur in the direction of the diagonal direction to the maximum horizontal stress.

(c) Cavity Expansion (CE): The fracturing fluid infiltrated into the specimen, and forms a large cave in front of the slit.

(d) Linear Fracture (LF): A single and straight fracture grew from the slit in the direction of maximum horizontal stress.

(e) Branched Fracture (BF): A branched and curved fracture grew from the slit in the direction of maximum horizontal stress.

These classifications were applied to the results obtained from the experiment, and the classification results were summarized in Table 6.1. Moreover, the followings were investigated from the experimental result [8,9].

- The permeability of the specimen remarkably influences the change in the fracture growth patterns.
- In case of that the fracture is formed, the maximum fluid pressure (breakdown pressure) increases with the permeability, the viscosity, and the pressurization rate.
- In case of Linear Fracture, although borehole pressure decreases rapidly after it becomes a peak, the decreasing rate gradually becomes low and the fluid pressure becomes an equilibrium state.
- The breakdown pressure is highest in case of Cavity Expansion.

124
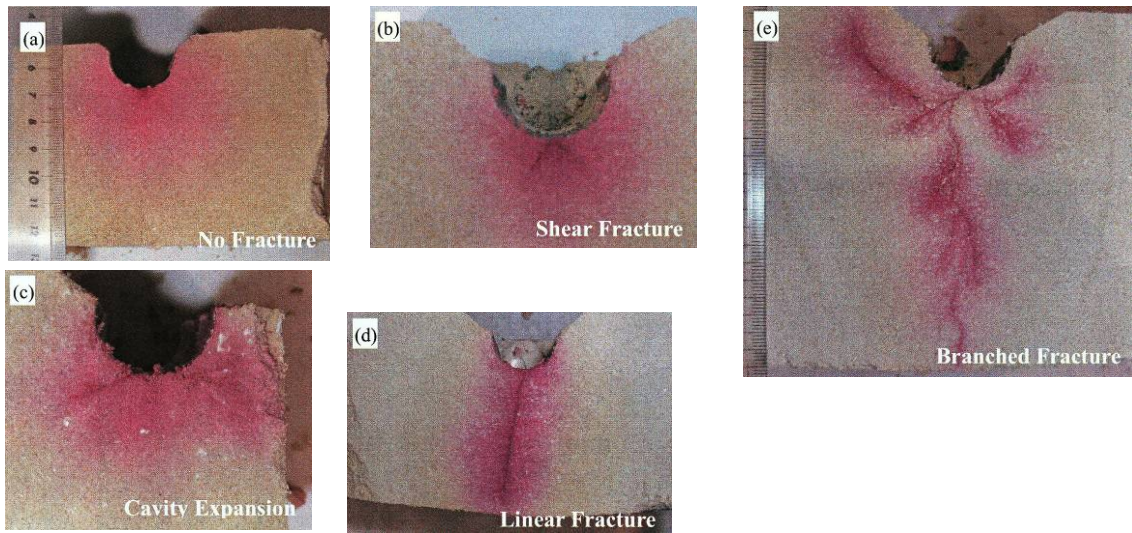
Fig.6.3 Various fracture shapes observed in the hydraulic fracturing experiments [8,9].

Table 6.1 Classification of fracture shapes [8,9].

Permeability [mD]	Flow rate [mL/min]	Viscosity [mPa·s]			
		300	500	900	1700
32	30	NF	-	-	-
	100	-	SF	-	CE
16	30	SF	-	CE	CE
	100	SF	-	-	BF
5	10	LF	-	-	-
	30	LF	-	-	LF
	100	BF	-	BF	BF/LF

6.3. Unconsolidated sands model

6.3.1 Feature of the unconsolidated sands

Though the DEM is the one of the discontinuum based numerical techniques, it can be applied also to the continuum by introducing bonds between particles.

Fig.6.4 shows demonstrations of DEM simulation using three kinds of models with different connection method of particle. Each model was dropped to the rigid wall.

Fig.6.4(a) shows the simplest model that does not use the bonding. Since the particles are not bonded each other, each particle moves individually and freely. Thus, the model collapses completely when the model comes in contact with the rigid wall.

Fig.6.4(b) show a consolidated hard rock model in which each particles are bonded with three kinds of springs, such as the normal spring, the shear spring, and the rotational spring [10-12]. In this case, although a fracture formed and the model divided into two pieces, the rock model remains its shape.

On the other hand, the unconsolidated sands specimen used in the hydraulic fracturing experiment that was conducted by Igarashi *et al*. contains the small quantity of water and have a little intergranular cohesion forces. The force is so small that the unconsolidated sands specimen can be easily deformed [8,9]. Therefore, the models showed in Fig.6.4(a) and Fig.6.4(b) cannot be applied to the unconsolidated sands. Then, to represent such character of the unconsolidated sands, the intergranular cohesion forces are represented by connecting the DEM particles with one spring in the unconsolidated sand model.

The strength of the springs used in the unconsolidated sand model is very small, and the springs can break easily. However, the connecting spring reproduces when the particle comes in contact. Thus, the unconsolidated sand model shows flexible behavior compared with the rock model as shown in Fig.6.4(c). The unconsolidated sand model can deform easily with repeating the disappearance and the reproduction of the interparticle cohesion forces.

Since the three-dimensional analysis needs huge computing time and the interpretation of the simulation results becomes significantly complex, simple two-dimensional models are used. Details of the algorithm of the unconsolidated sand model are described as follows. In this chapter, compressive stress and strain are expressed as positive.

0.0016sec 0.0319sec 0.0639sec 0.0958sec

(a) Unbonded model

0.0016sec 0.2746sec 0.2954sec 0.6387sec
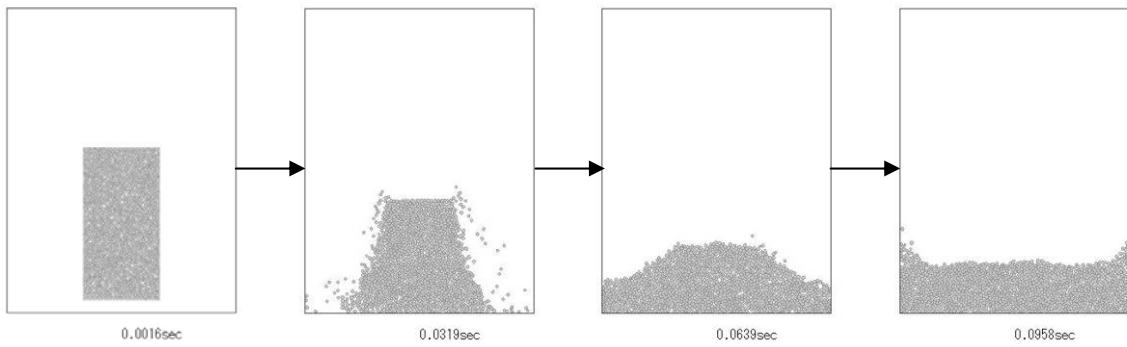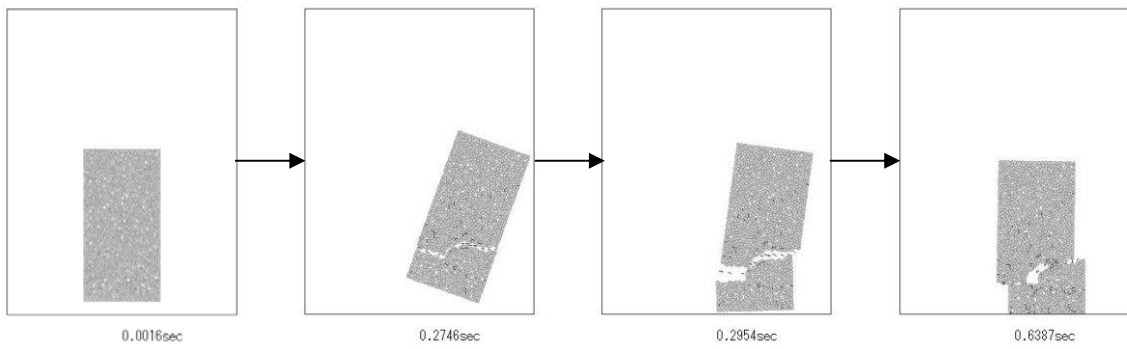
(b) Consolidated rock model

0.0016sec 0.0319sec 0.0639sec 0.0958sec
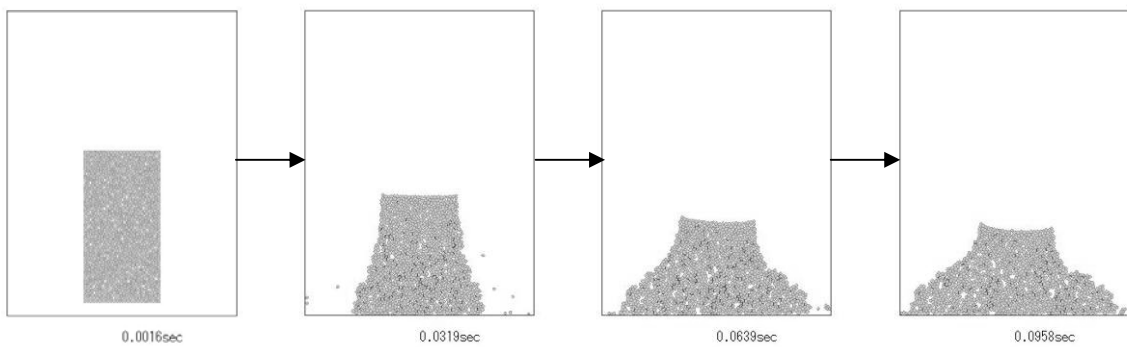
(c) Unconsolidated sand model

Fig.6.4   Fracturing behavior of three kinds of models.

6.3.2 Bonded particle model for unconsolidated sands

In the unconsolidated sand model, the intergranular cohesion forces are represented by connecting the DEM particles with one spring as shown in Fig.6.5, and the connecting spring reproduces when the particle comes in contact. The tensile force f_a acting between the particles is calculated as follows.

$$f_a = \begin{cases} k_a \cdot \{L - (r_i + r_j)\} & (0 < \varepsilon < \varepsilon_{max}) \\ 0 & (\varepsilon_{max} \le \varepsilon) \end{cases} \tag{6.1}$$

where, k_a and L are stiffness of the spring and distance between the centers of the bonded particles, respectively; r_i and r_j are the radii of the bonded particles. Fig.6.6 shows the relationship between the tensile force f_a and the strain ε of the spring given by the following equation.

$$\varepsilon = \frac{L - (r_i + r_j)}{r_i + r_j} \tag{6.2}$$
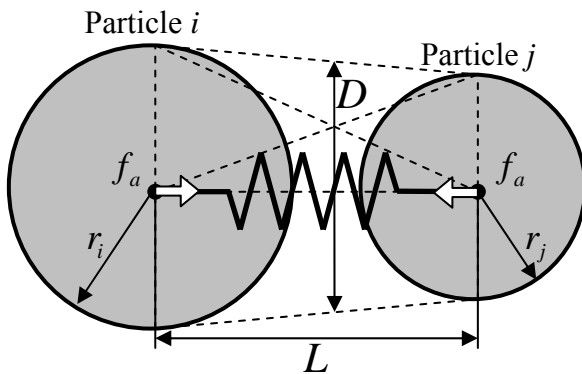
Fig.6.5   Bonded particles model for the unconsolidated sand.
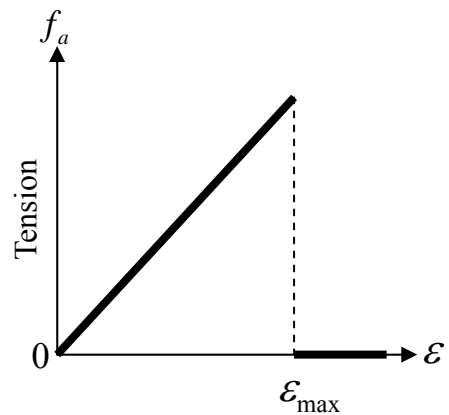
Fig.6.6   Relationship between tensile force and strain of the spring.

128

As shown in Fig.6.6, when the strain ε of the spring exceeds maximum value ε_{max}, the spring is broken. The break of the springs is considered as the generation of microcrack. After break of the spring, tensile force does not act until the particle comes in contact again and the connecting spring reproduces.

The contact damping represented by a dashpot operates on the relative velocities. The coefficients of viscous contact damping C_a are determined to provide critical viscous damping and given by

$$C_a = 2\sqrt{m_{ij} \cdot k_a} \tag{6.3}$$

where, m_{ij} is given by the weight of two particles m_i and m_j.

$$m_{ij} = 2\frac{m_i m_j}{m_i + m_j} \tag{6.4}$$

The stress σ acting between the particles is given by

$$\sigma = \frac{f_a}{D} \tag{6.5}$$

where, D is the bond diameter, and obtained from harmonic mean of the radius of two particles as follows.

$$D = 2 \cdot \frac{2r_i r_j}{r_i + r_j} \tag{6.6}$$

The stiffness of the spring k_a is calculated by the maximum tensile stress (tensile strength) σ_{max} and the maximum strain ε_{max}, and given by the following equation.

$$k_a = \frac{\sigma_{max}}{\varepsilon_{max}} \tag{6.7}$$

Thus, the microscopic parameters required to determine the connection of the interparticle is tensile strength σ_{max} and the maximum strain ε_{max} of the interparticle connection spring.

As shown in Fig.6.7, when the unbonded particles or particles with bond breakage are in contact each other, springs and dashpots are introduced into the contact points in both normal and tangential directions, and compressive normal force f_n and tangential (frictional) force f_s act at the contact points. As mentioned above, even after the spring breaks, the connecting spring reproduces when the particle comes in contact.

6.4. Simulation condition

6.4.1 Calibration - biaxial compression test and permeability test

The preliminary simulations of the biaxial compression tests using the unconsolidated sand model were performed to calibrate the microscopic parameters. The macroscopic mechanical properties, such as Young's modulus, friction angle and cohesion of the unconsolidated sand model, are adjusted to those of an actual unconsolidated sands specimen.

Fig.6.8 shows the unconsolidated sand model and the loading condition for the simulation of biaxial compression tests. The unconsolidated sand model of 10cm in width and 20cm in height was used. The casing pipe is not inserted in this model. The model is surrounded by the four confining walls. The left and the right walls can move to keep the confining pressure constant. The platen under the model was fixed and the upper loading platen was moved downward slowly at a certain displacement rate to simulate the biaxial compression tests. Frictional force has not acted between the model and the confining walls to avoid unnecessary frictional stress concentration.
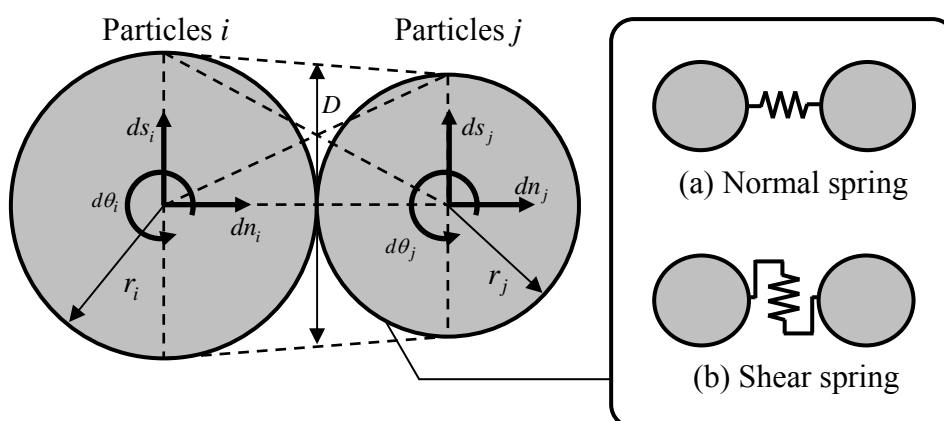
Fig.6.7   Mechanical behavior at the contact point.

The axial stress applied to the rock model during the compression test was calculated from total force acting on the upper loading platen from particles and model width. The strain is calculated by displacements of the four monitored particles as shown in Fig.6.8. The biaxial compression test was performed by two kinds of confining pressures of 3MPa and 6MPa.

Fig.6.9 shows the distribution of microcracks generated in the simulation with confining pressure 3MPa. Microcracks are expressed by solid lines. Fig.6.10 shows the stress-strain curves, and Fig.6.11 shows the Mohr's circle obtained from the simulation. The friction angle and cohesion of the model can be obtained from these figures.

The permeability of the model is adjusted by simulating the permeability test. As mentioned in section 5.2.1, the permeability of the entire rock model is determined by calibrating the assumed initial aperture w_0. Hydraulic pressure P_{in} and P_{out} at both ends of the model was assumed to be 0.2MPa and 0.1MPa, respectively.
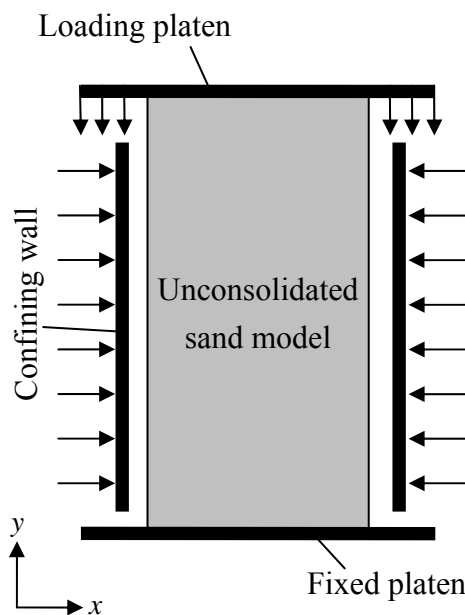
Fig.6.8 Loading condition for the simulation of biaxial compression tests.
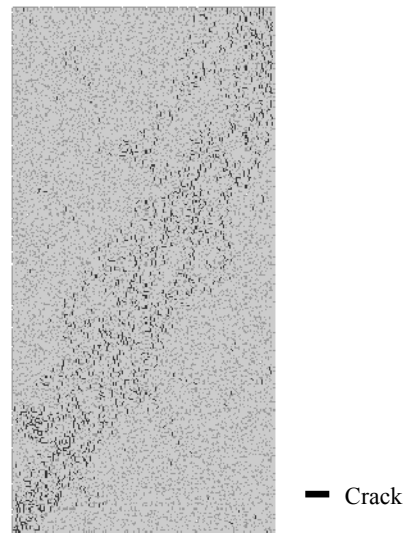
Fig.6.9 Spatial distribution of all cracks obtained from the simulation of the biaxial compression test.
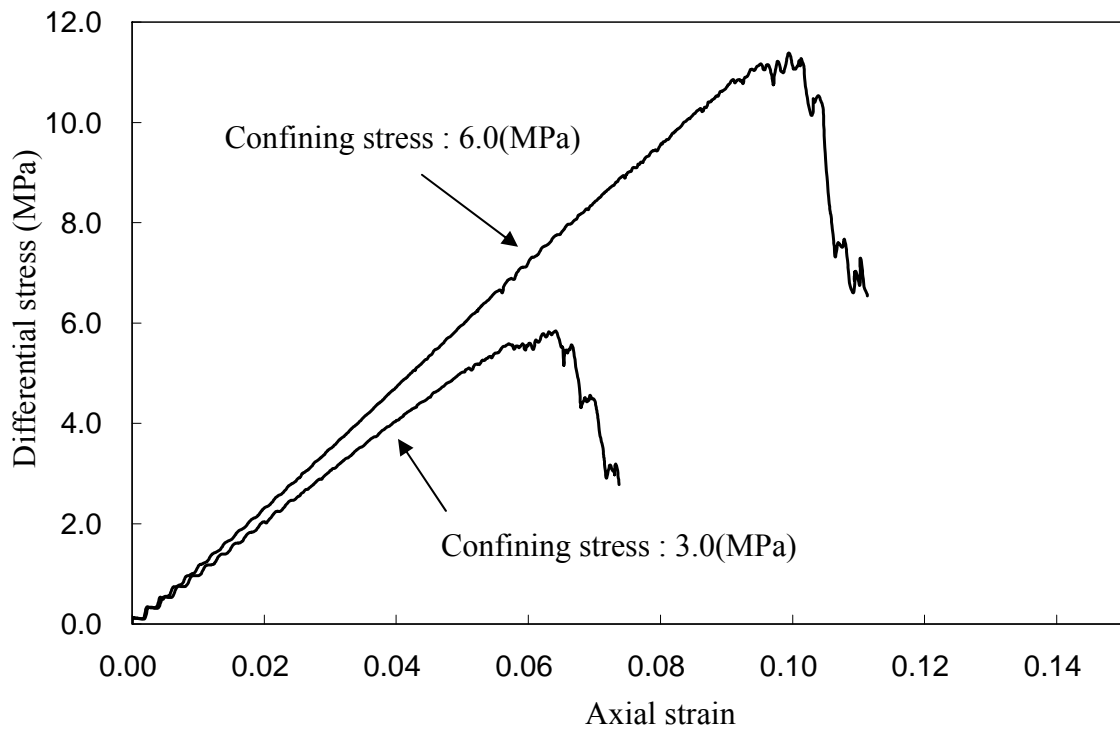
Fig.6.10   Result of the simulation of biaxial compression test.

Friction coefficient = 0.548
Friction angle (deg) = 28.709
Cohesion (MPa) = 0.087
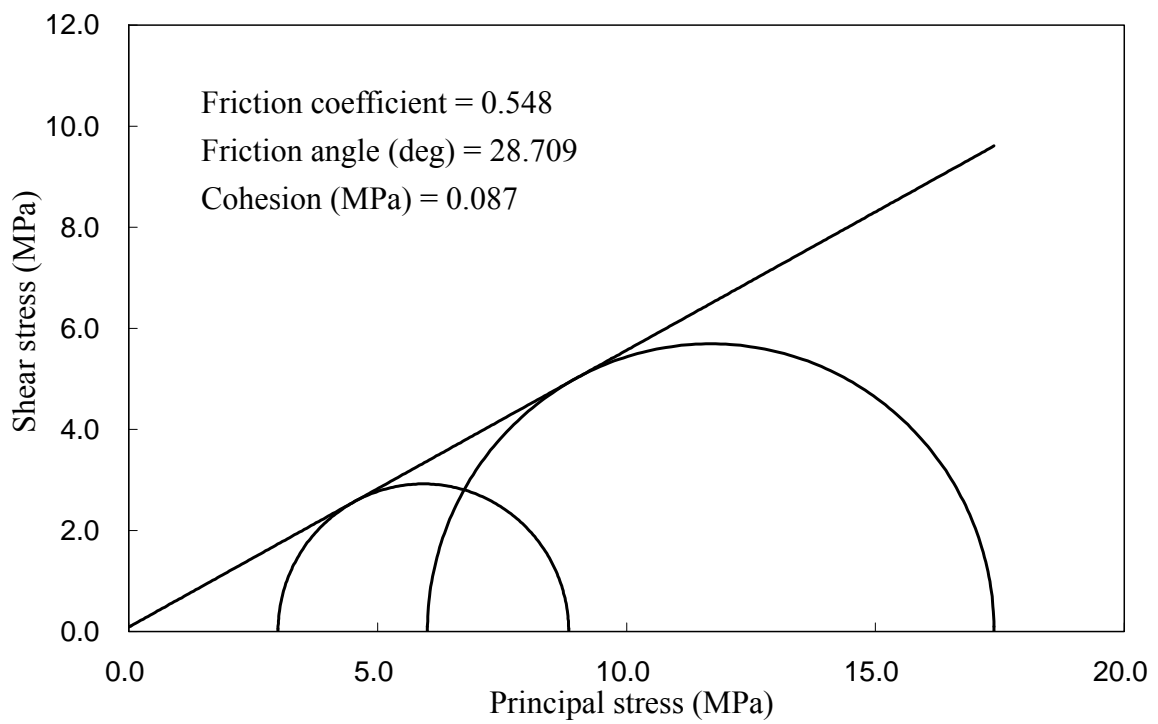
Fig.6.11   Mohr's circle for the simulation.

6.4.2 Specimen model and loading condition

Fig.6.12(a) illustrates the unconsolidated sand model and the loading condition for the hydraulic fracturing. The model is surrounded by the four rigid confining walls. These walls are supported by the springs to avoid pushing back when the pressure acting on the wall exceeds the confining pressure due to the fluid injection.

The stiffness of the spring supporting the confining wall was determined based on the Young's modulus of the unconsolidated sand model. The confining pressure is acted by moving the wall.

As shown in Fig.6.12(a), two confining pressures, 3MPa in the x-direction and 2MPa in the y-direction, were applied to the model. The model has a borehole similar to the experiment, and the casing is set up so that the borehole should not collapse by the confining pressure. As shown in Fig.6.12(b), the casing pipe is represented by the particles of equal size. These particles for casing pipe are connected by the procedure for the rock model shown in Fig.6.4(b).

Since the bonding of the particles for casing pipe has enough stiffness and strength, the deformation of the casing pipe can be ignored.

The fracturing fluid will be injected into the borehole with constant injection rate. The fracturing fluid does not flow out between the particles of casing pipe, and flows only throughout the slit that exists in the casing. The slit is located in direction of the maximum compressive stress (direction of the x-axis). These conditions are similar to the laboratory experiment that Igarashi *et al.* conducted.

The microscopic parameters used for the simulation are summarized in Table 6.2. Although bulk modulus of actual water is 2.1GPa, the bulk modulus of the fracturing fluid K_f is determined to 0.02GPa in order to evade long computing time and to obtain the stable solution [13,14].

Moreover, as shown in Table 6.2, friction coefficient of particle ($\tan \phi_p$) is very large, and cohesion of the model is small compared with actual unconsolidated sands. An actual grain of the soil and sand is not a simple sphere but is the extremely complex shape.

The unconsolidated sand specimen is formed by piling of such complex sand particles, and the complex skeletal structure is possessed. However, in this DEM simulation, the sand particle is replaced with a circular particle that is the simplest shape. It is thought that piling these circular particles may not reproduce the complex skeletal structure of actual unconsolidated sands [22]
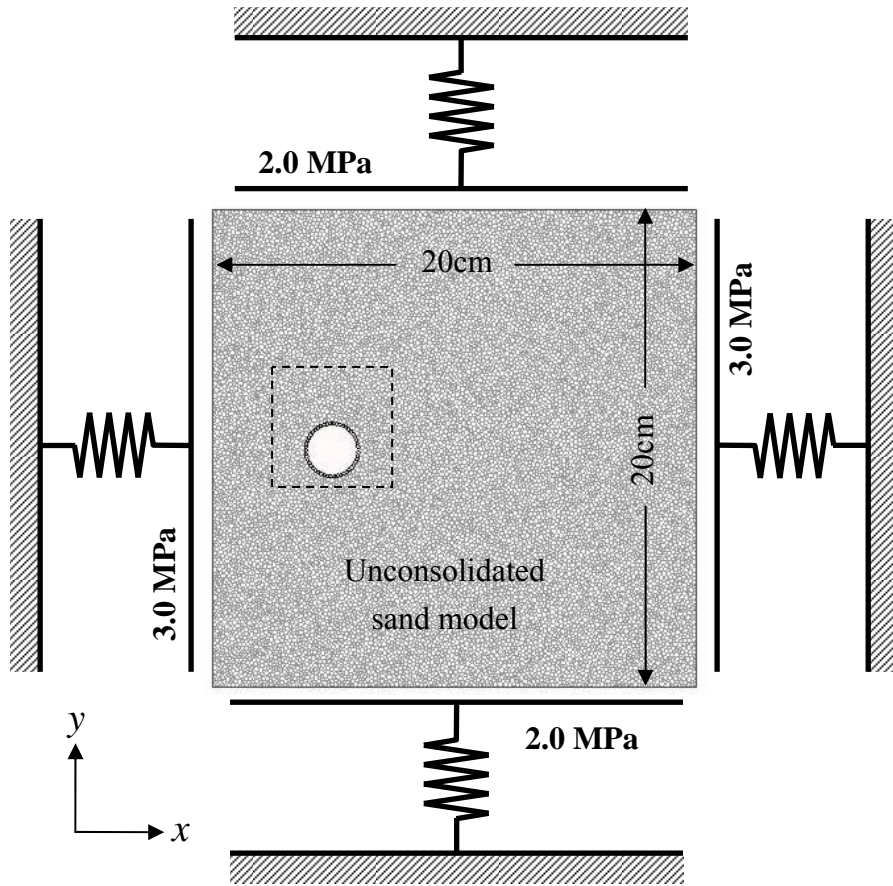
(a) Unconsolidated sand model and loading condition.
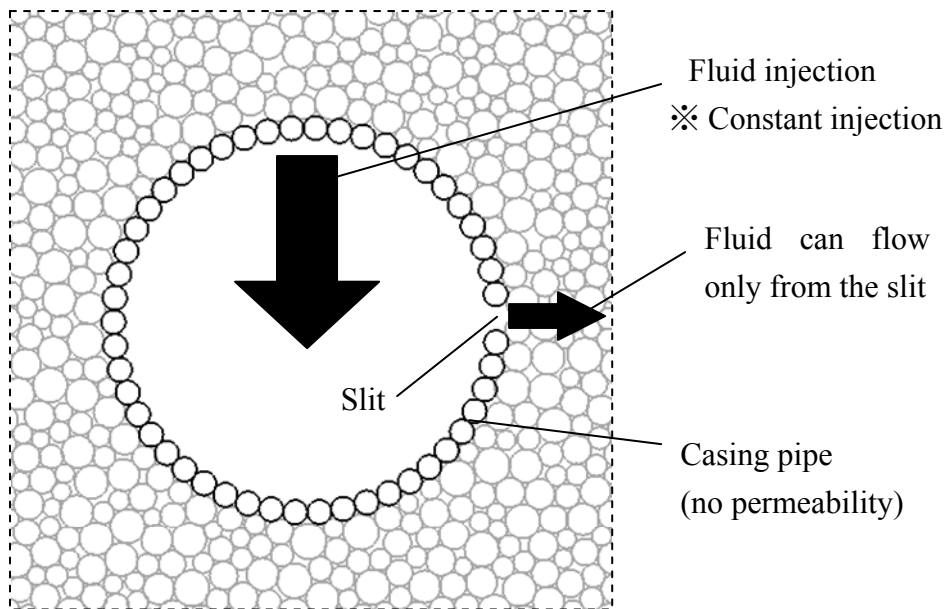
(b) Close-up view of the casing pipe.

Fig.6.12   Unconsolidated sand model for the simulation of hydraulic fracturing.

Table 6.2 Rock model properties and input parameters.

Model Data

Width:	200 mm
Height:	200 mm
Number of particles:	17846
Maximum particle radius:	1.0 mm
Minimum particle radius:	0.5 mm
Porosity of the model:	16 %

Input Parameters

Particle density:	2660 kg/m^3
Young's modulus of wall (E_w):	200 GPa
Friction coefficient of wall ($\tan \phi_w$):	0.0
Poisson's Ratio of wall (v_w):	0.3
Young's modulus of particle (E_p):	500 MPa
Friction coefficient of particle ($\tan \phi_p$):	2.5
Poisson's Ratio of particle (v_p):	0.2
Maximum stress of bonding (σ_{max}):	0.3 MPa
Maximum strain of bonding (ε_{max}):	0.01
Assumed porosity of the model (po):	35 %
Initial saturation (S_t):	10 %

Results of Biaxial compression Test

	Experiment	Simulation
Young's modulus of the model:	100.0 MPa	108.6 MPa
Friction angle of the model:	30.0 deg	28.71 deg
Cohesion of the model:	0.30 MPa	0.087 MPa

Results of Permeability test

Bulk modulus of the fracturing fluid (K_f):	0.02 GPa
Initial aperture for 5mD model (w_0):	11.83 μm
Initial aperture for 100mD model (w_0):	22.02 μm

6.4.3 Consideration for the boundary between the model and the casing

Fig.6.13 shows the simulation sample of the hydraulic fracturing, and shows the distribution of pore water pressure and the microcrack. Generation of a microcrack is expressed by the solid line. The domain where the fluid pressure is large is displayed in red. As shown in Fig.6.13, the fracturing fluid progresses to the other side of the slit position along the surface of the casing. Although a number of simulation were performed varying the viscosity of fracturing fluid, the pressurization rate and the permeability of the specimen, most of the cases shows the similar fracture growth pattern that shown in Fig.6.13. This result suggests that the infiltration of the fluid and the fracture progression occur easily at the boundary of the casing and the model particle. A similar phenomenon is also observed in the laboratory experiment that Igarashi *et al.* conducted. In their experiment, this phenomenon was prevented by wrapping the thin rubber tape around the casing. Then, in this simulation, the strength, stiffness coefficient of friction and permeability between the casing and the unconsolidated sand model are modified as show in Table 6.3. By using these modified parameters, this phenomenon shown in Fig.6.13 was not observed.
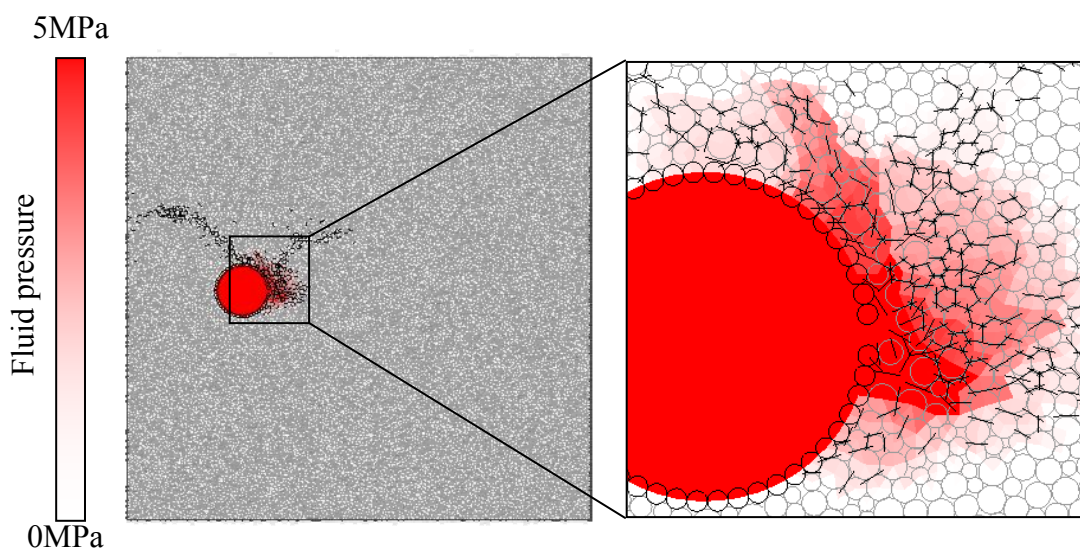
Fig.6.13　Leak off of the fluid from the boundary between the model and the casing.

Table 6.3　Modified input parameters for the contact between casing and particles.

Maximum stress of bonding between casing and particle:	6.5 MPa
Friction coefficient between casing and particle:	5.0
Iinitial aperture between casing and particle for 5mD model:	5.92 μm
Initial aperture between casing and particle for 100mD model:	11.01 μm

6.5. Results of the simulations

6.5.1 Classification of fracture growth patterns

Totally 31 cases of hydraulic fracturing simulation varying the permeability, viscosity, and injection rate was performed. The permeability of the model is 5mD, and 100mD. The viscosity of the fracturing fluid is 1, 2, 10,100, and $1000\,\mathrm{mPa \cdot s}$. The injection rate is 1, 5, 10, and 30 MPa/10^7step. In this study, the injection rate means the rise of fluid pressure in the casing pipe when the constant fluid injection is continued between 10^7steps without the outflow of the fluid from the slit.

The simulation results are summarized in Table 6.4 and 6.5. Table 6.4 shows the results when the permeability of the model is 100mD, and Table 6.5 shows the results when the permeability of the model is 5mD. Generation of a microcrack is expressed by the solid line. The domain where the fluid pressure is large is displayed in red. Although the connecting spring reproduces when the particle comes in contact even after the spring breaks, all the positions that the connecting spring has been broken even at once are displayed here as a microcrack.

Moreover, the classification of the fracture growth pattern is performed in Table 6.4 and 6.5. The fracture growth patterns observed in the simulations are successfully corresponding to the experimental result, and four types of fracture growth patterns, such as No Fracture (NF), Cavity Expansion (CE), Linear Fracture (LF) and Branched Fracture (BF) were observed.

6.5.2 Pressure-Time curves for each fracture growth patterns

Fig.6.14 shows pressure-time curves that clearly represent three kinds of typical tendencies. These pressure-time curves correspond to the fracture growth patterns.

In case of NF, the fluid pressure in the casing pipe rises smoothly with the fluid injection, and reaches in the equilibrium state finally. In case of CE, fluid pressure rises along with the fluid injection, and the slope of pressure-time curve has changed suddenly. In case of LF and BF, the fluid pressure decreases rapidly after it peaks, and the fluid pressure becomes an equilibrium state.

As shown in Fig.6.14, the pressure-time curves of LF and BF are almost the same. This fact suggests that LF and BF derive from the same fracture growth process. Moreover, it is also understood that the maximum pressure (breakdown pressure) of the fracturing fluid is the smallest in case of NF, and largest in case of CE.

These simulation results were in good agreement with the experimental results.

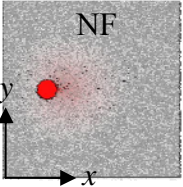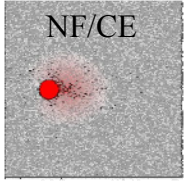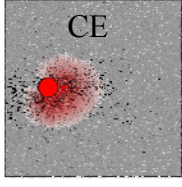Table 6.4 Classification of fracture shapes obtained from the simulations using the $k = 100$mD model.

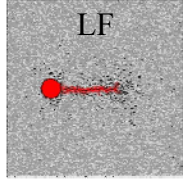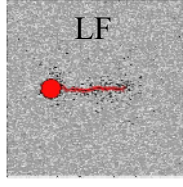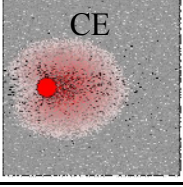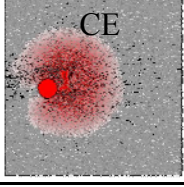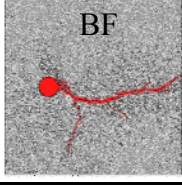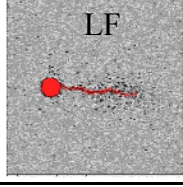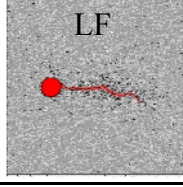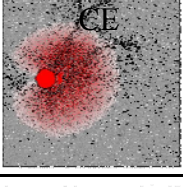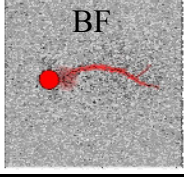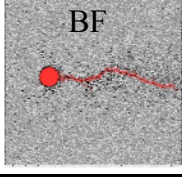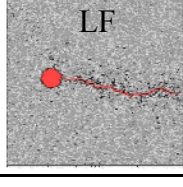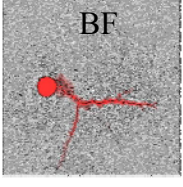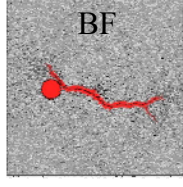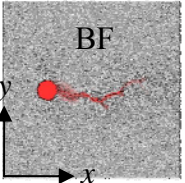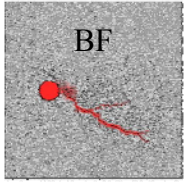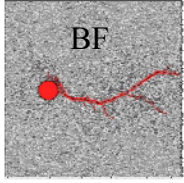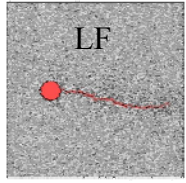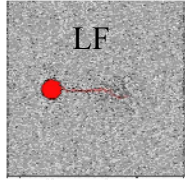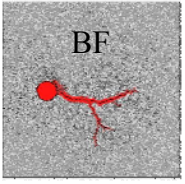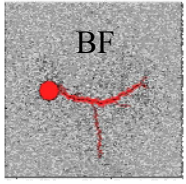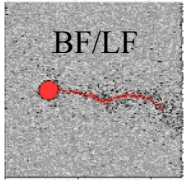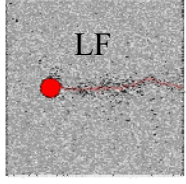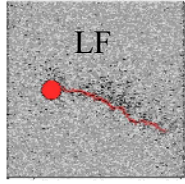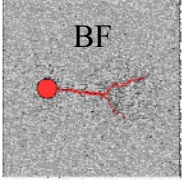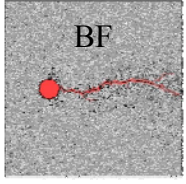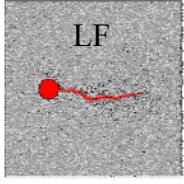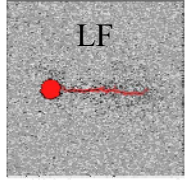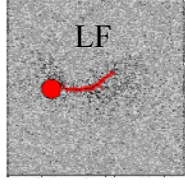| Permeability k [mD]	Flow rate q [MPa/10^{7}step]	Viscosity μ [mPa·s]				
		1	2	10	100	1000
100	1	NF	NF/CE	CE	LF	LF
	5	CE	CE	BF	LF	LF
	10	CE	BF	BF	LF	-
	30	BF	-	-	BF	-

Table 6.5　Classification of fracture shapes obtained from the simulations using the k = 5mD model.

Permeability	Flow rate	Viscosity μ [mPa·s]				
k [mD]	q [MPa/10^{7}step]	1	2	10	100	1000
5	1	BF	BF	BF	LF	LF
	10	BF	BF	BF/LF	LF	LF
	30	BF	BF	LF	LF	LF

Fig.6.14　Pressure-Time curves for various fracture shapes.

6.6. Discussion for No Fracture (NF)

6.6.1 Distribution of fluid pressure

Fig.6.15 shows pressure-time curve in case of permeability 100 [mD], injection rate 1 [MPa/10^7step], viscosity 1 [mPa $\cdot$ s], that shown the fracture growth pattern of NF.

In case of NF, the fluid pressure in the casing pipe rises smoothly with the fluid injection at first, and the amount of the fluid infiltrated into the model through the slit increases due to the rise of fluid pressure in casing pipe. When the amount of the fluid injected into the casing pipe and infiltrated into the model throughout the slit becomes equal, fluid pressure reaches in the equilibrium state.

Fig.6.16 shows the distribution of the fluid pressure at time step= 2354×10^5. Note that, time step is expressed by omitting "$\times 10^5$" in the text after this. Microcrack generation and slip occurrence are expressed by the black and green solid line, respectively. The domain where the fluid pressure is large is displayed in red

The left figure shows the entire model, and the right figure is the close-up view around the casing pipe. Although the clear fracture does not occur, a few microcracks were generated in the region around the slit where the fluid pressure is relatively high.

140
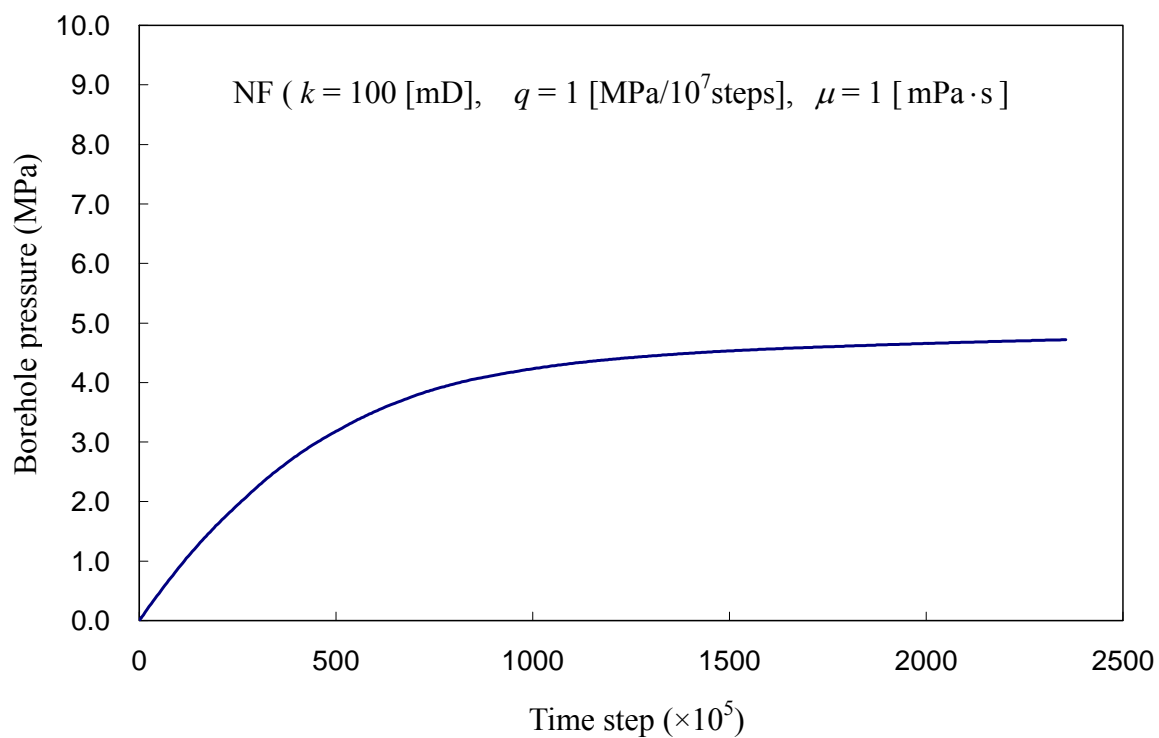
Fig.6.15　Pressure-Time curves for the case of no fracture (NF).
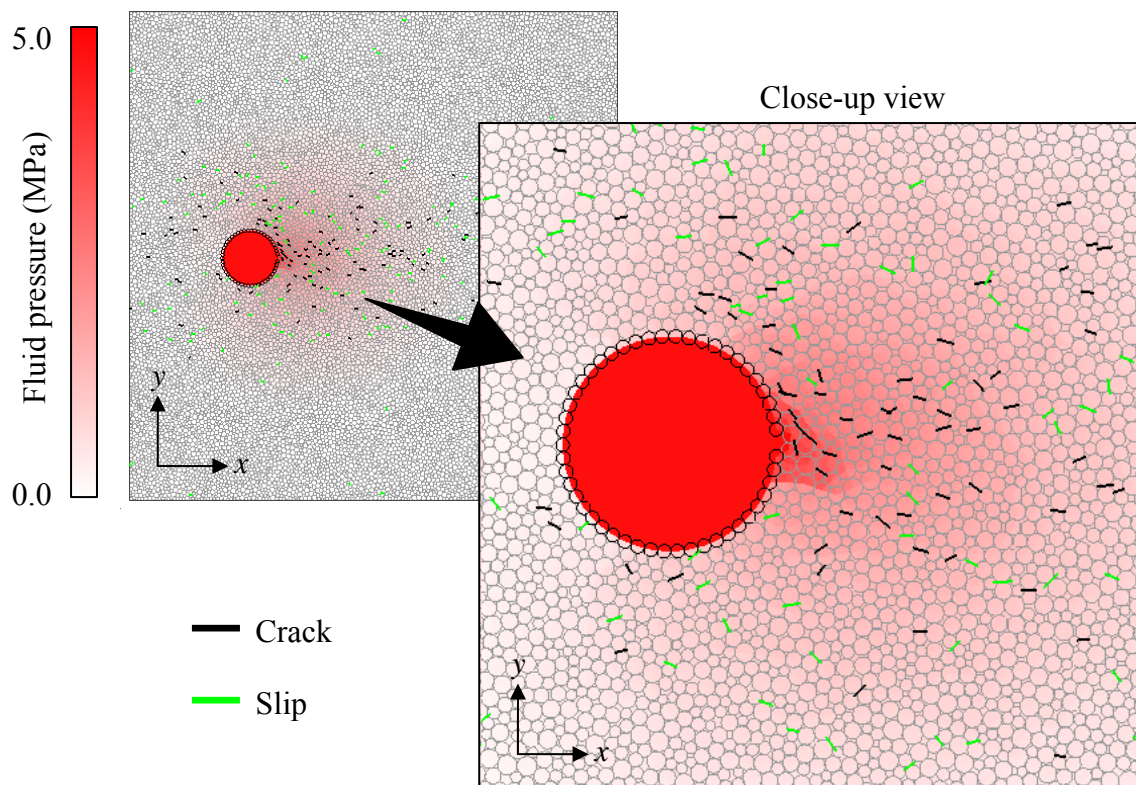
Fig.6.16　Spatial distribution of fluid pressure and micro crack generation at
time step= 2354.　(k = 100 [mD], q = 1 [MPa/10^{7}steps], μ = 1 [mPa $\cdot$ s])

6.6.2 Stress distribution during the fluid injection

Fig.6.17 shows the distribution of the maximum principal stress, the minimum principal stress and the maximum shear stress, at the initial state. The calculation procedure for the stress distribution in DEM model is described in APPENDIX. At this time, fluid injection was not started and only the confining pressure was acted on the model. The direction of the maximum principal stress is in the direction of the *x*-axis where maximum confining pressure 3MPa has been acted and the direction of the minimum principal stress is in the direction of the *y*-axis where minimum confining pressure 2MPa has been acted.
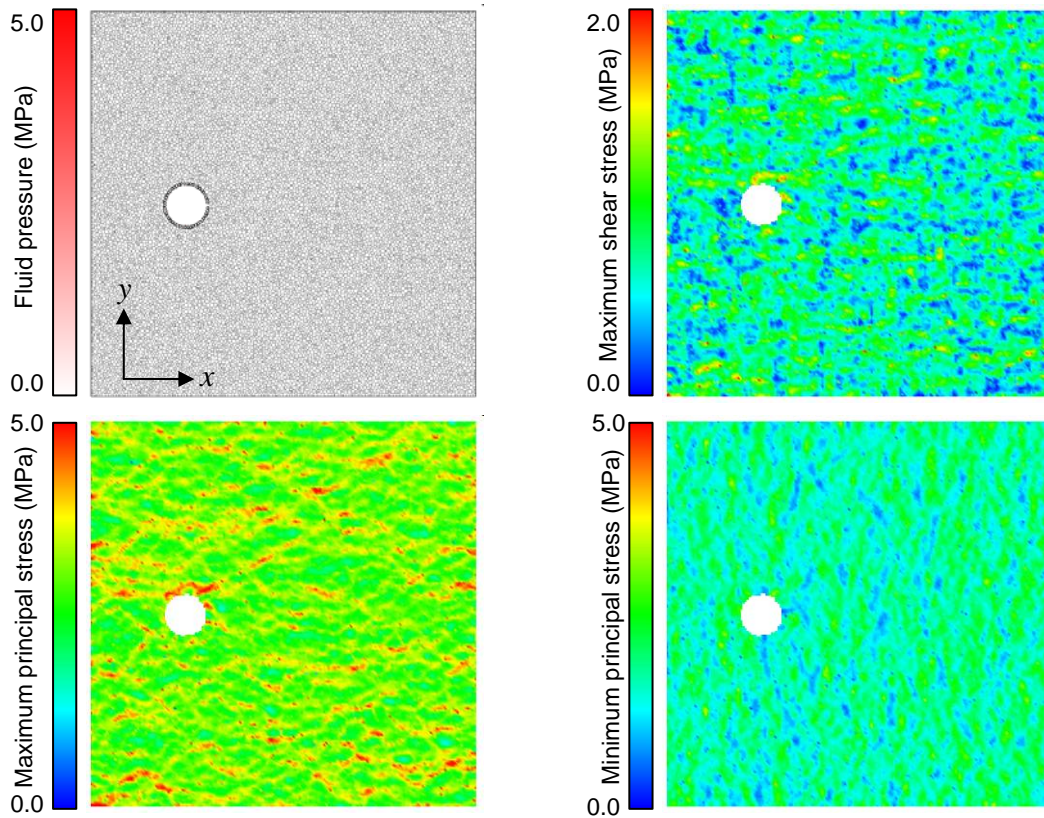
Fig.6.17   Stress state at time step= 0.
($k = 100$ [mD], $q = 1$ [MPa/10^7steps], $\mu = 1$ [mPa$\cdot$s])

On the other hand, Fig.6.18 shows the distribution of the principal stresses at time step 2354 when the fluid pressure almost becomes an equilibrium state. By comparing with initial state shown in Fig.6.18, it is found that the principal stresses around the casing pipe have been decreased. The distribution of the principal stresses is calculated based on the forces acting on the particles. Therefore, it can be said that Fig.6.17 and Fig.6.18 will show the distribution of the effective stress. This fact indicates that the principal stresses (effective stress) around the casing pipe is decreased due to the rise of fluid pressure, and that the occurrence of the microcrack and slip observed in Fig.6.16 is led by the decrease in effective stress. However, since the permeability of the model was very high in this case, the pressure gradient among the models is very low. Therefore, the microcrack did not develop any more, and the formation of a clear fracture was not observed.
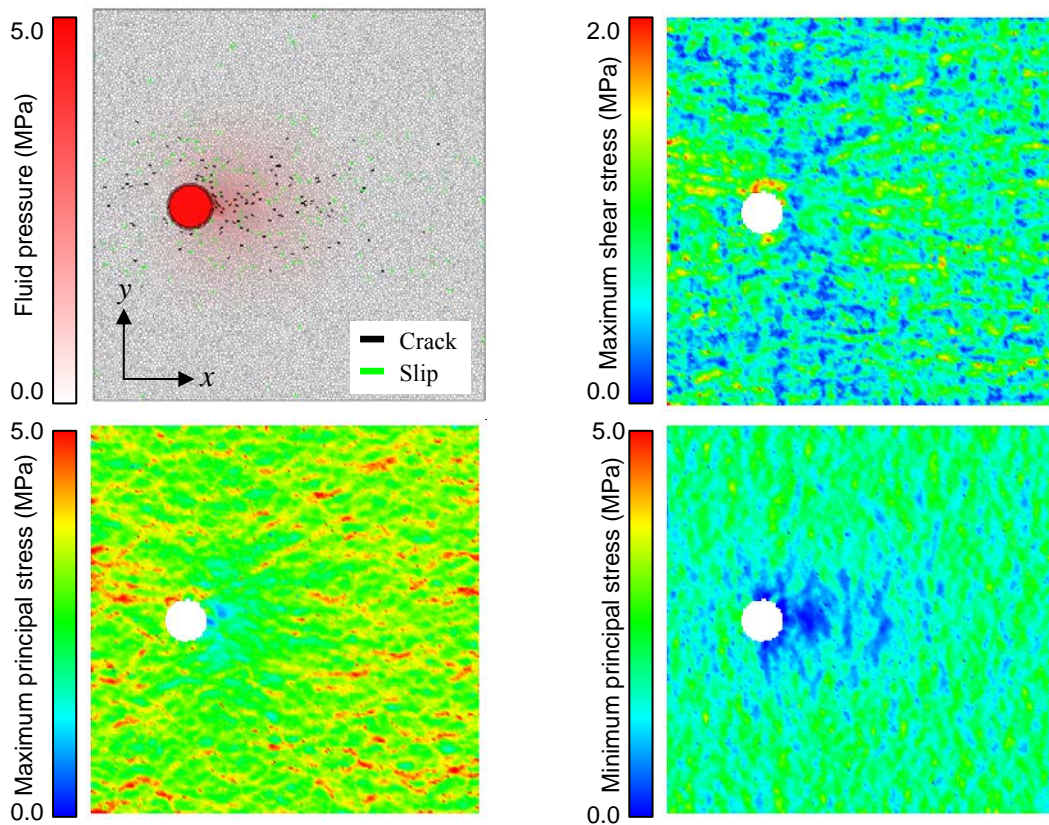

Fig.6.18   Stress state at time step= 2354.
($k = 100$ [mD], $q = 1$ [MPa/10^7steps], $\mu = 1$ [mPa $\cdot$ s])

6.7. Discussion for Cavity Expansion (CE)

6.7.1 Formation of dominant flow channel

Fig.6.19 illustrates five pressure-time curves that show the fracture growth pattern of CE. In case of CE, fluid pressure rises along with the fluid injection, and the slope of pressure-time curve is suddenly changed. Fig.6.20 shows the special distribution of the fluid pressure, microcracks and slip occurrences at the end of the simulation in case of the permeability 100 [mD], injection rate 5 [MPa/10^7step] and viscosity 2 [mPa·s]. Generation of a microcrack and occurrence of a slip are expressed by the black and green solid line, respectively. The domain where the fluid pressure is large is displayed in red. As shown in Fig.6.20, large cavity is formed in front of the slit.

Fig.6.21 shows pressure-time curve in the same case as shown in Fig.6.20. Fig.6.22 (upper) shows the distribution of the fluid pressure around the slit and the distribution of microcracks and slips at the time step156, 160 and 164. These were the time steps when the slope of pressure-time curve changed. Fig.6.22 (under) shows the distribution of the flow rate of the fracturing fluid at the time step156, 160 and 164. The domain where the flow rate is large is displayed in red, and the domain where the flow rate is small is displayed in blue. As shown in Fig.6.22, a lot of microcracks and slips occur in front of the slit at the time step 160, and a dominant flow channel with especially large flow rate was formed. The growth rate of the fluid pressure in the casing pipe decreases because large amount of fracturing fluid infiltrates into the model throughout the dominant flow channel. Thus, the slope of pressure-time curve suddenly changes as shown in Fig.6.21.

6.7.2 Process of the cavity expansion

Fig.6.23 and Fig.6.24 show the spatial distribution of the principal stress at the time step164 and 594, respectively. The time step 594 is the end of the simulation. At the time step 164, a dominant flow channel was formed and the slope of pressure-time curve changed. As shown in Fig.6.23, the fluid pressure is high around the dominant flow channel, and the principal stresses around the casing pipe were significantly decreased. Therefore, a lot of microcracks and slips were led by the decrease in effective stress due to the rise of fluid pressure around the dominant flow channel. However, a clear cavity expansion is not formed at this time. On the other hand, as shown in Fig.6.24, the region where the effective stress decreased was enlarged due to the fluid infiltration at time step 594. Such regions are surrounded by the region where maximum principal stress and the maximum shear stress are large, and a clear cavity expansion is observed.
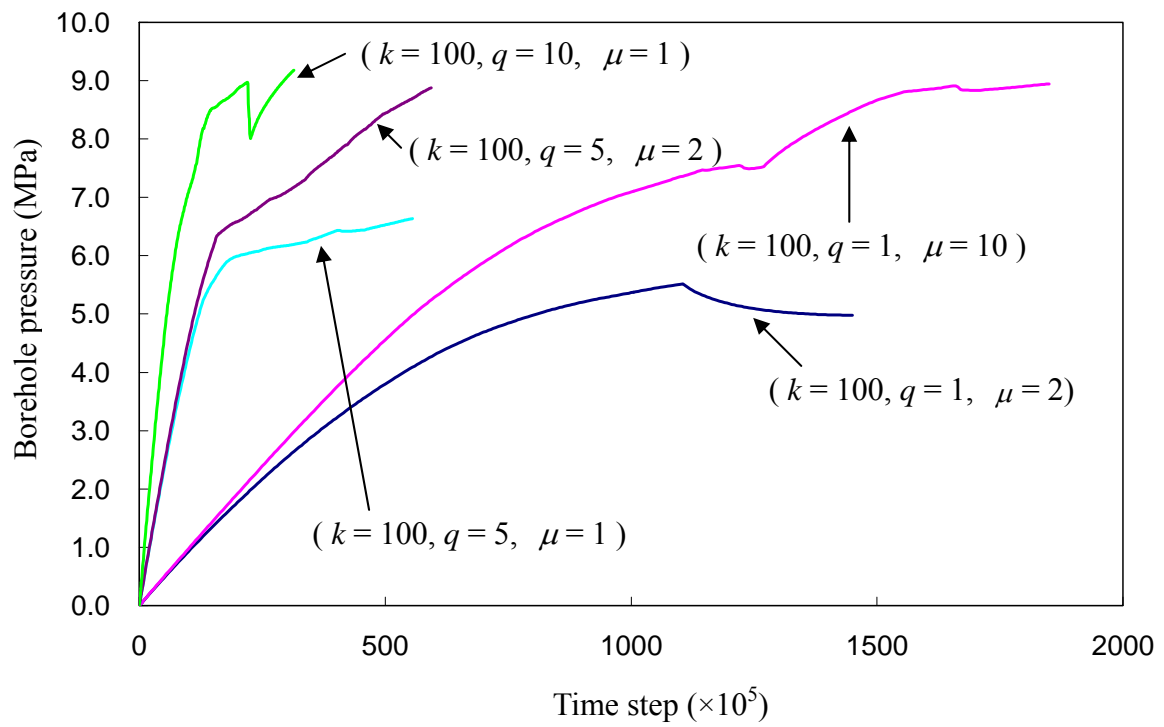
Fig.6.19 Pressure-Time curves for the case of cavity expansion (CE).

Close-up view

Crack

Slip
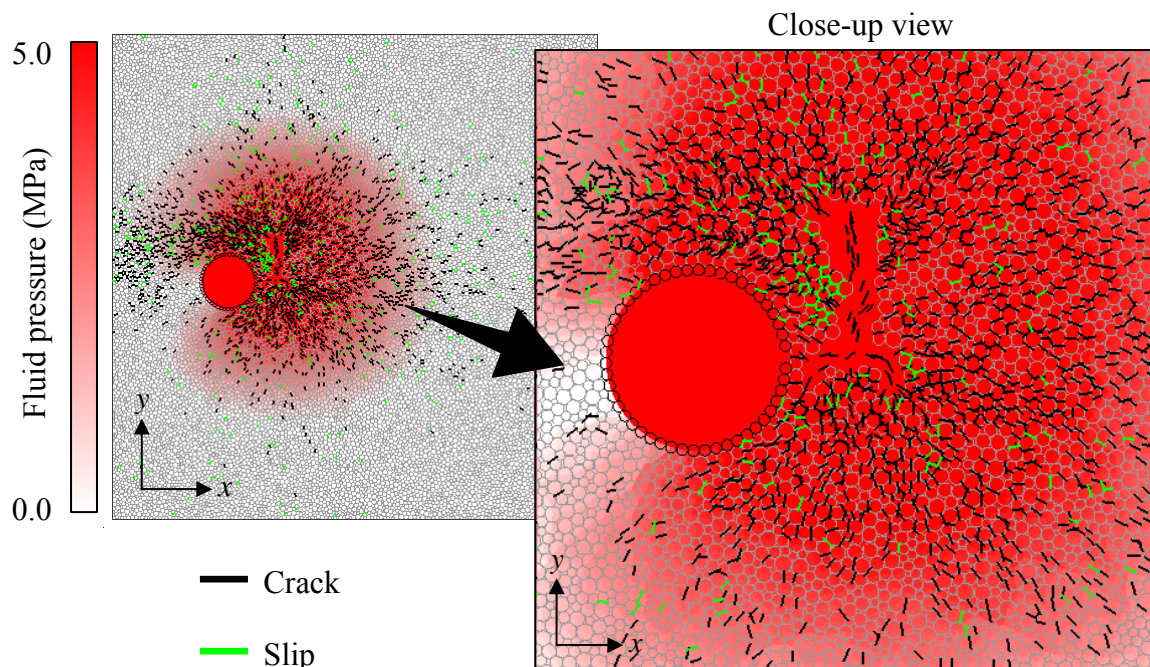
Fig.6.20 Spatial distribution of fluid pressure and micro crack generation at
time step= 594. (k = 100 [mD], q = 5 [MPa/10^7steps], μ = 2 [mPa·s])

Fig.6.21   Pressure-Time curves.
($k = 100$ [mD], $q = 5$ [MPa/10^7steps], $\mu = 2$ [mPa·s])

Fig.6.22   Spatial distribution of fluid pressure and micro crack generation (upper),
and flow rate distribution (lower).

146
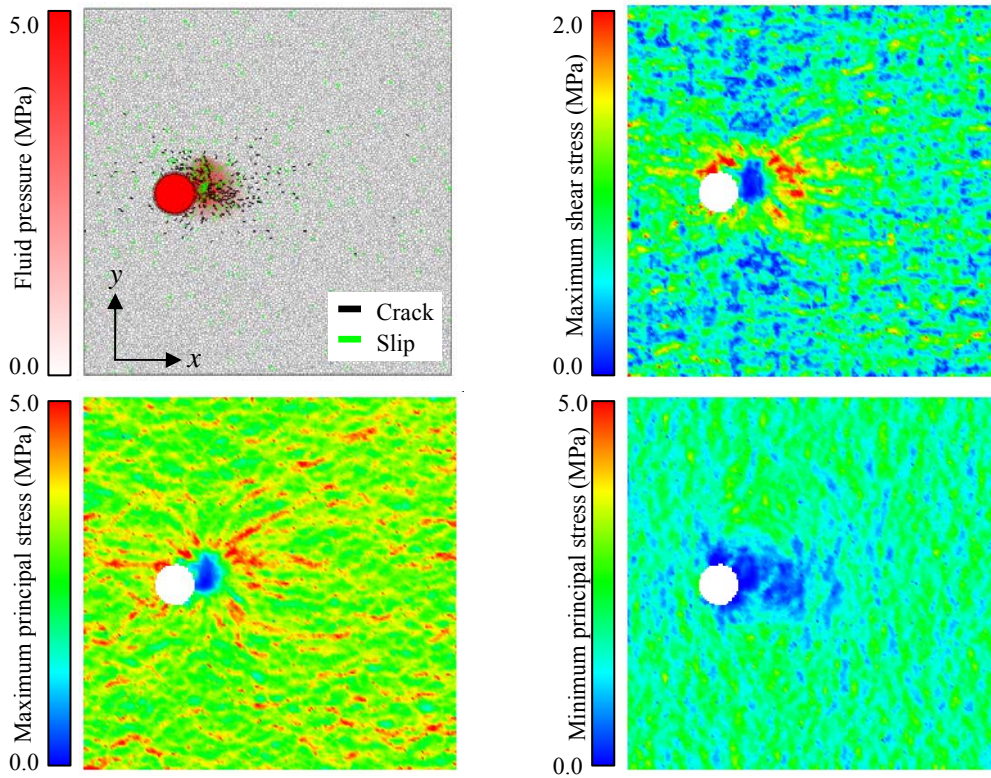
Fig.6.23 Stress state at time step= 164.
(k = 100 [mD], q = 5 [MPa/10^7steps], μ = 2 [mPa$\cdot$s])
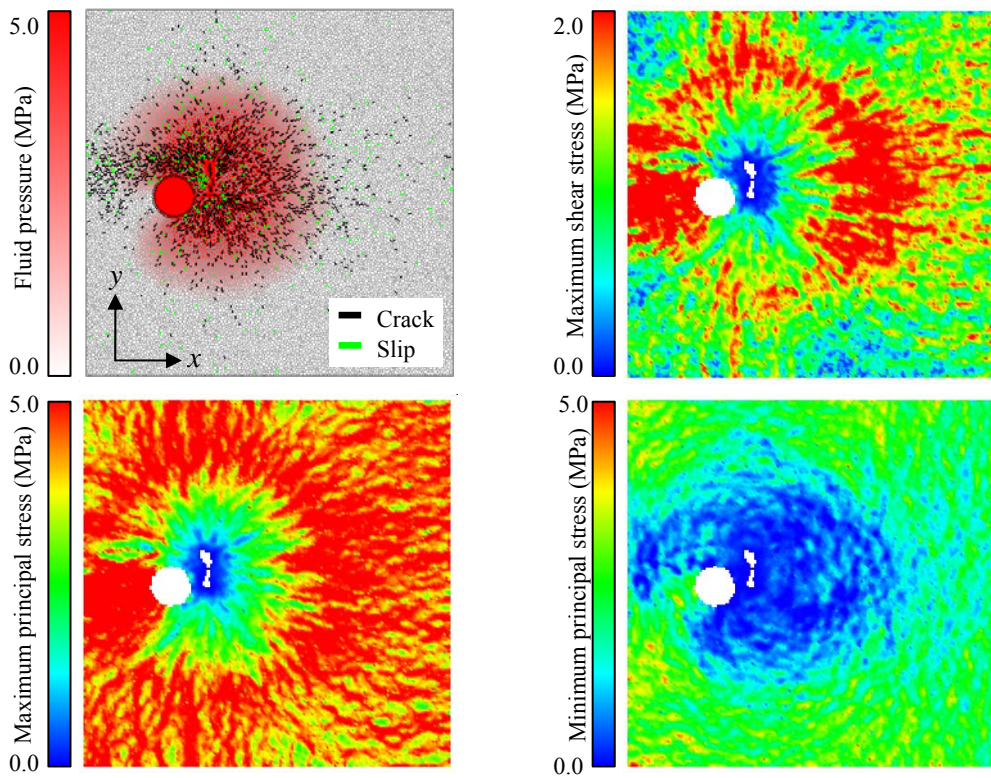
Fig.6.24 Stress state at time step= 594.
(k = 100 [mD], q = 5 [MPa/10^7steps], μ = 2 [mPa$\cdot$s])

(a) Initial step (Time step= 0)

(b)Final step (Time step= 594)
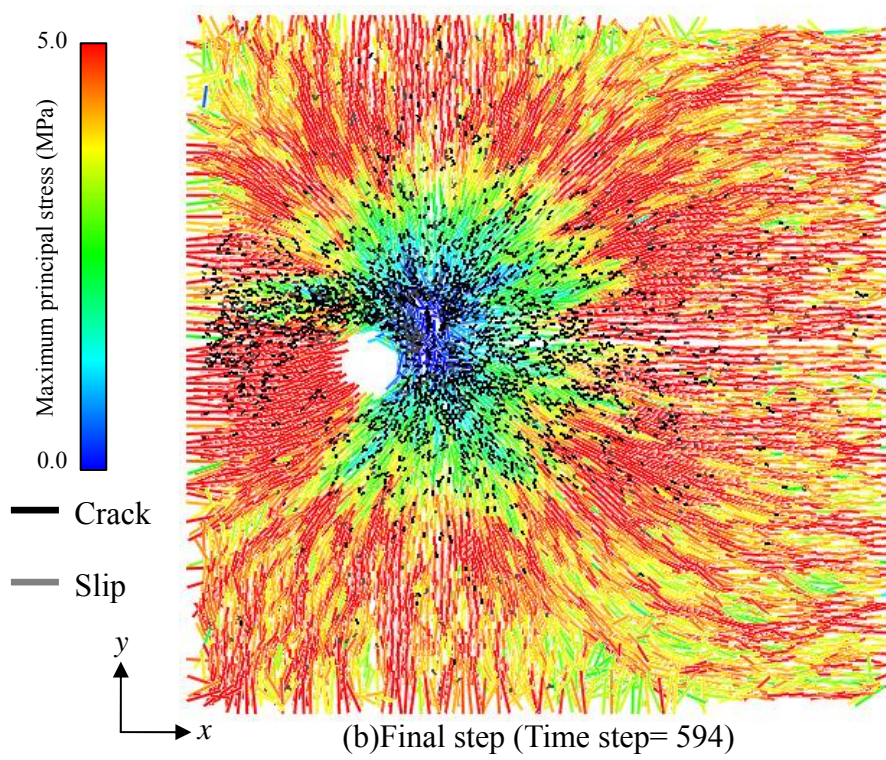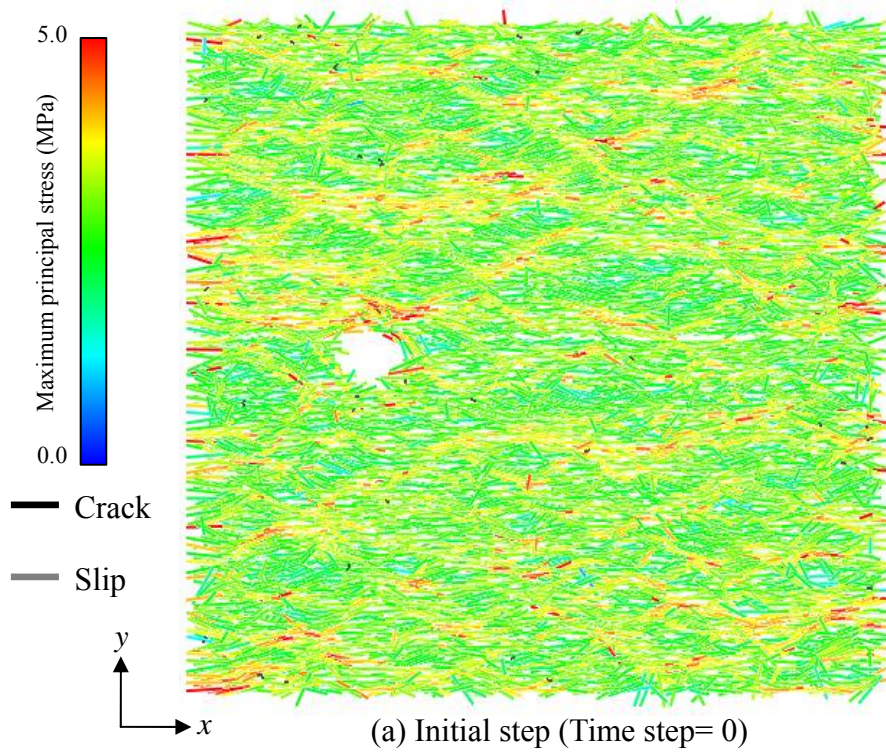
Fig.6.25   Magnitude and direction of the maximum principal stress.
($k = 100$ [mD], $q = 5$ [MPa/10^7steps], $\mu = 2$ [mPa$\cdot$s])

Fig.6.25(a) and (b) are the vector diagrams that indicate the magnitudes and the direction of maximum principal stress at the initial state and the time step 594, respectively. As shown in Fig.6.25(a), the maximum principal stress was in the direction of the maximum confining pressure at the initial state. On the other hand, at the time step 594, the maximum principal stress oriented parallel to the radial direction from the slit position. At this time, a lot of microcracks and slips occurred in the region where the effective stress has decreased, and the surrounding of the slit becomes a complete loose region by the generation of these microcracks and slips. Moreover, fluid pressure around the slit position is very high, and high pressure gradient exists from the slit position to the edge of the model. Therefore, particles that exist in the loosened area move from the slit position to the edge of the model due to the pressure gradient. As a result, the large cavity around the slit shown in Fig.6.20 is formed.

6.7.3 Consideration for Shear Fracture (SF)

The SF type fracture growth pattern shown in Fig.6.3(b) was not dearly observed in this simulation. However, the mechanism of the SF type fracture growth pattern can be presumed from the simulation results as follows.

Fig.6.26 shows pressure-time curve in case of permeability 100 [mD], injection rate 1 [MPa/10^7step], viscosity 2 [mPa·s]. As shown in Fig.6.26, time step 1105 is the time just before the slope of pressure-time curve changes. Time step 1110 is the time when the decrease in pressure began, and time step 1455 is the end of the simulation.

Fig.6.27 (upper) shows the distribution of the fluid pressure around the slit and the distribution of the microcracks and the slips, and Fig.6.27 (lower) shows the distribution of the flow rate of the fracturing fluid at the time step1105, 1110 and 1450, respectively. According to the distribution of the flow rate at the time step1105 and 1110 in Fig.6.27, the dominant flow channel is formed as well as the cases of Cavity Expansion, and the decrease in the fluid pressure has occurred. However, cavity expansion occurred at the arrowed position in Fig.6.27 (lower, time step 1450) is very small. As shown in Table 6.4, this simulation condition is located at the boundary of the NF and the CE condition, and the hydraulic transmissibility of the fracturing fluid is higher than the other cases of CE. Therefore, high pressure gradient enough to expand the cavity was not established in this case, and the cavity expansion is very small compared with other cases.

When the fluid injection is stopped and pressure decreases, such a minimum cavity diminishes and may be hardly observed in actual experiment. However, in the experiment, the red ink may remains in the formed dominant flow channel region and the mark of ink becomes similar shape to SF that shown in Fig.6.3(b).

Fig.6.26　Pressure-Time curves.
(k = 100 [mD], q = 1 [MPa/10^7steps], μ = 2 [mPa·s])
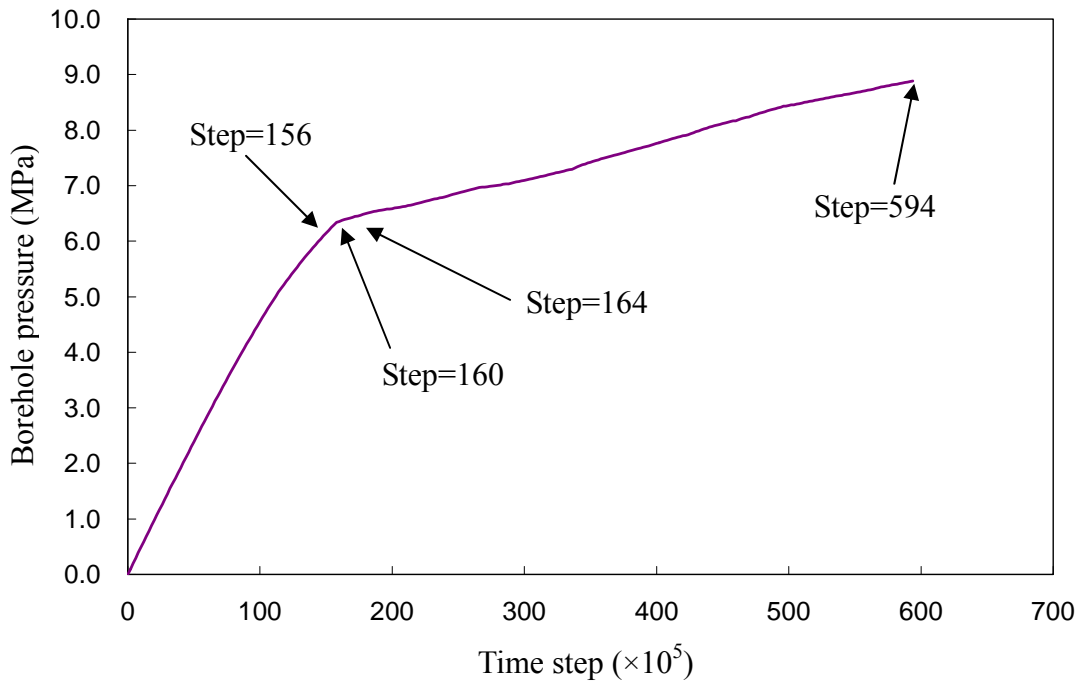

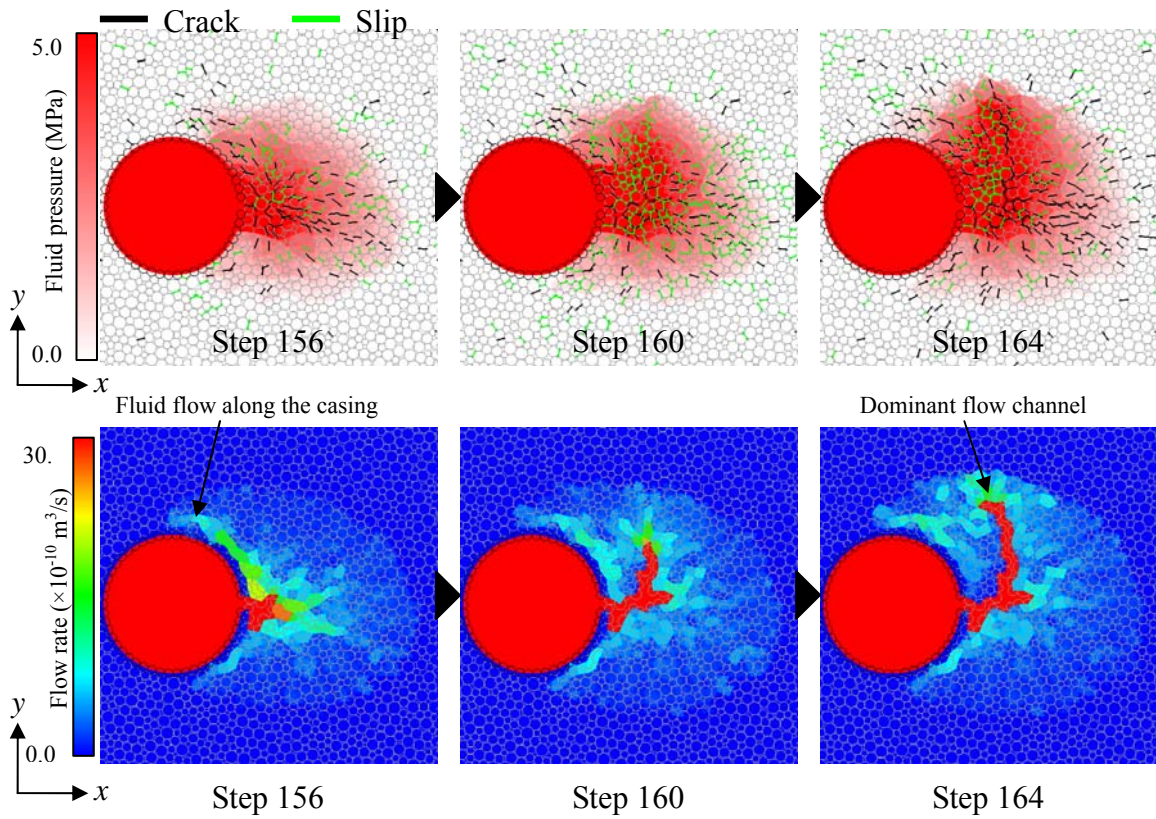Fig.6.27　Spatial distribution of fluid pressure and micro crack generation (upper), and flow rate distribution (lower).
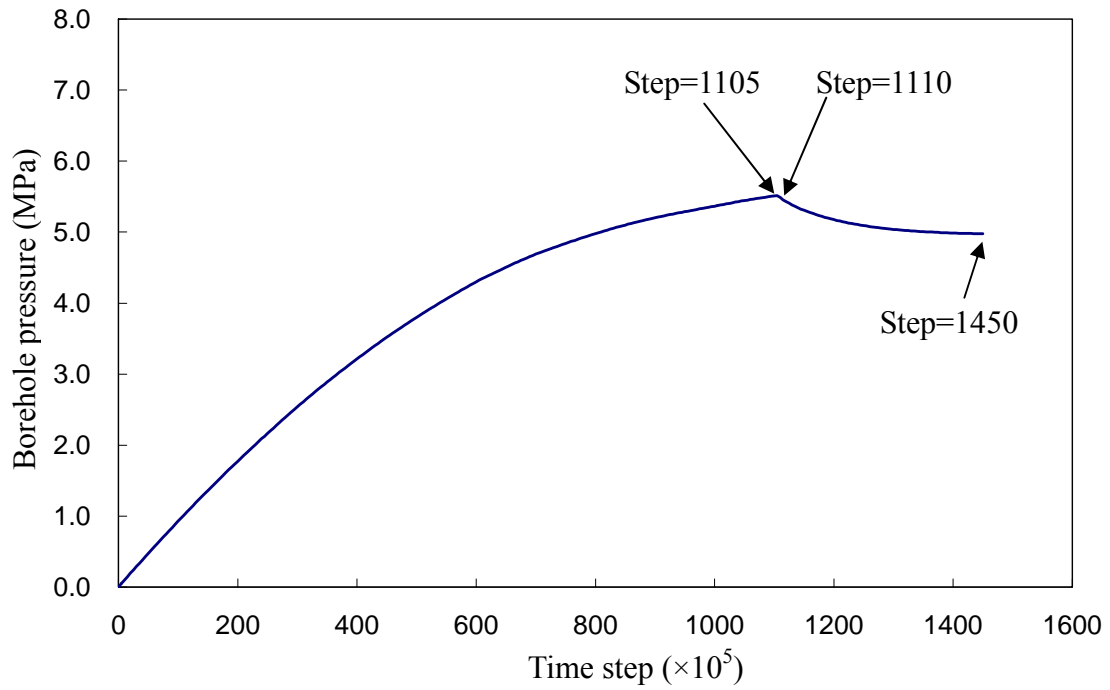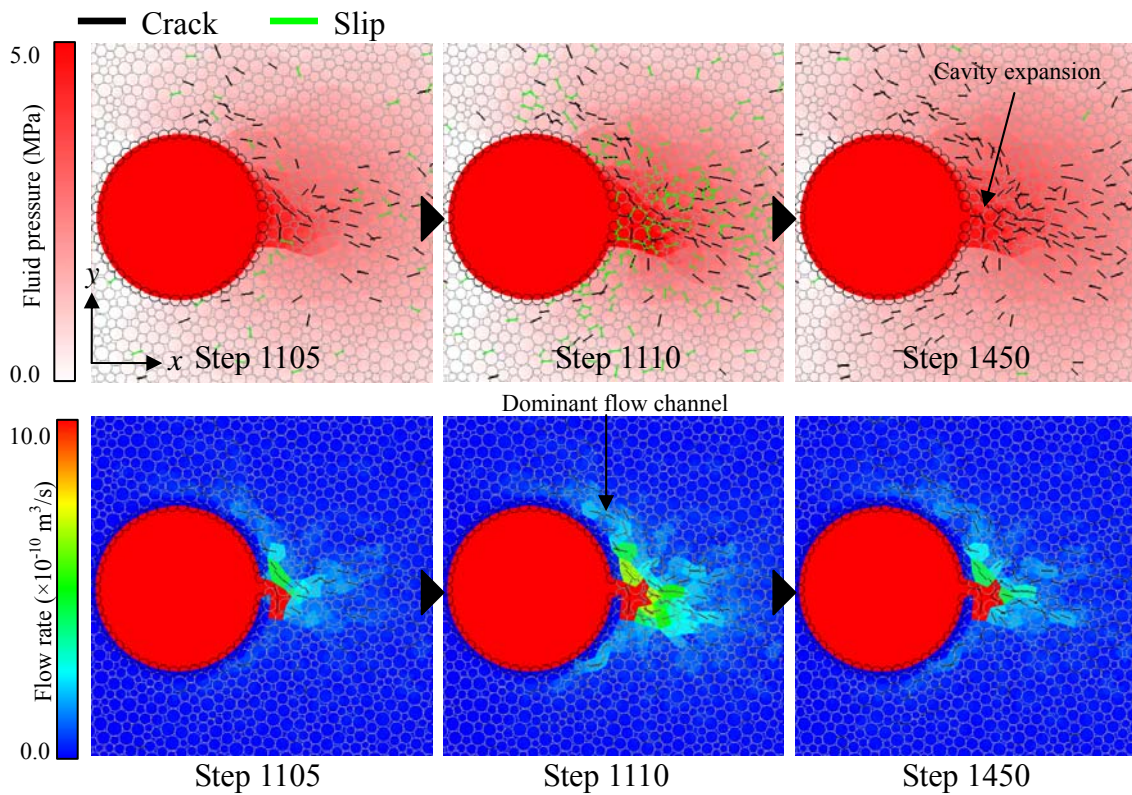
However, in the DEM simulation, the size of the particle in this simulation is relatively large compared with the fracture formed in Shear Fracture as shown in Fig.6.3(b). Moreover, as shown in Fig.6.25, the stress state of the model does not become completely uniform due to such large particles. Therefore, SF type fracture growth pattern shown in the experiment is difficult to be formed in this simulation. To reproduce SF type fracture shown in the experiment, it is necessary to imitate a micro structure of an actual specimen accurately by using a smaller particle.

6.8. Discussion for Linear Fracture (LF) and Branched Fracture (BF)

6.8.1 Propagation of the fracture

Fig.6.28 shows some pressure-time curves that show the fracture growth pattern of LF and BF. Fig.6.29(a) and (b) show the typical fracture shapes LF and BF, respectively. In these cases, the fluid pressure decreases rapidly after it peaks. Afterwards, the fluid pressure becomes an equilibrium state.

Fig.6.30 shows the close-up view of the pressure-time curve (dotted rectangle in Fig.6.28) in case of permeability 5 [mD], injection rate 1 [MPa/10^7step], viscosity 10 [mPa·s]. The distribution of the fluid pressure around the slit and the location of microcrack and slips at the six time steps (arrowed in Fig.6.30) are shown in Fig.6.31. The change of the fluid pressure and the fracture growth process in each time step are summarized as follows.

(a) A straight fracture starts developing, and the fluid pressure in the casing pipe starts decreasing along with it.

(b) The fracture keeps developing, and the decrease in pressure continues.

(c) Substantial change is not seen in the slope of pressure-time curve though some small branched fracture is formed.

(d) The growth of a small branched fracture stops, and the main fracture keeps developing continuously. Afterwards, though the main fracture diverges to two large fractures, the fluid pressure decreases constantly.

(e) The fluid pressure stops decreasing though two main fractures keep developing. Moreover, according to Fig.6.30, sudden decrease in pressure has occurred at this time. The particle closing the channel near the slit moves, and the channel was opened suddenly.

(f) The fluid pressure becomes an equilibrium state though the development of the main fracture continues. Finally, the fluid pressure decreases rapidly when the fracture reaches the edge of the model and the fracturing fluid leaks outside the model.
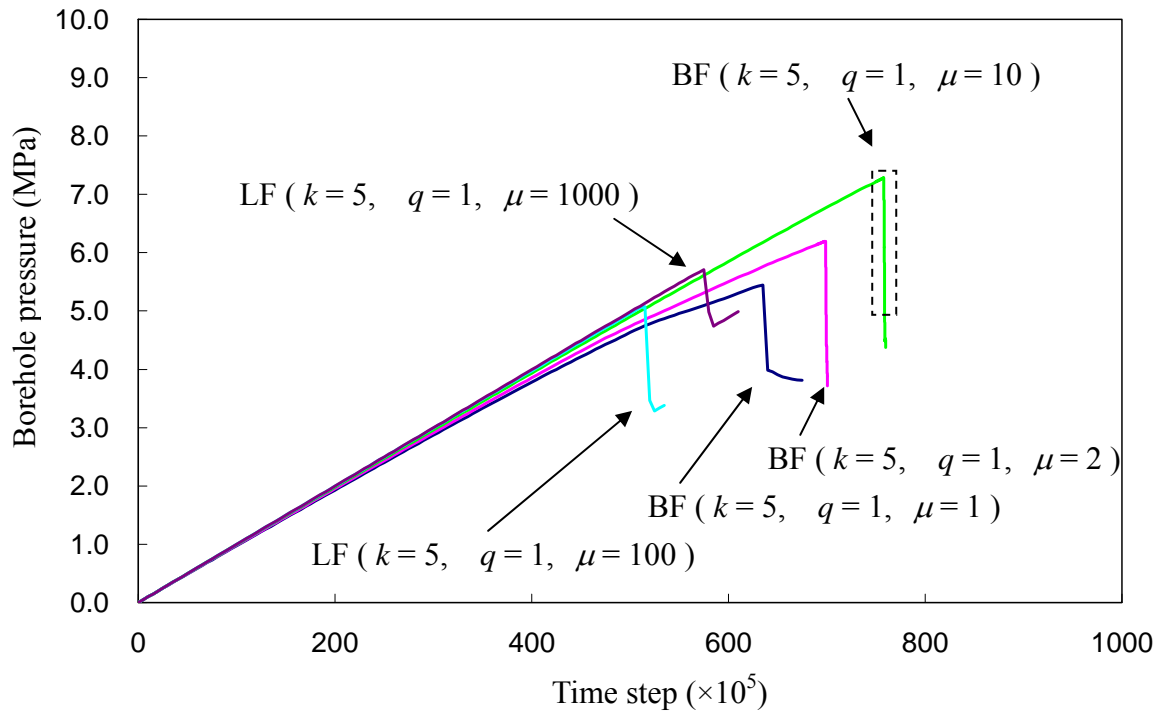
Fig.6.28   Pressure-Time curves for the case of linear fracture (LF) and branched
         fracture (BF).

(a) Linear Fracture.
($k = 5$, $q = 1$, $\mu = 100$)

(b) Branched Fracture.
($k = 5$, $q = 1$, $\mu = 10$)
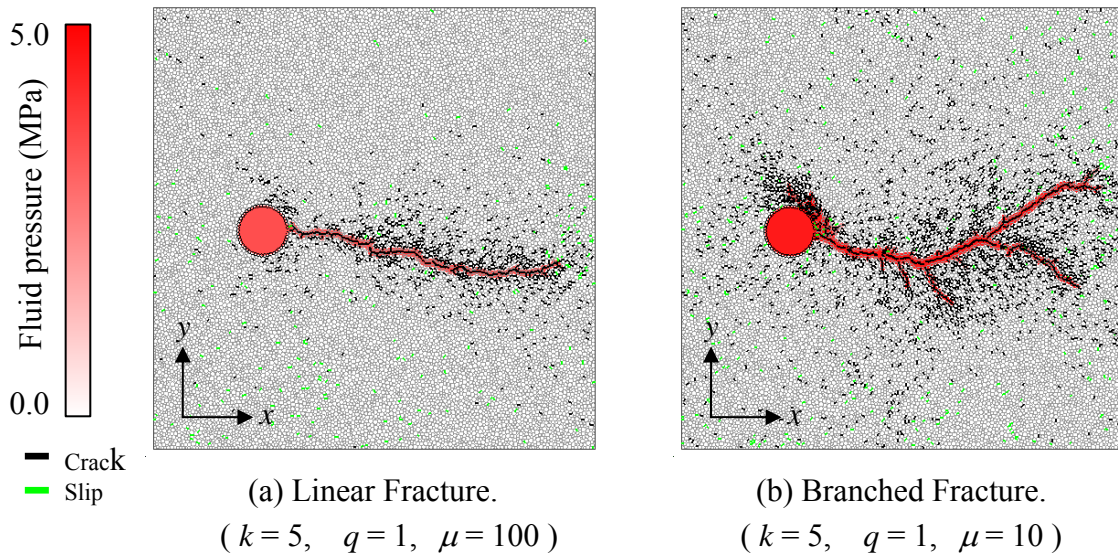
Fig.6.29   Spatial distribution of slip occurrences, micro crack generations
         and fluid pressure.
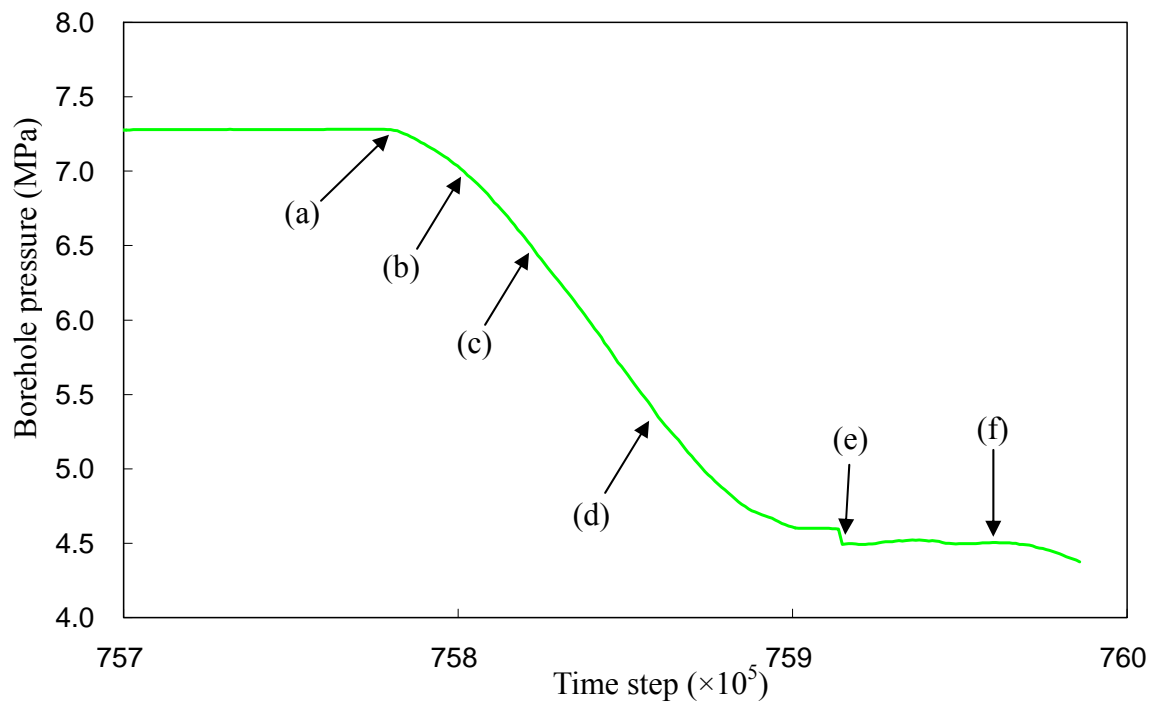
Fig.6.30   Close-up view of the Pressure-Time curve.
(k = 5 [mD], q = 1 [MPa/10⁷steps], μ = 10 [mPa·s])
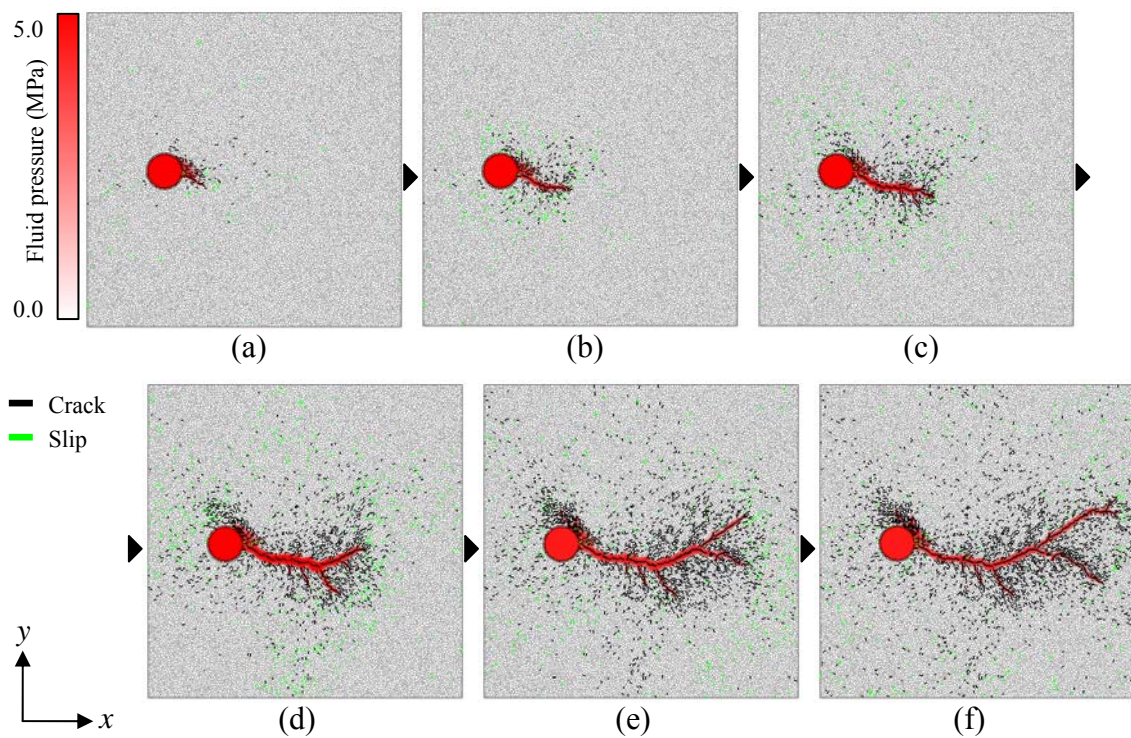
Fig.6.31 Fracture propagation process.
(k = 5 [mD], q = 1 [MPa/10⁷steps], μ = 10 [mPa·s])

153

6.8.2 Relationship between the fluid pressure and fracture growth

Fig.6.32 shows the the pressure-time curve, width of fracture opening and stresses that acting on the walls of each x- and y-directions. The pressure-time curve shown in Fig.6.32 is the same as the one shown in Fig.6.30. As shown in Fig.6.33, the interparticle distance of two selected particles located on the surface of the fracture is measured as the width of fracture opening. Fig.6.34(a), (b), (c), (d), (e), and (f) show the vector diagrams that indicate the magnitudes and the direction of maximum principal stress at the six time steps arrowed in Fig.6.30, respectively. From these figures, the change in the width of fracture opening in time step (a), (b), (c), (d), (e), and (f) can be explained as follows.

(a) The fracture tip has not reached the measurement position of fracture width yet though the fracture starts developing. Therefore, there is no opening of the fracture in the measurement point.

(b) The fracture tip reaches the measurement position, and the width of fracture opening increases. At this time, as shown in Fig.6.34(b), the direction of maximum principal stress around the fracture is perpendicular to the direction of the fracture propagation because the fluid pressure acted on the fracture surface.

(c) The fracture keeps developing and the fracture width increases continuously. As shown in Fig.6.34(c), since the area of the fracture surface that the fluid pressure acts increases along with the development of the fracture, the region where maximum principal stress is significantly large has enlarged. Moreover, when the influence of maximum principal stress with the fracturing fluid reaches even the confining wall, the confining wall suppresses the expansion of the model. Thus, the stress acting on the confining wall in y-direction starts increasing as shown in Fig.6.32.

(d) The fracture width reaches the peak and it changes into the decreasing tendency while the development of the fracture and the decrease in the fluid pressure continue. This is because the fluid pressure acting on the fracture surface became smaller than the confining pressure due to the decreasing in fluid pressure. As shown in Fig.6.34(d), the influence of the fluid pressure in the fracture is spreads and it reaches even the confining wall in x-direction. Therefore, the stress acting on the confining wall not only in y-direction but also in x-direction starts increasing.

154

Fig.6.32 Relationship among fluid pressure, wall pressures and fracture width.
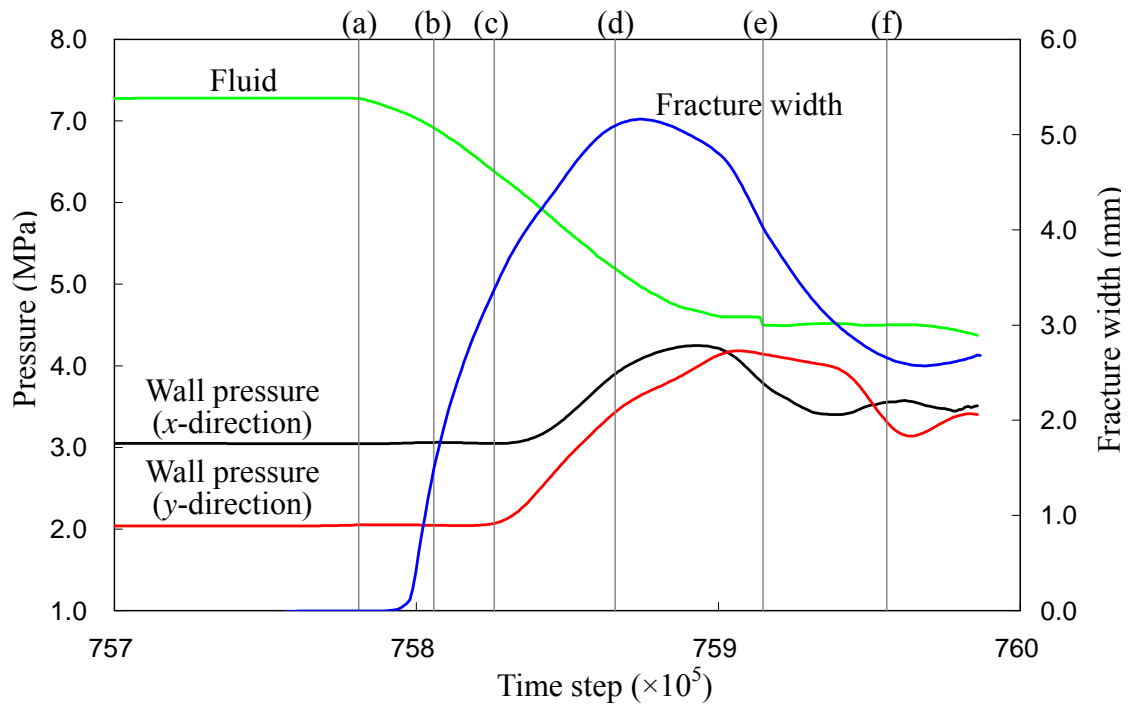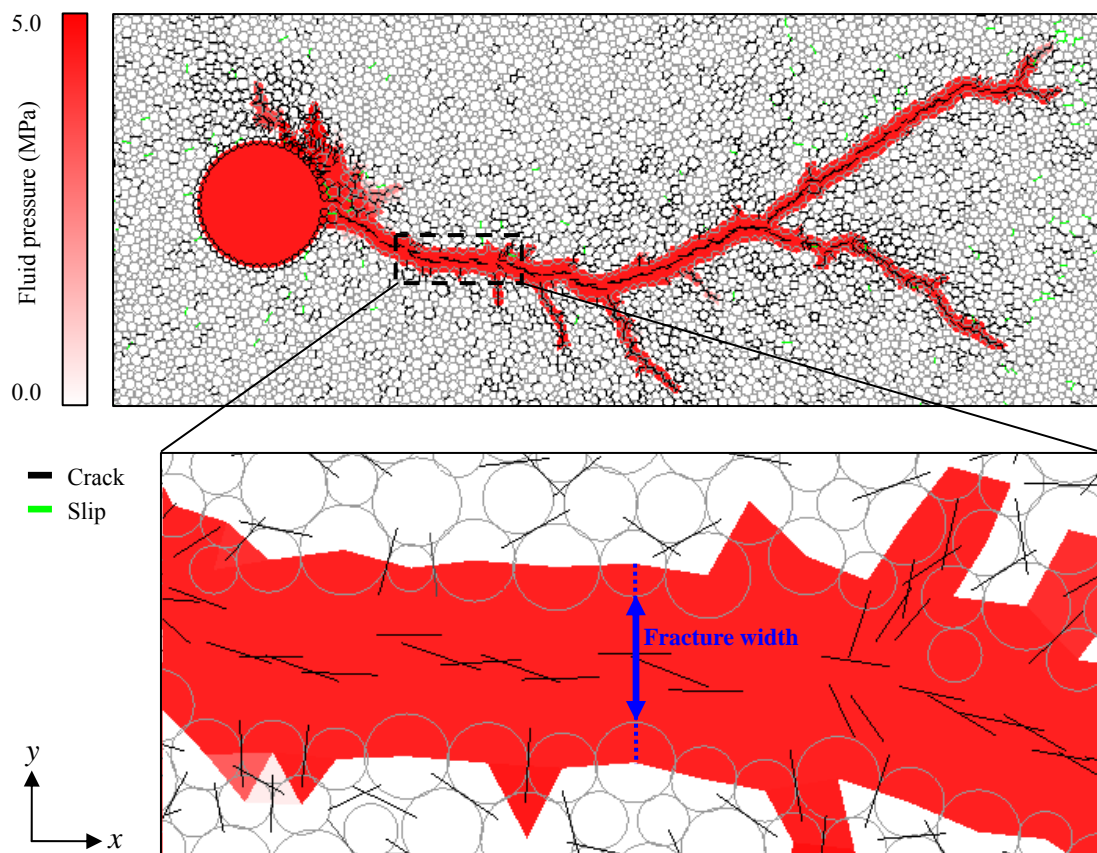

Fig.6.33 Fracture width measurement procedure.
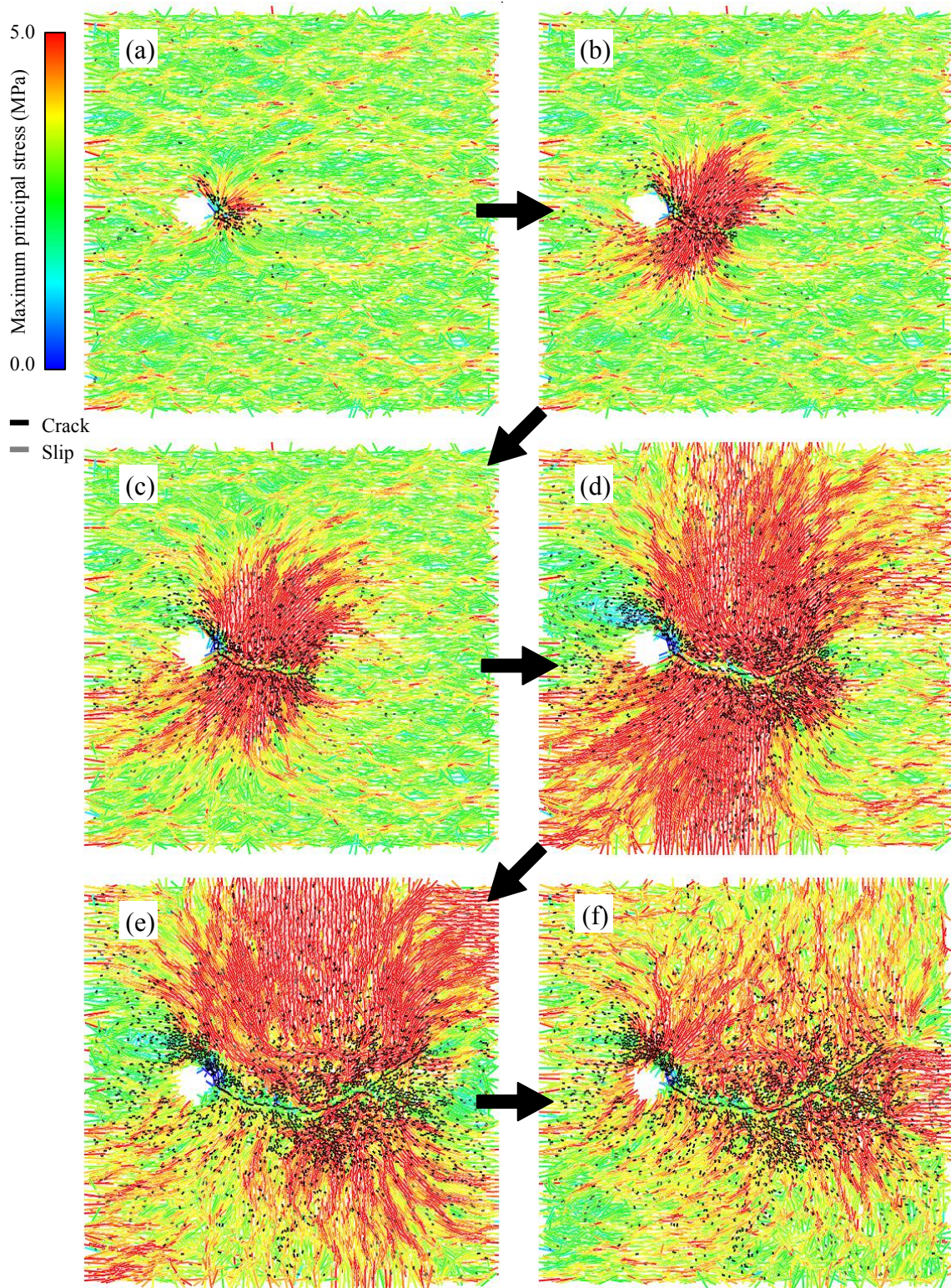
Fig.6.34 Magnitude and direction of the maximum principal stress at each time step.
($k = 5$ [mD], $q = 1$ [MPa/10^7steps], $\mu = 10$ [mPa $\cdot$ s])

(e) The fluid pressure decreases slowly because the decrease in the fluid pressure due to the fracture propagation exceeds the increase by the fluid injection. However, the decreasing in the fluid pressure is compensated by the decrease in fracture width due to the confining pressure. Therefore, the fluid pressure keeps almost constant value though the fracture keeps developing and the fracture width decreases. At this time, the stress that acts on the confining walls decreases with the decrease in fracture width.

(f) The decrease in fluid pressure due to the fracture propagation balances the increase by the fluid injection. Therefore, the fluid pressure, the fracture width and the stress acting on the walls continue the equilibrium states though the fracture keeps developing.

Consequently, it is understood that the fluid pressure retains a constant value when the decrease in fluid pressure due to the fracture propagation, the increase in fluid pressure by fluid injection, and the confining pressure are in balance. However, as show in Fig.6.32, the fluid pressure in the equilibrium state is larger than the confining pressure that acting in y-direction. One of the possible explanations is given as follows. Fig.6.34(d), (e), and (f) show that the fracture length is shorter than the confining walls. Therefore, such large fluid pressure is needed so that the fluid pressure acting on the fracture surface balances the confining pressure.

6.8.3 Fracture branching process

Pressure-time curve of the LF and the BF shows the same tendency as shown in Fig.6.28. Therefore, these fracture growth pattern can not be identified from the pressure-time curve. However, as shown in Table 6.5, when the permeability of the model is 5 [mD] and the viscosity of the fracturing fluid is 100 [mPa·s] or more, most cases show the fracture growth pattern of the LF. On the other hand, when the viscosity of the fracturing fluid is lower than 100 [mPa·s], most cases show the fracture growth pattern of the BF. These results suggest that the viscosity of the fracturing fluid have a large influence on the fracture growth process of LF and BF.

An extra simulation had been performed in order to clarify the effect of the fluid viscosity. Fig.6.35(a) shows the distribution of the fluid pressure around the slit and the location of microcracks and slips in case of permeability 5 [mD], injection rate 1 [MPa/10^7step], viscosity 10 [mPa·s] at the time step just before branching of the main fracture (the same time step as Fig.6.34(d)). When the viscosity of the fracturing fluid

retains 10 [mPa·s],the fracture branches as shown in Fig.6.35(b). However, the fracture went straight without branching as shown in Fig.6.35(c) when the viscosity of the fracturing fluid was changed from 10 [mPa·s] to 1000 [mPa·s].

Fig.6.36 is a close-up view of the region enclosed with a dotted rectangle in Fig.6.35 and shows the fracturing process at the branching point of the fracture. In Fig.6.36(a-1), (a-2), and (a-3), the viscosity of the fracturing fluid is 10 [mPa·s]. On the other hand, in Fig.6.36(b-1), (b-2), and (b-3), the viscosity of the fracturing fluid is 1000 [mPa·s]. When a particle exists on the course of the fracture as shown in Fig.6.36, the particle at the fracture tip receives large force from the fluid pressure in the arrowed direction in Fig.6.36(a-1) and (b-1).

(a) The time step before fracture branching.
(k = 5 [mD], q = 1 [MPa/10^7steps], μ = 10 [mPa·s])

(b) Fluid viscosity is 10 [mPa·s]

(c) Fluid viscosity is modified to1000 [mPa·s]
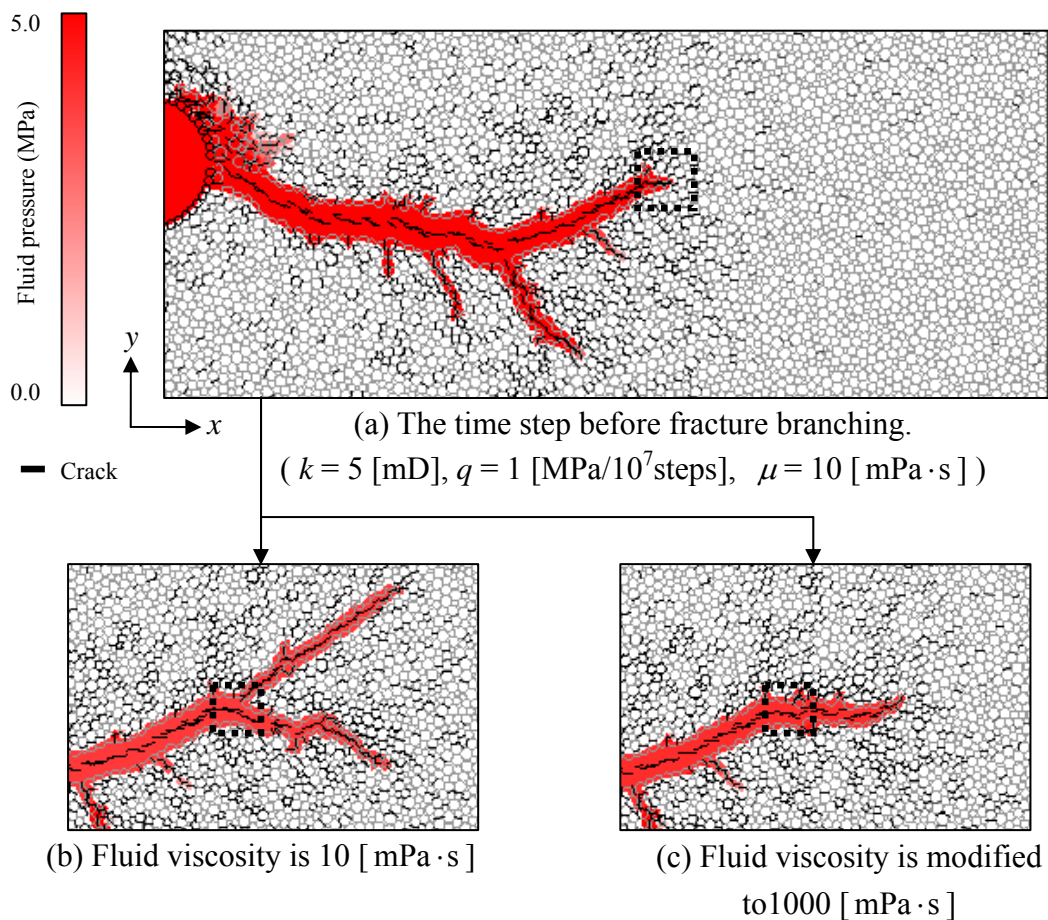
Fig.6.35 Difference of fracture propagation behavior due to the fluid viscosity.

158

(a) Fluid viscosity is 10 [mPa·s]   (b) Fluid viscosity is 1000 [mPa·s]
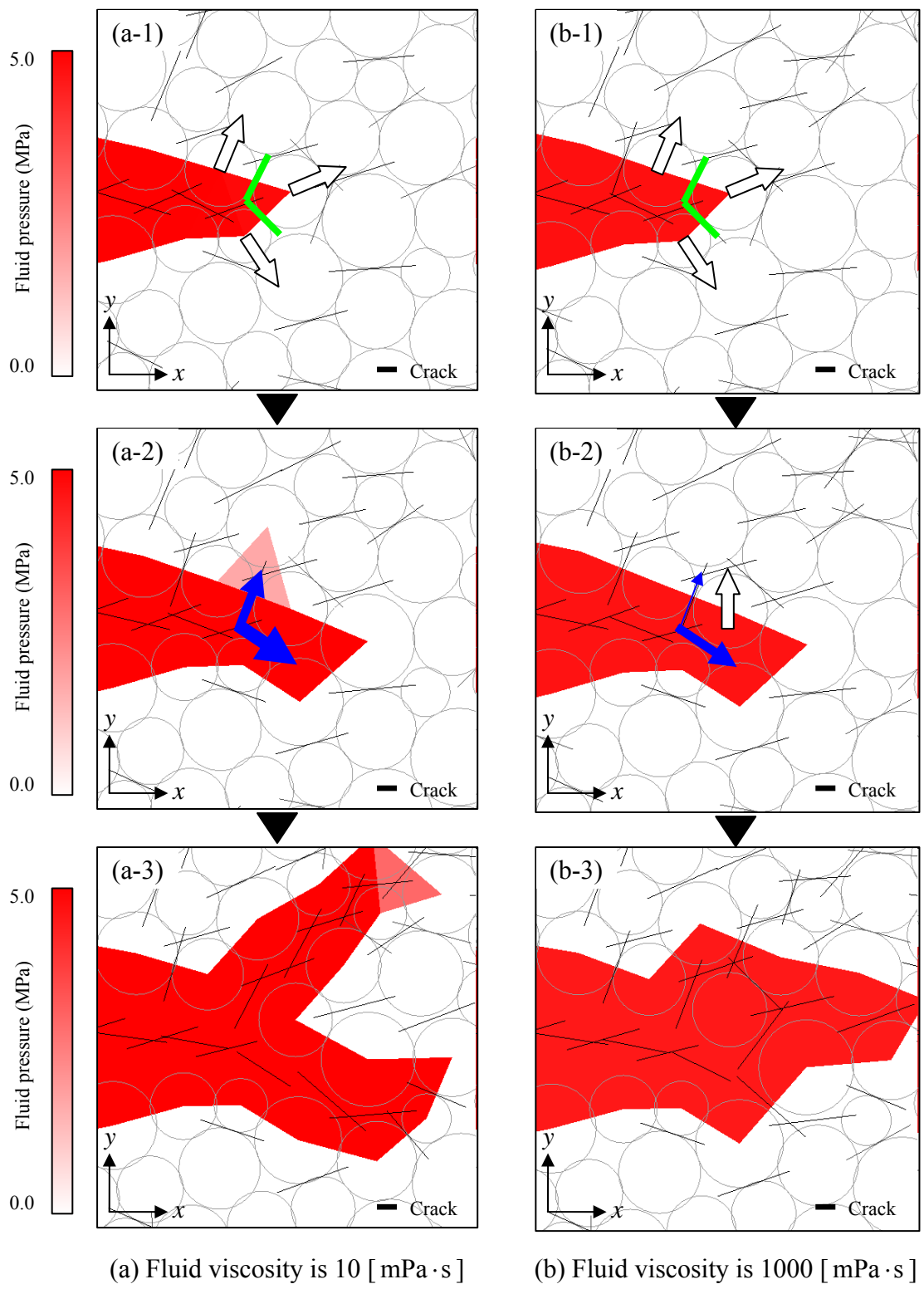
Fig.6.36   Fracture branching process.

Thus, the particle moves according to the fluid pressure, and the microcracks that branches up and down are generated as shown in Fig.6.36(a-1) and (b-1) by green solid lines. At this time, the opening of two branching microcracks becomes different according to arrangement of the particles. However, when the viscosity of the fracturing fluid is comparatively low, the fracturing fluid can be easily infiltrated into both microcracks almost simultaneously regardless of the difference of their microcrack opening. As a result, branching of the fracture occurs when the viscosity of the fracturing fluid is low as shown in Fig.6.36(a-3). On the other hand, when the viscosity of the fracturing fluid is high, the difference of microcrack opening strongly influences, and the fluid infiltrates mainly in the direction where microcrack opening is large as shown in Fig.6.36(b-2). When the fluid is infiltrated to one of the microcracks, the fluid pressure acts on the arrowed direction in Fig.6.36(b-2) and the other microcrack is shut. Thus, the difference of fluid flow for each microcrack increases more and more. As a result, the fracture goes straight without branching when the viscosity of the fracturing fluid is high as shown in Fig.6.36(b-3).

Fig.6.36 also reveals that branching of the fracture does not occur suddenly on the way of straight fracture but occurs smoothly along with the development of the fracture. Therefore, a clear difference was not seen in pressure-time curve of the LF and BF in Fig.6.28.

Moreover, as show in Fig.6.34, since large maximum principal stress is distributed in orthogonal direction of the fracture propagation, small branching fractures that exists in such region cannot be opened large. Therefore, as show in Fig.6.31, only one main fracture keeps developing and the other branching small fractures stops developing in the case of BF. In addition, the influence of the fluid pressure in the main fracture is comparatively small at the other side of the slit position. Therefore, the branching fractures can easily propagate to there. In fact, according to the experimental result of the BF in Fig.6.3(e), the branching fracture propagates to the other side of the slit position.

6.8.4 Influence of fluid injection rate

According to the discussion in previous section, when the viscosity of the fracturing fluid is large, and the permeability of the model is low, the fracture growth pattern becomes LF. Oppositely, when the viscosity of the fracturing fluid is small, and the permeability of the model is high, the fracture growth pattern becomes BF. This simulation results show good agreement with the actual experimental result shown in Table 6.1.

160

However, for the injection rate of the fracturing fluid, the simulation result shows the different tendency from the experimental results. According to the experimental result shown in Table 6.1, when the injection rate of the fracturing fluid is low, the fracture growth pattern becomes LF. Oppositely, when the injection rate of the fracturing fluid is high, the fracture growth pattern becomes BF.

On the other hand, according to the simulation result shown in Table 6.5 (in case of permeability: 5[mD], viscosity: 10[mPa·s]), when the injection rate is low (1[MPa/10^7 step]), the fracture growth pattern becomes LF. However, when the injection rate of the fracturing fluid is high (30[MPa/10^7 step]), the fracture growth pattern becomes LF.

Fluid Flow Algorithm used in this research mainly handles the change in fluid pressure, and the fluid flow is not calculated strictly though interparticle shear stress caused by viscous fluid flow is considered. When the flow velocity of the fracturing fluid in the fracture is large, the fluid pressure that acts on the particle at the fracture tip increases. This causes large opening of the branching microcracks, and the possibility of showing the fracture growth pattern of BF increases. However, neither the flow velocity of the fracturing fluid in the fracture nor fluid pressure according to it is properly considered in this simulation. As a result, the influence of fluid injection rate should be different from that observed in the actual experiment. It is necessary to develop a new algorithm that can consider the influence of the flow velocity in the fracture to discuss the influence of the injection rate of the fracturing fluid in detail.

6.9. Summary of the hydraulic fracturing behavior in the simulation

6.9.1 Maximum fluid pressure (breakdown pressure)

As shown in Fig.6.14, the maximum fluid pressure (breakdown pressure) was the largest in case of CE, and was smallest in case of NF. This result is corresponding to the experimental result that Igarashi *et al*. conducted.

In case of NF or CE, a clear fracture is not formed. For these cases, change in fluid pressure in casing pipe depends on the relation between injection rate and infiltration rate of fracturing fluid. The fluid pressure increases when the fluid infiltration is smaller than the fluid injection. Infiltration increases as the fluid pressure increases, and it becomes an equilibrium state.

When the permeability of the model is large, and the fluid viscosity and the fluid injection rate is small (in case of NF), the difference between the fluid injection and the infiltration is small. Therefore, it reaches in the equilibrium state before the fluid

pressure sufficiently increases to form a clear fracture, and the breakdown pressure becomes small.

On the other hand, when the permeability of the model is small, and the fluid viscosity and the fluid injection rate is large (in case of CE), the fluid injection is remarkably larger than the fluid infiltration. Therefore, the fluid pressure largely increases until the fluid injection and the fluid infiltration become equal.

However, when the difference between the fluid injection and the infiltration is significantly large, the fracture growth pattern does not become CE, but become LF or BF. In this case, the confining pressure strongly influences the breakdown pressure as discussed in section 6.8.2. There is a possibility of the maximum pressure is larger than that in case of the CE according to the setting of the confining pressure.

6.9.2 Interpretation by using the mobility

Fig.6.37 shows the change in pressure with distance from the slit position in direction of x-axis at the time step when the fluid pressure in the borehole reaches 4.5MPa. In a word, Fig.6.37 indicates the pressure gradient along a line from the slit position in five cases with a different fracture growth pattern. As the pressure gradient increases, the fracture growth pattern has sequentially changed into NF, CE, BF, and LF. This result indicates that the pressure gradient around the slit governs the fracture growth patterns.

In addition to the discussion of the previous section, this result also suggests that the hydraulic transmissibility of the fracturing fluid governs the fracture growth patterns in the hydraulic fracturing in unconsolidated sands because the pressure gradient is strongly affected by the hydraulic transmissibility.

The permeability of the model and the viscosity of fracturing fluid significantly influences on the hydraulic transmissibility of the fracturing fluid. Thus, the mobility (k/μ) is used as a parameter that indicates the hydraulic transmissibility of the fracturing fluid in the unconsolidated sand model. The larger the mobility is, the hydraulic transmissibility of the fracturing fluid increases, and the smaller the mobility is, the hydraulic transmissibility of the fracturing fluid decreases.

To clarify the relation between the mobility and the fracture growth pattern, additional 13 hydraulic fracturing simulations were performed. The condition and the results of the additional simulations are shown in Table 6.6. All the simulation results including existing results and new results are summarized in Table 6.7 according to the mobility. According to Table 6.7, when the mobility is large and the hydraulic transmissibility of the fracturing fluid is large, fracture growth pattern is NF. The fracture growth pattern changes in order of NF, CE, BF, and LF as the mobility

162

decreases. This result indicates that the mobility governs the fracture growth pattern in the hydraulic fracturing in unconsolidated sands.

However, even if the mobility is the same, the fracture growth pattern is different according to the combination of the viscosity of the fracturing fluid and the permeability of the model in the boundary of BF and LF. In this study, the flow rate in a flow channel is a function of the aperture between particles, and the permeability of the model is calibrated by changing assumed initial aperture w_0.
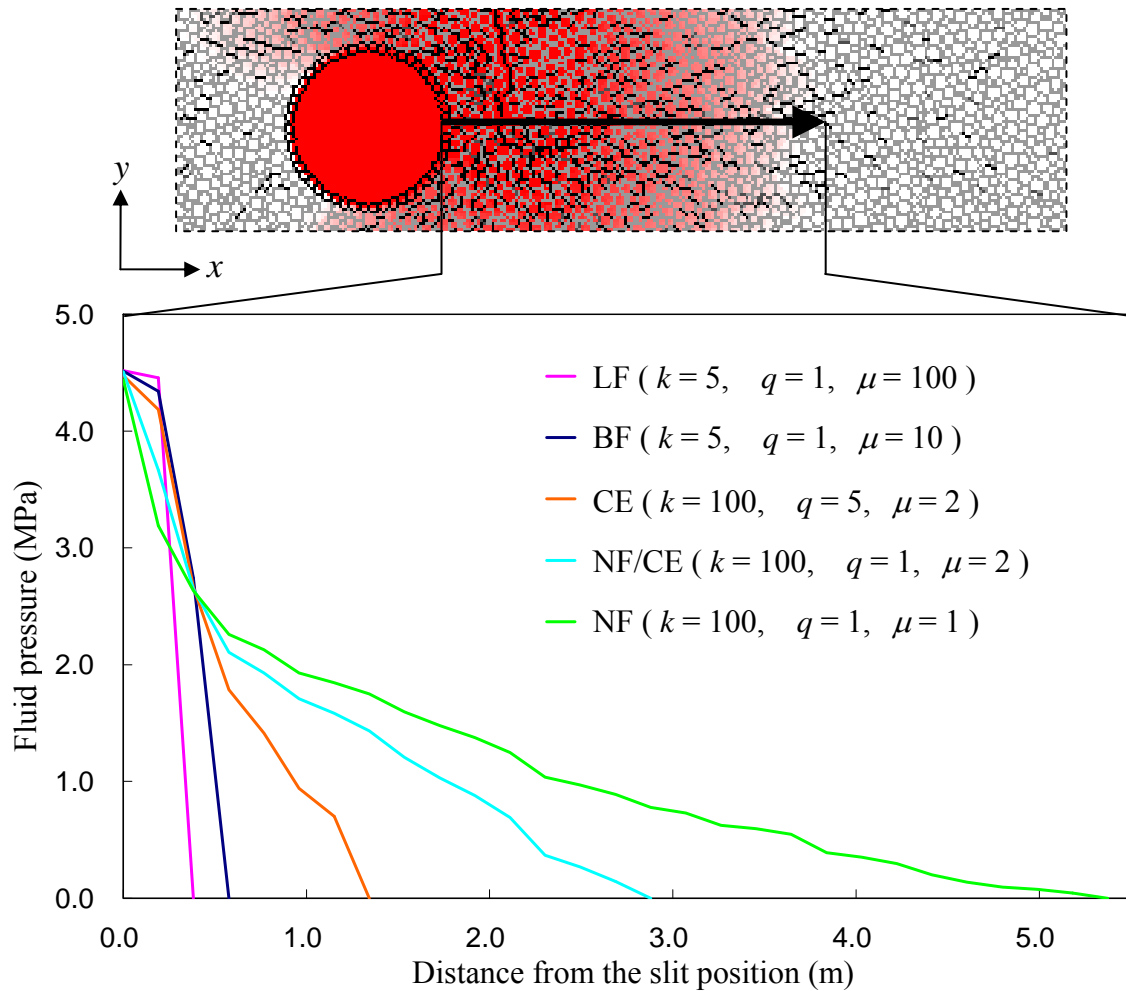
Fig.6.37   Pressure gradient for each fracture growth pattern.

Table 6.6 Classification of fracture shapes obtained from the additional simulations.
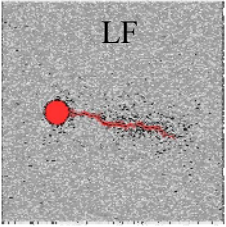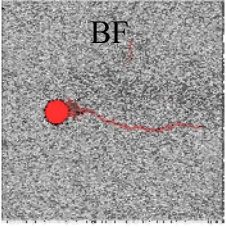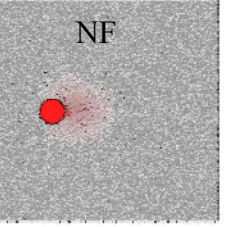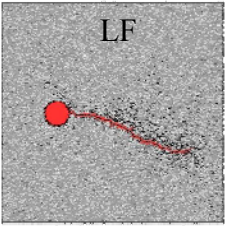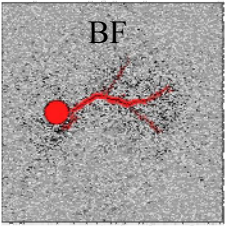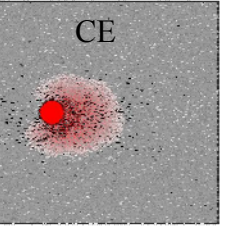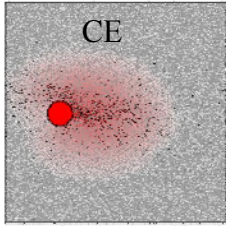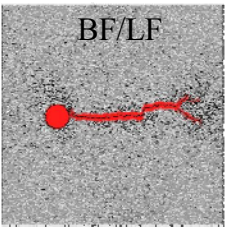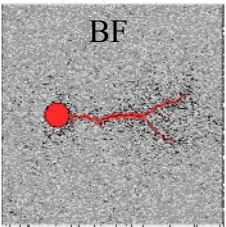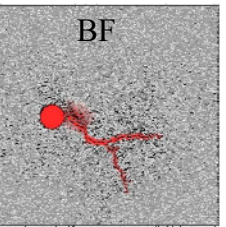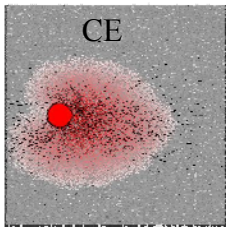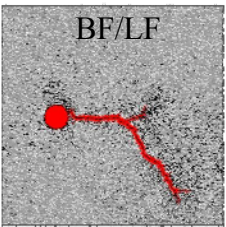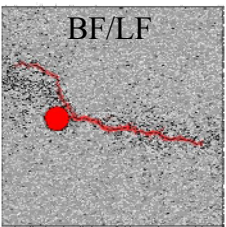
Flow rate q [MPa/10^7step]	Permeability: k = 100 [mD] Viscosity: μ = 200 [mPa $\cdot$ s]	Permeability: k = 5 [mD] Viscosity: μ = 5 [mPa $\cdot$ s]	Permeability: k = 5 [mD] Viscosity: μ = 0.1 [mPa $\cdot$ s]	Permeability: k = 5 [mD] Viscosity: μ = 0.05 [mPa $\cdot$ s]
1	LF	BF	NF	-
5	LF	BF	CE	CE
10	BF/LF	BF	BF	CE
30	BF/LF	BF/LF	-	-

Table 6.7   Classification of fracture growth patterns considering the value of the mobility.

Flow rate q [MPa/10⁷ step]	Mobility (k/μ)									
	0.005	0.05	0.1	0.5	1	2.5	5	10	50	100
	5/1000	5/100		5/10	5/5	5/2	5/1		5/0.1	5/0.05
			100/1000	100/200	100/100			100/10	100/2	100/1
1	LF	LF	LF	BF LF	BF LF	BF	BF	CE	NF NF/CE	NF
5	-	-	LF	- LF	BF LF	-	-	BF	CE CE	CE CE
10	LF	LF	-	BF/LF BF/LF	BF LF	BF	BF	BF	BF BF	CE CE
30	LF	LF	-	LF BF/LF	BF/LF BF	BF	BF			BF

(blue — 5 mD; red — 100 mD)

──── 5 mD

──── 100 mD

Therefore, when the fracture opens large as shown in the case of BF and LF, the interparticle aperture w significantly increases, and the influence of w_0, that is, the influence of the permeability of the model relatively becomes small.

On the other hand, since the influence of the viscosity of the fracturing fluid does not depend on the opening of the fracture, the viscosity of the fracturing fluid strongly influences the fracture growth pattern in case of BF and LF. As a result, as shown in Table 6.7, fracture growth pattern becomes LF when the viscosity was large, and BF when the viscosity was small.

6.10. Conclusions

A new DEM code corresponding to unconsolidated sand was developed, and the flow-coupled DEM simulations for the hydraulic fracturing were performed to gave the rational explanation to the hydraulic fracturing behavior that had been observed in the existing laboratory experiment. Totally 44 cases of hydraulic fracturing simulation varying the permeability, viscosity, and fluid injection rate were performed. These simulation results were in good agreement with the experimental results. This suggests that the DEM model may be more appropriate for the analysis of granular materials fracturing than the other numerical analysis techniques. Based on this result, the hydraulic fracturing mechanism in unconsolidated sands will be investigated in detail, and the findings are summarized as follows.

1. Pressure-time curve obtained by the simulation is classified into three typical shapes, and these correspond to the fracture growth patterns. In case of No Fracture (NF), the fluid pressure in the casing pipe rises smoothly with the fluid injection, and reaches in the equilibrium state. In case of Cavity Expansion (CE), fluid pressure rises along with the fluid injection, and the slope of pressure-time curve has changed rapidly. In case of Linear Fracture (LF) and Branched Fracture (BF), the fluid pressure decreases rapidly after it peaks. Afterwards, the fluid pressure becomes an equilibrium state.

2. In case of No Fracture (NF), since the difference between the fluid injection and the infiltration is small, the fluid pressure in the casing pipe rises smoothly with the fluid injection, and reaches in the equilibrium state before the fluid pressure sufficiently increases. Therefore, the maximum pressure becomes small. Although the clear fracture does not occur, a few microcracks were generated in the region

around the slit where the fluid pressure is relatively high. The occurrence of the microcrack and slip is led by decrease in effective stress due to the rise of fluid pressure.

3. In case of Cavity Expansion (CE), a lot of microcracks and slips occur around the slit, and a dominant flow channel with especially large flow rate is formed along with it. Since the amount of the fluid that infiltrates into the model rises significantly when the dominant flow channel is formed, the growth rate of the fluid pressure in the casing pipe decreases, and the slope of pressure-time curve suddenly changes.

4. In case of Cavity Expansion (CE), such microcracks and slips occurred in the region where the effective stress has decreased, and the surrounding of the slit becomes a complete loose region by the generation of these microcracks and slips. Moreover, a high pressure gradient exists from the slit position to the edge of the model. Therefore, particles that exist in the loosened area move from the slit position to the edge of the model due to the pressure gradient. As a result, large cavity around the slit is formed.

5. The fracture growth pattern of Shear Fracture (SF) shown in the experiment conducted by Igarashi *et al*. was not observed in the simulation. It is presumed that a major cause concerning this problem is the particle size used for the simulation. The fracture formed in case of SF is small compared with other cases, and the size of the particle in this simulation is relatively large compared with the shear fracture. Moreover, the stress state among models does not become completely uniform due to such large particles. Therefore, the clear Shear Fracture shown in the experiment is difficult to be formed in this simulation. To reproduce clear shear fracture shown in the experiment, it is necessary to imitate a micro structure of an actual specimen accurately by using a smaller particle.

6. In case of Linear Fracture (LF) and Branched fracture (BF), it is understood that the fluid pressure retains a constant value when the decrease in fluid pressure by propagation of the fracture, the increase in fluid pressure by fluid injection, and the confining pressure are in balance. Since the fracture length is shorter than the confining walls, and the maximum principal stress around the fracture is scattered at the position far from the fracture, large fluid pressure is needed so that the fluid pressure acting on the fracture surface balances the confining pressure. Therefore,

the fluid pressure in the equilibrium state is larger than the confining pressure that acting in *y*-direction.

7. When a large particle exists on the course of the fracture, the particle moves according to the fluid pressure, slips and microcracks that branches up and down are generated. When the viscosity of the fracturing fluid is comparatively low, the fracturing fluid is infiltrated into both microcracks almost simultaneously regardless of the difference of their microcrack opening. As a result, branching of the fracture occurs. On the other hand, when the viscosity of the fracturing fluid is high, fracturing fluid is infiltrated into one of the microcrack that opens large. As a result, the fracture goes straight without branching.

8. Since large maximum principal stress is distributed due to the fluid pressure in the main fracture in orthogonal direction of the fracture propagation, small branching fractures that exist in such region cannot be opened large. Therefore, as show in Fig.6.31, only one main fracture keeps developing and the branching small fractures stops developing at once in the case of BF.

9. The breakdown pressure was the largest in case of CE, and was smallest in case of NF. In case of NF or CE, change in fluid pressure in casing pipe depends on the relation between injection rate and infiltration rate of fracturing fluid. On the other hand, when the difference between the fluid injection and the infiltration is significantly large, the fracture growth pattern becomes LF or BF. In case of LF and BF, the confining pressure strongly influences the breakdown pressure.

10. The permeability of the model k and the viscosity of fracturing fluid μ significantly influences on the hydraulic transmissibility of the fracturing fluid. The mobility (k/μ) governs the fracture growth pattern in the hydraulic fracturing in unconsolidated sands. When the mobility is large and the hydraulic transmissibility of the fracturing fluid is large, fracture growth pattern is NF. The fracture growth pattern changes in order of NF, CE, BF, and LF as the mobility decreases.

References

[1] Milkov AV. Global estimates of hydrate-bound gas in marine sediments: how much is really out there? Earth-Science Reviews, 2004; 66: 183-197.

[2]   Mori A, Tamura M and Fukui Y. Fracturing pressure of soil ground by viscous materials, Soils and Foundations, Japanese Society of Soil Mechanics and Foundation Engineering, 1990; 30(3): 129-136.

[3]   Abou-Sayed A, Zaki K, Wang G, Meng F and Sarfare M. Fracture propagation and formation disturbance during injection and frac-pack operations in soft compacting rocks. In SPE Annual Technical Conference and Exhibition, Houston, TX, 2004; 26-29. (SPE 90656).

[4]   Yanagisawa E and Panah AK. Two dimensional study of hydraulic fracturing criteria in cohesive soils, Soils and Foundations. Japanese Society of Soil Mechanics and Foundation Engineering, 1994; 34(1): 1-9.

[5]   Khodaverdian M, McElfresh PM. Hydraulic fracturing stimulation in poorly consolidated sand: mechanisms and consequences. SPE Annual Technical Conference and Exhibition, 2000; 1-4. (SPE 63233).

[6]   Chang H. Hydraulic Fracturing in Particulate Materials. Ph.D thesis, Georgia Institute of Technology, 2004.

[7]   Bohloli B and de Pater CJ. Experimental study on hydraulic fracturing of soft rocks: influence of fluid rheology and confining stress. J Pet Sci Eng, 2006; 53: 1-12.

[8]   Ito T, Igarashi A and Yamamoto K. Laboratory Test of Hydraulic Fracturing in Unconsolidated Deformable Rocks, Proc. of the 4th Biot Conf. on Poromechanics, 2009;1001-1006.

[9]   Igarashi T. PhD thesis, Tohoku University, 2008. (in Japanese).

[10] Shimizu H, Murata S and Ishida T. Distinct element analysis for rock failure under uniaxial compression. Journal of MMIJ, 2008; 125(3): 91-97. (in Japanese).

[11] Shimizu H, Koyama T, Ishida T, Chijimatsu M, Fujita T and Nakama S. Distinct element analysis for ClassII behavior of rock under uniaxial compression. Int J Rock Mech Min Sci, 2009; (in press).

[12] Potyondy DO and Cundall PA. A bonded- particle model for rock. Int J Rock Mech Min Sci, 2004; 41: 1329-1364.

[13] Kiyama H, Nishimura T and Fujimura H. An advanced distinct element model coupling with pore water. J Geotec Eng, 1994; 499(III-28): 31-39.

[14] Okada Y and Ochiai H. Numerical analysis of changes in pore-pressure in undrained triaxial-compression tests. Journal of the Japan Landslide Society, 2007; 44(1): 15-24.

[15] Maeda K and Hirabayashi H. Influence of Grain Properties on Macro Mechanical Behaviors of Granular Media by DEM. J Appl Mech, 2006; 9: 623-630.

Chapter 7
Concluding remarks

In this thesis, the Distinct Element Method (DEM) code that can model not only the fundamental microcracking behavior in brittle materials but also hydraulic fracturing behavior in consolidated and unconsolidated materials is presented, and a series of simulations are performed by own DEM code in order to solve many rock mechanics problems as mentioned in Chapter 1. The main conclusions drawn from the present study are summarized as follows.

In chapter2, summary of the Distinct Element Method (DEM) code used in this research had been presented, and a series of rock test simulations, such as uniaxial compression test, uniaxial tension test and Brazilian test are performed to investigate the effects of particle number and size distribution on macroscopic mechanical properties of rock models. Each simulation result is in good agreement with actual experimental results conducted by previous researchers, and the findings obtained from this study can be summarized as follows. The variation of calculated values of macroscopic mechanical properties decreases with increasing the number of particles. When the number of particles is 10000 or more, stable results are obtained as a rock test. Moreover, macroscopic mechanical properties of rock model, such as uniaxial compressive strength, Young's modulus and uniaxial tensile strength are significantly affected by porosity of the rock model. Since small particles fill the space among large particles, the porosity of the rock model decreases with increasing the maximum/minimum radius ratio of the particles, and particles are densely packed in the rock model. When the particle is closely arranged, the displacement of each particle is restrained with the adjacent particles even if the bond between particles breaks. As a result, the macroscopic mechanical properties of rock model increase greatly.

In chapter3, as the fundamental research of rock fracturing, the uniaxial compression test of rock was simulated by using the DEM and discussed the influence of the slip at crack surface to a relative number of AE events. Simulation result is well in agreement with the AE activities observed in an actual experiment. Moreover, it provides the new findings to solve the disagreement; the conventional theories and microscopic observations suggest that tensile cracks cause AE events, whereas an abundance of shear AE events is observed in the experiments. The simulation results indicate that the energy released from a tensile crack is very small compared with that from a shear crack, due to the tensile strength much smaller than the compressive strength. Since it is thought that such a small AE is easily buried in a noise and hard to be measured in an

experiment, shear AE events would be observed dominantly in an actual AE monitoring experiment. These results, including the new findings to solve the conflict, indicate that DEM is an effective numerical analysis technique for studying the dynamics of microcracking in brittle materials like rock. According to the simulation, AE mainly generated from new tensile cracks when the stress level is low, and the main sources of AE shift to the slip at the existing crack surface as the macroscopic failure approaches. This result suggests that the burst of AE events during the formation of macroscopic fractures is led by the slip occurrence at the existing crack surface.

In chapter4, the Class II behavior of rocks was simulated by introducing the radial strain control method for uniaxial compression tests in the Distinct Element Method (DEM) codes. The microscopic parameters used in the DEM models were determined based on laboratory uniaxial compression tests and Brazilian tests carried at Äspö Hard Rock Laboratory, Sweden. The numerical simulation results show good agreement with the complete stress-strain curves for Class II obtained from the laboratory experiments. These results suggest that the DEM can reproduce the Class II behavior of the rock successfully and have made possible the discussion on the mechanism of the Class II behavior in detail from the microscopic point of view. The results have also clarified that the loading condition and microscopic structure of rocks will play an important role for the Class II behavior.

In chapter5, a series of simulations for hydraulic fracturing in hard rock was performed by using the flow-coupled DEM code to discuss the influence of the fluid viscosity and the particle size distribution. The simulation results show good agreement with the actual experimental results that contains the AE measurement data. As a result, the followings were found. When the low viscous fluid is used, the fluid is infiltrated into the fracture instantaneously. On the other hand, when the highly viscous fluid is used, the fluid is infiltrated slowly into the crack after the fracture extends first. Although most of cracks in all cases were tensile cracks as theoretically expected, a few shear cracks are generated during the fracture propagation. When the fluid pressure acting on the fracture tip sufficiently increase, shear cracks that emit significantly large energy are formed to connect these tensile cracks. This fracturing process is similar to the Hill's model which is originally proposed for volcanic earth quake swarms. In addition, shear cracks are also generated even when the fracturing fluid did not infiltrated into the fracture. Although the macroscopic fracture seems to develop straight, individual micro cracks are generated in various directions along the direction of the particle boundary. When the particle boundary located diagonally across the direction of maximum confining stress, confining stress and borehole pressure act on the particle

boundary as shear stress. Thus, shear cracks generated along the grain boundaries that diagonally across the direction of maximum confining stress. In addition, although the tensile cracks are dominantly generated in the simulation, the energy released from a tensile crack becomes small because the tensile strength of rock is obviously small compared with the compressive strength. Such a small AE is easily buried in a noise and hard to be measured in an experiment. Therefore, in AE measurement experiments, shear type of AE with large energy is dominantly observed.

In chapter6, the flow-coupled DEM simulations are performed to better understand the hydraulic fracturing mechanism in unconsolidated sands. Totally 44 cases of hydraulic fracturing simulation varying the permeability, viscosity, and fluid injection rate was performed. As a result, four types of fracture growth patterns, such as No Fracture (NF), Cavity Expansion (CE), Linear Fracture (LF) and Branched Fracture (BF) were successfully simulated, and it is found that the fracturing behavior is obviously affected by the viscosity of fracturing fluid and the permeability of the specimen. These simulation results were in good agreement with the experimental results, and gave the rational explanation to the hydraulic fracturing behavior that had been observed in the existing laboratory experiment. The permeability of the model k and the viscosity of fracturing fluid μ significantly influences on the hydraulic transmissibility of the fracturing fluid. The mobility (k/μ) that indicates the hydraulic transmissibility of the fracturing fluid governs the fracture growth pattern in the hydraulic fracturing in unconsolidated sands. When the mobility is large and the hydraulic transmissibility of the fracturing fluid is large, fracture growth pattern is NF. The fracture growth pattern changes in order of NF, CE, BF, and LF as the mobility decreases.

The DEM model induces complex macroscopic behaviors without using complicated constitutive laws, and realistic representation of fracturing behavior both in consolidated and unconsolidated materials. The results of the DEM simulation could explain many rock mechanics problems observed in the laboratory experiments conducted by previous researchers. However, all the works presented in this thesis are in two-dimensional and in laboratory scale. For the successful design of various rock engineering projects, such as the production of hydrocarbon reservoirs, exploitation of geothermal energy, the long-term disposal of High-level Radioactive Waste (HLW), more detailed analysis using not only two-dimensional simulation but also three-dimensional and field scale simulation would be required according to the situation of each engineering problems. This is my future work.

APPENDIX
Calculation procedure for the stress distribution in DEM model

In the DEM, a particle is in contact with a lot of particles, and the contact forces, such as normal and tangential force acting on each contact point, are calculated individually. These contact forces are in various directions according to the direction of contact. Therefore, to discuss the stress state in the DEM model, the contact forces acting on each contact point should be converted into the stress distribution. In this research, the stress acting on a particle is calculated by the following procedure.

As shown in Fig.A.1, the normal and tangential contact force f_n and f_s are acting on a particle, and the imaginary forces f_n' and f_s' are assumed. The two sets of forces f_n' and f_n, f_s' and f_s are of the same magnitude and opposite in direction, respectively. The normal force f_n is parallel to the x-axis. Suppose that these forces are acting on a small area as shown in Fig.A.1, and being in equilibrium. The stresses that acts on the small area are given by

$$\sigma_x = \frac{f_n}{D} \tag{A.1}$$

$$\sigma_y = 0 \tag{A.2}$$

$$\tau = \frac{f_s}{D} \tag{A.3}$$

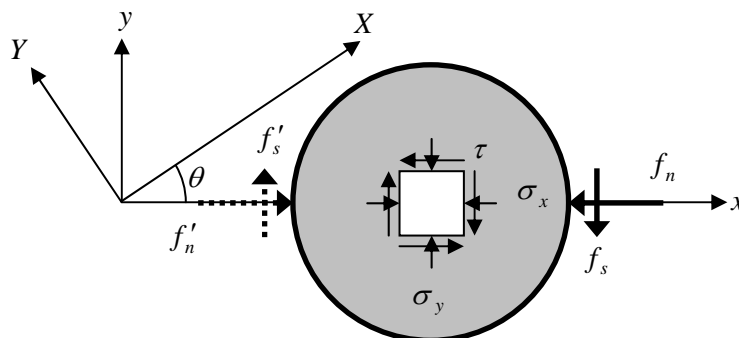where D is contact width that given by equation (2.5).

Fig.A.1　Normal and shear stress acting on a particle.

Then, the normal and shear stresses, σ_x, σ_y, and τ_{xy} are obtained at the center of the particle, expressed with respect to the local coordinates xy. As shown in Fig.2.7, the new global coordinate set XY will now be considered, and the new stresses, σ'_x, σ'_y, and τ'_{xy} expressed in the global coordinate set XY are given by

$$\sigma'_x = \frac{\sigma_x + \sigma_y}{2} - \frac{\sigma_x - \sigma_y}{2} \cdot \cos 2\theta + \tau_{xy} \sin 2\theta \tag{A.4}$$

$$\sigma'_y = \frac{\sigma_x + \sigma_y}{2} - \frac{\sigma_x - \sigma_y}{2} \cdot \cos 2\theta - \tau_{xy} \sin 2\theta \tag{A.5}$$

$$\tau'_{xy} = -\frac{\sigma_x - \sigma_y}{2} \cdot \sin 2\theta + \tau_{xy} \cos 2\theta \tag{A.6}$$

where θ is an rotation angle from the local coordinates xy. Counterclockwise angles are positives.

These calculations are applied to all contact points of one particle, and the total stresses, σ_X, σ_Y, and τ_{XY} are obtained from the accumulation of the stress at each contact point. Since the imaginary forces f'_n and f'_s are assumed, the total stresses are divided by two. The total stresses, σ_X, σ_Y, and τ_{XY} are given by

$$\sigma_X = \frac{\sum \sigma'_{xi}}{2} \tag{A.7}$$

$$\sigma_Y = \frac{\sum \sigma'_{yi}}{2} \tag{A.8}$$

$$\tau_{XY} = \frac{\sum \tau'_{xyi}}{2} \tag{A.9}$$

Consequently, the stresses that act on the each particle are obtained. However, these are discrete data. To investigate the tendency and/or the character of the stress distribution in detail, the continuation of obtained discrete data (interpolation) is necessary. In this research, Inverse Distance Weighting (IDW) was used as a technique for interpolation.

As shown in Fig.2.8, IDW is one of the most commonly used techniques for interpolation, and based on the assumption that the interpolating surface is a weighted average of the discrete data and the weight assigned to each discrete data diminishes as

the distance from the interpolation point to the data point increases. The simplest form of IDW is called "Shepard's method" [1]. The equation used is as follows:

$$Z_j = \frac{\sum_{i=1}^{n} Z_i \cdot d_{ij}^{-m}}{\sum_{i=1}^{n} d_{ij}^{-m}} \tag{A.10}$$

where Z_j denotes an interpolated (arbitrary) value, Z_i is an discrete data (i=1,2,…,n), d_{ij} is the distance from the data point to the interpolation point. n is the total number of data points within the maximum distance from the interpolation point. m is a positive real number, called the power parameter and controls how the weighting factors drop off as distance from the reference point increases. For $0 < m < 1$ interpolated value Z_j has smooth peaks over the interpolated points, while as $m > 1$ the peaks become sharp. Here, the maximum distance from the interpolation point to the data point is four times as large as maximum particle radius in DEM simulation, and the power parameter r=1 is employed in this research.

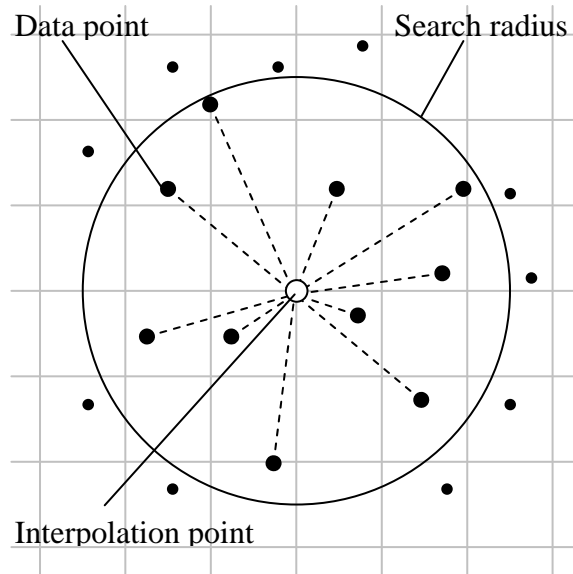
Fig.A.2   Concept of Inverse Distance Weighting (IDW).

References

[1] Shepard D. A two-dimensional interpolation function for irregularly-spaced data. Proc. of the 1968 ACM National Conference, 1968; 517-524.

PUBLICATION LIST
-Relating to this work-

Chapter 2
-Publications Appearing in Peer-Reviewed Scientific Journals-

1. **Shimizu H**, Murata S and Ishida T., Effects of particle number and size distribution on macroscopic mechanical properties of rock models in DEM, Journal of the society of materials science, Japan, (2009) (in press) (in Japanese)

Chapter 3
-Publications Appearing in Peer-Reviewed Scientific Journals-

2. **Shimizu H**, Murata S and Ishida T., The applicability of distinct element modeling for rock fracture, Journal of the Mining and Materials Processing Institute of Japan, Vol.124, No.12, pp.777-784 (2008) (in Japanese)

3. **Shimizu H**, Murata S and Ishida T., Distinct element analysis for rock failure under uniaxial compression, Journal of the Mining and Materials Processing Institute of Japan, Vol.125, No.3, pp.91-97 (2009) (in Japanese)

-Publications Appearing in Refereed Conference Proceedings-

a) <u>**Shimizu H.**</u>, Murata S. and Ishida T., Distinct element analysis for rock fracturing under uniaxial compression, Proc. of EIT-JSCE Joint Seminar on Rock Engineering 2007 (Bangkok, Thailand) September-2007

b) <u>**Shimizu H.**</u>, Murata S. and Ishida T., Distinct element analysis for rock failure considering AE events generated by the slip at crack surfaces, Proc. of 19th International Acoustic Emission Symposium (Kyoto, Japan) December-2008

Chapter 4
-Publications Appearing in Peer-Reviewed Scientific Journals-

4. **Shimizu H**, Koyama T, Ishida T, Chijimatsu M, Fujita T and Fujita T, Numerical simulations for Class II behavior of rocks under uniaxial compression using Distinct Element Method, Journal of the Mining and Materials Processing Institute of Japan, (2009) (in press) (in Japanese)

5. **Shimizu H**, Koyama T, Ishida T, Chijimatsu M, Fujita T and Nakama S, Distinct element analysis for ClassII behavior of rock under uniaxial compression, International Journal of Rock Mechanics and Mining Sciences, (2009), doi:10.1016/j.ijrmms.2009.09.012

Chapter 5

-Publications Appearing in Peer-Reviewed Scientific Journals-

6. **Shimizu H**, Murata S and Ishida T., The distinct element analysis for hydraulic fracturing with fluid having different viscosity, Journal of the Mining and Materials Processing Institute of Japan, (2009) (to be submitted) (in Japanese)

-Publications Appearing in Refereed Conference Proceedings-

c) **<u>Shimizu H.</u>**, Murata S., Ito T. and Ishida T., Distinct element modeling for hydraulic fracturing, Proc. of The Fifth International Conference on Flow Dynamics (Sendai, Japan) November-2008

d) **<u>Shimizu H.</u>**, Murata S. and Ishida T., The Distinct element analysis for hydraulic fracturing considering the fluid viscosity, Proc. of 43rd U.S.Rock Mechanics (Asheville, USA) June -2009

Chapter 6

-Publications Appearing in Refereed Conference Proceedings-

e) **<u>Shimizu H.</u>**, Murata S., Ito T. and Ishida T. Distinct Element Modeling for Hydraulic Fracturing in Unconsolidated Sands, Proc. of The Sixth International Conference on Flow Dynamics (Sendai, Japan) November-2009